

**Impact of Poly(ADP-ribose) polymerase 1
on phenotypic and molecular features
in *KRAS*-driven intrahepatic
cholangiocarcinoma**

Dissertation
zur Erlangung des Grades
Doktor der Naturwissenschaften

am Fachbereich Biologie
der Johannes Gutenberg-Universität Mainz

vorgelegt von Friederike Luise Keggenhoff, geb. Mahn
geboren am 27.08.1990 in Mainz, Deutschland

Mainz, Januar 2022

Erklärung

Hiermit erkläre ich an Eides statt, dass ich diese Arbeit selbständig verfasst und keine anderen als die angegebenen Quellen und Hilfsmittel verwendet habe.

Ort, Datum

Friederike Keggenhoff

Dekan: [REDACTED]

1. Berichterstatter: [REDACTED]

2. Berichterstatter: [REDACTED]

Tag der mündlichen Prüfung: 03.05.2022

Abstract

Intrahepatic cholangiocarcinoma (iCCA) is the second most common primary liver cancer with an increasing incidence over recent decades. Due to the complex pathogenesis and pronounced genetic heterogeneity of iCCA, treatment options are still limited, and the prognosis of patients remains dismal. Activating *KRAS* mutations are observed in around 12-16% of iCCA patients and characterized by poor response to chemotherapy and reduced overall survival, highlighting the need for novel therapeutic approaches in this subgroup. Several findings indicate that expression of DNA damage response protein Poly (ADP-ribose) polymerase 1 (PARP-1) is preferentially enhanced in *KRAS*-mutant tumors. However, the exact role of PARP-1 in cholangio-carcinogenesis is poorly understood. In this study, we investigated the impact of *PARP-1* in *KRAS*-mutant iCCA *in vitro* and *in vivo*. *PARP-1* depletion was generated by siRNA-mediated knockdown and CRISPR/Cas9-mediated knockout and impact on proliferation *in vitro* was analyzed by viability assay as well as colony and sphere formation. Further, we examined induction of DNA damage response, apoptosis, and oxidative stress upon PARP-1 knockout and control conditions. To investigate impact of PARP-1 deficiency in *KRAS*-driven tumor initiation, we combined a *PARP-1* knockout mouse model with an inducible *KRAS*-driven mouse model using hydrodynamic tail vein injection (HDTV). Transcriptome analyses of CRISPR/Cas9 *PARP-1* knockout clones and *in vivo* tumor samples were employed to further investigate molecular mechanisms. siRNA-mediated knockdown of *PARP-1*, as well as treatment with PARP-1 inhibitor olaparib preferentially impaired cell viability and tumorigenicity in *KRAS*-mutated cell lines. Further, *KRAS*-mutated cell lines showed higher induction of DNA double-strand breaks and enhanced ROS levels upon PARP-1 knockout compared to wildtype cells. *PARP-1* deficiency further considerably impaired biliary carcinogenesis and induced a shift from dominant iCCA towards HCC phenotype in a *KRAS*-dependent manner *in vivo*. Transcriptome analyses of CRISPR/Cas9 *PARP-1* knockout clones and *in vivo* tumor specimens revealed differential expression of DNA damage response pathways as well as other cellular pathways known to be affected by PARP-1, e.g. inflammation, oxidative stress, and cell death signaling. Altogether, this study delineates a preferential sensitivity of *KRAS*-mutant iCCA towards PARP-1-based interventions. PARP-1 inhibition induces functional impairment of tumorigenic capacity as well as oxidative stress response. Integration of *in vivo* and *in vitro* transcriptomic data with different established prognostic subgroups of PLC, demonstrated that *KRAS*-mutant iCCA switch from poor to good prognosis upon *PARP-1* depletion. Taken together, these findings suggest an unrecognized prognostic and therapeutic role of *PARP-1* in iCCA patients with oncogenic *KRAS* signaling.

Zusammenfassung

Das intrahepatische Cholangiokarzinom (iCCA) ist der zweithäufigste primäre Leberkrebs mit steigender Inzidenz in den letzten Jahrzehnten. Aufgrund der komplexen Pathogenese und der ausgeprägten genetischen Heterogenität sind die Behandlungsmöglichkeiten weiterhin begrenzt und die Prognose der Patienten eingeschränkt. Aktivierende *KRAS*-Mutationen werden bei etwa 12-16% der iCCA-Patienten beobachtet. Diese sind durch ein schlechtes Ansprechen auf Chemotherapie und reduzierte Überlebensdauer gekennzeichnet, was den Bedarf an neuen therapeutischen Ansätzen unterstreicht. Mehrere Studien deuten darauf hin, dass die Expression des DNA-Reparaturproteins Poly(ADP-Ribose)-Polymerase 1 (*PARP-1*) in *KRAS*-mutierten Tumoren signifikant erhöht ist. Die genaue Rolle von *PARP-1* in der Cholangiokarzinogenese ist jedoch kaum erforscht. Ziel dieser Studie war die Untersuchung des Einflusses von *PARP-1* in *KRAS*-mutierten iCCA *in vitro* und *in vivo*. Die *PARP-1*-Depletion wurde durch siRNA-vermittelten Knockdown und CRISPR/Cas9-vermittelten Knockout erzeugt und mittels Viabilitätsassay und Kolonie- und Sphärenbildung der Einfluss auf die Proliferation *in vitro* analysiert. Weiterhin wurde die Induktion von DNA-Reparaturmechanismen, Apoptose und oxidativem Stress nach *PARP-1* Knockout untersucht. Um die Auswirkungen der *PARP-1*-Depletion auf die *KRAS*-induzierte Tumorigenität *in vivo* zu untersuchen, kombinierten wir ein *PARP-1*-Knockout-Mausmodell mit einem *KRAS*-induzierten Mausmodell unter Verwendung der hydrodynamischen Schwanzveneninjektion (HDTV). Transkriptomanalysen von CRISPR/Cas9-*PARP-1*-Knockout-Klonen und *in vivo*-Tumorproben wurden durchgeführt, um die molekularen Mechanismen weiter zu untersuchen. Der siRNA-vermittelte Knockdown von *PARP-1* sowie die Behandlung mit dem *PARP-1*-Inhibitor Olaparib beeinträchtigten bevorzugt die Zellviabilität und Tumorigenität in *KRAS*-mutierten Zelllinien. Außerdem zeigten *KRAS*-mutierte Zelllinien eine höhere Induktion von DNA-Doppelstrangbrüchen und erhöhte ROS-Werte nach *PARP-1*-Knockout im Vergleich zu Wildtyp-Zellen. *In vivo* führte die *PARP-1*-Depletion außerdem zu einer Veränderung der Gallengangskarzinogenese, die eine Verschiebung vom iCCA- zum HCC-Phänotyp in einer *KRAS*-abhängigen Weise induziert. Transkriptomanalysen von CRISPR/Cas9-*PARP-1*-Knockout-Klonen und *in vivo* Tumorproben zeigten eine unterschiedliche Expression von DNA-Schadens-reaktionswegen sowie anderer zellulärer Wege, von denen bekannt ist, dass sie von *PARP-1* beeinflusst werden, z. B. Entzündung, oxidativer Stress und Apoptose. Insgesamt beschreibt diese Studie eine spezifische Sensitivität von *KRAS*-mutierten iCCA gegenüber *PARP-1*-basierten Interventionen. *PARP-1*-Inhibition induziert eine funktionelle Beeinträchtigung der tumorigenen Kapazität sowie der oxidativen Stressantwort. Die Integration von *in vivo* und *in vitro* transkriptomischen Daten mit verschiedenen etablierten prognostischen Untergruppen von primären Lebertumoren zeigte, dass *KRAS*-mutierte iCCA bei *PARP-1*-Depletion von einer schlechten zu einer guten Prognose wechseln. Zusammengefasst deuten diese Ergebnisse auf eine unerkannte prognostische und therapeutische Rolle von *PARP-1* bei iCCA-Patienten mit onkogener *KRAS*-Aktivität hin.

Table of content

List of figures	IV
List of tables	VII
List of abbreviations	VIII
1. Introduction	1
1.1 General aspects of the biliary tract cancer.....	1
1.1.1 Classification of cholangiocarcinoma.....	1
1.1.2 Epidemiology and risk factors of iCCA.....	3
1.1.3 Diagnosis and biomarker of iCCA.....	3
1.1.4 Cells of origin	4
1.1.5 Signaling and molecular networks implicated in intrahepatic cholangio- carcinogenesis.....	6
1.1.6 Therapeutic options in iCCA	11
1.1.7 Models to study iCCA	12
1.2 Poly(ADP-ribose) polymerases.....	16
1.2.1 Role of PARP-1 in DNA damage response	17
1.2.2 Pro-tumorigenic properties of PARP-1 beyond DNA damage response	19
1.2.3 Drugs targeting PARP-1	21
2. Aim	23
3. Materials and methods	24
3.1 Materials	24
3.1.1 Electronic devices and laboratory equipment	24
3.1.2 Consumables.....	25
3.1.3 Chemicals and reagents	27
3.1.4 Primary cell lines, established cell lines, and bacteria	29
3.1.5 Oligonucleotides	29
3.1.6 Enzymes	30
3.1.7 Antibodies	31
3.1.8 Kits and mass rulers	32
3.1.9 Inhibitors	32
3.1.10 Software.....	32
3.2 <i>In vitro</i> experiments.....	34
3.2.1 Cell culture	34
3.2.2 Transfection of iCCA cell lines	34
3.2.3 Functional assays	35
3.2.4 Immunofluorescence staining of iCCA cell lines	37

3.2.5	Western Blot	38
3.2.6	DNA isolation	39
3.2.7	RNA isolation	39
3.2.8	Next-Generation Sequencing	41
3.3	<i>In vivo</i> experiments	42
3.3.1	Hydrodynamic tail vein injection	42
3.3.2	Histology and immunohistochemistry	43
3.4	Statistical analysis.....	44
4.	Results	45
4.1	Clinicopathological information of iCCA patients	45
4.1.1	Frequency of <i>KRAS</i> mutation in iCCA patient cohorts.....	46
4.2	Transcriptomic analyses of Mainz iCCA patient cohort	47
4.3	<i>PARP-1</i> and <i>KRAS</i> expression in CCA databases	53
4.4	<i>PARP-1</i> expression in primary and established cholangio-carcinoma cell lines	56
4.5	<i>PARP-1</i> inhibition via Olaparib treatment	57
4.5.1	Transient <i>PARP-1</i> inhibition by Olaparib in iCCA cell lines	58
4.6	siRNA-mediated knockdown of <i>PARP-1</i> expression in iCCA cell lines	60
4.6.1	Functional effects of siRNA-mediated <i>PARP-1</i> knockdown in iCCA cell lines	61
4.7	CRISPR/Cas9-mediated <i>PARP-1</i> knockout of iCCA cell lines	62
4.7.1	Functional analyses of CRISPR/Cas9-mediated <i>PARP-1</i> knockout in iCCA cell lines.....	64
4.7.2	Transcriptomic profiling of CRISPR/Cas9-mediated <i>PARP-1</i> knockout	72
4.8	iCCA tumor initiation via hydrodynamic tail vein injection in <i>Parp-1^{+/+}</i> and <i>Parp-1^{-/-}</i> mice	81
4.8.1	Histology and immunohistochemistry staining of HDTV-induced tumor tissue sections	82
4.8.2	Quantification of HDTV-induced tumor burden	90
4.8.3	Histopathological assessment and classification of HDTV-induced tumor tissue sections	92
4.8.4	Transcriptomic profiling of HDTV-induced tumor samples.....	93
4.9	Integrative prognostic analysis of <i>PARP-1</i> depletion <i>in vitro</i> and <i>in vivo</i>	102
5.	Discussion.....	105
5.1	<i>PARP-1</i> expression is abundant in <i>KRAS</i> -mutant iCCA and correlates with poor prognosis	105
5.2	<i>KRAS</i> -mutant iCCAs show preferential sensitivity towards <i>PARP-1</i> inhibition <i>in vitro</i>	108
5.3	Ambiguous effects of CRISPR/Cas9-mediated <i>PARP-1</i> knockout clones on DNA damage and oxidative stress.....	110

5.4	Impact of <i>PARP-1</i> depletion on transcriptomic profile of <i>KRAS</i> -mutant iCCA cell lines	111
5.5	Hepatobiliary carcinogenesis is altered in <i>Kras/Tp53</i> -driven tumors under <i>Parp-1</i> deficiency	113
5.6	Impact of <i>Parp-1</i> deficiency on transcriptomic profile of <i>Kras/Tp53</i> -induced cholangiocarcinogenesis via HDTV	115
5.7	<i>PARP-1</i> expression as prognostic factor in <i>KRAS</i> -mutant iCCA	116
6.	Summary.....	118
7.	References.....	XI
8.	Appendix.....	XXIII

List of figures

Figure 1.1: Anatomical architecture of the biliary tract and classification of cholangio-carcinoma.	2
Figure 1.2: Potential cell of origin of intrahepatic cholangiocarcinoma.	5
Figure 1.3: Signaling pathways involved in molecular pathology of iCCA.	7
Figure 1.4: Inflammation-related signaling pathways and tumor micro-environment in iCCA.	10
Figure 1.5: Principle of hydrodynamic tail vein injection.	14
Figure 1.6: PARP domains, PARylation and PAR turnover.	16
Figure 1.7: Function of PARP-1 in detection and repair of DNA damage.	18
Figure 1.8: Role of PARP-1 beyond DNA damage response.	20
Figure 3.1: Structure of HDTV constructs.	43
Figure 4.1: Differential gene expression in <i>KRAS</i> -mutant tumor versus matched normal surrounding liver tissue.	47
Figure 4.2: Canonical pathways and toxicity analyses of <i>KRAS</i> -mutant tumor versus matched normal surrounding liver tissue.	49
Figure 4.3: Enriched gene sets in <i>KRAS</i> -mutant tumor tissue versus matched normal surrounding liver tissue.	50
Figure 4.4: Expression of DNA damage response genes in <i>KRAS</i> -mutant and <i>KRAS</i> -wildtype iCCA tumor tissue.	51
Figure 4.5: Differential gene expression between <i>KRAS</i> -mutant tumor versus <i>KRAS</i> -wildtype tumor tissue normalized to normal liver tissue.	52
Figure 4.6: Microarray analysis of <i>PARP-1</i> expression.	53
Figure 4.7: GEPIA2 transcriptomic and correlation analysis of <i>PARP-1</i> and <i>KRAS</i> expression in TCGA and GTEx database.	54
Figure 4.8: Correlation and expression analysis of <i>PARP-1</i> -associated gene set on a CCA tissue microarray.	55
Figure 4.9: Transcriptomic and protein expression of PARP-1 in primary and established iCCA cell lines.	56
Figure 4.10: Determination of IC50 values of Olaparib treatment in primary and established iCCA cell lines.	57
Figure 4.11: Effect of PARP-1 inhibition via Olaparib treatment on colony and sphere formation capacity.	58
Figure 4.12: Cell viability of <i>KRAS</i> -mutant and <i>KRAS</i> -wildtype iCCA cell lines after combined treatment with Olaparib and DNA-damaging agent Doxorubicin.	59
Figure 4.13: PARP-1 protein expression in primary and established iCCA cell lines after siRNA-mediated knockdown.	60
Figure 4.14: Effect of siRNA-mediated knockdown of <i>PARP-1</i> on colony and sphere formation capacity.	61
Figure 4.15: PARP-1 protein expression in primary and established iCCA cell lines after CRISPR/Cas9-mediated knockout.	62
Figure 4.16: Morphology of <i>KRAS</i> -mutant and <i>KRAS</i> -wildtype iCCA cell lines and their respective <i>PARP-1</i> KO clones.	63

Figure 4.17: Determination of IC50 values of Olaparib treatment in <i>PARP-1</i> KO clones.....	64
Figure 4.18: Effect of <i>PARP-1</i> KO on colony and sphere formation capacity.....	65
Figure 4.19: Cell viability of <i>PARP-1</i> KO clones after treatment with DNA-damaging agent Doxorubicin.....	66
Figure 4.20: Determination of induction of DNA damage response via irradiation..	67
Figure 4.21: Determination of IC50 value of cisplatin treatment in <i>PARP-1</i> KO clones.....	68
Figure 4.22: Determination of induction of DNA damage response after cisplatin treatment.....	70
Figure 4.23: Determination of oxidative stress of <i>PARP-1</i> KO clones.....	72
Figure 4.24: Differential gene expression in <i>KRAS</i> -mutant iCCA cell lines upon <i>PARP-1</i> KO versus control clones.....	73
Figure 4.25: Canonical pathways and toxicity analyses of <i>KRAS</i> -mutant iCCA cell lines upon <i>PARP-1</i> KO versus control clones.....	74
Figure 4.26: Enriched gene sets in <i>KRAS</i> -mutant iCCA cell lines upon <i>PARP-1</i> KO versus control clones.....	75
Figure 4.27: Canonical pathways and toxicity analyses of <i>KRAS</i> -mutant versus <i>KRAS</i> -wildtype iCCA cell lines upon <i>PARP-1</i> KO.....	77
Figure 4.28: Enriched gene sets in <i>KRAS</i> -mutant versus <i>KRAS</i> -wildtype iCCA cell lines upon <i>PARP-1</i> KO.....	78
Figure 4.29: Expression of DNA damage response genes in <i>KRAS</i> -mutant and <i>KRAS</i> -wildtype iCCA cell lines.....	79
Figure 4.30: Differential gene expression genes in <i>KRAS</i> -wildtype iCCA cell lines upon <i>PARP-1</i> KO versus control clones.....	80
Figure 4.31: Experimental design of iCCA tumor initiation via hydrodynamic tail vein injection in <i>Parp-1^{+/+}</i> and <i>Parp-1^{-/-}</i> mice.....	81
Figure 4.32: Histology of liver sections injected with <i>Kras/Trp53</i> via HDTV.....	83
Figure 4.33: Immunohistochemistry staining of liver sections of mice injected with <i>Kras/Trp53</i> via HDTV.....	85
Figure 4.34: Quantification of Parp-1, Ki67 and p-yH2ax expression in liver sections after HDTV with <i>Kras/Trp53</i>	86
Figure 4.35: Histology of liver sections injected with <i>Akt/Nicd</i> via HDTV.....	87
Figure 4.36: Immunohistochemistry staining of liver sections injected with <i>Akt/Nicd</i> via HDTV.....	88
Figure 4.37: Quantification of Parp-1, Ki67 and p-yH2ax expression in liver sections after HDTV with <i>Akt/Nicd</i>	89
Figure 4.38: Histology of liver sections injected with empty vector via HDTV.....	90
Figure 4.39: Quantification of liver weight / body weight-ratio.....	91
Figure 4.40: Quantification of <i>in vivo</i> tumor growth with classifications.....	91
Figure 4.41: Differential expressed genes after HDTV with <i>Kras/Trp53</i> in <i>Parp-1^{-/-}</i> versus <i>Parp-1^{+/+}</i> mice.....	94
Figure 4.42: Canonical pathways and toxicity analyses upon HDTV with <i>Kras/Trp53</i> in <i>Parp-1^{-/-}</i> versus <i>Parp-1^{+/+}</i> mice.....	95

Figure 4.43: Enriched gene sets in <i>Parp-1^{-/-}</i> mice injected with <i>Kras/Tp53</i> versus <i>Parp-1^{+/+}</i> mice.....	97
Figure 4.44: Differential expressed genes after HDTV with <i>Akt/Nicd</i> in <i>Parp-1^{-/-}</i> versus <i>Parp-1^{+/+}</i> mice.	98
Figure 4.45: Canonical pathways and toxicity analyses upon HDTV with <i>Akt/Nicd</i> in <i>Parp-1^{-/-}</i> versus <i>Parp-1^{+/+}</i> mice.....	98
Figure 4.46: Enriched gene sets in <i>Parp-1^{-/-}</i> mice injected with <i>Akt/Nicd</i> versus <i>Parp-1^{+/+}</i> mice.....	99
Figure 4.47: Expression of DNA damage response genes in <i>Parp-1^{-/-}</i> and <i>Parp-1^{+/+}</i> mice upon <i>Kras/Tp53</i> injection.....	100
Figure 4.48: Differential expressed genes after HDTV with EV in <i>Parp-1^{-/-}</i> versus <i>Parp-1^{+/+}</i> mice.	101
Figure 4.49: Integration of <i>in vitro</i> transcriptomic data with prognostic subgroups of CCA patients.	104
Figure 4.50: Integration of <i>in vivo</i> transcriptomic data with prognostic subgroups of CCA patients.	104

List of tables

Table 3.1: Applied instruments.....	24
Table 3.2: Applied consumables.....	25
Table 3.3: Applied chemicals and reagents.....	27
Table 3.4: List of primary cell lines.....	29
Table 3.5: List of established cell lines.....	29
Table 3.6: Applied short interfering RNA.....	29
Table 3.7: Applied Primers.....	29
Table 3.8: Applied plasmids and vectors.....	30
Table 3.9: Applied enzymes.....	30
Table 3.10: Applied primary antibodies.....	31
Table 3.11: Applied secondary antibodies and dyes.....	31
Table 3.12: Applied kits and mass rulers.....	32
Table 3.13: Applied inhibitors.....	32
Table 3.14: Applied Software.....	32
Table 3.15: Pipetting scheme for cDNA synthesis.....	39
Table 3.16: Steps of cDNA synthesis.....	40
Table 3.17: Pipetting scheme for qRT-PCR.....	40
Table 3.18: Steps of qRT-PCR.....	40
Table 4.1: Demographic and clinicopathological information of Mainz iCCA patient cohort.....	45
Table 4.2: Frequency of KRAS mutation in iCCA patient cohorts.....	47
Table 4.3: Results of Sanger sequencing.....	64
Table 4.4: List of experimental groups.....	82
Table 4.5: Pathological classification of <i>in vivo</i> tumors after HDTV.....	93
Table 4.6: Pathological classification of <i>in vivo</i> tumors after HDTV.....	93
Table 4.7: Overview of transcriptomic analyses.....	102

List of abbreviations

ADP	adenosine diphosphate
AIF	apoptosis-inducing factor
ASBT	apical sodium dependent bile acid transporter
AQP1	aquaporin 1
BER	base excision repair
BSA	bovine serum albumin
BSEP	bile salt export pump
CA19-9	carbohydrate antigen 19-9
cAMP	cyclic adenosine monophosphate
CCA	cholangiocarcinoma
CEA	carcinoembryonic antigen
CFTR	cystic fibrosis transmembrane conductance regulator
CK19	cytokeratin 19
COX-2	cyclooxygenase-2
DAPI	4',6-diamidino-2-phenylindole
dCCA	distal cholangiocarcinoma
DDR	DNA damage response
DMEM	Dulbecco's modified eagle's medium
DMSO	dimethyl sulfoxide
DNA	deoxyribonucleic acid
DNMT 1	DNA methyl transferase 1
DSBR	double-strand break repair
eCCA	extrahepatic cholangiocarcinoma
ECM	extracellular matrix
EGF	epidermal growth
EMT	epithelial-mesenchymal transition
ERK	extracellular signal-regulated kinase
FBS	fetal bovine serum
FDR	false discovery rate
FGFR2	fibroblast growth factor receptor 2
GAPDH	glyceraldehyde-3-phosphate dehydrogenase
GEMM	genetically engineered mouse model
GSEA	gene set enrichment analysis

HBV	hepatitis B virus
HCC	hepatocellular carcinoma
HCO ₃ ⁻	hydrogen carbonate
HCV	hepatitis C virus
HGF	hepatocyte growth factor
HIV	human immunodeficiency virus
HR	homologous recombination
HRP	horse radish peroxidase
HDTV	hydrodynamic tail vein injection
iCCA	intrahepatic cholangiocarcinoma
IDH1/2	isocitrate dehydrogenase 1/2
IL-6	interleukin 6
IPA	ingenuity pathway analysis
JAK	janus kinase
KRAS	kirsten rat sarcoma
lncRNAs	long non-coding RNAs
MAPK	mitogen-activated protein kinase
MEK	mitogen activated protein kinase (MAPK) kinase
MDR3	multidrug resistance protein 3
mRNA	messenger RNA
miRNAs	micro RNAs
MRP2	multidrug resistance-associated protein 2
mTOR	mammalian target of rapamycin
mut	mutant
NADPH	nicotinamide adenine dinucleotide
NAFLD	non-alcoholic fatty liver disease
NASH	non-alcoholic steatohepatitis
NER	nucleotide excision repair
NGS	next-generation sequencing
NHEJ	non-homologous end joining
NO	nitric oxide
OS	overall survival
OST α -OST β	organic solute transporter α / β
PARP-1	poly (ADP-ribose) polymerase 1

PBC	primary biliary cirrhosis
PBS	phosphate-buffered saline solution
PCA	principal components analysis
pCCA	perihilar cholangiocarcinoma
PDGF	platelet-derived growth factor
pDNA	plasmid DNA
PFS	progression-free survival
PI3K	phosphatidylinositol-3-kinase
PIP ₃	phosphoinositol triphosphate
PLC	primary liver cancer
PMCA	plasma membrane Ca ²⁺ ATPase
PSC	primary sclerosing cholangitis
PTEN	phosphatase and tensin homolog
qRT-PCR	quantitative real-time polymerase chain reaction
RIN	RNA integrity number
RNA	ribonucleic acid
ROS	reactive oxygen species
RT	room temperature
SB	sleeping beauty
SDS	sodium dodecyl sulphate
SDS-PAGE	sodium dodecyl sulphate-polyacrylamide gel electrophoresis
sgRNA	single guide RNA
siRNA	short interfering RNA
SSBR	single-strand break repair
STAT	signal transducer and activator of transcription
TBS	tris-buffered saline solution
TGFβ	transforming growth factor beta
TMB	tumor mutational burden
TP53	tumor protein 53
VEGF	vascular endothelial growth factor
VEGFR	vascular endothelial growth factor receptor
WT	wildtype
YAP	yes-associated protein

1. Introduction

1.1 General aspects of the biliary tract cancer

The liver is the second largest organ in the human body and is responsible for several metabolic functions and processes [1, 2]. In its capacity as the largest exocrine gland of the human body, it houses the intrahepatic bile duct system, a conduction system that transports and secretes bile from hepatocytes via the gallbladder into the duodenum [3]. The biliary tract and its functions are conserved in all vertebrates and loss of patency is incompatible with life regardless of age. The unique biliary morphology provides vital physiological processes; however, it is also linked with numerous diseases [4, 5]. Development and diseases of the biliary system are complex and yet incompletely understood. Common disorders are immune-mediated cholangiopathies such as primary biliary cirrhosis (PBC), primary sclerosing cholangitis (PSC), or drug-induced cholangitis. Congenital disorders such as biliary atresia or choledochal cysts occur relatively rare, though causing cirrhosis and inflammation leading to cholangitis and thereby increasing the risk of cholangiocarcinoma (CCA) [6]. Altogether, they share similar pathogenic mechanisms, including inflammation, fibrosis, apoptosis, altered development, and neoplastic transformation of cholangiocytes [7]. The term biliary tract cancer describes a group of epithelial malignancies deriving from every part of the biliary tree, namely gallbladder cancer, ampulla of vater cancer, and cholangiocarcinoma (CCA) [8]. CCA, accounting for 3% of all gastrointestinal malignancies, can be further differentiated into intrahepatic (iCCA) and extrahepatic (eCCA) cholangiocarcinoma [8, 9].

1.1.1 Classification of cholangiocarcinoma

The biliary system is a complex network of tubular conduits and can be divided into two major sections based on anatomical location and function: the intrahepatic and the extrahepatic biliary tract. The first, intrahepatic section consists of the secretory units, the bile canaliculi, and a branching conduit system of larger bile ductules (Canals of Hering) and interlobular bile ducts. The extrahepatic units comprise extrahepatic bile ducts, the common hepatic duct, the cystic duct, the gallbladder, and the common bile duct, which drains bile liquid into the duodenum via the hepatopancreatic ampulla of vater [4, 10] (Figure 1.1). According to the anatomical location cholangiocarcinoma are classified as intrahepatic CCA (iCCA) and extrahepatic CCA (eCCA).

Extrahepatic CCA can be further distinguished into perihilar CCA (pCCA) and distal CCA (dCCA). For pCCA and dCCA, the insertion of the cystic duct serves as the anatomical point of distinction (Figure 1.1). 50-60% of CCA cases account for pCCA and 20-30% for dCCA [11, 12]. Extrahepatic CCA are most frequently mucinous adenocarcinoma with poorly defined nodular sclerosing or less commonly, intraductal papillary characteristics. Further, they show phenotypic traits of pancreatic cancer and are associated with PSC and preceding preneoplastic lesions like intraductal papillary neoplasms [12, 13].

iCCA arise from second-order bile ducts and small bile ducts inside the liver parenchym. The frequency of iCCA cases accounts for 10-20% of all CCA cases. [11, 12]. Pronounced inter- and intratumoral heterogeneity in this type of cancer are observed and emphasized in different growth patterns and histological features. Classifications based on histology and growth pattern provide further information and infer different cells of origin, etiology, risk factors, molecular profiles, clinical outcome, and treatment response [12]. The growth

pattern of iCCA can be differentiated in mass-forming, periductal infiltrating, and intraductal growing iCCA (Figure 1.1) [12].

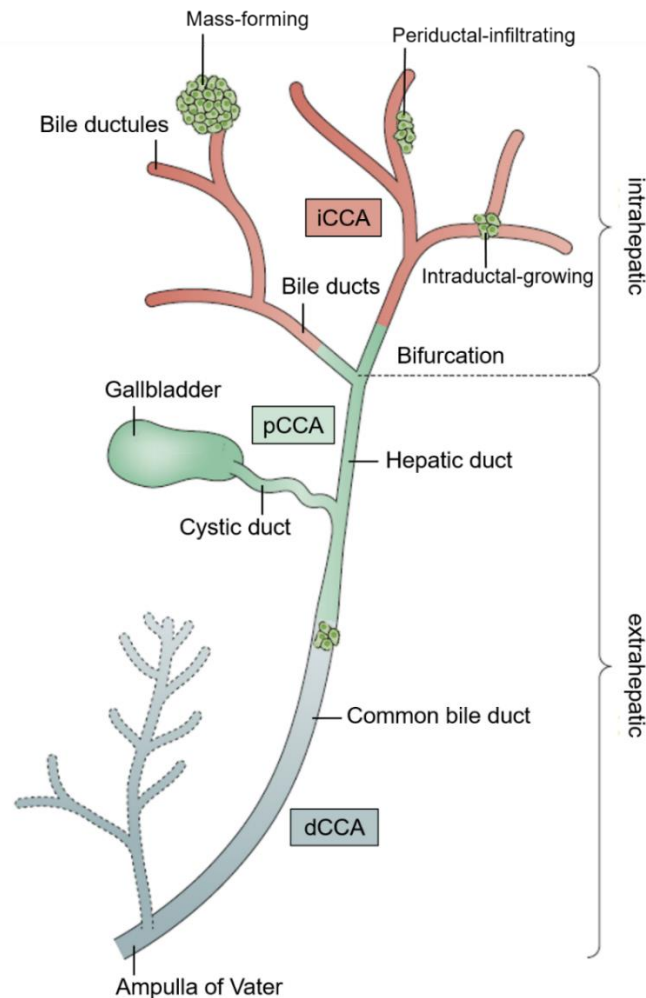


Figure 1.1: Anatomical architecture of the biliary tract and classification of cholangiocarcinoma.

This figure gives an anatomical overview of different parts of the biliary tree. CCA classification is displayed according to its anatomical location in the biliary tree and different growth patterns (modified from Marquardt *et al.*, 2015 [14]).

In addition, histology-based classifications are frequently used to differentiate iCCA subtypes: small bile ductular (mixed) type and large bile ducts (mucinous) type.

i) Small bile ductular type iCCA arises from small intrahepatic bile ducts showing predominantly mass-forming growth patterns. Those small-sized tubular or acinar adenocarcinoma show nodular growth invading liver parenchyma and no to minimal mucin production. Predominant molecular alterations characteristic for this subtype are *isocitrate dehydrogenase 1 and 2 (IDH1/2)* mutations and fusions of *fibroblast growth factor receptor 2 (FGFR2)* [15-17]. The genetic background of iCCA will be further discussed in chapter 1.1.5.1.

ii) Arising from large bile ducts, the second type of iCCA shows mucin-producing columnar tumor growth and, similar to pCCA and dCCA, association with PSC and preceding preneoplastic lesions. Growth patterns of this iCCA sub-type are mainly periductal infiltrating or intraductal. Mutations in *Kirsten rat sarcoma viral oncogene homologue (KRAS)* and *tumor protein 53 (TP53)* genes are often diagnosed [12, 13].

1.1.2 Epidemiology and risk factors of iCCA

Epidemiology of iCCA reflects geographical variations and differences in underlying risk factors and genetic predisposition. Global incidence rates range between 0.3-6 cases per 100,000 people per year (excluding high incidence regions with > 6 cases / 100,000 people). [13]. iCCA is classified as a rare cancer in most western countries with < 6 cases / 100,000 people in Europe, North America, and Australia. In high incidence regions, such as Asia (Thailand, China, South Korea) cases range between 7.1-85 / 100,000 people [11]. Over the past few decades, iCCA incidence progressively increased worldwide [11, 13]. In contrast, incidences of pCCA and dCCA remained stable or decreased regionally in the same period of time [12]. Age-standardized mortality of iCCA increased during 2000-2014 with 1-6 deaths / 100,000 people yearly, not considering regions with incidences > 6 cases / 100,000 people (South Korea, China, Thailand) [18]. Moreover, the 5-year survival between 5-20% reflects high lethality and aggressiveness of the malignancy [11, 13]. Diagnosis is based on non-specific serum biomarkers, biopsies, and imaging. Due to asymptomatic progression in early stages and lack of specific serum markers, diagnosis of iCCA frequently occurs in late stages when iCCA often already metastasized [19]. Several meta-analyses exploring different iCCA risk factors found both subtype-specific and geographic differences and dependencies [11, 20, 21]. Despite the majority of iCCA develop *de novo* (~80%), a common feature shared amongst all risk factors is chronic inflammation [12]. Those inflammatory diseases comprise hepatolithiasis, biliary tract stone diseases, biliary-enteric anastomosis, PBC, or liver cirrhosis. Despite a relatively low prevalence PSC was reported to be the strongest independent risk factor for iCCA [22]. Further, parasitic and viral infections, toxins, and congenital biliary duct disorders could be associated with the development of iCCA. In East Asian countries, especially Thailand, infection with liver flukes (*Opisthorchis viverrini* and *Clonorchis sinensis*) and hepatitis B virus (HBV), due to the regional high prevalence, are the most important causes of iCCA. In Europe and other Western countries, infection of hepatitis C virus (HCV) and influences of the metabolic syndrome are more pronounced. Global obesity pandemic associated with diabetes mellitus type II and other lifestyle factors like tobacco and alcohol consumption were shown to impact iCCA incidence in the Western world [11, 12]. Further, metabolic fatty liver disease in particular non-alcoholic steatohepatitis (NASH) is a strong predictor of iCCA development [23]. Also, several toxic and environmental factors are known as risk factors for iCCA, like nitrosamine contaminated food, asbestos, dioxins, vinyl chlorides, thorotrast, isoniazid, and oral contraceptives [12]. Congenital choledochal cysts, Caroli disease, and congenital hepatic fibrosis were further classified as risk factors for iCCA [11].

1.1.3 Diagnosis and biomarker of iCCA

Progression of intrahepatic cholangiocarcinoma is usually asymptomatic in the early disease stage. Rare and mostly unspecific symptoms like jaundice, asthenia, abdominal pain, malaise, nausea, anorexia, and weight loss are reported [12]. As standard imaging-based diagnosis serve (contrast-enhanced) ultrasonography, computed tomography (CT), and magnetic resonance imaging (MRI). Histological confirmation is mandatory to conclusively establish the diagnosis of iCCA and rule out other diagnoses [13]. However, less than one-third of iCCA cases are detected in early disease progression, when surgical resection is still applicable [24]. This is due to the lack of symptoms and missing non-invasive, specific biomarkers of initial stages. Classic cytokine and protein marker, carbohydrate antigen 19-9 (CA19-9) and carcinoembryonic antigen (CEA) are widely used.

Yet, they show low sensitivity and specificity, especially in the early stages [25]. Several promising biomarkers were identified and examined in past years. These were mainly based on the novel 'omic'-based approaches (i.e. transcriptomics, proteomics) investigating blood, bile, urine, extracellular vesicles, and tumor tissue [25]. In addition, soluble fragments of CA19-9 (CYFRA 21-1) and osteopontin show promising predictive value regarding survival in progressed disease stages [26, 27]. Most recently, Lapitz *et al.* identified RNA profiles of urine and serum extracellular vesicles, which allowed them to clearly distinguish patients with iCCA, HCC, and PSC from healthy individuals [28]. Another promising approach is screening for iCCA-specific oncogenic mutations in serum containing cell-free DNA [29]. High diagnostic capacity of the bile liquid was demonstrated by the identification of CCA-predictive bile micro-RNAs (miR9, miR145) [30]. Combined detection of CA19-9 with miR1537 further increased diagnostic value [31]. Tumor tissue biomarkers represent tumor- and iCCA-specific expression patterns of factors such as KRAS, TP53, FGFR2, IDH1/2, SOX9, VEGF, SMAD7, or PTEN. These biomarkers are mainly of interest for the prediction of overall survival (OS), recurrence, and treatment response for resected iCCAs [25]. Here, a significant obstacle in the precise identification of tumor tissue biomarkers is the profound phenotypic and molecular heterogeneity of iCCA. For instance, activating mutations in *KRAS* and *TP53* loss-of-function mutation, two abundant alterations in iCCA, were associated with poor OS and early recurrence [15, 32]. Overall, several pre-clinical and early clinical studies aimed to evaluate non-invasive and accurate biomarkers of iCCA at the early stages. However, precise diagnostic evaluation remains challenging and requires further research.

1.1.4 Cells of origin

The complexity of the biliary tree is also reflected on a cellular level. Biliary epithelium comprises two parenchymal cell types: cholangiocytes and hepatocytes. Non-parenchymal cells include liver sinusoidal endothelial cells, Kupffer cells, lymphocytes (natural killer cells), hepatic stellate cells, and hepatic progenitor cells. These cell types play an important role in the biliary physiology as well as in pathophysiological conditions also affecting the biliary system [2]. The two parenchymal cell types, namely hepatocytes and cholangiocytes, are involved in bile production. Hepatocytes are the most common parenchymal cells in the liver, accounting for 80% of liver volume [33]. Primary canalicular bile is produced by hepatocytes and further modified by both secretory and absorptive processes mediated by the second most common parenchymal cells (3-5%), the cholangiocytes [34].

Cholangiocytes are a heterogeneous population of epithelial cells, differing in size, morphology, and function depending on their position in the biliary tree [35]. To modify the primary bile to secondary/liver bile by secretion of hydrogen carbonate ions (HCO_3^-) the cells express numerous channels, transporters, and exchangers on both plasma membranes [10]. Further, intrahepatic cholangiocytes express tissue characteristic membrane proteins such as cytokeratin 7 and 19 (CK7 / CK19), which allow immunohistochemical identification of biliary epithelium [36]. These biomarkers are also associated with intrahepatic cholangiocarcinoma. Expression of CK19, along with CK7 and CK20 allows differentiation between hepatocyte-derived tumors (hepatocellular carcinoma; HCC) and cholangiocyte-derived tumors [37].

The cellular origin of CCA is in the focus of intensive investigation and controversial scientific discussions [38]. Differences between extra- and intrahepatic CCA are evident due to the embryonic origin of cells that form extra- and intrahepatic ducts. During

embryonal development, the ventral foregut buds into a cranial part (*pars hepatica*), developing into the liver and intrahepatic biliary tract, and a caudal part (*pars cystica*) representing the anlage of the gallbladder, extrahepatic biliary tree, and pancreas [39]. Thus, embryonically, intrahepatic cholangiocytes derive from hepatic progenitor cells (HPCs), so-called hepatoblasts. Extrahepatic cholangiocytes have an embryonic link to epithelial cells of the duodenum and pancreas [35, 40].

These embryonic traits are reflected in the putative cells of origin of iCCs [35]. In general, tumors can arise from (cancer) stem and progenitor cells and differentiated cells, such as hepatocytes and cholangiocytes [14]. Several studies based on lineage tracing experiments of iCCA were performed, yet no definite determination of cells of origin was possible [41-43]. However, given the intra- and intertumoral heterogeneity of CCA, several lines of evidence suggest different cells of origin depending on iCCA subtype [35].

Small bile ductular type iCCA might derive from HPCs or cuboidal cholangiocytes. Both phenotypic and genotypic profiles indicated a correlation to bipotent HPCs, which separate toward cholangiocytes or hepatocytes depending on the step of progenitor cell differentiation [13, 14]. Further, these small bile ductular type iCCAs were associated with CK19-positive HCC or HCC-CCA mixed tumors and underlying chronic liver diseases, characterized by hepatic progenitor cell activation [12].

Precursor cells of large bile duct type iCCAs, pCCA, and dCCA are columnar mucous cholangiocytes or peribiliary glands showing embryonical similarities to extrahepatic biliary tree and pancreatic duct system. Further, large bile duct iCCA type was linked to intraductal papillary neoplasms and chronic inflammation mediated by PSC or liver fluke infections [13].

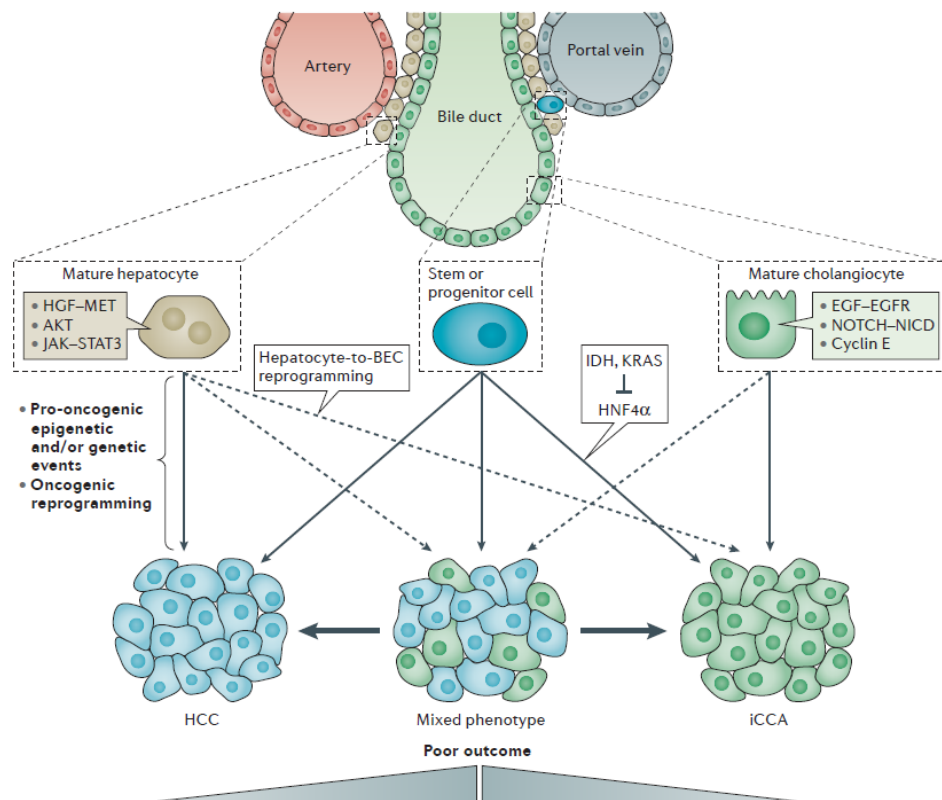


Figure 1.2: Potential cell of origin of intrahepatic cholangiocarcinoma.

The figure illustrates the differential fate decision in PLC dependent on affected progenitor cells and malignant transformation. Potential cells of origin are stem or progenitor cells, mature hepatocytes, or mature cholangiocytes (modified after Marquardt *et al.*, 2015 [14]).

Cell lineage tracing systems and GEMMs have demonstrated that any cell type in mouse hepatic lineage (HPCs, mature hepatocytes, and cholangiocytes) can undergo oncogenic reprogramming resulting in hepato- and cholangiocarcinogenesis (Figure 1.2) [43]. Several molecular factors have been identified to influence fate decisions (e.g., *IDH1/2*, *KRAS*, *YAP/NOTCH*, *PTEN*) [14, 43-45]. Recent studies suggest adult hepatocytes as origin in iCCA. Depending on diverse factors such as oncogenic events and environmental changes, hepatocytes can undergo malignant transformation (*NOTCH/YAP* signaling, chronic liver injury, predisposing *KRAS/Tp53* mutations [46, 47]). Notably, these experimental models of hepatobiliary carcinogenesis and lineage tracing cannot fully recapitulate pathogenesis in a chronic inflammatory microenvironment. Hence, interpretation and determination of the cellular origin of cholangiocarcinoma require further research.

1.1.5 Signaling and molecular networks implicated in intrahepatic cholangiocarcinogenesis

Molecular pathogenesis of intrahepatic cholangiocarcinoma is a complex process induced by dysregulation of multiple intra- and extracellular factors as well as signaling pathways. An inflammatory tumor microenvironment promotes cumulative DNA damage and induces alterations leading to increased expression and/or activation of cell surface receptors and signaling pathways, finally resulting in uncontrolled proliferation, survival, angiogenesis, invasion, and metastasis [13, 48].

A number of pathways involved in biliary development, including Notch, WNT, Hedgehog, and HIPPO were discovered predominantly active during inflammatory conditions and iCCA pathogenesis [13]. In healthy tissue, Notch signaling is essential for embryonic development and maturation of liver architecture, besides biliary repair, fibrosis, and maintenance of stem cell niche [13, 49]. Notch pathway is known to be a key regulator of iCCA development and progression [13]. Analyses of patient cohorts showed overexpression of aberrant Notch receptor and upregulation of *NOTCH1* and *NOTCH2* in 82.9% and 56.1% of cases, respectively [49, 50]. Aberrant Notch signaling promotes EMT by enhancing the expression of α -SMA and vimentin while reducing E-cadherin expression [51]. Interestingly, *in vivo* studies showed that activated NOTCH1/3 enables transdifferentiation of hepatocytes towards biliary cells during cholangiocarcinogenesis. Moreover, the development of iCCA in mouse models was achieved by overexpression of the intracellular domain of NOTCH1 (NICD1) via hydrodynamic tail vein injection (HDTV) [41, 42, 52].

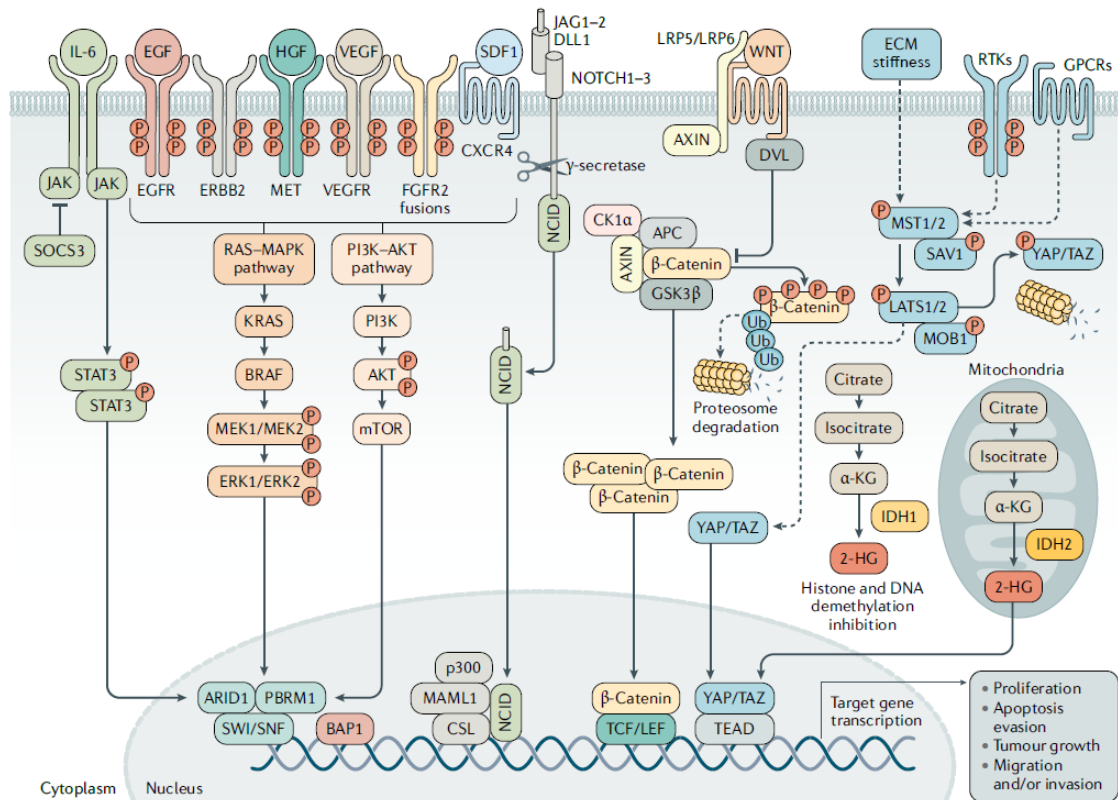


Figure 1.3: Signaling pathways involved in molecular pathology of iCCA.

Multiple signaling pathways are associated with intrahepatic cholangiocarcinoma. Here displayed pathways are commonly dysregulated in iCCA due to mutations or amplification of prominent pathway members (*KRAS*, *BRAF*, *ARID1*, *BAP1*, *IDH1/2*) (modified after Banales *et al.*, 2020 [13]).

Besides revealing pronounced dysregulation in developmental pathways, several next-generation sequencing studies showed a high genomic complexity in iCCA. Prevalent oncogenic signaling pathways, such as microenvironmental and inflammation-related signaling (*TGFβ*, *SMAD4*, *IL-6/JAK/STAT*), cell survival and death pathways (*BRAF*, *ERBB2*, *p38 MAPK*, *EGFR*, *PTEN*, *HGF/MET*, *PI3K-AKT-mTOR*), cell cycle control and genomic instability (*TP53*, *CDKN2A*, *CCND1*, *ROBO2*, *BRCA1/2*), epigenetic regulation (*PBRM1*, *ARID1A/B*, *ARID2*, *SMARCA2/4*, *BAP1*, *MLL2*, *MML3*, *KMT2C*, *KDM4A*) and metabolic processes (*IDH1/2*) (Figure 1.3) [13, 48, 53].

1.1.5.1 Genetic alterations

Analyses of genetic alterations in CCA showed distinct mutational profiles of iCCA specific genes (*FGFR2* fusions, *IDH1/2*, *EPHA2*, *BAP1* mutations), eCCA-specific genes (*PRKACA/B* fusions, *ELF3*, *ARID1B* mutations) and iCCA/eCCA shared genes (*KRAS*, *SMAD4*, *ARID1A*, *GNAS*) [15, 54]. Whole-transcriptome analyses revealed two distinct molecular subclasses in iCCA. Activation of oncogenic signaling pathways (*RAS-RAF-ERK-MAPK*, *MET*, *EGFR*, *PI3K/AKT/mTOR*, *IGFR1*, *HIPPO*), accounting for 62% of cases, was associated with a “proliferation” subclass with poor prognosis. Whereas the “inflammation subclass” (inflammatory cytokines, constitutive *STAT* activation) was associated with a better prognosis and included 38% of cases [48, 55].

Knowledge about inherited predisposing genetic risk factors in iCCA is limited [56]. In contrast, the mutational profile of iCCA and well-known oncogenic drivers have been

identified by high-throughput next-generation sequencing in recent years. Several genes involved in cell survival (*BRAF*, *ERBB2*, *p38 MAPK*, *EGFR*, *PTEN*, *HGF/MET*, *PI3K-AKT-mTOR*) and cell cycle control and genomic instability (*TP53*, *CDKN2A*, *CCND1*, *ROBO2*, *BRCA1/2*) were discovered [13, 48, 57]. Activating mutations in *KRAS* downstream of *EGFR* are amongst the abundant somatic mutations in iCCA (12-16%). *KRAS* mutations, predominantly present in codon 12, have been detected early during disease stages and therefore likely to contribute to the malignant transformation of cholangiocytes [13, 58]. The most frequent mutations *KRAS*^{G12D}, *KRAS*^{G12V}, and *KRAS*^{G12C} result in an amino acid substitution that leads to a disturbed GTP hydrolysis causing constitutive activation of the protein. *KRAS* plays an important role in the proliferation and survival of iCCA tumor cells as it affects numerous downstream signaling pathways such as *RAF/MEK/ERK* and *PI3K/AKT/mTOR* [58-60]. *TP53*, a master regulator of genomic stability is another gene frequently mutated in iCCA with around 13-20% of patients bearing loss-of-function mutations in this tumor suppressor [13]. Liver fluke-positive tumors showed high a prevalence of *TP53* mutations, reaching 44% [61, 62]. These genetic alterations in *KRAS* and *TP53* are associated with poor OS and early recurrence [58]. Combination of *KRAS* and *TP53* alterations enhanced aggressive tumor growth and metastatic properties [57, 59]. In addition, there is growing evidence that RAS-driven malignancies are highly dependent on non-oncogenic cellular processes that promote tumorigenic fitness, such as DNA damage response and proteotoxic stress [59, 60]. *In vivo*, genetically engineered mouse model (GEMM) and transposon-based models with combined *KRAS* activation and *TP53* inactivation develop mostly iCCA recapitulating pathological and molecular features of the human disease [59, 63, 64].

1.1.5.2 Novel hotspot mutations

Isocitrate dehydrogenase 1 and 2 (*IDH1/2*) genes encode metabolic enzymes converting isocitrate to α -ketoglutarate (α -KG) in conjunction with the generation of NADPH. Upon mutation, in hotspot codons 132 and 172, abnormal enzymatic activity leads to a reduction of α -KG to 2-hydroxyglutarate (2-HG), a metabolite with oncogenic properties. 2-HG inhibits multiple dioxygenase enzymes resulting in altered cell differentiation and survival [17, 49, 65]. *IDH1/2* mutations are found specifically in iCCA and occur in ~15% of iCCA cases. Those mutations often co-occur with increased levels of p53 and DNA hypermethylation [48]. Overall survival of patients with *IDH1/2* mutations showed a better prognosis compared to *KRAS*- and *TP53*-mutant patients [15, 32].

FGFR2 are tyrosine kinases serving as cell surface receptors for fibroblast growth factors and are known to be involved in the regulation of proliferation, differentiation, migration, and apoptosis. In iCCA several constitutively active *FGFR2* fusions were revealed. The same fraction of *FGFR2* receptor (exon 1-19) was found to be fused with different partners through genomic breakpoints within the same intronic region. In 3-50% of iCCA *FGFR2* fusions were detected, with the most abundant fusions of *FGFR2-BICC1*, *-PPHLN1*, *-CCDC6*, *-MGEA5*, and *-TACC3* [13, 49]. Results of a study conducted by Sia *et al.* suggest an association between *FGFR2-PPHLN1* and *-BICC1* fusions with activating *KRAS* mutations [66]. While Arai *et al.* showed that *FGFR2-AHCYL1* and *-BICC1* fusions are mutually exclusive to *KRAS/BRAF/ROS1* alterations, Vogel *et al.* revealed a *KRAS*-like signature in iCCA patient samples with *FGFR2*-fusions [16, 67] (Vogel *et al.* in revision). Less abundant *FIG-ROS* fusions were also reported in iCCA [68]. The discovery of *IDH1* and *IDH2* hotspot mutations and *FGFR2*-fusions was the first clinically significant genomic breakthrough in iCCA.

Selective inhibitors for IDH1/2 (AG-120/121) and FGFR2 (BGJ398) (NCT03773302) are assessed in phase III clinical trials [69, 70].

1.1.5.3 Inflammation-related signaling pathways and tumor micro-environment

Despite differences in risk factors and driving mutations in iCCA and eCCA, chronic biliary inflammation and biliary damage are prominent promoters of malignant transformation in cholangiocarcinogenesis [15, 71]. Inflammatory processes and extracellular factors (proinflammatory cytokines, growth factors, and bile acids) promote neoplastic processes including damage of proto-oncogenes, DNA mismatch repair proteins/genes, and tumor suppressor genes, further influencing apoptosis, invasiveness, and neoangiogenesis [13]. Aberrant bile acid signaling affects cell surface receptors (EGF, VEGF, HGF, and bile duct transporters) activating downstream effectors and pathways (NF- κ B, EGFR, COX-2, IL-6/JAK/STAT, Mcl-1, PI3K/AKT/mTOR, RAS/ERK) [13, 72, 73].

Several studies demonstrated that the release of interleukin-6 (IL-6) is increased in iCCA cell lines and biopsies of iCCA patients. IL-6 plays an important role in cholangiocarcinogenesis via a p38-mediated decrease in p21 expression, resulting in uncontrolled proliferation [73]. Moreover, IL-6 signaling impacts resistance to apoptotic processes via Mcl-1 upregulation. This effect was closely linked to the activation of the JAK/STAT signaling pathway. JAK/STAT mediates inhibition of apoptosis and activation of AKT pathways, promoting cell survival, mitosis, migration, and angiogenesis [73, 74]. TNF α -mediated activation of AID (activation induced cytidine deaminase), an enzyme creating DNA mutations by converting cytosine to uracil, was shown to endorse the generation of somatic mutations of tumor-relevant genes (*TP53*, *c-MYC*) [74]. Furthermore, the expression of cyclooxygenase-2 (COX-2) showed upregulation in iCCA [74]. It is responsible for the generation of prostaglandins during inflammation and is linked to mitogenic effects in CCA progression [73]. COX-2 expression and production of nitric oxide (NO) by inducible NO-synthase (iNOS) is further associated with inhibition of DNA repair and subsequent accumulation of DNA damage and mutations in cholangiocarcinogenesis (Figure 1.4) [74].

Besides soluble factors, like IL-6, pro-inflammatory signaling networks are associated with malignant transformation in the early stages of tumor formation. One of them is the nuclear factor 'kappa-light-chain-enhancer' of activated B-cells (NF- κ B) signaling, a key regulator of inflammatory processes [75, 76]. NF- κ B signaling in iCCA is activated upon exposure to conjugated bile acids, IL-6, or TNF α and affects the growth of human iCCA cells (Figure 1.4) [77]. Liu *et al.* showed that NF- κ B-mediated release of proinflammatory cytokines is further enhanced in a TLR2-dependent manner promoting growth and metastatic properties of iCCA [78]. NF- κ B is also overexpressed in iCCA patients with liver fluke infection. Consistently, inhibition of NF- κ B activity leads to reduced proliferation and increased apoptosis in iCCA cell lines. Moreover, in a mouse model of liver fluke-induced CCA tumor size was reduced upon NF- κ B inhibition [79].

TGF β signaling is essential for numerous cellular functions such as growth, differentiation, migration, apoptosis, adhesion, survival, and immunity. In CCA, overexpression of TGF β -1, TGF β -R1/2, as well as alterations in downstream mediator *SMAD4*, are frequently reported [15]. These alterations stimulate the expression of downstream transcription factors Snail, Slug, and Twist, targeting E-cadherin and thereby enhancing invasive properties [80, 81]. Loss of tumor suppressor *SMAD4* abrogates its protective role via

regulation of cell cycle in interaction with PTEN [74]. Moreover, TGF β , as the main regulator of epithelial-mesenchymal transition (EMT), induces mesenchymal traits in iCCA stroma [13].

TGF β is released by CCA cells and tissue-resident macrophages into iCCA stroma, together with FGF and PDGF, and significantly stimulates fibroblast activation. Thus, iCCAs are often characterized as desmoplastic tumors surrounded by a stroma enriched with cancer-associated fibroblasts (CAFs) [82, 83]. Intense crosstalk between stromal CAFs and CCA cells via paracrine factors (IL-1 β , heparin-binding EGF-like growth factor, SDF1, PDGF-B) providing a reservoir for oncogenic support by enhancing tumor progression by proliferation, migration, invasiveness, and chemoresistance [72] [84]. CAFs and CCA cells orchestrate numerous tissue-resident inflammatory cells (M2 macrophages, neutrophils, natural killer, and T cells) creating an immunosuppressive microenvironment (Figure 1.4). Those processes further lead to remodeling of an ECM with enhanced stiffness and expression of matricellular proteins (tenascin C, osteopontin, periostin) [84]. Moreover, CAFs play an important role in tumor progression. Selective depletion of CAFs resulted in CCA cell apoptosis, due to the loss of survival signals produced by CAFs [72].

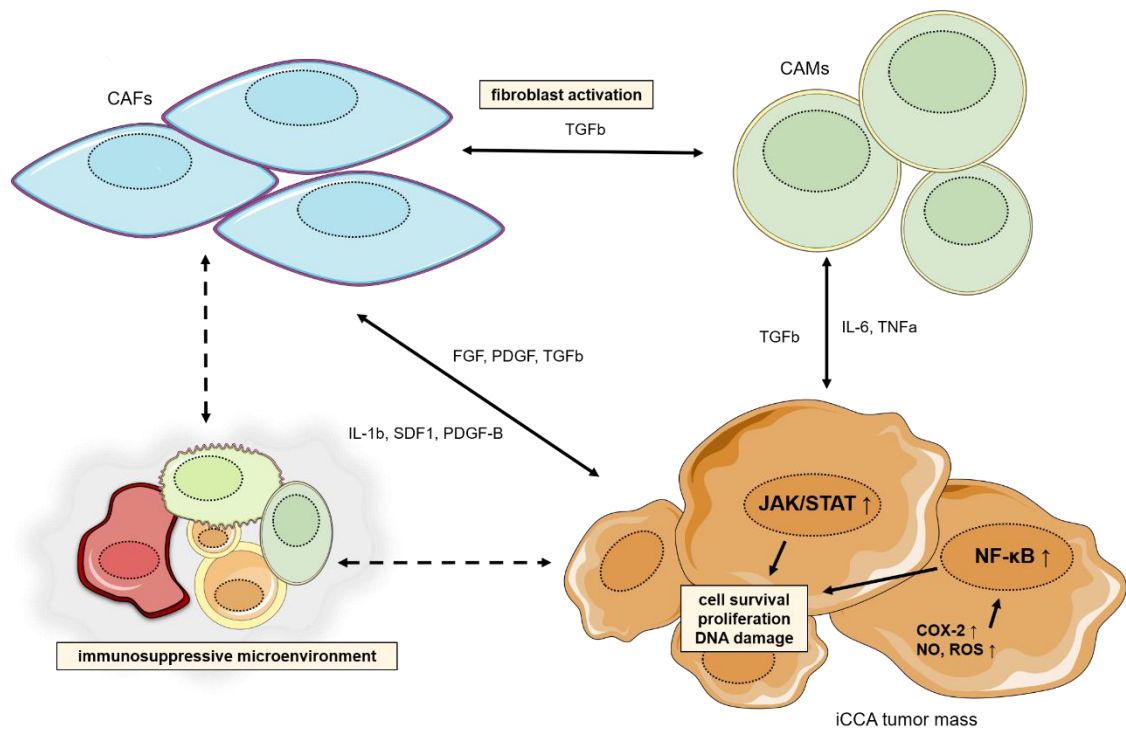


Figure 1.4: Inflammation-related signaling pathways and tumor micro-environment in iCCA.

Tumor microenvironment related to cholangiocarcinoma includes cancer-associated fibroblasts (CAFs) and macrophages (CAMs) and numerous tissue-resident inflammatory cells (M2 macrophages, neutrophils, natural killer, and T cells). Scheme displays the crosstalk among the different microenvironmental factors enhancing the activation of CCA oncogenic signaling.

1.1.5.4 DNA damage response

DNA damage mediated by inflammatory cytokines and nitric oxide-dependent mechanisms is an important driver of initiation, promotion, and progression of cholangiocarcinoma [85]. Production of nitric oxide (NO) and reactive oxygen species (ROS) in response to inflammatory cytokines is associated with increased levels of DNA damage and provides a direct link between chronic inflammation, DNA damage repair (DDR), and tumorigenesis

[12, 85]. In addition to these extrinsic factors germline as well as somatic mutations in DNA damage response genes can result in accumulation of DNA damage with subsequent induction of genetic alterations which mediates an elevated risk for cholangiocarcinogenesis [86]. Hereditary *BAP1* cancer predisposition syndrome and defects in mismatch repair (MMR; Lynch syndrome) could be associated with the development of biliary tract adenocarcinoma [87, 88]. Mutations in DDR genes (e.g., *MSH6*, *BRCA1*, *BRCA2*, *ATM*, *MLH1*, *MSH2*) occur relatively rare in biliary tract cancers but might confer therapeutic implications [89-91]. Abdel-Wahab *et al.* determined a distinct pattern of DDR mutations in iCCA with a mutational frequency of 45.2% in 270 patients. Mutations detected in genes directly related to DDR (e.g., *ATM*, *BRCA1/2*, *FANCA*, *MLH1*, *MSH2*, *MSH6*, *PALB2*, *POLD1*, *POLE*) accounted for 13%, whereas 36.7% of mutations affected “caretaker” genes (e.g., *BAP1*, *CDK12*, *MLL3*, *TP53*, *BLM*) [92]. Tumor mutational burden (TMB) is an indicator for genetic and chromosomal instability due to the extensive accumulation of genomic mutations. TMB in CCA is considered intermediate (6-19 mut/Mb) and present with a frequency of 13.3% in iCCA [86, 92]. Lin *et al.* found a high number of mutations associated with homologous recombination (HR) (14.75%) in iCCA patients (n=122) and confirmed enhanced TMB in selected PLC patients [93]. Further evidence indicates that alterations in DDR are involved in chemoresistance in CCA. ERCC1, a protein linked to nucleotide excision repair (NER) and TLK1 are overexpressed in iCCA mediating the repair of cisplatin-induced DNA damage. In addition, the process of double-strand break repair via homologous recombination (HR) was induced by the upregulation of *RAD51*. Defects in mismatch repair (MMR) proteins are associated with genetic instability, poor prognosis, and higher chemoresistance in CCA, mediated by the downregulation of *MSH2*, *MSH3*, *MSH6*, *MLH1*, or *PMS2* [12].

1.1.6 Therapeutic options in iCCA

Due to asymptomatic progression and lack of specific biomarkers, diagnosis of iCCA frequently occurs at late stages of the disease. At the date of diagnosis only 35% of the patients present with curative disease stages, e.g. are eligible for surgery. Despite surgical resection being the treatment of choice, median survival upon resection remains low with 3 years and a recurrence rate of up to 60% [13, 49, 94]. After resection of iCCA an adjuvant therapy with capecitabine for 6 months is recommended. The phase III clinical study BILCAP investigated adjuvant therapeutic options and found an increased median OS (51.1 months) after treatment with capecitabine compared to observation (median OS 36.4 months) [95]. However, the majority of iCCA patients are not applicable for resection and are treated with palliative systemic chemotherapy. The prognosis of these patients is dismal with a life expectancy of around 1 year and 5-year survival of 5% [96, 97]. As first-line therapy for iCCA a combination of gemcitabine and cisplatin is recommended. This therapy shows a median OS of 11.7 months with a median progression-free survival (PFS) of 8 months [24, 98]. Gemcitabine, a widely used chemotherapeutic agent, inhibits DNA synthesis and promotes apoptosis through caspase signaling [99]. Cisplatin further interferes with DNA integrity causing DNA damage by its capacity to crosslink purine bases, subsequently disturbing DNA repair mechanisms and enhancing apoptosis in cancer cells [100]. Second-line treatment options are limited, recommending administration of FOLFOX, a combinational treatment of folinic acid, 5-fluorouracil, and oxaliplatin-based on findings in phase III clinical study ABC-06. Administration of FOLFOX in combination with active symptom control showed higher median OS (6.2 months) and 12 months OS rate (25.9%)

than active symptom control regime alone (5.3 months OS, 11.4% 12 months OS) [101]. Until today only limited options of molecular targeted therapy have been proven for effective iCCA treatment. Patient stratification based on molecular biomarkers is essential for clinical success, even though only a few promising candidates are available [13]. The discovery of *FGFR2* fusions and *IDH1/2* hotspot mutations gave rise to the first promising targeted therapy options. Inhibitors of *FGFR2* (BGJ398) and *IDH1/2* (AG-120/121) are currently examined in phase III clinical studies [69, 70, 102]. The first results of Abou-Alfa *et al.* (ClarIDHy study) showed significantly improved PFS in patients with *IDH1*-mutant cholangiocarcinoma upon treatment with ivosidenib, an *IDH1*-inhibitor, compared to placebo (median PFS 2.7 months vs. 1.4 months ($p < 0.0001$)). Further, median OS was increased in Ivosidenib group (10.8 months) compared to the placebo group (9.7 months) [69]. A phase II clinical study investigating the *FGFR2* inhibitor showed an overall response rate of 31% and a median PFS of 6.8 months and a median OS of 12.5 months [103, 104]. Currently, BGJ398 is tested in phase III clinical studies in comparison with combined treatment with cisplatin and gemcitabine [70, 105, 106]. Targeting of MAPK pathway, especially targeting *BRAF* mutations, is another promising strategy. Lavingia *et al.* demonstrated that dual inhibition of *BRAF* and *MEK* showed promising clinical response in two case reports [107]. A current phase II study, including 43 patients with BTC regardless of the anatomical location showed promising results in an overall response of 47% [108]. Other agents in early clinical development are compounds targeting *ERBB2* receptors, *FIG-ROS1* fusions, *JAK/STAT* pathway, and developmental pathways (*Wnt- β -catenin*, *Hedgehog*) [102]. Treatment strategies directed to DNA damage response showed promising results in Breast Cancer 1/2 (*BRCA1/2*)-mutated iCCA via *PARP-1* inhibition. Patients treated with Olaparib showed enhanced PFS and OS [109]. Currently, phase II clinical studies using Niraparib and Olaparib are ongoing in patients with CCA showing aberrant DNA gene mutations (NCT04042831, NCT03207347) [102]. Clinical data on immune-directed therapies (IT) in BTC remain limited [13]. KEYNOTE-158 phase II clinical trial showed beneficial therapeutic results with PFS of 4.2 months and OS of 24.3 months in iCCA patients harboring mismatch repair deficiency and microsatellite instability using programmed cell death protein-1 (*PD-1*) inhibitor pembrolizumab [110, 111]. However, in unselected iCCA patients monotherapeutic approach showed modest efficacy [110-112]. Early clinical trials with combined treatment of IT and chemotherapeutics showed promising efficacy in iCCA patients [112, 113]. Currently, TOPAZ-1 (NCT03875235) and KEYNOTE-966 (NCT04003636) phase III trials are investigating the combined treatment of gemcitabine and cisplatin alone or with durvalumab or pembrolizumab. Despite first promising results, further investigations are needed and a distinct molecular profile for the identification and prediction of response should be determined.

1.1.7 Models to study iCCA

Over the last decades, several different murine models to investigate cholangiocarcinogenesis have been developed. The most prominent are genetically engineered mouse models (GEMM), liver electroporation models, and somatic gene transfer models. Other methods employ chemically induced tumorigenesis or the transplantation of genetically engineered fetal liver cells or biliary organoids [114].

Classical GEMMs are based on the constitutive knockout of one or more genes. Over the past decades, different knockout strategies have been developed: e.g. tamoxifen-inducible organ-specific *Cre-lox* systems or adeno-associated-virus based AAV8 with liver-specific promoters in order to mimic the physiological expression levels of transgenes [114].

Whereas many conditional iCCA GEMMs are based on Notch and Pten constructs, conditional GEMMs exploring the most abundant genetic alteration in human iCCA: activating *Kras* mutations and loss of function mutations of tumor suppressor gene *Tp53* are relatively rare [59, 63, 114]. Liver electroporation models combine a direct injection of plasmid DNA (pDNA) into the hepatic parenchyma with an electric pulse administered at the injection site, leading to focal tumor growth. Gürlevik and colleagues showed cholangiocarcinogenesis after SB-mediated expression of *Kras*^{G12V} in *Tp53*^{fl/fl} mice after electroporation [64]. A more recent study demonstrated that electroporation-mediated injection of *Myc* and *Nras*^{G12V}, or *Myc* and *Akt1* induced iCCA or mixed iCCA-HCC tumor growth [115]. Limitations of these models and differences to human cholangiocarcinogenesis are tumor development in absence of inflammation and constitutive expression of oncogenes.

Zhang *et al.* and Liu *et al.* first described the method of hydrodynamic tail vein injection (HDTV) in 1999 as an alternative to viral gene transfer into a target organ. They found out that the rapid injection of a high volume of a physiological solution containing pDNA into the tail vein created a hydrodynamic force whereby inducing a sporadic pDNA transfer (Figure 1.5) [116, 117]. The researchers identified the liver as the main site of transgene expression, besides the kidney, spleen, lung, and heart. Transfection was observed predominantly in parenchymal cells and the expression level of an injected pCMV-plasmid containing firefly luciferase cDNA was positively correlated to the injection rate, injection volume, and DNA dose [117]. Most efficient was an injection rate of 7-10 seconds, a plasmid amount of 10 µg, and an injection volume of 8-12% of body weight. Mechanistically the method can be explained based on the induced hydrodynamic force, which leads to transient cardiac congestion and subsequent retrograde flow of the injected liquid into the liver sinusoids. Due to the hydrodynamic pressure, permeabilization of the capillary endothelium and parenchymal plasma membrane enables the uptake of pDNA into the hepatocytes [116, 117]. The mechanism of pDNA uptake into the hepatocytes was a matter of different hypotheses for a long time. In addition to the most accepted notion of transient enhancement of membrane permeability [118], non-specific processes [119], receptor-mediated uptake [120], and vesicle-mediated transfer mechanisms [121] were discussed. As a consequence of the injection, liver volume and bodyweight increased with a peak after 30 minutes and reversed after 2,5 h back to normal state. The mice recovered within 1 h after injection. Investigation of liver enzymes and serum markers showed a slight elevation of liver enzyme ALT (alanine aminotransferase) levels in the blood [122]. Several lines of evidence showed that hepatocytes are most affected showing a transfection efficiency of 2-10% [123]. Investigations of Zhang *et al.* showed that transfection predominantly was present in hepatocytes at the pericentral region (zone 3 of liver acinus) [118].

After establishment, a limitation of the method was the transient plasmid expression, which lasted for about 1 week and needed multiple administration for maintenance [116, 117]. In 2000, Yant *et al.* overcame this limitation by combining transposon technology with HDTV [124]. Transposons are naturally occurring “jumping” gene elements that are able to integrate into a host genome through non-homologous insertion [125]. The here introduced Sleeping beauty (SB) transposase is a synthetic transposable element originating from the Tc1/*mariner* transposon superfamily. This superfamily transfers transposable elements through a “cut-and-paste” mechanism. The mechanism is mediated through the binding of an enzyme, the so-called transposase, to short-inverted repeat (IR) sequences flanking the transposable element and subsequent reinsertion at another location within a TA dinucleotide [125, 126]. Yant *et al.* established the method of somatic integration of naked pDNA *in vivo* by injecting two plasmids: one containing SB transposase and one containing

the gene of interest under a mammalian promoter and flanked by IR sequences (ratio 1:10-1:25). This combined injection resulted in the long-term expression of the integrated transgenes in 2-10% of hepatocytes [123, 124].

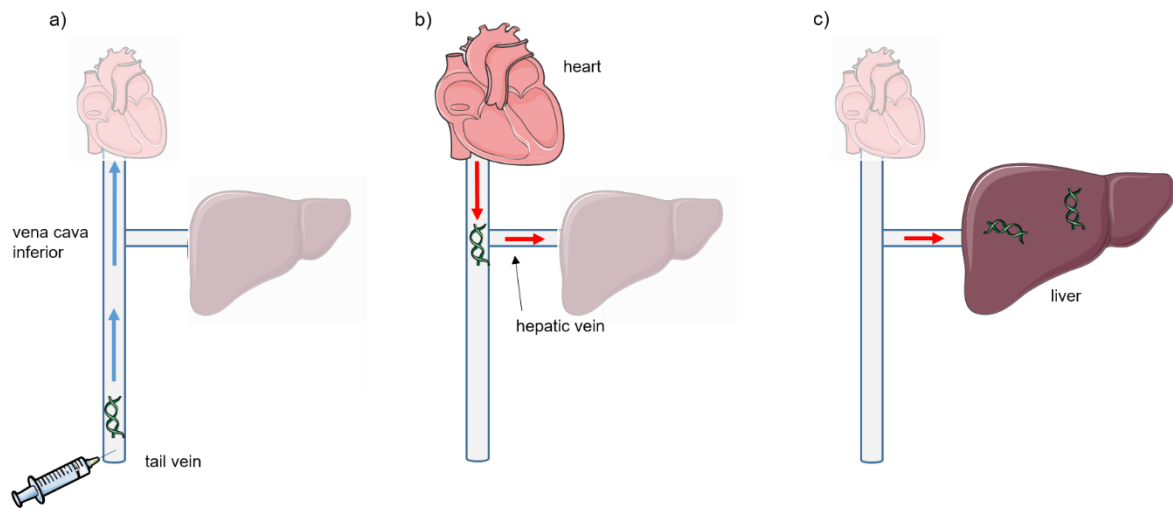


Figure 1.5: Principle of hydrodynamic tail vein injection.

a) Injection of pDNA solution via tail vein leads to increased intravascular pressure in the vena cava inferior. b) Cardiac congestion and retrograde drive of pDNA solution into the hepatic vein. c) Increase of the permeability of the hepatocytes by loosening of tight junctions and gene transfer into the hepatocytes.

Since numerous genetic alterations involved in the development of PLC are well known [14, 32, 127], several studies have shown that the injection of those genes via HDTV is an effective and reliable model for transfection of hepatocytes in order to initiate primary liver tumor growth *in vivo* during the last two decades. Injection of e.g. *Myr-Akt*, *Nras* or *Nras^{V12}/myrAkt* resulted in tumors showing HCC features [123, 128, 129]. Models of sole iCCA growth via HDTV were achieved by injection of *Nicd1* alone or in combination with *myrAkt* into wildtype mice [17, 130]. Development of iCCA and HCC were found in diverse RAS-driven approaches [64, 131] [132].

HDTV with naked pDNA offers several technical advantages over viral gene-transfer methods: i) safe, cheap, and easy production of plasmids, ii) low storage requirements, iii) low risk of recombination, iv) few side effects in the test animal, such as unwanted immune response. Besides the above-mentioned technical advantages also mechanistic advantages regarding HDTV as a model for carcinogenesis particularly noticeable: i) sporadic expression of the transgene in hepatocytes resembles the process of hepatobiliary carcinogenesis in human; ii) injection in 6-8 week old mice does not interfere with mouse embryonic development; iii) multiplex mechanism of hepatobiliary carcinogenesis can be mimicked by injecting plasmid combinations, employing CRISPR/Cas9 technology or using different genetic backgrounds; iv) a low number of animals are needed [123, 124]. Like any other tumor model, HDTV has some limitations. In humans, PLCs often arise in a fibrotic or cirrhotic liver microenvironment. This cannot be reflected by an injection of pDNA into healthy, 6-8 weeks old mice. Further studies with a combination of pretreatment with liver toxins such as carbon tetrachloride (CCl₄) or thioacetamide and HDTV could give further insights. In a study by Matter *et al.* liver tumor growth was induced by HDTV with AKT-CAT and AKT-NRAS^{G12V} constructs, followed by administration of DCC diet and CCl₄ injection. The researchers provided evidence that

tumor phenotype changes dependent on the inflammatory microenvironment and driving oncogenes [133]. However, the absorption capacity and delivery efficiency of fibrotic liver tissue, and the ability of liver toxins to cause mutations in hepatocytes themselves must be considered. Another limitation is the question of the cellular origin of hepatic tumor cells. As mentioned above, predominantly hepatocytes are transfected, which are located in zone 3 of the liver acinus near the portal vein. In contrast, biliary cells are located in zone 1 of the liver acinus near the Glisson triad. Several studies with lineage tracing showed that iCCA could originate from hepatocytes [14, 17, 41, 43, 64]. In addition, HDTV is limited in examining tumor initiation, whereas tumor progression and metastasis remain uninvestigated by this model.

1.2 Poly(ADP-ribose) polymerases

Poly(ADP-ribosylation) (PARylation) is a reversible post-translational modification conserved in eukaryotic organisms, where it possesses important cellular functions. PARylation of target molecules, in particular proteins, can modify their enzymatic activity, their binding properties, their stability and can act as a signaling scaffold for the recruitment of binding partners [134]. This phylogenetically ancient process was first described in the early 1960s, followed by the discovery of numerous associated enzymes and functions, yet not all features of PARylation are fully understood until today [135, 136]. PARylation is mediated by nuclear enzymes called Poly(ADP-ribose) polymerases (PARP). These proteins are involved in several cellular processes such as DNA damage response (DDR), genomic stability, chromatin modification, transcription regulation, energy metabolism, and programmed cell death. PARP-1 is the most prominent member of the PARP family, a group consisting of 17 members, all discovered based on their homology to PARP-1 [137].

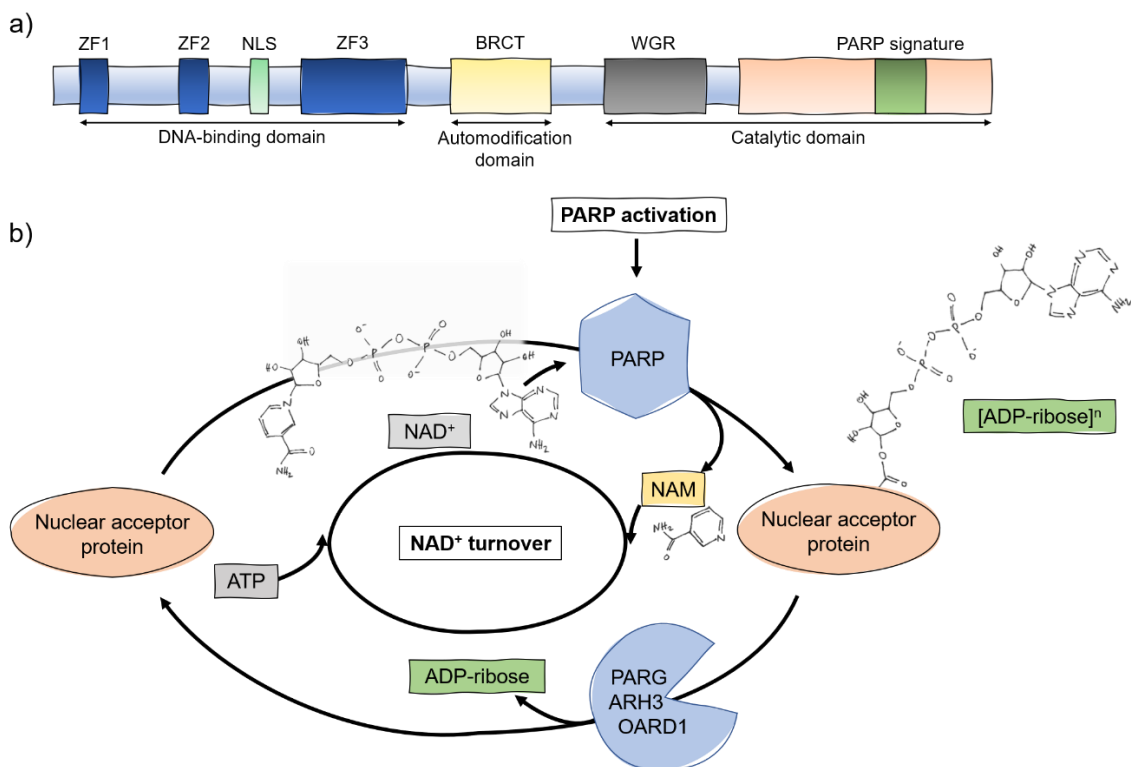


Figure 1.6: PARP domains, PARylation and PAR turnover.

a) The illustration shows the functional domains of *PARP-1*. The N-terminal DNA-binding domain consisting of three zinc-finger motifs (ZF1-3) and the nuclear localization signal (NLS). The central automodification domain containing an interaction motif (BRCA1 C terminus (BRCT) domain). The C-terminal catalytic domain containing the conserved signature of PARP proteins and the active site binding NAD⁺ and the Trp-Gly-Arg (WGR) domain. b) Upon activation PARP enzymes cleave nicotinamide adenine dinucleotide (NAD⁺) into nicotinamide (NAM) and ADP-ribose. ADP-ribose units are polymerized onto nuclear acceptor proteins. Catabolism of PAR chains is processed by Poly(ADP-ribose) glycohydrolase (PARG), ADP-ribosylhydrolase 3 (ARH3), and O-acyl-ADP-ribose deacetylase 1 (OARD1) via ADP-ribose cleavage leading to NAD⁺ turnover.

Based on domain architecture, four sub-families can be classified: DNA-dependent PARPs (PARP-1, PARP-2, PARP-3), Tankyrases (Tankyrase 1/PARP-5A, Tankyrase 2/PARP-5B), CCCH-PARPs (TIPARP, PARP-12, PARP-13.1, PARP-13.2) and Macro-PARPs (PARP-9, PARP-14, PARP-15). Activation of DNA-dependent PARPs is mediated upon binding of

their N-terminal DNA-binding domain to altered DNA structures (Figure 1.6 a) [138]. Tankyrases are TRF1-interacting, ankyrin-related ADP-ribose polymerases associated with telomere homeostasis and vesicle trafficking. PARPs with CCCH (Cys-Cys-Cys-His) zinc finger domains were shown to play an important role in RNA processing and function. Macro-PARPs contain macro-domain folds, which facilitate their localization to sites of PARylation, acting as transcriptional cofactor/co-repressor. Further studies show their role in promoting B-cell lymphoma migration and host-virus response [139-141]. Another classification is based on the catalytic activity: PARPs mediating PolyADP-ribosylation (PARP-1, PARP-2, VPARP, Tankyrase 1/2), PARPs mediating MonoADP-ribosylation (PARP-3, PARP-10, PARP-14, PARP-15) and PARPs being catalytically inactive or requiring specific (yet undetermined) cofactors for ADP-ribosylation (PARP-7, PARP-8, PARP-9, PARP-11, PARP-12, PARP-13, PARP-16) [138].

All members of the PARP-1 family catalyze ADP-ribosylation. This process describes the transfer of ADP-ribose residues from NAD⁺ onto target substrates or via automodification, subsequently changing their functional properties and recruiting other downstream factors [142, 143]. ADP-ribose molecules are attached to lysine residues or the carboxyl group of glutamate or aspartate of target substrates. The covalent bond formation either results in elongation (via $\alpha(1\rightarrow2)$ O-glycosidic bonds of adenine-proximal ribose) or in branching (via joining of two nicotinamide-proximal ribose rings). PAR structures can account for up to 200 units in size, 100 nm in length with branching events with every 20-50 elongation reaction [138, 144]. PARylation occurs upon metabolic, oxidative, or genotoxic stress and influences cellular metabolic status by enhanced NAD⁺ and ATP consumption. Thus, PAR turnover comprising of PARP activation and PAR degradation by PAR glycohydrolase (PARG), ADP-ribosylhydrolase 3 (ARH3), and O-acyl-ADP-ribose deacylase 1 (OARD1) is rapidly and tightly regulated (Figure 1.6 b) [145, 146].

1.2.1 Role of PARP-1 in DNA damage response

Human cells are constantly exposed to endogenous and exogenous noxes and stressors producing thousands of new DNA lesions every day. These damages can be base modifications, DNA single- or double-strand breaks, DNA cross-links, or abasic sites [147]. DNA damage response (DDR) detects and repairs these alterations or induces programmed cell death, in case of irreparable damage [147]. DDR pathways can be distinguished in single-strand break repair (SSBR; nucleotide excision repair (NER), base excision repair (BER), mismatch repair (MMR)) and double-strand break repair (DSBR; homologous recombination (HR), non-homologous end joining (NHEJ)). Recognition of DNA damage sites and initiation of DNA damage response is associated with PARP family members and their PARylation activities [86].

Of all PARP family members, regulation and activation of DNA-dependent PARP-1 are best understood. First, the modular architecture of PARP-1 protein gives information about the functions and properties of the polymerase. The DNA-binding domain is N-terminal located and contains two zinc finger structures, which are essential for the recognition of changes in DNA secondary structure (e.g., single-/double-strand breaks, bends, cruciforms). A central domain mediates nuclear homing, containing a bipartite nuclear localization signal (NLS) and a caspase-3 cleavage site. PARP automodification occurs in another central domain, harboring a BRCA-C-terminus (BRCT) motif constituting the major interface for protein-protein interactions with nuclear partners. At C-terminus, the smallest PARP-1 domain retains the catalytic polymerase activity (Figure 1.7) [142].

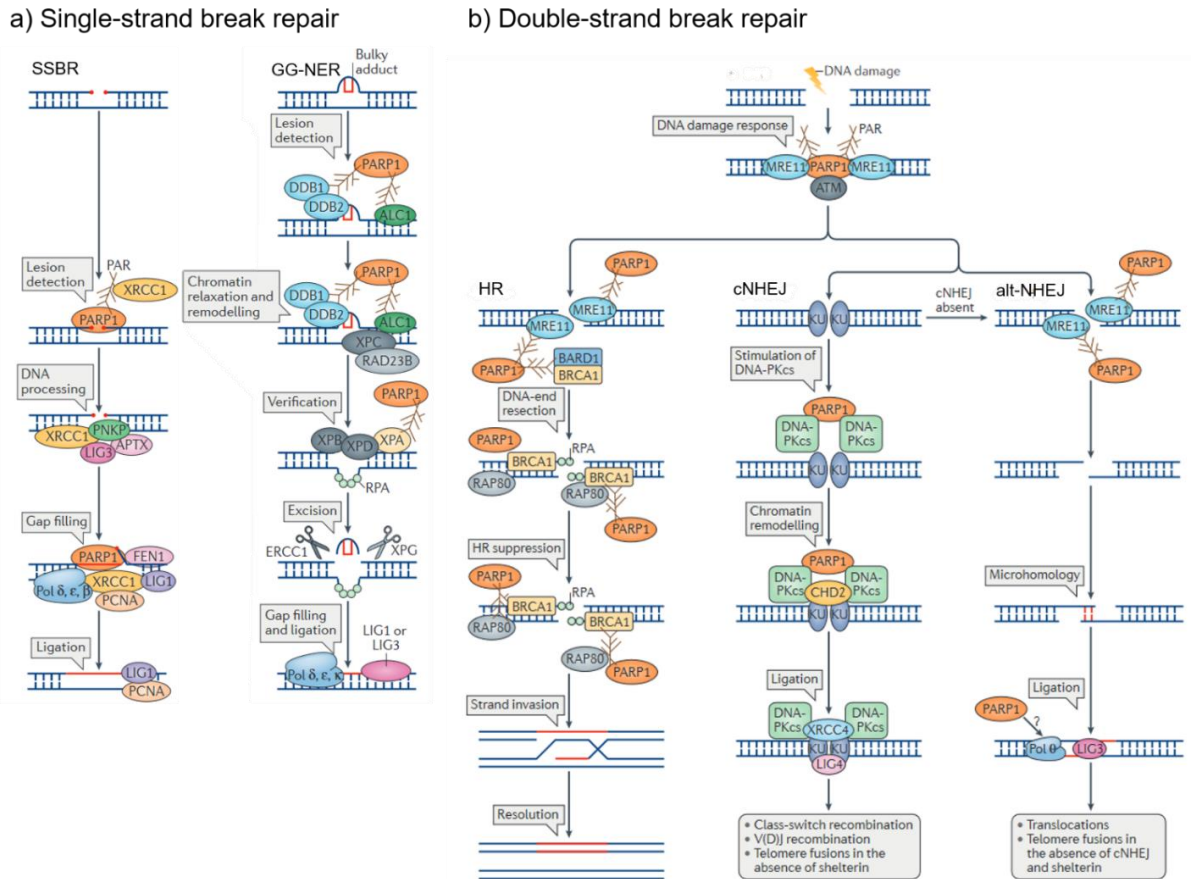


Figure 1.7: Function of PARP-1 in detection and repair of DNA damage.

Role of PARP-1 in a) single-strand break repair (SSBR) pathway and global genomic nucleotide excision repair (GG-NER). Further, PARP-1 is involved in double-strand break repair (DSBR) pathways such as homologous recombination (HR), canonical non-homologous end joining (c-NHEJ), and alternative non-homologous end joining (alt-NHEJ). PARP-1 activity and PARylation are required in several steps of SSBR and DSBR such as lesion detection, recruitment, and interaction with several repair proteins and gap filling (modified after Chaudhuri *et al.*, 2017 [145]).

Upon DNA binding, conformational changes in PARP-1 protein structure close to the ADP-ribosyl transferase active site occur, resulting in a 500 to 1000-fold increase in catalytic activity [138, 148]. The negative charge of ADP-ribose polymers affects the conformation of target proteins and their affinity to DNA. Common targets are chromatin-associated proteins (Histon variant H1, H2B, High Mobility Group (HMG) proteins, lamin B) or DNA metabolism proteins (DNA replication factors). Through decondensation of chromatin around damage sites and by automodification, PARP-1 is able to recruit proteins of repair machinery and accelerates DNA damage repair by serving as a DNA damage sensor as well as a signal transducer to downstream effectors [145]. Initially, PARP-1 was especially well-recognized for its role in DNA base excision repair (BER) and in DNA double-strand break (DSB) repair by alt-NHEJ [149]. However, over the last decade studies demonstrated that PARP-1 is involved in all DDR pathways (Figure 1.7). Despite a growing understanding of underlying mechanisms, some details remain unexplained [149, 150]. DNA single-strand breaks are rapidly detected and bound by PARP-1. Subsequent PARylation of PARP-1 itself results in PARylation of target proteins (LIG3, DNA polymerase β , PNKP) and their recruitment (XRCC1) to the site of damage [145]. Also, recognition of DSB by PARP-1

mediates the early recruitment of DNA double-strand repair sensors and initiators (MRE11, NBS1, BRCA1) in the homologous recombination pathway. Here, PARP-1 functions mainly as control and fine-tuning element [151]. Deficiency in PARP-1 revealed a delayed activation of DSB repair, yet no complete abolishment of the process [152]. In the classic NHEJ pathway, PARP-1 is responsible for the recruitment of XRCC4 and to stimulate the kinase activity of DNA-PKcs, which leads to stimulation of other NHEJ factors. Interestingly, an alternative, error-prone NHEJ pathway exists, which is associated with PARP-1 activity. PARP-1 competes with KU70/80, effector proteins of canonical NHEJ, for access to ends of DNA strands. By recruitment of MRN complex and DNA polymerase θ and its terminal transferase activity, alt-NHEJ pathway is promoted. This process is based on the establishment of microhomologies between two DNA ends to facilitate ligation and inherently mutagenic generation of insertions and deletions at sites of repair [153].

PARP-2 was discovered due to residual DNA-dependent PARP activity in embryonic fibroblasts derived from *Parp-1* deficient mice [154, 155]. With 69% homology, it shows the highest resemblance of the catalytical domain to PARP-1, though only 10% of PARylation activity following genotoxic stress accounts for PARP-2 [154, 156]. PARP-2 interacts with PARP-1 and shares common partners in SSB (XRCC1, DNA polymerase β , LIG3). Moreover, specific PARP-2 functions in chromatin modification, telomere biology (TRF2), and mitotic spindle checkpoint were demonstrated. Overall, several studies show that the functions of PARP-1 and PARP-2 are complementary, but do not fully overlap [143].

The role of PARP-1 in DNA damage response and tumorigenesis was underlined in the generation of *Parp-1* deficient mouse models two decades ago [157-159]. *Parp-1* expression is not required for viability, as *Parp-1* knockout mice show normal development with no predisposition to early-onset tumors [157, 158]. However, upon ionizing irradiation and alkylating agents, *Parp-1* deficient mice were hypersensitive, displaying chromatid breaks, micronuclei, and spontaneous genetic alterations [160, 161]. *Parp-1* knockout studies further showed that under physiological conditions with limited DNA damage *Parp-1* acts as a surviving factor, promoting DNA repair (BER) and p53-mediated apoptosis. Conversely, under pathological conditions with excessive DNA damage *PARP-1* overexpression shows pro-tumorigenic features including depletion of NAD⁺ and cell necrosis [162]. Several tumor entities show elevated levels of *PARP-1* mRNA and protein expression. *PARP-1* overexpression is further associated with poor prognosis and shorter OS [149, 163-165]. Loss or depletion of *Parp-1* showed reduced tumor development, due to loss of pro-tumorigenic properties regarding DNA damage response but also due to its impact on inflammation and energy metabolism *in vivo* [149, 166]. Taken together, PARP-1 exhibits a multifaceted and controversial role in DNA damage response, and its dysregulation is associated with carcinogenesis.

1.2.2 Pro-tumorigenic properties of PARP-1 beyond DNA damage response

Besides its impact on tumorigenesis via DNA damage response, PARP-1 is associated with several other hallmarks of cancer including cellular energetics, apoptosis, inflammatory signaling, genome instability, angiogenesis, metastasis, and proliferation [167, 168].

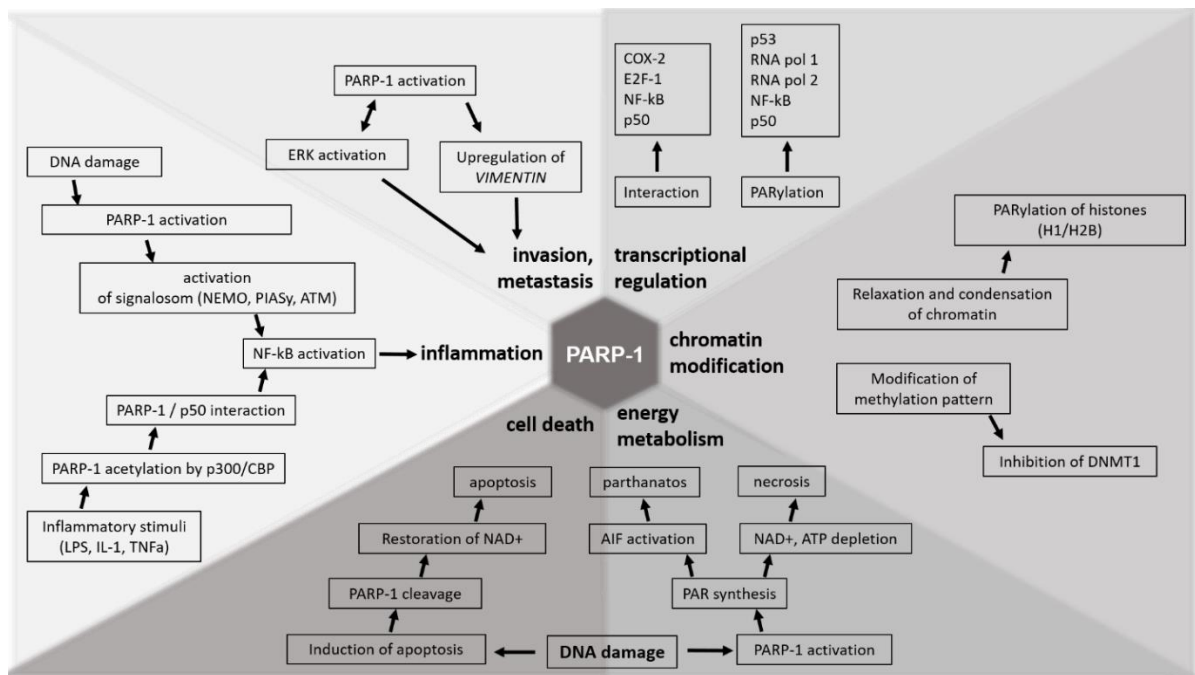


Figure 1.8: Role of PARP-1 beyond DNA damage response.

Schematic illustration of roles of PARP-1 in inflammation, cell death, energy metabolism, chromatin modification, transcriptional regulation, invasion, and metastasis.

Cancer cells show characteristic changes in energy metabolism ensuring rapid proliferation and viability in hypoxic conditions. Nicotinamide adenine dinucleotide (NAD⁺) is a co-enzyme of several cellular reactions important for the maintenance of cancer cell metabolism, such as glycolysis, DNA repair, gene expression, and stress response [169]. Hence, PARP-1 and its substrate NAD⁺ are important regulators of cellular energy metabolism and cell death pathways. However, the multifaceted role of PARP-1 in cell death signaling is not yet fully understood but is dependent on cellular metabolic status (NAD⁺, ATP levels), extent of DNA damage, and level of PARylation (Figure 1.8) [149]. PARP-1 inactivates caspase 8, subsequently reducing caspase-mediated apoptotic signaling [167]. Upon excessive DNA damage, high PAR synthesis leads to a depletion of NAD⁺ and ATP levels. This energy deprivation induces necrotic cell death, enhancing inflammatory processes and reciprocal amplification of DNA damage [170]. Further, PAR can translocate to the cytosol, interact with apoptosis-inducing factor (AIF) at the mitochondrial surface and lead to enhanced DNA fragmentation [171, 172]. This process was described as a PARP-1-dependent cell death mechanism called parthanatos (Figure 1.8) [173]. Prevention of this inflammatory and necrotic route is facilitated by caspase-mediated cleavage of PARP-1 into an 89 kDa fragment and a 24 kDa fragment with the remaining DNA binding domain. Thus, cleaved PARP-1 is a widely used marker for apoptotic processes [174, 175]. The 24 kDa cleavage product irreversibly binds to DNA strand breaks and thereby blocks DNA damage repair [176]. PARP-1 cleavage occurs already early during apoptosis, maximizing in later stages of cell death. Thus, cleavage of PARP-1 and subsequent low PARylation levels restore NAD⁺ and ATP levels despite massive DNA fragmentation in the late stages of apoptosis and thereby ensuring programmed cell death (Figure 1.8) [167].

Another role of PARP-1 in inflammatory processes was shown with the PARP-1 mediated regulation of the transcriptional activity of NF-κB (Figure 1.8). Under influence of oxidative stress, LPS, or inflammatory cytokines (IL-1, TNFα), PARP-1 is activated and positively

mediates NF- κ B activity through direct and indirect interactions [149]. Direct interaction is mediated via PARP-1 acetylation by p300/CBP, which leads to enhanced interaction of PARP-1 with p50 and subsequent NF- κ B activation. Upon detection of DNA damage PARP-1 indirectly mediated NF- κ B activation by the formation of a signaling complex with NEMO, PIASy, and ATM, where activation of IKK and NF- κ B is mediated. These processes enhance NF- κ B nuclear translocation and NF- κ B dependent gene expression [177, 178]. Moreover, studies with *Parp-1* knockout mice provide evidence that these animals are protected against inflammatory and immune-mediated diseases [179, 180].

Besides enhancing inflammatory signaling, several studies showed an impact of PARP-1 activation on other tumorigenic processes such as invasiveness, angiogenesis, and metastasis. MAPK/ERK signaling is known as an important mediator of these processes, as ERK activation promotes cancer cell survival, tumor progression, and metastasis (Figure 1.8) [167]. Cohen-Armon *et al.* showed that PARP-1 is activated by direct interaction with phosphorylated ERK2, leading to enhanced phosphorylation of target transcription factors and gene expression [181]. Properties of ERK signaling in angiogenesis and metastasis are further enhanced by PARP-1 promoting transcription of *VIMENTIN* (Figure 1.8) [182]. PARP-1 inhibition leads to loss of ERK2 stimulation whereby subsequently inducing a decrease in VEGF, SDC-4, PECAM1/CD31, and HIF1 α expression, resulting in reduced angiogenesis, inflammation, and metastasis [167].

Besides direct interaction with pro-tumorigenic proteins, direct binding of PARP-1 at DNA elements or transcription factors can be recognized with a significant effect on signal transduction (Figure 1.8). Notably, the expression of oncogene *MYC* can be enhanced by PARP-1 binding to transcription factor E2F-1, increasing its promoter activity [183]. In contrast, PARP-1 exhibits anti-tumorigenic properties in binding to the inhibitory element of *COX-2*, a mediator of inflammation and VEGF-mediated pro-angiogenesis [184]. Other pro-tumorigenic features of PARP-1 are mitotic regulation and modification of chromatin structure and methylation patterns [167]. PARP-1, localized at centromeres and centrosomes during mitosis, is involved in the assembly and function of the spindle apparatus. Thus, PARP-1 inhibition can also lead to genomic instability due to a reduced stringency of mitotic checkpoints [185]. PARylation of histones alters chromatin structure, subsequent DNA accessibility, and gene expression (Figure 1.8) [186]. Although more research on epigenetic regulation of PARP-1 is needed, preliminary findings show PARP-1-mediated block of methylation by dimerization with DNA methyltransferase 1 (DNMT1) (Figure 1.8) [187].

1.2.3 Drugs targeting PARP-1

PARP-1 inhibitors are small molecules mimicking NAD⁺. Via competitive binding to the NAD⁺ site at the catalytic domain, they prevent PARylation and mediate catalytic inhibition [149]. This mechanism is called PARP trapping. Two inhibitory mechanisms of PARP-1 trapping are proposed: i) PARP trapping prevents the release of PARP from DNA by inhibition of autoPARylation, ii) PARP trapping leads to allosteric changes that enhance DNA avidity [188, 189]. PARP-DNA complex is cytotoxic, leading to the collapse of the stalled replication fork and lethal DNA damage [149].

The first PARP-1 inhibitor, Olaparib was approved by FDA in 2014 as monotherapy in patients with advanced ovarian cancer with a germline mutation in the *BRCA1/2* gene utilizing PARP-1-dependency in the HR-deficient background [190]. In HR-deficient

background, PARP-1 inhibition leads to synthetic lethality, as both DNA double-strand break repair routes are blocked [191]. Additionally, the multiple roles of PARP-1 beyond DNA repair, such as chromatin modification, inflammation, cell death, and energy metabolism, also contribute to the antitumor properties of PARP inhibitors and extend the scope of application [167]. In recent years three other PARP-1 inhibitors were FDA-approved (Niraparib 2017, Rucaparib 2016, Talazoparib 2019) and the therapeutic spectrum was extended to e.g. germline *BRCA*-mutated breast cancer [149, 192, 193]. Currently ~150 completed, running, or recruiting clinical trials for PARP-1 inhibition (Niraparib, Olaparib, Rucaparib, Talazoparib, Veliparib (not yet approved by FDA/EMA)) are registered (www.clinicaltrials.gov, June 2021). Several new tumor entities are under investigation, such as pancreatic, biliary, NSCLC, liver, colorectal, oesophageal, gastric, uterine, carcinosarcoma, brain cancer [193]. Importantly, PARP-1 inhibitors are commonly employed as monotherapy in patients with DNA repair defects. New approaches explore the efficacy of chemotherapeutics (platinum, taxanes), hypoxic agents or with ATM, WEE1, or PI3K inhibitors in combination with PARP-1 inhibitors and show promising results in tumors with no clear alterations in DNA repair [194-197]. In addition, combined immunotherapy with immune checkpoint inhibitors is under intensive investigation [149]. Lack of selectivity between PARP-1 and PARP-2 was reported to be a putative explanation for resistance development or adverse reactions in patients treated with PARP-inhibitors. Underlying mechanisms, for both resistance and side effects, are poorly understood [192, 198]. However, an *in vivo* mouse model with double *Parp-1* and *Parp-2* knockout revealed embryonic lethality, underlining increased cellular toxicity of unspecific PARP inhibition [199]. Thus, a new generation of specific PARP-1 inhibitors seems beneficial. Putative inhibitory mechanisms resembling target activation mechanisms unique to PARP-1 or more specific NAD⁺ mimics are also under investigation [149].

As discussed earlier, DNA damage response plays a crucial role in cholangiocarcinogenesis. Furthermore, options for targeted therapy in CCA patients are still limited and, thus, contribute to the dismal prognosis [200]. Hence, PARP-inhibition in iCCA becomes a new and promising strategy. Currently, three phase II clinical trials with Olaparib as monotherapy or in combination with ATR inhibitor or PD-L1-targeting immunotherapy are recruiting patients with *IDH1/2*-mutated cholangiocarcinoma (NCT03212274, NCT03991832, NCT03878095). Another phase II trial investigates the impact of Niraparib in CCA patients with *BAP1* or other DDR deficiencies (NCT03207347) ([200], www.clinicaltrials.gov, June 2021). In addition, a comprehensive meta-analysis of Ku *et al.* confirmed a reduced proliferation induced by PARPi in *KRAS*-mutant cells compared to *KRAS*-wildtype. Thus, the researchers hypothesized that *KRAS*-mutant cells are defective in DNA damage response pathways indicating synthetic lethality or vulnerability as a promising approach for these cancers [201]. However, the impact of *PARP-1* expression in *KRAS*-mutant iCCA is not entirely clear and requires comprehensive investigations.

2. Aim

Intrahepatic cholangiocarcinoma (iCCA) is the second most common primary liver cancer with an increasing incidence and mortality rate over recent years [202]. Due to the complexity of iCCA pathogenesis and profound genetic heterogeneity, cholangiocarcinomas are commonly diagnosed at late diagnosis and treatment options are still limited [56]. Activating *KRAS* mutations are observed in a sizeable subgroup of iCCA patients and characterized by poor response to chemotherapy and reduced overall survival, highlighting the need for novel therapeutic approaches in this subgroup of patients [14, 58]. Besides direct pro-tumorigenic properties accelerated RAS-signaling results in intracellular stress which renders RAS-driven tumors particularly dependent on non-oncogenic mechanisms that mitigate stress, apoptosis, oxidative stress response, and DNA damage response [59, 60]. Several lines of evidence suggest that inhibition of DNA damage response protein Poly(ADP-ribose) polymerase 1 (PARP-1) might selectively affect the survival of *KRAS*-mutant tumor cells of different entities [166, 201, 203]. PARP-1 is the most prominent member of the PARP family, a group of proteins involved in several cellular processes such as DNA repair, genomic stability, and programmed cell death, by transferring ADP-ribose residues onto acceptor proteins modifying thereby their functional properties and recruiting other downstream factors [137]. However, the mechanistic and therapeutic role of PARP-1 and PARP-1 inhibition in the context of iCCA is yet incompletely understood. Based on these observations, the here presented research project aims to investigate the potential interaction between *KRAS* activation and *PARP-1* expression in iCCA and characterize the functional and prognostic implications during the development and progression of iCCA. Further, the potential of PARP-1-based inhibition as a therapeutic approach in *KRAS*-driven iCCA will be experimentally characterized.

The following questions will be addressed

- i) How frequent are activating *KRAS* mutation in iCCA and is there an association between *KRAS* mutation and *PARP-1* expression?
- ii) Does inhibition of PARP-1 differentially affect *KRAS*-mutant iCCA?
- iii) What are the molecular features of PARP-1 affecting tumorigenicity of *KRAS*-mutant versus *KRAS*-wildtype iCCA and which underlying signaling pathways, as well as downstream molecules, are involved?
- iv) What is the impact of *Parp-1* expression for cholangiocarcinogenesis in *Kras*-driven versus non-*Kras*-driven iCCA *in vivo*?
- v) Can the obtained findings be translated to human CCA and other cancer entities?

3. Materials and methods

3.1 Materials

3.1.1 Electronic devices and laboratory equipment

Table 3.1: Applied instruments.

Name	Manufacturer
Agarose gel electrophoresis system	Analytik Jena AG, Jena, Germany
Analytic scale Sartorius research R 300 S	Sartorius Lab Instruments GmbH & Co. KG, Göttingen, Germany
Aspiration system Integra Biosciences™ Vacusafe™ Comfort	Thermo Fischer Scientific, Braunschweig, Germany
Autoclave Systec V75	Systec, Osnabrück, Germany
Automated Cell Counter LUNA™	Logos Biosystems, Anyang-si, South Korea
Bioanalyzer Agilent 2100	Agilent, Santa Clara, USA
Biological Safety Cabinet NuAire	NuAire, Inc., Plymouth, USA
Centrifuge Heraeus Biofuge fresco	Thermo Fischer Scientific, Braunschweig, Germany
Centrifuge Heraeus megafuge 1.0R	Thermo Fischer Scientific, Braunschweig, Germany
Chemi-Doc MP Imaging System	Bio-Rad Laboratories GmbH, Hercules, USA
Confocal microscope LSM 710 NLO	Carl Zeiss AG, Oberkochen, Germany
Dishwasher Miele professional G 7883	Miele & Cie. KG, Gütersloh, Germany
Dry cabinet Heraeus Instruments	Thermo Fischer Scientific, Braunschweig, Germany
Electrophoresis power supply Consort E231	Sigma Aldrich, Steinheim, Germany
Fluorometer TECAN infinite M200Pro	Tecan, Crailsheim, Germany
Freezer -86°C Hera freeze	Thermo Fischer Scientific, Braunschweig, Germany
Freezer Liebherr Premium	Liebherr, Bulle, Switzerland
Gammacell-2000 irradiator	Nuclear Data Inc., Palatine, USA
Gel-Doc EZ Imager	Bio-Rad Laboratories GmbH, Feldkirchen, Germany
Heating plate Leica HI1220	Leica Mikrosysteme Vertrieb GmbH, Wetzlar, Germany
Ice machine Scotsman AF 124 Ice Flaker	Scotsman International, Milan, Italy
Incubator NuAire DH autoflow CO ₂ air-jacketed	NuAire, Inc, Plymouth, USA
Magnetic stirrer IKAMAG RCT	IKA®-Werke GmbH & Co. KG, Staufen, Germany
Microplate reader Azure Ao	Azure biosystems, Dublin, USA
Microscope AxioVert 25	Carl Zeiss Microscopy GmbH, Jena, Germany
Microscope AxioVert.A1	Carl Zeiss Microscopy GmbH, Jena, Germany
Microscope AxioPlan	Carl Zeiss Microscopy GmbH, Jena, Germany
Microtome Leica RM2245	Leica Mikrosysteme Vertrieb GmbH, Wetzlar, Germany

Name	Manufacturer
Microwave Severin 700	SEVERIN Elektrogeräte GmbH, Sundern, Germany
Minicentrifuge Ministar Silverline	VWR International, Darmstadt, Germany
NanoDrop 1000 Spectrophotometer	NanoDrop Technologies, Wilmington, USA
pH meter inoLab Ph7110	WTW, Weilheim, Germany
Pipette Eppendorf Research Plus 1000 µl, 200 µl, 20 µl, 10 µl	Eppendorf, Hamburg, Germany
Pipette multi-channel Eppendorf Research Plus 100 µl	Eppendorf, Hamburg, Germany
Pipetboy Acu 2 Pipette Controller	INTEGRA Biosciences AG, Zizers, Switzerland
Real-Time PCR System CFX Connect	Bio-Rad Laboratories GmbH, Hercules, USA
Refrigerator Liebherr MediLine	Liebherr, Bulle, Switzerland
Scale DL-510	Denver Instruments GmbH, Göttingen, Germany
SDS gel casting system Mini-PROTEAN® Tetra	Bio-Rad Laboratories GmbH, Hercules, USA
Shaking dry bath	Thermo Fischer Scientific, Braunschweig, Germany
Shaking plate Duomax 1030	Heidolph Instruments GmbH & Co. KG, Schwabach, Germany
Steamer MultiGourmet	B. Braun, Melsungen, Germany
Thermocycler Biometra TGradient	Biometra GmbH, Göttingen, Germany
Thermocycler FlexCycler ²	Analytik Jena AG, Jena, Germany
Tissue Embedding Center Leica EG1150 C	Leica Mikrosysteme Vertrieb GmbH, Wetzlar, Germany
Tissue Processor Leica TP 1020	Leica Mikrosysteme Vertrieb GmbH, Wetzlar, Germany
Vortex Heidolph REAX top	Heidolph Instruments GmbH & Co. KG, Schwabach, Germany
Water Bath Isotemp GPD 28	Thermo Fischer Scientific, Braunschweig, Germany
Western Blot system Mini Trans-Blot® Cell	Bio-Rad Laboratories GmbH, Hercules, USA

3.1.2 Consumables

Table 3.2: Applied consumables.

Name	Manufacturer
1000 µl Tips	Starlab GmbH, Ahrensburg, Germany
200 µl Tips	Starlab GmbH, Ahrensburg, Germany
0.1-20 µl GradienteTips	Starlab GmbH, Ahrensburg, Germany
6, 12, 24, 48, 96 well-plates flat bottomed	Greiner Bio-One, Frickenhausen, Germany
BD microlance 27G x 3/4" Nr. 20	Becton Dickinson GmbH, Heidelberg, Germany
BD microlance 21G x 1½" Nr. 2	Becton Dickinson GmbH, Heidelberg, Germany
Cell culture dish 15 cm	Corning GmbH, Wiesbaden, Germany
Cell culture flasks (75 cm ²)	Thermo Fischer Scientific, Braunschweig, Germany
Cell culture TC Dish 100	SARSTEDT AG & Co. KG, Nümbrecht, Germany

Name	Manufacturer
Cell scraper	SARSTEDT AG & Co. KG, Nümbrecht, Germany
Cell strainer (30 µm and 70 µm)	Miltenyi Biotec, Bergisch Gladbach, Germany
Chamber Slides (µ-Slides 8 Well)	Ibidi, Gräfelfing, Germany
Conical centrifuge tubes (15 ml and 50 ml)	SARSTEDT AG & Co. KG, Nümbrecht, Germany
Cryo tubes	Greiner Bio-One, Frickenhausen, Germany
Dako Pen	Dako Deutschland GmbH, Hamburg, Germany
Feather Scalpel Nr. 23	Feather Safety Razor CO., LTD, Osaka, Japan
Knittel glass cover slips 24*650 mm	Waldemar Knittel, Braunschweig, Germany
Laboratory glass-ware	DWK Life Sciences GmbH, Mainz, Germany
Luna™ Cell Counting Slides	Logos Biosystems, Anyang-si, South Korea
Microscope coverslips Ø11 mm	Thermo Fischer Scientific, Braunschweig, Germany
Microtome blade S35 MX 35 premier 34/80 mm	Feather Safety Razor CO., LTD, Osaka, Japan
Nitrocellulose Amersham Protan 0.45 µm NC	Sigma Aldrich, Steinheim, Germany
Nunc™ F96 MicroWell™ Polystyrolplatte weiß	Thermo Fischer Scientific, Braunschweig, Germany
Omnifix Luer 3 ml syringes	B. Braun Melsungen, Melsungen, Germany
One-time reagent reservoir	Carl Roth GmbH, Karlsruhe, Germany
Parafilm M	Bemis Company, Neenah, USA
Pasteur Pipettes	Carl Roth GmbH, Karlsruhe, Germany
PCR TW 8-Tube Strip, 0.2ml	Biozym Scientific GmbH, Hessisch Oldendorf, Germany
Pestle	VWR International, Darmstadt, Germany
Polysine slides	Thermo Fischer Scientific, Braunschweig, Germany
Restrainer	VWR International, Darmstadt, Germany
ROTILABO® aluminum foil	Carl Roth GmbH, Karlsruhe, Germany
ROTILABO® blotting paper	Carl Roth GmbH, Karlsruhe, Germany
ROTILABO® syringe filters	Carl Roth GmbH, Karlsruhe, Germany
Safe-lock tubes 1.5 ml, 2.0 ml	Eppendorf, Hamburg, Germany
Serological pipette, sterile (5, 10, 25 ml)	Greiner Bio-One, Frickenhausen, Germany
Superfrost ultra plus slides	Thermo Fischer Scientific, Braunschweig, Germany
Syringes 10 ml, 20 ml, 50 ml	Becton Dickinson GmbH, Heidelberg, Germany
Tubes 0.5 ml, 0.2 ml	Biozym Scientific GmbH, Hessisch Oldendorf, Germany
Western Blot Box	VWR International, Darmstadt, Germany

3.1.3 Chemicals and reagents

Table 3.3: Applied chemicals and reagents.

Name	Manufacturer
4',6-diamidino-2-phenylindole (DAPI)	Carl Roth GmbH, Karlsruhe, Germany
Acetone	AppliChem GmbH, Darmstadt, Germany
Acrylamide/Bis Solution, 37.5:1	Serva Heidelberg, Germany
Agarose	Carl Roth GmbH, Karlsruhe, Germany
Ammonium persulfate (APS)	Sigma Aldrich, Steinheim, Germany
Ampicillin 100mg/ml	Sigma Aldrich, Steinheim, Germany
Antibiotic-Antimycotic	Gibco Life Technologies, Karlsruhe, Germany
β -mercaptoethanol	Sigma Aldrich, Steinheim, Germany
Bovine Serum Albumin (BSA)	Carl Roth GmbH, Karlsruhe, Germany
Clarity Western ECL Substrate	Bio-Rad Laboratories GmbH, Hercules, USA
Crystal Violet	Sigma Aldrich, Steinheim, Germany
DEPC treated water	Gibco Life Technologies, Karlsruhe, Germany
Dihydro-dichlorofluorescein diacetate (H ₂ DCFDA)	Sigma Aldrich, Steinheim, Germany
Dimethyl sulfoxide (DMSO)	Carl Roth GmbH, Karlsruhe, Germany
Dulbecco's modified eagle medium (DMEM)	Gibco Life Technologies, Karlsruhe, Germany
Eosin	Thermo Fischer Scientific, Braunschweig, Germany
Ethanol Technical grade	Thermo Fischer Scientific, Braunschweig, Germany
Horse serum	LINARIS Biologische Produkte GmbH, Dossenheim, Germany
Ethylendiamintetraacetat (EDTA)	Merck KGaA, Darmstadt, Germany
Eukitt	O. Kindler GmbH & Co, Freiburg, Germany
Fetal bovine serum (FBS)	Pan-Biotech, Aidenbach, Germany
FluorSave Reagent	Merck KGaA, Darmstadt, Germany
Halt™ Protease und Phosphatase Inhibitor-Cocktails	Thermo Fischer Scientific, Braunschweig, Germany
Hank's balanced salt solution (HBSS)	Gibco Life Technologies, Karlsruhe, Germany
Hematoxylin	Merck KGaA, Darmstadt, Germany
Hydrogen peroxide 30%	Carl Roth GmbH, Karlsruhe, Germany
Gel loading dye purple (6x)	New England Biolabs, Frankfurt a.M., Germany
GelRed	LINARIS Biologische Produkte GmbH, Dossenheim, Germany
Glycine	Carl Roth GmbH, Karlsruhe, Germany
Isoflurane	AbbVie Inc. North Chicago, USA
Isopropyl alcohol	Aug. Hedinger GmbH & Co. KG, Stuttgart, Germany
Laemmli SDS sample buffer	ThermoFischer, Kandel, Germany
Lipofectamine 2000 / 3000	Thermo Fischer Scientific, Braunschweig, Germany

Name	Manufacturer
Liquid 3,3'-Diaminobenzidine (DAB)+ Substrate Chromogen System	Dako Deutschland GmbH, Hamburg, Germany
Luria Broth (LB) Agar	Carl Roth GmbH, Karlsruhe, Germany
Luria Broth (LB) Medium	Carl Roth GmbH, Karlsruhe, Germany
Methanol Technical grade	Thermo Fischer Scientific, Braunschweig, Germany
Milk powder	Carl Roth GmbH, Karlsruhe, Germany
M-Per Mammalian Protein Extr. Kit	Thermo Fischer Scientific, Braunschweig, Germany
NuPAGE MOPS Running Buffer	Thermo Fischer Scientific, Braunschweig, Germany
Opti-MEM™, Reduced Serum Medium	Gibco Life Technologies, Karlsruhe, Germany
Paraffin	Carl Roth GmbH, Karlsruhe, Germany
Paraformaldehyde (PFA)	Carl Roth GmbH, Karlsruhe, Germany
Penicillin/Streptomycin	Sigma Aldrich, Steinheim, Germany
Phosphate-buffered saline solution (PBS)	Gibco Life Technologies, Karlsruhe, Germany
Plasmocin™ - Mycoplasma Elimination Reagent	InvivoGen Europe, Toulouse, France
Plasmocure™ - Mycoplasma Elimination Reagent	InvivoGen Europe, Toulouse, France
Ponceau S	Sigma Aldrich, Steinheim, Germany
Propidium iodide	Thermo Fischer Scientific, Braunschweig, Germany
Proteinase K	Qiagen GMBH, Hilden, Germany
Puromycin	Gibco Life Technologies, Karlsruhe, Germany
RNase A Solution	Qiagen GMBH, Hilden, Germany
RNase-free DNase Set	Sigma Aldrich, Steinheim, Germany
ROTIPHORESE®50x TAE Puffer	Carl Roth GmbH, Karlsruhe, Germany
RPMI-1640	Sigma Aldrich, Steinheim, Germany
S.O.C. medium	Thermo Fischer Scientific, Braunschweig, Germany
Sodium azide (NaN ₃)	Carl Roth GmbH, Karlsruhe, Germany
Sodium chloride (NaCl)	Carl Roth GmbH, Karlsruhe, Germany
Sodium chloride 0.9% solution	B. Braun Melsungen, Melsungen, Germany
Sodium dodecyl sulfate (SDS)	Carl Roth GmbH, Karlsruhe, Germany
Sodium hydroxide (NaOH)	Carl Roth GmbH, Karlsruhe, Germany
Tetramethylethylenediamine (TEMED)	Carl Roth GmbH, Karlsruhe, Germany
Tris	Carl Roth GmbH, Karlsruhe, Germany
Tris-HCl	Carl Roth GmbH, Karlsruhe, Germany
Triton X-100	Carl Roth GmbH, Karlsruhe, Germany
Trypan Blue	Sigma Aldrich, Steinheim, Germany
Tween 20	Carl Roth GmbH, Karlsruhe, Germany
WST-1	Roche Holding AG, Basel, Switzerland
Xylene	Applichem, Darmstadt, Germany

3.1.4 Primary cell lines, established cell lines, and bacteria

3.1.4.1 Primary cell lines

Table 3.4: List of primary cell lines.

Name	Description
CCC16	iCCA, male, 62Y, KRAS ^{G12D} [77]
CCC33	iCCA, male, 59Y, KRAS wildtype [77]

3.1.4.2 Established cell lines

Table 3.5: List of established cell lines.

Name	Description
HuCCT-1	iCCA, male, 56Y, KRAS ^{G12D} [204]
RBE	iCCA, female, 64Y, KRAS ^{G12V} [205]
WITT	eCCA, KRAS wildtype (kindly provided by Dr Jesper B Anderson (Copenhagen, Denmark) [32]
HuH28	iCCA, female, 37Y, KRAS wildtype [206]

3.1.4.3 Bacteria

In this study chemical competent *Escherichia coli* strain DH5 α with the genotype fhuA2 Δ (argF-lacZ) U169 phoA glnV44 Φ 80 Δ (lacZ) M15 gyrA96 recA1 relA1 endA1 thi-1 hsdR17 was used for amplification of HDTV and CRISPR/Cas9 plasmids (New England Biolabs, Ipswich, USA).

3.1.5 Oligonucleotides

Table 3.6: Applied short interfering RNA.

Name	Sequence 5' \rightarrow 3'	Manufacturer
<i>nonsense_siRNA</i>	5'-GAAGAUUAGACCAGGGUAGAC-3'	Eurofins Genomics, Ebersberg, Germany
<i>siPARP-1 a</i>	5'-ACCGAGAAAUCUCUACCUCU-3'	Eurofins Genomics, Ebersberg, Germany
<i>siPARP-1 b</i>	5'-GCAGUGAAGAAGCUGACAGUA-3'	Eurofins Genomics, Ebersberg, Germany

Table 3.7: Applied Primers.

Name	Sequence 5' \rightarrow 3'	Manufacturer
GAPDH <i>forward</i>	5'-CAACGACCACTTTGTCAAGC-3'	Eurofins Genomics, Ebersberg, Germany
GAPDH <i>reverse</i>	5'-TCTTCCTCTTGTGCTCTTGC-3'	Eurofins Genomics, Ebersberg, Germany
PARP-1 <i>forward</i>	5'-CGAATGCCAGCGTTACAAGC-3'	Eurofins Genomics, Ebersberg, Germany

Name	Sequence 5' → 3'	Manufacturer
PARP-1 <i>reverse</i>	5'-AACATGTAGCCTGTACAGGG-3'	Eurofins Genomics, Ebersberg, Germany
PARP-2 <i>forward</i>	5'-TCCCCTGCCAAGAAACTCG-3'	Eurofins Genomics, Ebersberg, Germany
PARP-2 <i>reverse</i>	5'-TCAGAGACCCTTTTGCTGGC-3'	Eurofins Genomics, Ebersberg, Germany
PARP-1 A	5'-TTGATGGCCGGGAGCTGCTTCTT-3'	Eurofins Genomics, Ebersberg, Germany
PARP-1 B	5'-GGCCAGATGCGCCTGTCCAAGAAG-3'	Eurofins Genomics, Ebersberg, Germany
PARP-1 C	5'-GGCGAGGATCTCGTCGTGACCCATG-3'	Eurofins Genomics, Ebersberg, Germany
T7 promoter	5'-TAATACGACTCACTATAGGG-3'	Eurofins Genomics, Ebersberg, Germany

Table 3.8: Applied plasmids and vectors.

Name	Manufacturer
pcDNA 3.1/Hygro (+)	Thermo Fischer Scientific, Braunschweig, Germany
pNV-sgRNA-Cas9-2A-GFP A 5'-CCACCTCAACGTCAGGGTGC-3' B 5'-TCCAACAGAAGTACGTGCAA-3' C 5'-CGGTCAATCATGCCTAGCTG-3' SC 5'-CGAGTCGAGTACGCCCAAGG-3'	Applied Biological Materials Inc., Richmond, Canada
pT3-EF1a-Kras ^{G12V}	Kindly provided by Matthias Matter, Universitätsspital Basel
pT3-EF1a-shRp53-844-866	Kindly provided by Matthias Matter, Universitätsspital Basel
pT3-EF1a-Nicd (myc-tagged)	Kindly provided by Matthias Matter, Universitätsspital Basel
pT3-EF1a-myrAkt	Kindly provided by Matthias Matter, Universitätsspital Basel
pCMV-HSB2	Kindly provided by Matthias Matter, Universitätsspital Basel

3.1.6 Enzymes

Table 3.9: Applied enzymes.

Name	Manufacturer
BamHI HF	New England Biolabs, Ipswich, USA
Collagenase type IV	Gibco Life Technologies, Karlsruhe, Germany
EcoR1 HF	New England Biolabs, Ipswich, USA

Name	Manufacturer
HindIII HF	New England Biolabs, Ipswich, USA
IQ SybrGreen	Bio-Rad Laboratories GmbH, Hercules, USA
KpnI HF	New England Biolabs, Ipswich, USA
NheI HF	New England Biolabs, Ipswich, USA
OneTaq Quick Load 2x Master Mix	New England Biolabs, Ipswich, USA
SacI HF	New England Biolabs, Ipswich, USA
Sall HF	New England Biolabs, Ipswich, USA
T4 DNA Ligase	New England Biolabs, Ipswich, USA
Trypsin/EDTA	Pan-Biotech, Aidenbach, Germany
XbaI HF	New England Biolabs, Ipswich, USA

3.1.7 Antibodies

Table 3.10: Applied primary antibodies.

Antigen	Host	Dilution*	Manufacturer
β -actin	mouse	1:2000 WB	Santa Cruz Biotechnology, Inc., Dallas, USA
cytokeratin 19	mouse	1:80 IHC	Dako Deutschland GmbH, Hamburg, Germany
Ki67	rabbit	1:200 IHC	Cell Signaling Technology, Danvers, USA
PARP-1	rabbit	1:1000 WB 1:400 IHC	Cell Signaling Technology, Danvers, USA
PARP-2	mouse	1:1000 WB	Merck, KGaA, Darmstadt, Germany
phospho- γ H2AX	rabbit	1:1000 WB 1:500 IHC	Cell Signaling Technology, Danvers, USA
Sox9	rabbit	1:1000 IHC	Sigma Aldrich, Steinheim, Germany

*in 1x TBS-Tween20 with 0,02 % sodium azide

Table 3.11: Applied secondary antibodies and dyes.

Host	Conjugation	Dilution*	Manufacturer
anti-mouse	HRP	1:1000	Thermo Fischer Scientific, Braunschweig, Germany
anti-rabbit	HRP	1:1000	Thermo Fischer Scientific, Braunschweig, Germany
streptavidin	HRP	1:200	Rockland Immunochemicals Inc., Limerick, USA
One-Step Polymere anti-Mouse/Rabbit	HRP	Ready to use	Zytomed Systems GmbH, Berlin, Germany

Host	Conjugation	Dilution*	Manufacturer
anti-mouse	Biotinylated	1:1000	GE Healthcare UK Limited, Little Chalfont, UK
anti-rabbit	Biotinylated	1:1000	GE Healthcare UK Limited, Little Chalfont, UK
anti-mouse	Alexa 488	1:200	Cell Signaling Technology, Danvers, USA
anti-rabbit	Alexa 488	1:200	Cell Signaling Technology, Danvers, USA

*in 1x TBS-Tween20

3.1.8 Kits and mass rulers

Table 3.12: Applied kits and mass rulers.

Name	Manufacturer
BCA Protein Assay Kit	Thermo Fischer Scientific, Braunschweig, Germany
GeneRuler 1 kb Plus DNA ladder	Thermo Fischer Scientific, Braunschweig, Germany
innuPrep Gel Extraction Kit	Analytik Jena AG, Jena, Germany
iScript cDNA Synthesis Kit	Bio-Rad Laboratories GmbH, Hercules, USA
NucleoBond Xtra Midi EF	Macherey-Nagel GmbH & Co KG, Düren, Germany
Page Ruler Prestained Protein Ladder	Thermo Fischer Scientific, Braunschweig, Germany
peqGOLD Tissue DNA Mini Kit	VWR International, Darmstadt, Germany
peqGOLD total RNA kit	VWR International, Darmstadt, Germany
QIAprep Spin Miniprep Kit	Qiagen GMBH, Hilden, Germany
Venor®GeM Mycoplasma Detection Kit	Minerva Biolabs, Berlin, Germany

3.1.9 Inhibitors

Table 3.13: Applied inhibitors.

Name	Manufacturer
Cisplatin	Accord Healthcare GmbH, München, Germany
Doxorubicin	Selleckchem, Houston, USA
Olaparib / AZD2281	Chemietek, Indianapolis, USA

3.1.10 Software

Table 3.14: Applied Software.

Software	Manufacturer
Ascent Software for Fluoroskan Ascent FL	Thermo LabSystems, Vantaa, Finland
Bio-Rad CFX Manager 3.1	Bio-Rad Laboratories GmbH, Hercules, USA

Software	Manufacturer
Corel Draw Graphics Suite X7	Corel Cooperation, Ottawa, Kanada
Endnote x9	Clarivate Analytics, Philadelphia, USA
Finch TV 1.4.0.	Geospiza Inc., Seattle, USA
FlowJo	FlowJo LLC, Ashland, USA
GSEA	Broad Institute Inc., Cambridge, USA
ImageJ 1.50i	National Institutes of Health (NIH) Image, Bethesda, USA
ImageLab 6.0.1	Bio-Rad Laboratories GmbH, Hercules, USA
Ingenuity pathway analysis	Qiagen GmbH, Hilden, Germany
Microsoft Office 2010, Word & Excel	Microsoft Deutschland GmbH, Unterschleißheim, Germany
NanoDrop ND-1000 3.5.1	NanoDrop Technologies, Inc., Wilmington, USA
Prism GraphPad 6	Systat Software GmbH, San Diego, USA
TECAN i-control 3.4.2.0	Tecan, Männedorf, Switzerland
ZEN 2.3	Carl Zeiss Microscopy GmbH, Jena, Germany

3.2 *In vitro* experiments

3.2.1 Cell culture

Primary and established cholangiocarcinoma cell lines were cultured in DMEM (Gibco) supplemented with 5% fetal bovine serum (FBS, Pan-Biotech), 1% penicillin/streptomycin (P/S, Sigma Aldrich) at 37°C in a humidified 5% CO₂ incubator (NuAire). HuH28 was cultured in RPMI-1640 medium (Sigma Aldrich) supplemented with 10% FBS, 1% Penicillin/Streptomycin (P/S). The medium was regularly changed, and cells were passaged at 80-90% confluency. For passaging, cells were washed with 1x phosphate-buffered saline (PBS, Gibco) and dissociated by incubation with 1x trypsin (Pan-Biotech) solution for 5 min at 37°C. The reaction was stopped by adding DMEM supplemented with 5% FBS. The cell suspension was transferred to a 15 ml falcon tube, centrifuged at 400x g for 5 min at room temperature (RT), and re-suspended in 2 ml DMEM containing 5% FBS. Cell number was determined using trypan blue vital dye by LUNA™ Automated Cell Counter (Logos Biosystems). Cells were plated at the required density according to each experimental protocol in 10 cm dishes or multi-well plates. For long-term preservation, cells were frozen in DMEM containing 10% DMSO (Carl Roth) and 40% FBS and were stored first at -80°C, then transferred to liquid nitrogen (-196°C). For re-cultivation, frozen cells were thawed in a water bath at 37°C, transferred into 10 ml of DMEM containing 10% FBS, and centrifuged at 400x g for 3 min at RT. Cell pellets were re-suspended in fresh DMEM and plated in a 10 cm dish. Contamination with mycoplasma was checked regularly using Venor®GeM Mycoplasma Detection Kit (Minerva Biolabs) and in case of infection, cells were treated with plasmocure and plasmocin (InvivoGen) according to manufacturer's instructions.

3.2.2 Transfection of iCCA cell lines

For transfection with siRNA or plasmid DNA, cells were detached and counted as described in chapter 3.2.1. Next, cells were plated at low confluency (30-50%) in 6-well plates and were incubated in DMEM containing 10% FBS and 1% P/S at 37°C for 24 hours. After 24 hours, the medium was changed to DMEM containing 10% FBS without antibiotics. Transfection reagent Lipofectamine 3000 (Thermo Fischer), as well as 100 pmol siRNA (Eurofins Genomics) or 2 µg plasmid DNA (Applied Biological Materials), were diluted in OptiMEM medium (Gibco) according to the manufacturer's protocol. Next, Lipofectamine and siRNA or plasmid DNA solutions were gently mixed 1:1 and incubated for 20 min at RT. After incubation, the transfection solution was added dropwise to each well and incubated at 37°C overnight. On the next day, the medium was changed back to DMEM containing 10% FBS and 1% P/S. Subsequent functional assays were conducted 72 hours after transfection (see chapters 3.2.3.2, 3.2.3.3).

Cells transfected with Clustered Regularly Interspaced Short Palindromic Repeats/Caspase9 (CRISPR/Cas9) plasmids were transferred to 10 cm dishes and after reaching 80-90% confluency sorted into single cells based on the integrated selection marker GFP using BD FACSAria optimally 5-7 days after transfection (Core Facility Flow Cytometry, Paul-Klein Center for Immune Intervention, University Medical Center Mainz). Single-cell clones were sorted into u-bottom shaped 96-well plates in DMEM supplemented with 20% FBS and incubated at 37°C with 5% CO₂ atmosphere. The medium was changed regularly, and single-cell clones were propagated into 10 cm dishes. Then, aliquots of cells were deep-frozen for long-term preservation and cell pellets were deep-frozen for RNA, DNA, and protein isolation. The first verification of knockout was performed by the protein level determination on Western Blot. Therefore, the proteins were isolated from a frozen

cell pellet following the protocol described in chapter 3.2.5.1. Further validation of CRISPR/Cas9 knockout clones, selected by Western blot, was conducted via Sanger sequencing showing the exact deletions on both alleles. For this purpose, DNA was isolated from a frozen cell pellet and a ~300 bp-long segment flanking the sgRNA target site was amplified via polymerase chain reaction (PCR) using specific primers adding restriction sites of BamHI and NheI (New England Biolabs). PCR products were cleaned, restricted, and ligated into an expression vector pcDNA 3.1 hygro (+) (Thermo Fischer). Ligated vectors were transformed into DH5 α competent *E. coli* bacteria (New England Biolabs) and plated on LB (Luria broth; Carl Roth) agar plates containing ampicillin. After 18 hours of incubation at 37°C, single colonies were picked and cultured in LB Medium (Carl Roth) containing ampicillin at 37°C overnight. On the next day, bacteria were centrifuged at 6800x g at RT and the amplified plasmid DNA was isolated using Qiaprep spin miniprep kit (Qiagen) according to the manufacturer's instructions. DNA concentration was determined using NanoDrop 1000 Spectrophotometer (NanoDrop Technologies) and restriction of plasmid was conducted to verify the correct transformation of amplified plasmids. Verified plasmids (700 ng) together with corresponding T7 primer were sent for Sanger sequencing (StarSEQ GmbH, Mainz, Germany).

3.2.3 Functional assays

3.2.3.1 Dose-response and cell viability analysis by WST-1 assay

Cell viability and proliferation were determined using WST-1 assay (Roche) in a 96-well plate format. This spectrophotometric assay is based on the cleavage of tetrazolium salts to formazan by intracellular enzymes in viable cells. Detection of formazan (at maximum absorption of 440 nm) correlates with the number of living cells and hence shows cytotoxic and cytostatic effects of applied drugs. In order to prepare a 200 mM stock solution, Olaparib (Chemietek) was dissolved in dimethyl sulfoxide (DMSO) according to the manufacturer's instructions. Cisplatin (Accord) (1 mg/ml stock solution) was obtained from the Pharmacy, University Medical Center Mainz. Working solutions for Olaparib and cisplatin were prepared by serial dilutions in DMEM containing 10% FBS, as follows: Olaparib 2048; 1536; 1024; 768; 512; 256; 128; 64; 32; 16; 8 μ M / cisplatin 256; 128; 64; 32; 16; 8; 4; 2; 1; 0.5; 0.25 μ M. Cells of the iCCA cell lines were plated in 96-well plates at a density of 5x10³ cells/well and incubated overnight. Next, the medium was replaced with 100 μ l of serial dilutions of the chemicals and incubated for 72 hours. DMSO was used as vehicle control. To assess cell viability, a working solution of WST-1 was prepared in DMEM (10% FBS) according to the manufacturer's instructions. The old medium was removed and replaced with 100 μ l of WST-1 solution in each well. Absorbance was measured at 450 nm every 30 min for the next two hours using a microplate spectrophotometer Azure Ao (Azure biosystems). Reference wavelength was read at 660 nm and the blank was measured in wells only containing WST-1 working solution without cells. Cell viability was defined as the absorbance of each treatment concentration in comparison to the control shown in percentage \pm SD (n=3). IC₅₀ values were calculated from dose-response curves of three independent experiments by non-linear regression analysis using GraphPad Prism 6.

3.2.3.2 Colony-forming unit (CFU) assay

Colony formation assay is a quantitative *in vitro* assay based on the capability of a single cell to grow into a colony through clonal expansion. This assay was performed after 72 hours of siRNA-mediated *PARP-1* knockdown, inhibition of *PARP-1* via Olaparib treatment (IC₅₀), or CRISPR/Cas9-mediated *PARP-1* knockout. Control cells, as well as treated cells,

were dissociated, counted, and seeded at a density of 1×10^3 per well in 6-well plates containing 3 ml of DMEM (10% FBS). Cells were incubated at 37°C , 5% CO_2 atmosphere to grow colonies for up to two weeks with regular change of culture medium. After incubation time, the medium was removed, and cells were washed twice with 1x PBS. Crystal violet (Sigma Aldrich) working solution was prepared in 1x PBS (1:10) and 1 ml added to each well. After 30 min of staining at RT, crystal violet solution was removed, and wells were washed with dH_2O . To quantify the number of colonies, an image of each plate was taken using Chemi-Doc MP Imaging System (Bio-Rad Laboratories), and colonies were counted using Cell counter software (V.0.2.1 by Nghia Ho). Colony formation capacity was defined as the number of colonies of each treatment group in comparison to the control group in percentage \pm SD ($n=3$).

3.2.3.3 Spheroid-forming unit (SFU) assay

Spheroid formation assay is a quantitative *in vitro* assay that measures the capability of single cells to proliferate in semi-solid 3D matrices. To simulate a 3D extracellular matrix, a so-called semi-solid soft agar in which the single cells are seeded, is produced. This assay was performed after 72 hours of siRNA-mediated *PARP-1* knockdown, inhibition of *PARP-1* via Olaparib treatment (IC_{50}), or CRISPR/Cas9-mediated *PARP-1* knockout. Agarose (Carl Roth) solution (2%) in 1x PBS was prepared and autoclaved. Each well of a 48-well plate was pre-layered with 300 μl of a 1.3% agarose base. Therefore, 6 ml DMEM (20% FBS) was mixed with 4 ml of 2% agarose (pre-heated to 47°C) in a 15 ml falcon tube and added to each well. This base layer was incubated until solidified. Control cells, as well as treated cells, were dissociated, counted, and re-suspended in 700 μl of DMEM (20% FBS) at a density of 7×10^3 . Next, 100 μl of preheated 2% agarose was added to the cell suspension and 120 μl was added to each well as a top layer containing 1000 cells per well with a final concentration of 0.25% soft agar. After 24 hours 300 μl of DMEM (10% FBS) was added and routinely changed every 3 days. Cells were incubated at 37°C , 5% CO_2 atmosphere to grow spheroids for up to two weeks with regular change of culture medium. After incubation time, spheroids (diameter > 3 mm) were counted manually under a microscope and the average number of spheroids in five view fields per well was calculated. Spheroid formation capacity was defined as the number of spheroids of each treatment group in comparison to the control group in percentage \pm SD ($n=3$).

3.2.3.4 Detection of redox status

Intracellular oxidative stress is reflected by the generation of reactive oxygen species (ROS) (e.g. hydrogen peroxide, superoxide, hydroxyl radicals). 2',7'-dichlorodihydrofluorescein-diacetate (DCH₂FC-DA; Sigma Aldrich) was used to monitor oxidative stress in the iCCA cells. The method is based on the intake of non-fluorescent DCH₂FC-DA into the cells by diffusion, where it gets hydrolyzed to 2',7'-dichlorofluorescein (DCFH) and is trapped inside the cells. Upon cellular oxidative stress, DCFH is oxidized by ROS to the highly fluorescent form 2',7'-dichlorofluorescein (DCF), which can be detected at a specific excitation/emission spectrum (495 nm / 535 nm) using a microplate spectrofluorometer (TECAN infinite M 200Pro). Oxidation of DCFH is correlated quantitatively to the level of oxidative stress mediated by H_2O_2 (Carl Roth) and other reactive oxygen species [207]. This assay was performed in cell lines with and without CRISPR/Cas9-mediated *PARP-1* knockout. Control cells, as well as treated cells, were plated in white 96-well plates at a density of 1×10^4 cells/well in 100 μl DMEM (10% FBS) and incubated overnight. To reduce photo-oxidation and bleaching of DCH₂FC-DA and H_2O_2 solutions the following steps were performed under low light conditions and all solutions were protected from light. In order to prepare a 10 mM

stock solution DCH₂FC-DA was dissolved in DMSO according to the manufacturer's instructions. The working solution of DCH₂FC-DA (5 μM in 1x HBSS; Gibco) was prepared shortly before the experiment. Next, the medium was removed, cells were washed once with 1x HBSS and 100 μl DCH₂FC-DA working solution was added. After a loading time of 45 min at 37°C in darkness, DCH₂FC-DA solution was removed, and cells were washed with 1x HBSS again. For induction of oxidative stress, cells were treated with increasing concentrations of H₂O₂ (12.5 – 800 μM) for 20 min at 37°C in darkness. Fluorescence was measured at excitation/emission spectrum (495 nm / 535 nm) using a microplate spectrofluorometer (TECAN infinite M 200Pro). Blank was measured in wells only containing DCH₂FC-DA working solution without cells. ROS levels were defined as the mean fluorescence intensity of each treatment concentration in comparison to the control shown in percentage ± SD (n=3).

3.2.3.5 Induction of DNA damage via irradiation

The iCCA cell lines were seeded on coverslips placed in 3 cm plates (1x10⁵ cells) and cultured in DMEM (10% FBS) for 24 hours. Next, cells were placed into an irradiator (Gammacell 2000) and irradiated with 5 Gy (500 rad = 1:59 sec). After incubation for 1 hour at 37°C, cells were fixed, and immunofluorescence staining was performed (see chapter 3.2.4).

3.2.4 Immunofluorescence staining of iCCA cell lines

The iCCA cell lines were plated on cover-slips (1x10⁵ cells/well) and cultured in DMEM (10% FBS) for 24 hours. After treatment/incubation time cells were fixed with 4% paraformaldehyde (PFA; Carl Roth) at 4°C. Cells were rehydrated in dH₂O, washed with 1x PBS containing 0.1% Tween20 (Carl Roth) (PBS-T), and permeabilized with 0.3% Triton X-100 (Carl Roth) in 1x PBS for 5 min at RT. After another washing step with PBS-T, cells were incubated with blocking solution (10% BSA in PBS-T) for 1 hour at RT to prevent unspecific binding. Primary antibodies, diluted in PBS-T supplemented with 0.1% bovine serum albumin (BSA; Carl Roth), were applied and incubated in a humidified chamber overnight. Next, cells were washed with PBS-T and incubated with fluorophore-coupled corresponding secondary antibodies (Cell Signaling Technology; 1:500 in PBS-T) for 1 hour in darkness. Counter-staining of the nuclei was performed with DAPI (Carl Roth; 1:1000 in PBS-T) for 20 min in darkness. Slides were enclosed with coverslips and FluoroSave embedding medium (Merck) and stored at 4°C in darkness until visualization.

All immunofluorescent stainings were visualized and recorded using a Laser Scanning Microscope LSM-710 (Zeiss) with 63 x magnification oil objective. Obtained pictures were further processed in Zen Software and quantification of apoptotic cells was performed using ImageJ. Total cell number was determined, foci were highlighted and the number of foci per cell was calculated. Quantification (fold change) indicates the number of cells with >5 foci shown as % of total cell number ± SD (n=3).

3.2.5 Western Blot

3.2.5.1 Isolation of protein lysates

For protein isolation, iCCA cell lines were plated either in 10 cm dishes or 6-well plates according to experimental design and treatment. Cells were washed with 1x PBS and directly scraped with a cell scraper after adding 60-200 μ l of M-PER lysis buffer (Thermo Fischer). The cell lysate was transferred into a 1.5 ml tube, incubated for 20 min on ice, and centrifuged at 14,000x g for 30 min at 4°C. Next, the supernatant was collected in a new 1.5 ml tube and stored at -80°C until further use.

3.2.5.2 Determination of protein concentration

Protein concentration was determined using the bicinchoninic acid (BCA) protein assay kit (Thermo Fischer), a colorimetric assay based on the combined reaction of biuret with BCA to quantify total protein concentration. BSA stock solution (2 mg/ml) was used to prepare a standard curve by serial dilution. For sample preparation, 5 μ l of protein-containing supernatant was diluted in 45 μ l H₂O. To both samples and standard concentrations, 1 ml of BCA working solution was added and incubated for 30 min at 60°C. 150 μ l of the solution was then transferred into a 96-well plate and measured at 595 nm in a microplate spectrophotometer (Azure biosystems). The colorimetric intensity of the purple-colored reaction product is proportional to the protein concentration. Each sample and standard concentration was measured in triplicates and protein concentration was determined using the BSA standard curve and under consideration of dilution factors.

3.2.5.3 SDS-polyacrylamide gel electrophoresis and Western Blotting

After photometric determination of protein concentration, 20-30 μ g of proteins in 15 μ l dH₂O was transferred to a new 1.5 ml tube, mixed with 5x loading buffer (Thermo Fischer), and incubated at 95°C for 5 min. SDS-polyacrylamide gels were placed into an electrophoresis chamber and filled with 1x NuPAGE MES running buffer (Thermo Fischer). Next, samples and protein ladder were loaded into the wells. Electrophoresis was run at 80-100 V for 1.5-2 hours.

To transfer the electrophoretically separated proteins onto a nitrocellulose membrane (Sigma Aldrich), the method of Western Blotting was employed. The blot-sandwich, consisting of gel holder cassette, blotting pads, cellulose filter paper, nitrocellulose membrane, and SDS-polyacrylamide gel was set together in the following order: blotting pad, 2x filter paper, membrane, gel, 2x filter paper, blotting pad (Bio-Rad Laboratories). The closed gel holder cassette was then placed into the blotting module inside the blotting chamber with the membrane facing the anode. All steps were performed in a 1x transfer buffer and all bubbles between membrane and gel were carefully removed to ensure complete protein transfer. The blotting chamber was filled with 1x transfer buffer, and the transfer was performed at 100 V for 1 hour at 4°C. The blotting chamber was further cooled by an ice pack and by constant stirring using a magnetic stirrer.

3.2.5.4 Immunodetection of proteins

Following protein transfer the membrane was transferred into a Western Blot Box filled with 1x Tris-buffered saline (TBS), containing 0.1% of Tween20 (TBS-T). Next, the membrane was incubated with blocking buffer (5% milk in TBS-T or 5% BSA (Carl Roth)) at 25 rpm agitation for 1.5 hours at RT to block unspecific binding sites. After washing with TBS-T, primary antibodies (1:1000 or 1:2000 in TBS-T, 0.1% sodium azide) were added to the membrane and incubated overnight at 4°C at 25 rpm. On the next day, the membrane was

again washed with TBS-T and then incubated with corresponding HRP-conjugated secondary antibodies (1:1000 in TBS-T) shaking for 1 hour at RT. After a final washing step, the chemiluminescence activity of HRP was detected using ECL solution (Bio-Rad Laboratories) and visualized with Chemi-Doc MP Imaging System (Bio-Rad Laboratories). For re-probing, membranes were washed with TBS-T, incubated with mild stripping buffer for 1 hour at RT, and then re-blocked with 5% milk or BSA. Densitometric evaluation of protein bands was performed in relation to β -actin or α -tubulin reference protein bands using ImageJ.

3.2.6 DNA isolation

Isolation of DNA of iCCA cell lines and tissue samples was performed using peqGold tissue DNA mini kit (VWR International) following the manufacturer's instructions. Briefly, 20-30 mg of tissue or 1×10^6 cells were mechanically disassociated and lysed in 400 μ l lysis buffer containing RNase A and proteinase K. Cell lysates were incubated for 15-30 min at 50°C under agitation, tissue samples were incubated for 1 hour at 50°C under agitation. After centrifugation, the supernatant was collected, mixed with DNA binding buffer, and transferred into a PerfectBind DNA column. After washing steps, DNA was eluted in 200 μ l of elution buffer. DNA concentration and purity were determined using NanoDrop ND-1000 spectrophotometer (NanoDrop Technologies). *KRAS* mutations were kindly determined by Prof. Dr. Timo Gaiser performing pyro- and Sanger sequencing following standard procedure at the Institute of Pathology, University Medical Center Mannheim (Germany).

3.2.7 RNA isolation

Isolation of total RNA of iCCA cell lines and tissue pieces was performed using peqGOLD total RNA kit (VWR International) following the manufacturer's instructions. Briefly, 20-30 mg of tissue or 1×10^6 cells were mechanically disassociated and lysed in 400 μ l lysis buffer. The lysate was further filtered through a DNA-removing column and flow-through was mixed with an equal amount of 70% ethanol. Next, the lysate was loaded on an RNA-binding column. The membrane was further washed and incubated with DNase to remove the remaining DNA. After following washing steps, RNA was eluted in 50 μ l of nuclease-free H₂O. RNA concentration and purity were determined using NanoDrop ND-1000 spectrophotometer (NanoDrop Technologies).

3.2.7.1 cDNA synthesis

Complementary DNA (cDNA) synthesis was performed using the iScript cDNA synthesis kit (Bio-Rad Laboratories) following the manufacturer's instructions. Briefly, 1 μ g of RNA was mixed with nuclease-free H₂O, 5x iScript reaction mix, and iScript Reverse Transcriptase according to the pipetting scheme below (Table 3.15) and gently mixed. The reaction mix then was placed into a thermo-cycler (Analytic Jena) and a PCR program according to Table 3.16 was run. The cDNA was diluted 1:25 with nuclease-free H₂O for further use.

Table 3.15: Pipetting scheme for cDNA synthesis.

Substance	Amount / Volume
RNA	1 μ g
iScript reaction mix (5x)	4 μ l
iScript Reverse Transcriptase	1 μ l
Nuclease-free H ₂ O	filled up to the final volume of 20 μ l

Table 3.16: Steps of cDNA synthesis.

Step	Temperature	Time
Priming	25 °C	5 min
Reverse transcription	46°C	20 min
RT inactivation	95°C	1 min
Hold	4°C	∞

3.2.7.2 Quantitative real-time polymerase chain reaction

To analyze the expression level of different genes the method of quantitative real-time PCR (qRT-PCR) was employed. qRT-PCR was carried out in 96-well plate format using Real-Time PCR System CFX Connect (Bio-Rad Laboratories). All following steps were performed on ice. For master mix preparation, SybrGreen (Bio-Rad Laboratories), nuclease-free H₂O, and forward and reverse primer were mixed according to the pipetting scheme (Table 3.17) and distributed on the 96-well plate. Next, 5 µl of cDNA solution was added to each well. The qRT-PCR was run according to the scheme in Table 3.18. The resulting fluorescence of SybrGreen intercalating with newly amplified double-stranded cDNA strands was measured by the qRT-PCR cyclers and shown in CFX Manager software. The relative number of cycles to reach the critical cycle threshold (Ct) for each gene was further analyzed by calculating ΔCt , $\Delta\Delta Ct$, and $2^{-\Delta\Delta Ct}$. ΔCt shows the number of cycles of a target gene subtracted by the number of cycles of the housekeeping gene. $\Delta\Delta Ct$ represents the ΔCt of a target gene subtracted by the ΔCt of a control sample. Last, $2^{-\Delta\Delta Ct}$ gives information whether the mRNA expression in the considered sample is down or upregulated, with values over 1 showing upregulation and values below 1 showing downregulation. GAPDH was used as a housekeeping gene. Quality control was performed by melting curve analysis and agarose gel confirmation of amplified products.

Table 3.17: Pipetting scheme for qRT-PCR.

Substance	Volume
cDNA	5 µl
SybrGreen	6,4 µl
Forward primer	0,08 µl
Reverse primer	0,08 µl
Nuclease-free H ₂ O	3,5 µl

Table 3.18: Steps of qRT-PCR.

Step	Temperature	Time
1. Polymerase activation and DNA denaturation	95°C	3 min
2a. Denaturation	95°C	15 sec
2b. Annealing, Elongation, read fluorescence	60°C	1 min >30 cycles, steps 2a/b
3. Melt curve analysis	65°C-95°C, 0.5°C increment 2-5 sec/step	15 sec
4. Cooldown	25°C	30 sec

3.2.8 Next-Generation Sequencing

3.2.8.1 RNA Sequencing

Transcriptome sequencing services were provided by Novogene (UK) Company Limited, Cambridge, UK. RNA isolation of the following samples was performed as described in chapter 3.2.6. Isolated RNA from each 3 biological replicates of all CRISPR/Cas9-mediated *PARP-1* knockout clones as well as corresponding control clones treated with scrambled control were sent for RNA sequencing. Also, total RNA was isolated from tumor tissue of 69 iCCA patients and from normal surrounding liver tissue of 10 iCCA patients that underwent resection between 2013 and 2018 at the Department of Surgery, University Medical Center Mainz, Germany. Further, the total RNA of mouse tumor samples (n = 5 per experimental group) was collected and sent for RNA sequencing. RNA purity was checked photometrically and RNA integrity and quantitation were assessed using RNA Nano 6000 Assay Kit (Agilent 2100 Bioanalyzer). Only samples with RNA integrity number (RIN) equal to or higher than 6 were used. The required amount of total RNA was 2 µg. Next, library preparation for transcriptome sequencing was generated using NEBNext® Ultra™ RNA Library Prep Kit for Illumina® following the manufacturer's instructions. Library preparation is essential to convert mRNA into a suitable template library for subsequent cluster generation and sequencing. Briefly, RNA is first fragmented, converted to cDNA, then the addition of sequencing adaptors, size selection, and PCR amplification are performed. Last, PCR products were purified, and library quality and concentration were assessed. Next, samples were sequenced with an S4 flow cell with PE150 by Illumina Novaseq 6000. To obtain clean data, raw reads were filtered by removing reads containing adapter and poly-N sequences and reads with low quality. The high-quality reads were aligned to the human/mouse reference genome sequence (ENSEMBL Homosapiens.GRCh38 and Mus musculus grcm38) using HISAT2 (hisat2-2.0.2-beta) and feature counts were determined by read summarization with featureCounts (subread-2.0.0). R programming language and related packages were used to further analyze RNA Sequencing data. The feature counts were analyzed by Bioconductor package DESeq2 for differential expression analysis and significance testing was performed by Wald Test statistics. Principal Components Analysis (PCA) and unsupervised hierarchical clustering were conducted using ComplexHeatmap [208].

3.2.8.2 Subsequent analyses of transcriptomic data

Gene set enrichment analysis was performed using GSEA software provided by Broad Institute (Broad Institute Inc, Cambridge, USA). GSEA provides information about the enrichment of gene sets against a collection of annotated gene sets in the molecular signature database (MSigDB). Raw count files of RNA Sequencing experiments were uploaded, and experimental groups were compared. Gene sets with nominal p-value <0.05 and false discovery rate (FDR) < 0.25 were considered enriched in a priori defined set of genes [209].

Ingenuity Pathway Analysis (IPA) online tool provided by Qiagen was used to identify the regulation of pathways and networks. Significantly expressed genes (Wald test) were uploaded and expression analysis based on log-ratio was performed. This analysis determines the most significantly affected pathways. The z-score displays calculated activation or inhibition in color (red = activated, blue = inhibited). Core analyses were performed with a p-value cut off < 0.05. Comparative analyses were used to identify

commonly expressed gene signatures between experimental groups. Fisher's *t*-test of $-\log(p\text{-value} > 1.3)$ was used to determine statistical significance [210].

Gene expression profiling interactive analysis (GEPIA2) is an online tool to explore transcriptomic data of The Cancer Genome Atlas Program (TCGA) and the Genotype-Tissue Expression (GTEx) project [211]. It comprises RNA sequencing expression data of 9736 tumor tissue and 8597 normal tissue samples [211]. The data set of cholangiocarcinoma (CHOL) includes 36 tumor samples and 9 normal samples. The data set of liver hepatocellular carcinomas (LIHC) consists of 369 tumor samples and 160 normal samples. Analyses of gene expression profiles were based on selected datasets of cholangio-carcinoma and hepatocellular carcinoma ("TCGA tumors versus TCGA normal + GTEx normal"). The expression profiles and correlation analysis of *PARP-1* and *KRAS* in CHOL and LIHC in tumor versus normal tissue were obtained. Differential analysis was calculated with one-way ANOVA, using disease state (tumor or normal) after $\log_2(\text{TPM}+1)$ transformation. $\log_2\text{FC}$ was defined as $\text{median}(\text{tumor}) - \text{median}(\text{normal})$ and genes with higher $|\log_2\text{FC}| = 1$ and $q\text{-value} < 0.01$ were considered differentially expressed [211].

3.3 *In vivo* experiments

All procedures were performed in accordance with the guidelines of the National Animal Protection Guidelines following approval (G-18-1-045, NTP-ID 00022187-1-2) by the Federal Investigation Office of Rhineland-Palatinate (Landesuntersuchungsamt, Rheinland-Pfalz). To investigate the impact of *Parp-1* and *Kras* on cholangiocarcinogenesis a *Parp-1* knockout mouse model was used. *Parp-1* knockout mouse strain with 129/Sv x C56BL/6J genetic background was first developed in 1997 by Menissier de Murcia [158]. The homozygous *Parp-1* knockout mice are viable and fertile. PCR-based genotyping was performed using ear biopsies after fast DNA extraction protocol. Specific PCR products were analyzed after agarose gel electrophoretic separation [212].

3.3.1 Hydrodynamic tail vein injection

To induce sporadic hepatic tumorigenesis the method of hydrodynamic tail vein injection (HDTV) was used. HDTV is based on the rapid injection (5-7 sec) of a relatively high volume of plasmid DNA solution (10% of the bodyweight) through the tail vein. The resulting hydrodynamic pressure leads to short-term failure of the right heart and the volume is pushed back through the hepatic vein into the liver. Herein, physical force by the injection enhances endothelial and parenchymal cell permeability followed by subsequent sporadic uptake of plasmid DNA into hepatocytes [123]. The plasmids contain a specific construct expressing the mutated form of *Kras*^{G12V}. To achieve a stable and long-term transfection, an additional plasmid containing Sleeping Beauty Transposase (*HSB2* under a CMV promoter) is injected into the target gene, which enables a stable integration of the target gene into the host genome. The transfection efficiency is expected in about 10-15% of liver cells, which resembles the sporadic development of a liver tumor in humans. Since the sole expression of mutant *Kras* is not sufficient to initiate tumorigenesis, a combination with shRNA-mediated knockdown of an established tumor suppressor gene *Tp53* (targeting position 844-866 of *Tp53* mRNA-Sequence) was injected (*Kras*^{G12V}/*shRp53*; combination referred to as *Kras/Tp53*) [68, 133]. To dissect the relevance of activated *Kras* in *Parp-1* deficient background, the *in vivo* experiments were performed in comparison to a non-KRAS

driven iCCA model (*myrAkt/myc-tagged Nicd*; combination referred to as *Akt/Nicd*) (Figure 3.1).

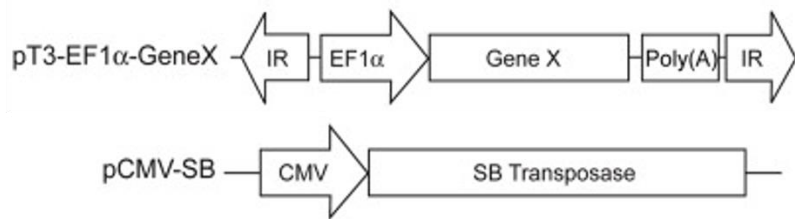


Figure 3.1: Structure of HDTV constructs.

Structure of pT3-EF1α vector containing target gene under the control of an EF1α promoter added Poly(A) sequence and flanking inverted repeats (IR). Structure of pCMV-SB vector containing SB transposase under control of a CMV promoter (modified after Chen & Calvisi, 2014 [123]).

A plasmid DNA solution, containing 5000 µg *Kras/Tp53* and 2500 µg *Akt/Nicd* plasmids were injected, *HSB2* in a ratio of 1:5 and accounting for 10% of body weight was injected intravenously within 5-7 seconds [123, 133]. Plasmid DNA solutions were prepared freshly before each injection in sterile 1x PBS. The solutions were pre-warmed to RT and pre-filled into 3 ml syringes. Male mice were randomized and injected at the age of 7-8 weeks, depending on their body weight (between 20g and 25g). After weighing mice were placed in a restrainer and the tail vein was made more visible and dilated by short exposure to red light. The plasmid solution was injected with 27G needles and mice were kept under tight monitoring for the next 1 hour. The mice were checked weekly for any signs of tumor growth, liver failure, or ascites. Bodyweight was determined to monitor severe weight loss. Mice injected with *Kras/Tp53* were sacrificed after 10-15 weeks, mice injected with *Akt/Nicd* after 7-8 weeks. After sacrifice, the liver was dissected and either fixed in 4% PFA or preserved at -80°C. RNA isolation and further analysis via qRT-PCR and RNA sequencing were performed (described in chapter 3.2.8).

Plasmids for HDTV injection were kindly provided by Matthias S. Matter, Institute of Pathology, University Hospital Basel, Switzerland. Needed amounts of plasmid were produced via transformation of competent *E. coli* strain DH5α (New England Biolabs) and plasmid DNA isolation using NucleoBond Xtra Midi EF kit (Machery-Nagel) following standard protocol. The correct sequence was evaluated by digestion of each plasmid with specific restriction enzyme combinations. The plasmids were stored as aliquots at -20°C.

3.3.2 Histology and immunohistochemistry

Tissue samples of dissected mouse livers were fixed in 4% PFA and further embedded in paraffin by Leica TP 1020 automated embedder according to the manufacturer's instructions. Paraffin-embedded tissue samples were cut into 3.5 µm sections using Leica RM2245 microtome. Paraffin sections were kept on a heating plate at 40°C overnight to dry. For deparaffinization and rehydration, the slides were placed in xylene (Applichem) and decreasing alcohol series (100-70% EtOH, Thermo Fisher), followed by dH₂O.

Hematoxylin-eosin (H&E) staining was performed according to standard protocol using Mayer's Hemalum Solution (Merck) and Eosin-y alcoholic solution (Thermo Fischer). Following the staining, slides were dehydrated with increasing alcohol series (70-100% EtOH) and final incubation in xylene. Sections were enclosed with coverslips and xylene-based mounting medium (O. Kindler GmbH & Co) and dried overnight under the hood.

Before immunohistochemical staining, slides were cooked in citrate buffer (pH 6.0) for 1 hour. Next, slides were washed with dH₂O and 1x PBS containing 0.1% Tween20 (PBS-T). Permeabilization was performed using 0.3% Triton X-100 in 1x PBS for 5 min at RT. After another washing step with PBS-T, endogenous peroxidases were quenched using 3% H₂O₂ (Carl Roth) in dH₂O for 5 min at RT. After washing, cells were incubated with blocking solution (2% Horse Serum, 1% BSA in PBS-T) for 1 hour at RT to prevent unspecific binding. Primary antibodies, diluted in PBS-T supplemented with 0.1% BSA, were applied and incubated at 4°C in a humidified chamber overnight. Next, cells were washed with PBS-T and incubated with HRP-coupled corresponding secondary antibodies (Thermo Fisher) for 30 min at RT. DAB staining was performed according to the manufacturer's instructions (Dako). Next, counterstaining of the nuclei was done with Hematoxylin (Merck) for 1 min. After dehydration, slides were enclosed with coverslips and xylene-based mounting medium (O. Kindler GmbH & Co) and dried overnight under the hood.

All immunohistochemical stainings were visualized and recorded using a Zeiss AxioPlan microscope with 5x, and 10x magnification objectives. Obtained pictures were further processed in Zen Software.

Representative paraffin-embedded tumor and liver tissue sections were kindly histopathologically examined and classified by Prof. Dr. Beate Straub, Institute of Pathology, University Medical Center Mainz. PAS reaction and Trichrome-Gomori staining were performed following standard staining procedure at the Institute of Pathology, Mainz.

3.4 Statistical analysis

Statistical analyses were performed using Student's t-test or Mann-Whitney U test. All results were presented as means ± standard deviation (SD) from at least three independent experiments. Statistical significance was indicated as * $p < 0.05$, ** $p < 0.01$ and, *** $p < 0.001$. IC₅₀ values were calculated from dose-response curves of three independent experiments by non-linear regression analysis using GraphPad Prism 6.

4. Results

4.1 Clinicopathological information of iCCA patients

Fresh tumor tissue from 71 iCCA patients, who underwent resection at the Department of Surgery of the University Medical Center, Mainz (Germany) between 2012 and 2019, was collected. In the Mainz iCCA patient cohort, gender distribution was nearly equal (54% female, 46% male). The median age on the day of surgery was 65 years (female 67 years, males 62 years). The majority of the iCCA tumors were well to moderately differentiated with a total percentage of 68% (well to moderate – 3%; moderate 65%), while a small number of tumors (28%) showed moderate to poor differentiation (moderate to poor 7%; poor 21%). Tumor grading showed that 68% of iCCA were low graded (G1-G2, G2) and 28% were high graded (G2-G3, G3). Differentiation and tumor grading of the remaining 4% was not determined or available. Tumor sizes ranged from 0.5 cm to 18 cm in diameter with an average of 7 cm (± 4 cm) (Table 4.1).

Table 4.1: Demographic and clinicopathological information of Mainz iCCA patient cohort.

Sample ID	Gender	Age	Size (cm)	TNM	Grading	Differentiation	Analysis	
							DNA	RNA
CCA1	M	48	1.4	N/A	G2	Moderate	x	x
CCA2	F	77	13.0	pT1, pN0, M0, R0	G2	Moderate	x	x
CCA3	F	64	6.0	pT2b, pN0, M0, R0	G1-G2	Well to moderate	x	x
CCA4	F	77	6.5	pT2b, pN0, M0, R1	G2	Moderate	x	x
CCA5	F	71	10.3	pT1, pN0, M0, R0	G2	Moderate	x	x
CCA6	M	69	3.5	pT1, pN0, M0, R0	G2	Moderate	x	x
CCA7	M	55	12.0	pT2a, pN0, M0, R0	G2	Moderate	x	x
CCA8	F	75	5.0	pT1, pN0, M0, R0	G2	Moderate	x	x
CCA9	F	59	6.4	pT3, pN0, M0, R0	G2	Moderate	x	x
CCA10	F	78	5.9	pT3, pN1, M0, R0	G2	Moderate	x	x
CCA11	M	32	8.2	N/A	G2	Moderate	x	x
CCA12	F	55	0.5	pT2, N0, M0, pR1	G3	Poor	x	x
CCA13	M	64	4.3	pT3, pN1, M0, R0	G2	Moderate	x	
CCA14	M	74	3.5	N/A	G2	Moderate	x	x
CCA15	F	79	12.0	pT2b, pN0, M0, R0	G2	Moderate	x	x
CCA16	M	62	10.0	pT3, pN1, M0, R0	G3	Poor	x	x
CCA17	M	68	14.5	pT3, pN1, M0, R1	G2-G3	Poor to Moderate	x	x
CCA18	F	64	10.2	pT2a, pN1, M0, R0	G3	Poor	x	x
CCA19	M	62	7.3	pT3, pN1, M0, R0	G2	Moderate	x	x
CCA21	M	57	8.0	rpT3, pN0, M0, R0	G2	Moderate	x	x
CCA22	M	68	9.0	pT2a, pN0, M0, R0	G3	Poor	x	x
CCA23	F	69	N/A	pT1, N0, M0, R0	G2	Moderate	x	x
CCA24	M	79	3.0	pT1, pNX, M0, R0	G2	Moderate	x	x
CCC25	M	62	0.5	ypT1, ypN0, Mx, yR0	N/A	N/A	x	
CCA26	F	55	6.2	pT3, pN0, pM1, R0	G2	Moderate	x	x
CCA27	F	80	5.5	pT1, pNx, M0, R0	G2	Moderate	x	x
CCA28	M	82	2.6	N/A	N/A	N/A	x	x
CCA29	F	76	0.6	pT2b, pN0, Mx, R0	G2	Moderate	x	x
CCA30	F	66	14.0	pT2b, pN0, M0, R0	G2	Moderate	x	x
CCA31	M	79	7.5	pT2a, N0, M0, R0	G3	Poor	x	x
CCA32	M	62	1.2	ypT3, ypN0, M0, R0	G2-G3	Poor to Moderate	x	x

Sample ID	Gender	Age	Size (cm)	TNM	Grading	Differentiation	Analysis	
							DNA	RNA
CCA33	M	59	8.5	pT2a, pN1, M0, R0	G3	Poor	x	x
CCA34	F	70	2.5	rpT1, Nx, M0, R0	G2	Moderate	x	x
CCA35	F	61	13.8	pT2b, N0, M0, R0	G2	Moderate	x	x
CCA38	F	51	17.0	pT1, pN0, M0, R0	G3	Poor	x	x
CCA41	M	78	5.5	pT1, pN1, M0, R0	G3	Poor	x	x
CCA42	F	77	1.9	rpT2b, Nx, M0, R0	G2	Moderate	x	x
CCA43	F	75	3.5	pT2b, pN1, M0, R0	G3	Poor	x	x
CCA44	M	36	2.5	rpT2, rpNX, M1, R0	G3	Poor	x	x
CCA45	M	59	10.5	ypT1, ypN0, M0, R0	G2-G3	Poor to Moderate	x	x
CCA46	F	63	6.5	pT3, pN1, pM1, R0	G2	Moderate	x	x
CCA47	M	62	2.3	pT1, pN0, M0, R0	G2	Moderate	x	x
CCA48	M	57	10.0	pT1, pN0, M0, Rx	G2	Moderate	x	x
CCA49	F	65	11.5	pT1, pN1, M0, R0	G2	Moderate	x	x
CCA50	M	48	11.0	pT3, pN0, M0, R0	G2	Moderate	x	x
CCA51	F	48	7.0	pT1, pN1, M0, R0	G1-G2	Well to moderate	x	x
CCA52	F	63	1.8	rpT1, rpNx, M0, R0	G2	Moderate	x	x
CCA53	M	73	5.0	pT1, pNx, M0, R1	G2	Moderate	x	x
CCA54	F	83	7.0	pT1, pN0, M0, R0	G3	Poor	x	x
CCA55	F	50	6.0	pT2b, pN0, M0, R0	G3	Poor	x	x
CCA56	M	78	18.0	pT2, pN0, M0, R0	G2	Moderate	x	x
CCA57	F	80	N/A	N/A	N/A	N/A	x	x
CCA58	M	49	2.0	N/A	G2	Moderate	x	x
CCA59	M	50	4.5	pT1a, pN1, M0, R0	G3	Poor	x	x
CCA60	F	77	8.0	pT1b, pNx, M0, R0	G2	Moderate	x	x
CCA61	M	49	3.5	pT2, pN0, Mx, R1	G2-G3	Poor to Moderate	x	x
CCA62	M	57	9.0	pT1b, pN0, M0, R0	G2	Moderate	x	x
CCA63	F	60	6.7	pT2b, pN0, M0, R0	G2-G3	Poor to Moderate	x	x
CCA64	F	74	10.5	pT2, pN0, M0, R0	G2	Moderate	x	x
CCA65	F	37	5.5	pT2b, pN0, M0, R0	G2	Moderate		x
CCA66	F	48	2.0	pT2, pN0, pM1, R0	G2	Moderate		x
CCA68	F	75	6.1	rpT2, rpNx, M0, R0	G2	Moderate		x
CCA69	M	68	4.5	pT2b, pN0, M0, R1	G3	Poor		x
CCA70	M	66	1.8	pT1a, pNx, M0, R0	G2	Moderate		x
CCA71	F	69	11.5	pT1b, pN0, M0, R0	G2	Moderate		x
CCA72	M	78	7.5	pT2, pNx, M0, R0	G2	Moderate		x
CCA73	F	69	10.1	pT1b, pN1, M0, R1	G3	Poor		x
CCA74	F	74	6.7	pT2, pN0, M0, R1	G2	Moderate		x
CCA76	F	69	7.0	pT1b, pNx, M0, R0	G2	Moderate		x
CCA77	F	78	8.5	pT2, pN0, M0, Rx	G2	Moderate		x
CCA78	M	71	5.2	pT1b, pN1, M0, R1	G2	Moderate		x

4.1.1 Frequency of *KRAS* mutation in iCCA patient cohorts

First, we isolated DNA from iCCA tissue samples (n=59) to determine somatic mutations. Due to lack of availability or poor quality of the DNA isolate 21 samples were excluded from the analysis. The frequency of *KRAS* mutations was investigated in cooperation with Prof. Dr. Timo Gaiser, Institute of Pathology, University Medical Center Mannheim (Germany).

KRAS mutations on exon 2 were determined by pyrosequencing and Sanger sequencing and amounted to 8.47% (Table 4.2). Next, we compared our data to another iCCA patient cohort (Microarray iCCA cohort) [127]. The microarray iCCA cohort included 68 surgically resected CCA tissue samples collected from patients in Australia, Europe, and the United States during the period 1991-2008. In total, *KRAS* mutations were found in 9 patient samples, representing 13.24% (Table 4.2).

Table 4.2: Frequency of *KRAS* mutation in iCCA patient cohorts.

	total	<i>KRAS</i> ^{wt}	<i>KRAS</i> ^{mut}	%
Mainz iCCA cohort	59	54	5	8.47
Microarray iCCA cohort	68	59	9	13.24

4.2 Transcriptomic analyses of Mainz iCCA patient cohort

To further investigate molecular differences between *KRAS*-wildtype and *KRAS*-mutant iCCA tissue samples, we performed RNA sequencing on the iCCA tumor tissue samples (n=69) and matched normal surrounding liver tissue (n=10). Two samples were excluded due to the reduced amount and poor quality of the RNA isolate.

We analyzed transcriptomic profiles in *KRAS*-mutant iCCA samples and compared tumor tissue versus normal surrounding liver tissue. We identified a total of 6085 (2520 down, 3565 up) differentially expressed genes by performing Wald test with log-transformed data ($p < 0.05$). Unsupervised hierarchical cluster analyses based on these significantly differential expressed genes demonstrated that tumor tissue samples and normal liver tissue formed dense clusters, confirming a differential gene expression in *KRAS*-mutant tumor tissue. These findings were further confirmed by the corresponding PCA plot (Figure 4.1).

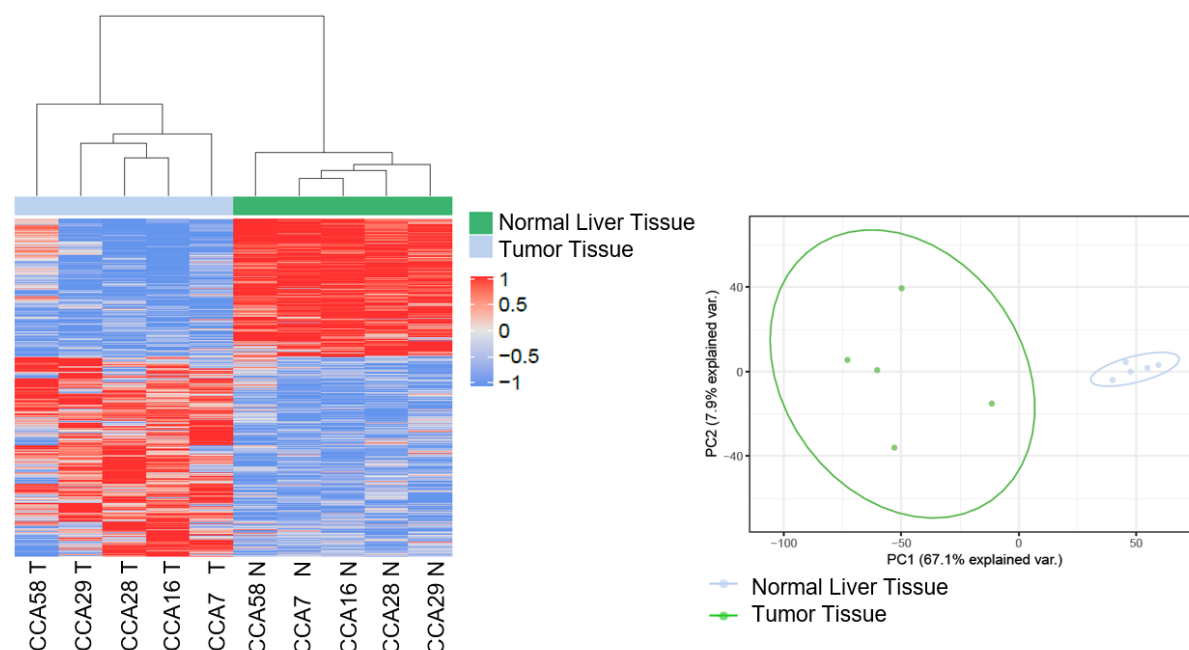


Figure 4.1: Differential gene expression in *KRAS*-mutant tumor versus matched normal surrounding liver tissue.

Unsupervised cluster and principal component analysis (PCA) of significant genes ($p < 0.05$) of *KRAS*-mutant tumor tissue vs. matched *KRAS*-mutant normal surrounding liver tissue.

Next, we applied Ingenuity Pathway Analysis (IPA) provided by Qiagen, an online tool for the identification and prediction of pathway and network regulation of RNA sequencing data. To determine differences in cellular pathways dependent on tumor tissue harboring *KRAS* mutation, we uploaded significantly expressed genes of *KRAS*-mutant iCCA tissue samples versus matched normal surrounding liver tissue samples. Genes were selected based on cut-off p-value < 0.05, resulting in a total number of 6085 genes of which 3565 were up- and 2520 were downregulated. We performed canonical pathway analysis, which determines the most significantly affected pathways and calculates directionality (z-score) displayed in color on pathways and networks (positive z-score = red/activated, negative z-score = blue/inhibited). Only pathways with significant regulation $-\log(\text{p-value}) > 1.3$ were selected. Canonical pathways related to cell cycle control, like G1/S checkpoint regulation and G2/M DNA damage checkpoint regulation, both with negative z-score, were found regulated, indicating dysregulation of cell cycle control in *KRAS*-mutant tumor tissue. Further, the z-score of DNA double-strand break repair-associated pathways (BRCA, ATM) predicted activation in *KRAS*-mutant tumors. Oxidative stress pathways (NRF-2 mediated oxidative stress response, HIF1 α signaling), as well as apoptosis-related pathways (Death receptor signaling, Apoptosis signaling, Necroptosis signaling, and Myc-mediated apoptosis) showed positive z-scores (Figure 4.2 a). These findings suggest a mutual activation of oxidative stress, apoptotic signaling, and enhanced DNA damage response dependent on activated *KRAS* signaling. Further, the regulation of several oncogenic pathways could be revealed. In detail, activation of signaling pathways associated with cholangiocarcinoma such as ERK/MAPK, Pi3K/AKT, NOTCH, and TGF β signaling was shown. Inhibition of pathways was shown in oncogenic pathways like p53, PTEN, HIPPO, AMPK, LXR/RXR, and NF- κ B signaling (Figure 4.2 a). Overall, IPA analyses confirmed that pathway activation and regulation in *KRAS*-mutant tumors differed significantly from matched surrounding liver tissue and linked activated *KRAS* signaling with enhanced apoptosis, oxidative stress, and DNA damage response.

IPA toxicity analyses predict the association of transcriptomic data to clinical outcomes. Our analyses confirmed the activation of apoptosis signaling. Furthermore, signaling pathways associated with liver diseases have been detected. Besides increased hyperplasia/proliferation, hepatitis, steatosis, and liver damage also sets of molecules known to be involved in hepatic fibrosis and cholestasis were enriched. Tumorigenesis-related features of liver proliferation, necrosis, and cell death as well as oxidative stress have been observed (Figure 4.2 b). Taken together these data confirm, that *KRAS* mutations enhance hepatotoxic processes, which are known to promote hepatobiliary carcinogenesis.

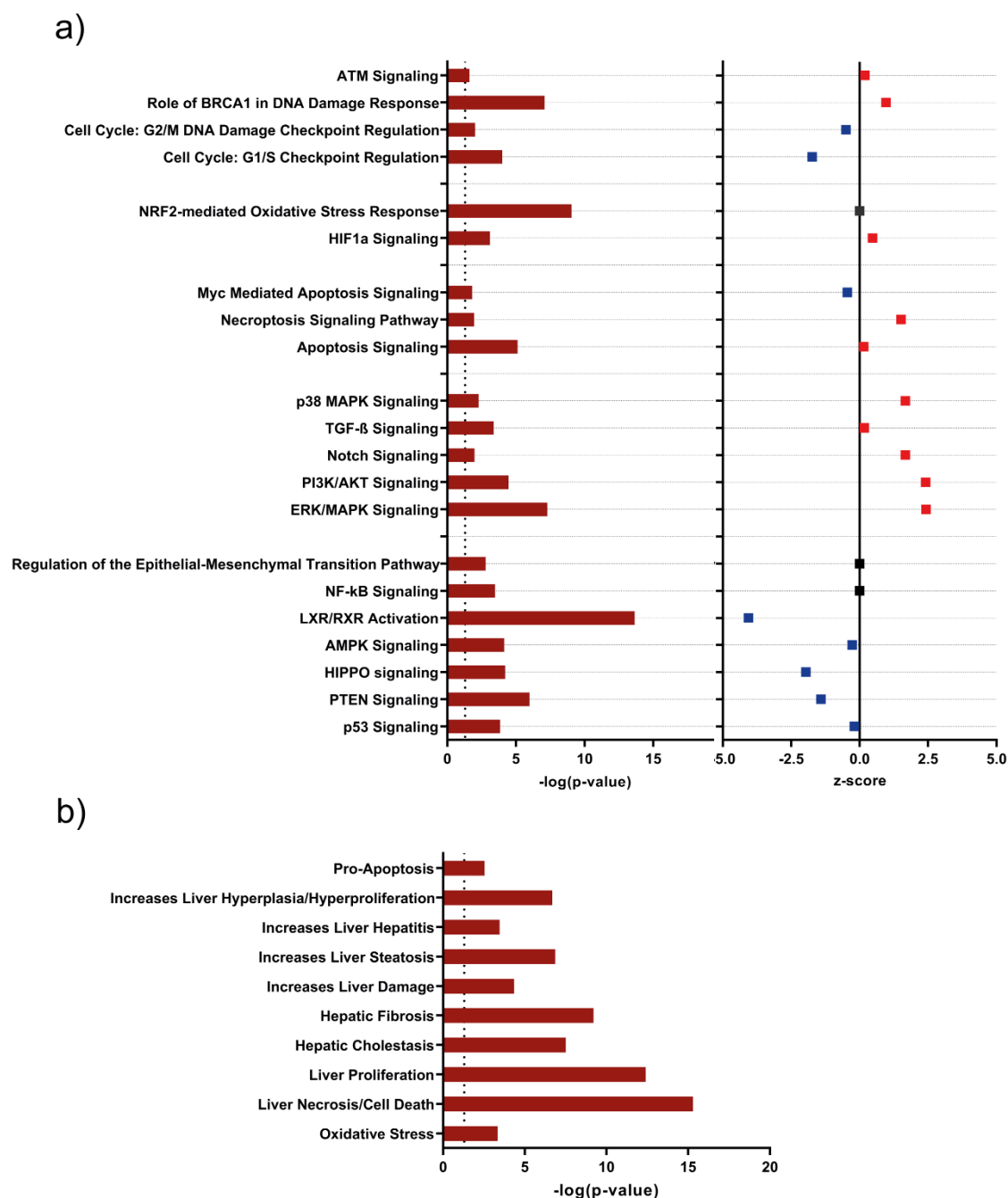


Figure 4.2: Canonical pathways and toxicity analyses of *KRAS*-mutant tumor versus matched normal surrounding liver tissue.

a) Canonical pathways significantly regulated in *KRAS*-mutant tumor vs matched normal surrounding liver tissue identified by IPA. The dashed line indicates the significance threshold of $-\log(p\text{-value}) > 1.3$. Shown are z-scores of respective canonical pathways (positive z-score = red/activated, negative z-score = blue/inhibited). b) Clinical pathology endpoints and networks significantly regulated in *KRAS*-mutant tumor vs matched normal surrounding liver tissue identified by IPA Toxicity analyses. Dashed line indicated significance threshold of $-\log(p\text{-value}) > 1.3$.

Next, we applied Gene set enrichment analysis (GSEA) to complement and confirm the IPA results (Figure 4.3). GSEA provides information on the enrichment of specific gene sets in a collection of annotated gene sets of the molecular signature database (MSigDB) from the Broad Institute. We uploaded raw count files of *KRAS*-mutant tumor tissue versus matched normal surrounding liver tissue samples. Only gene sets with nominal p-value < 0.05 and

FDR < 0.25 were selected. As expected, *KRAS*-mutant tumor tissue showed enrichment in gene sets associated with *KRAS* oncogenic signature. In addition, CK19 positive cholangiocarcinoma, and a CCA class2 cluster, associated with poor prognosis were significantly enriched in *KRAS*-mutant iCCAs. Further, GSEA confirmed enrichment in apoptosis and pathways associated with oncogenic processes (PI3K/AKT and TGF β signaling). In addition, *c-MYC* signaling and activation of *MYC* targets were found. Importantly, several DNA repair pathways were significantly enriched in *KRAS*-mutant tumor tissue. Besides single-strand break repair mechanisms (BER), also double-strand break repair pathways (NHEJ, HR) were found suggesting that activated *KRAS* signaling results in diverse DNA damage response and repair mechanisms.

Gene sets enriched in *KRAS*-mutant tumor tissue

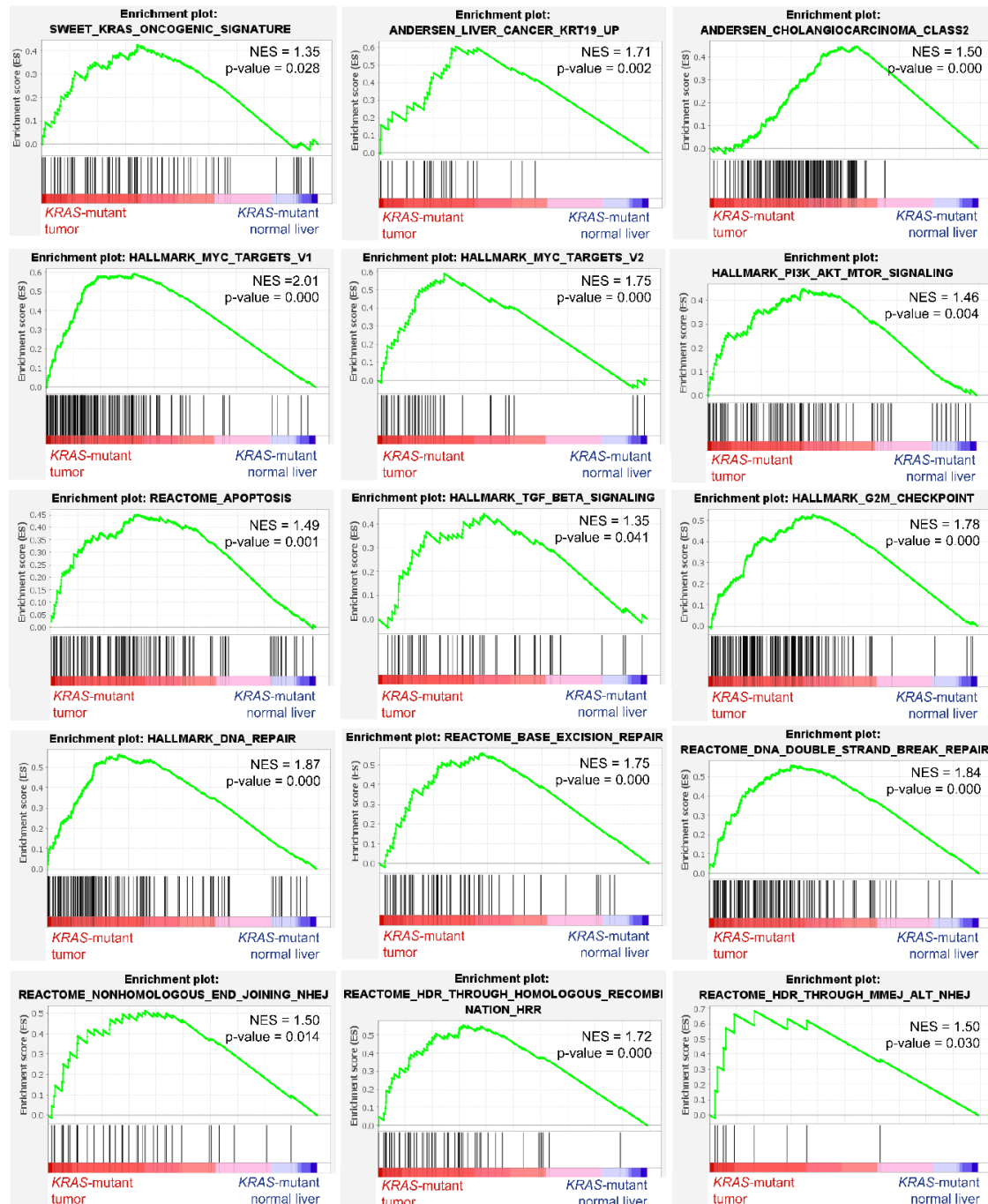


Figure 4.3: Enriched gene sets in *KRAS*-mutant tumor tissue versus matched normal surrounding liver tissue.

Gene set enrichment analysis (GSEA) of *KRAS*-mutant tumor. The selection of gene sets was based on statistical significance calculated by nominal p-value < 0.05 and FDR < 0.25. NES indicates the degree of overexpression for each group at the peak of the entire gene set.

IPA and GSEA analyses indicated differential activation of DNA damage response pathways in *KRAS*-mutant iCCA tissue samples. To further dissect which DNA damage response pathways are active in *KRAS*-mutant and *KRAS*-wildtype iCCA tissue samples, we examined the expression of 82 DNA damage response genes. Both *KRAS*-mutant and *KRAS*-wildtype iCCA tissue samples compared with their respective normal surrounding liver samples showed upregulation of genes associated with DNA double-strand break repair mechanisms. Genes associated with homologous recombination (HR; e.g. *BARD1*, *EXO1*, *RAD54L*, *CHEK1*, *UIMC1*, *RAD51*, *BRCA2*) and both canonical and alternative non-homologous end joining (c-NHEJ; e.g. *XRCC4*, *DCLRE1C*; alt-NHEJ; e.g. *POLQ*, *LIG1*, *FEN1*, *XRCC1*) were activated (Figure 4.4). *PARP-1* expression was significantly upregulated only in *KRAS*-mutant iCCA tumor tissue.

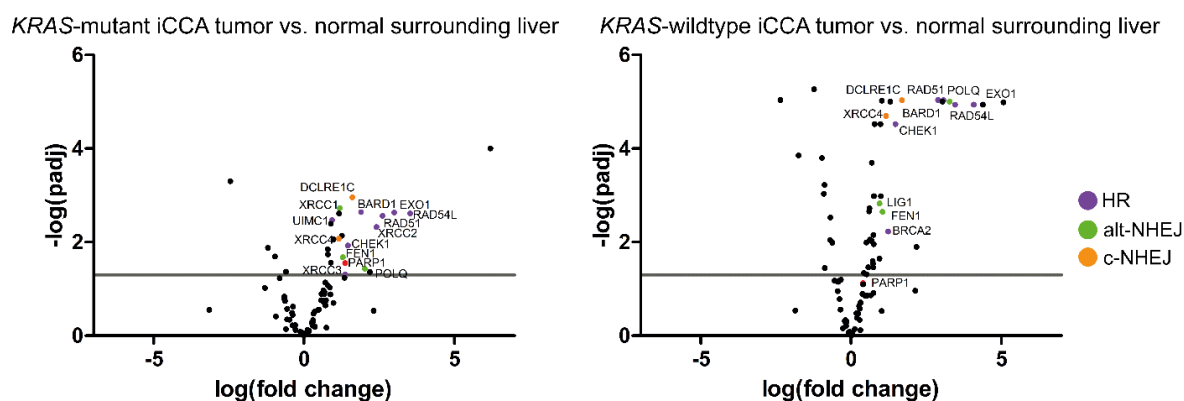


Figure 4.4: Expression of DNA damage response genes in *KRAS*-mutant and *KRAS*-wildtype iCCA tumor tissue.

Vulcano plots are depicted with the log(fold change) of each gene and the $-\log(\text{p-adjusted})$ was calculated by performing Wald test. Selected genes associated with HR, c-NHEJ, and alt-NHEJ are colored and gene names are displayed.

Finally, we normalized the raw counts of all tumor tissue samples of *KRAS*-mutant and *KRAS*-wildtype iCCAs to the 5 *KRAS*-wildtype normal liver samples. We found 2382 differentially expressed genes by performing Fisher's t-test. The normalized significantly expressed genes ($p < 0.05$) of *KRAS*-mutant tumor tissue samples formed a dense cluster amongst all *KRAS*-wildtype iCCA samples, indicating that *KRAS*-mutant iCCAs show a different gene expression pattern and hence, specific characteristic pathophysiological features. These findings were confirmed on the corresponding PCA plot (Figure 4.5 a).

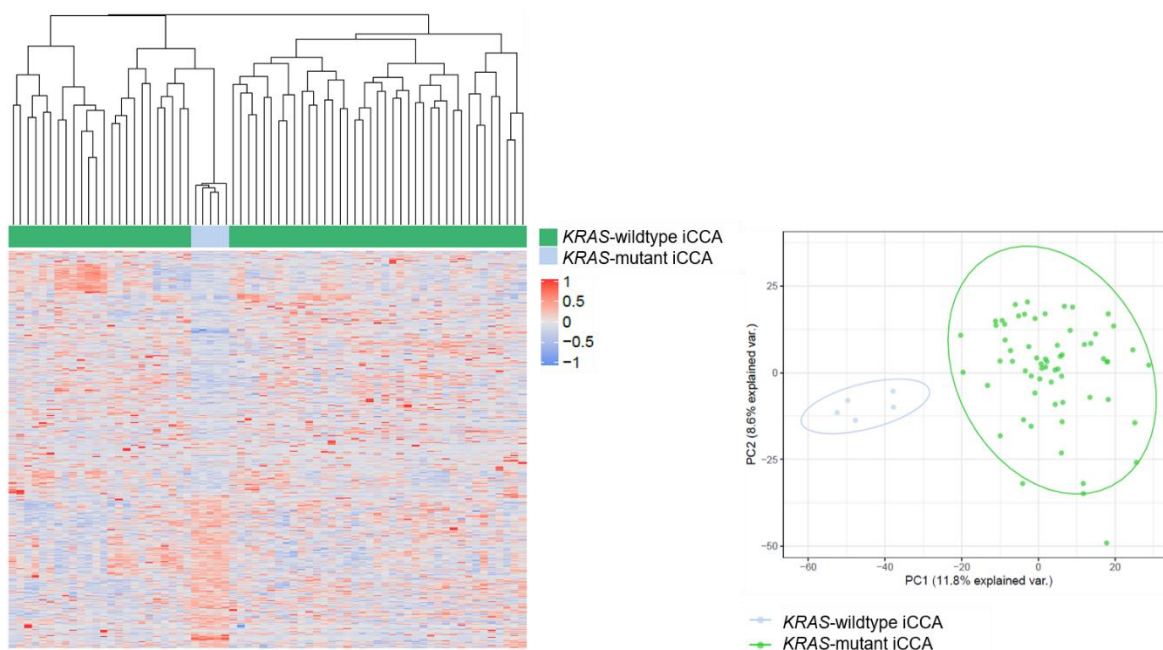


Figure 4.5: Differential gene expression between *KRAS*-mutant tumor versus *KRAS*-wildtype tumor tissue normalized to normal liver tissue.

Unsupervised hierarchical cluster and principal component analysis (PCA) of significant differentially expressed genes ($p < 0.05$) in normalized *KRAS*-mutant tumor tissue vs. *KRAS*-wildtype tumor.

Overall, the analyses of transcriptomic data confirmed that iCCA patients harboring activating *KRAS* mutations show distinct transcriptomic changes compared to normal surrounding liver tissue and *KRAS*-wildtype iCCA tumors. These significant changes in cell cycle control, DNA damage response, and oxidative and apoptotic processes might explain the highly aggressive phenotype of *KRAS*-mutant iCCA and the difficulties in treating them. All pathways of DNA double-strand break (HR, c-NHEJ, and alt-NHEJ) were found activated in both *KRAS*-mutant and *KRAS*-wildtype iCCA tumor tissue samples, however, *PARP-1* expression was only upregulated in *KRAS*-mutant iCCA.

4.3 *PARP-1* and *KRAS* expression in CCA databases

Given the abundance of DNA repair mechanisms, in particular HR and NHEJ, and the suggested association of *KRAS* mutations and *PARP-1* expression in other entities [166, 203], we analyzed the average signal intensity of *PARP-1* expression. We utilized the microarray cohort described above and compared the *PARP-1* expression in *KRAS*-mutant iCCA tissue samples (n=9) with normal intrahepatic bile ducts (n=6) [127]. Statistical analyses showed increased *PARP-1* expression in *KRAS*-mutant iCCA ($p = 0.0259$) (Figure 4.6).

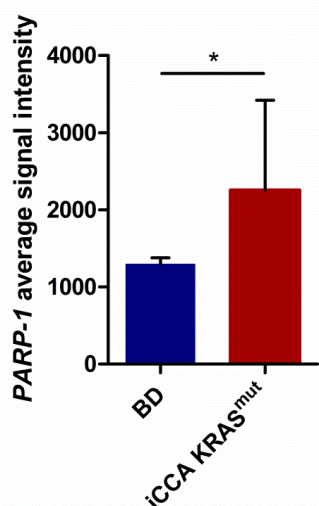


Figure 4.6: Microarray analysis of *PARP-1* expression.

Shown as average signal intensity in normal bile duct tissue (BD) vs. *KRAS*-mutant intrahepatic cholangiocarcinoma (iCCA). Mean \pm SD, $p < 0.05$ (*).

Next, GEPIA2 expression and correlation analyses of *PARP-1* and *KRAS* were investigated in independent patient cohorts of The Cancer Genome Atlas Program (TCGA) and the Genotype-Tissue Expression (GTEx) project [211, 213, 214]. The median transcriptomic expression of *PARP-1* was significantly upregulated in cholangiocarcinoma (CHOL) and hepatocellular carcinoma (LIHC) ($p < 0.01$). Analysis of median mRNA expression of *KRAS* showed significant upregulation in CHOL ($p < 0.01$), whereas LIHC tumor and normal samples showed similar *KRAS* expression (Figure 4.7 a/b). Furthermore, multiple comparison analyses of *PARP-1* and *KRAS* expression confirmed comparatively higher expression levels of both genes in CHOL tumor samples than in LIHC, indicating that *KRAS* mutations play an important role in cholangiocarcinogenesis. The density of color in the here shown multiple gene comparison represents the median expression value of *PARP-1* and *KRAS* in primary liver cancer normalized by maximum median expression values across all blocks. Data were plotted as $\log_2(\text{TPM}+1)$ transformed expression (Figure 4.7 c).

To further explore a potential association between *PARP-1* and *KRAS* expression in CHOL and LIHC, we performed a pair-wise correlation analysis. These analyses were performed using the Pearson correlation coefficient visualized as $\log_2(\text{TPM})$. A positive correlation was observed for both tumor entities, however CHOL showed higher correlation of expression data ($r = 0.6$, $p = 1.5 \times 10^{-05}$) than LIHC ($r = 0.35$, $p = 3.3 \times 10^{-13}$) (Figure 4.7 d/e). Overall, *PARP-1* expression is significantly upregulated in both tumor entities but seems to have a higher association to *KRAS*-mutant tumors in iCCA.

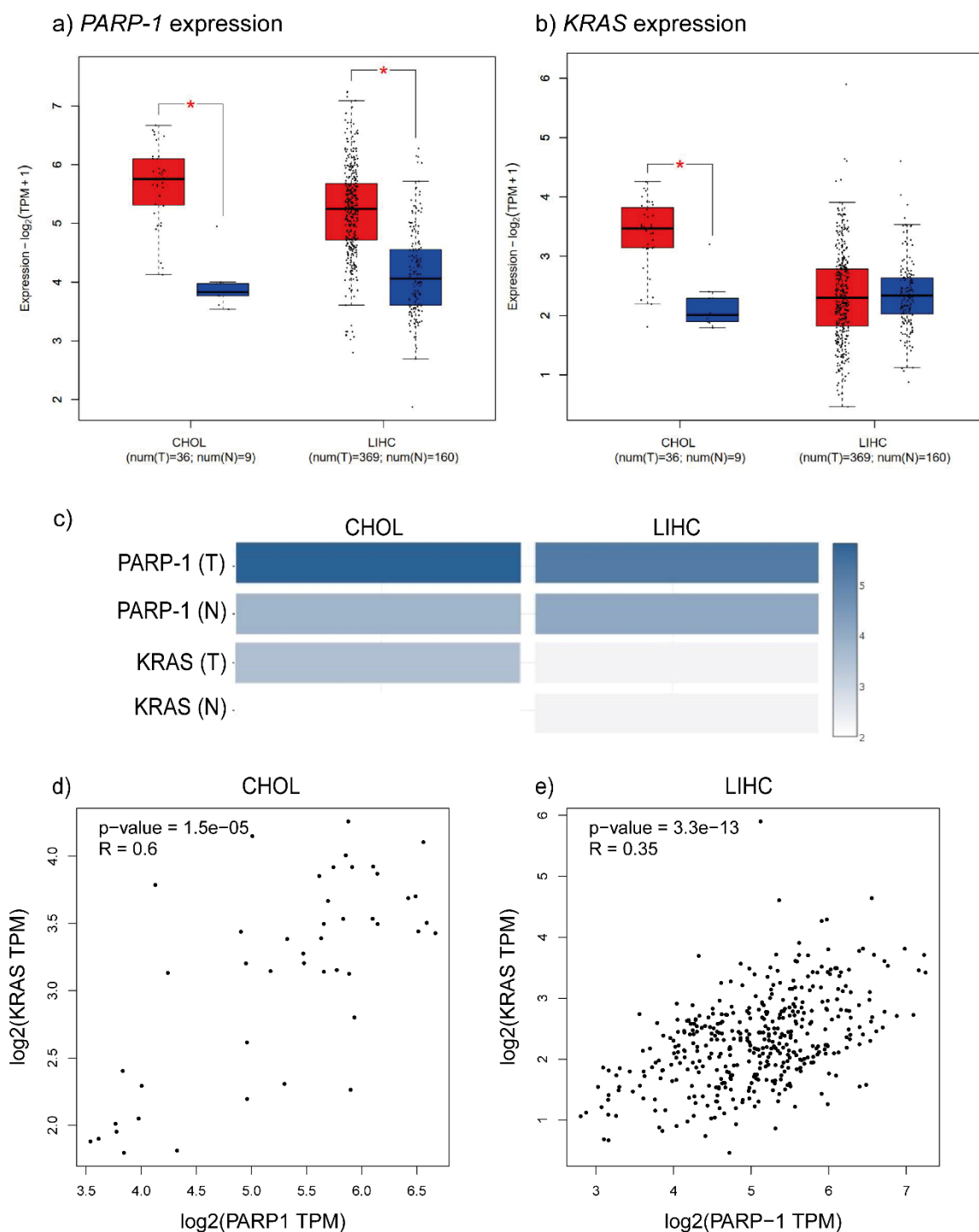


Figure 4.7: GEPIA2 transcriptomic and correlation analysis of *PARP-1* and *KRAS* expression in TCGA and GTEx database.

a) *PARP-1* and b) *KRAS* gene expression profiles (TCGA, GTEx) in cholangiocarcinoma vs. normal liver tissue (CHOL) and liver hepatocellular carcinoma vs. normal liver tissue (LIHC) presented in box plots. Values of $p < 0.01$ (*) were considered as of significant difference. c) Multiple comparisons of *PARP-1* and *KRAS* expression in cholangiocarcinoma vs. normal liver tissue (CHOL) and hepatocellular carcinoma vs. normal liver tissue (LIHC) ($\log_2(\text{TPM}+1)$). d) Pair-wise gene expression correlation analysis of *PARP-1* and *KRAS* expression in cholangiocarcinoma (CHOL) (Pearson correlation coefficient, TCGA CHOL Tumor/TCGA CHOL normal). e) Pair-wise gene expression correlation analysis of *PARP-1* and *KRAS* expression in hepatocellular carcinoma (LIHC) (Pearson correlation coefficient, TCGA LIHC Tumor/TCGA LIHC normal).

To underline the association of *PARP-1* expression and enhanced DNA damage response in CCA we integrated a set of DNA damage response-related genes in the CCA tissue microarray provided by Jesper B. Andersen [127, 215]. The CCA tissue microarray included 153 patient tissue samples (82 tumor samples, 71 benign samples, with 49 tumor/surrounding liver matched pairs). Correlation analyses showed a distinct separation of benign (green) from tumor (red) samples on basis of the gene set expression (Figure 4.8 a). Volcano plot showed differential expression of 50 out of 82 genes in CCA tumor samples ($p < 0.01$) (Figure 4.8 b). Overall, these investigations suggest that DNA damage response pathways play an important role in cholangiocarcinogenesis in general and that *PARP-1* expression seems to be positively correlated particularly in *KRAS*-mutant iCCA tissue samples.

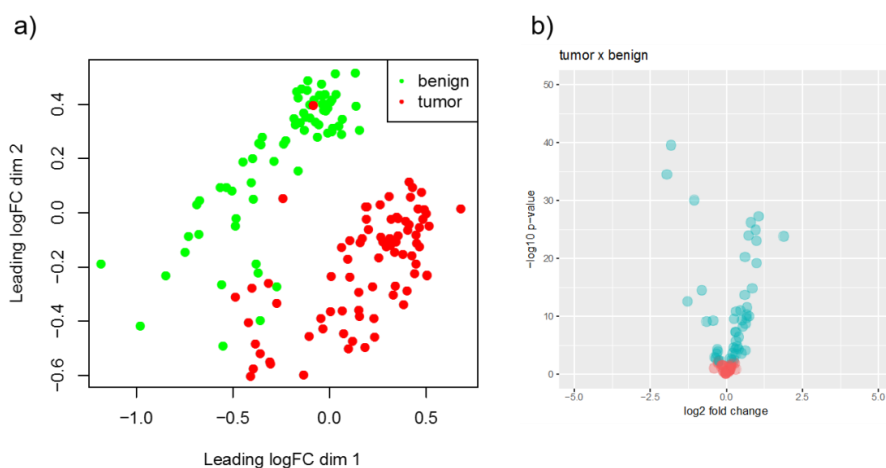


Figure 4.8: Correlation and expression analysis of *PARP-1*-associated gene set on a CCA tissue microarray.

- a) Correlation analysis of *PARP-1*-associated gene set (82 genes) on a CCA tissue microarray ($n=153$) with 71 benign tissue samples (benign) and 82 cholangiocarcinoma tissue samples (tumor).
b) Differential expression analysis of *PARP-1*-associated gene set in tumor vs. benign microarray tissue samples ($p < 0.01$).

4.4 *PARP-1* expression in primary and established cholangiocarcinoma cell lines

Several publically available iCCA cell lines with activating *KRAS* mutation have been established and characterized [204, 205, 216]. In this study, we used HuCCT and RBE. HuCCT harbors the mutation variant *KRAS*^{G12D}, whereas RBE carries the variant *KRAS*^{G12V}. As control served two *KRAS*-wildtype CCA cell lines HuH28 and WITT. In previous studies, our laboratory isolated, established, and characterized several primary intrahepatic cholangiocarcinoma cell lines [77]. Of these patient-derived cell lines (PDCL), a *KRAS*-mutant cell line CCC16 (*KRAS*^{G12D}), and a *KRAS*-wildtype cell line CCC33 were used in this study. None of the cell lines used have a loss of function variant in *BRCA1/2* [58, 216, 217].

After indications of a potential correlation between increased *PARP-1* expression and *KRAS* mutation in iCCA, we examined the above-mentioned iCCA cell lines regarding their *PARP-1* expression. On transcriptomic level we found a significantly enhanced expression of *PARP-1* mRNA predominantly in *KRAS*-mutant iCCA cell lines CCC16, HuCCT, and RBE (CCC33 vs. CCC16 $p = 0.0240$; WITT vs. HuCCT $p = 0.0142$; WITT vs. RBE $p = 0.0034$; HuH28 vs. HuCCT $p = 0.0113$; HuH28 vs. RBE $p = 0.0023$) (Figure 4.9 a).

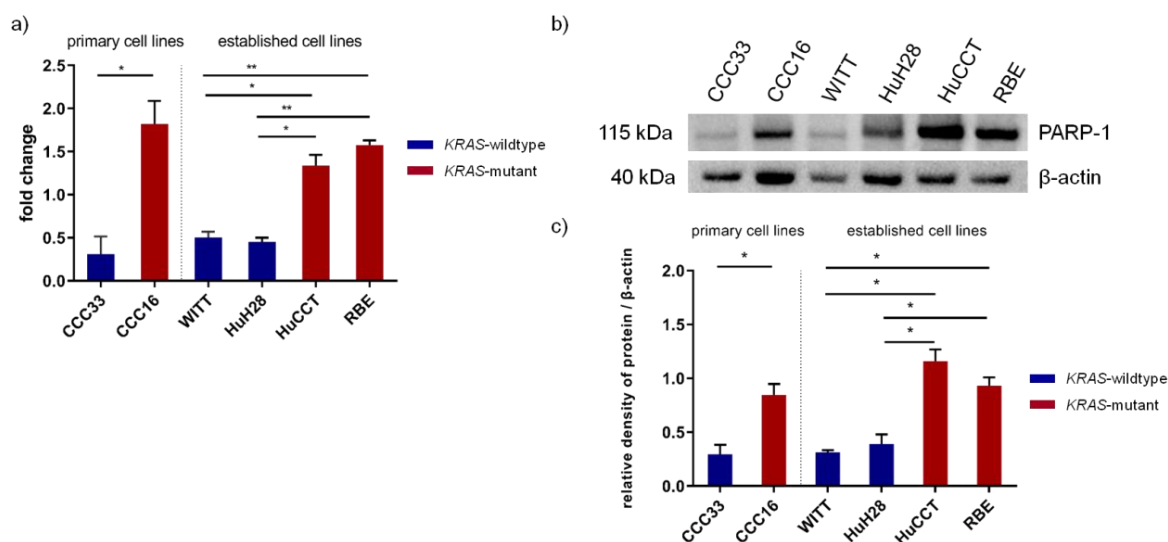


Figure 4.9: Transcriptomic and protein expression of *PARP-1* in primary and established iCCA cell lines.

a) Fold change of basal *PARP-1* expression levels normalized to normal liver tissue in *KRAS*-mutant (CCC16, HuCCT, RBE; red) and *KRAS*-wildtype iCCA cell lines (CCC33, WITT, HuH28; blue). Mean \pm SD, $n=3$, $p < 0.05$ (*), $p < 0.01$ (**). b) Representative Western Blot and c) densitometry analysis of basal *PARP-1* protein expression in *KRAS*-mutant (CCC16, HuCCT, RBE; red) and *KRAS*-wildtype iCCA cell lines (CCC33, WITT, HuH28; blue). The relative density of protein normalized to β -actin is shown. Mean \pm SD, $n=3$, $p < 0.05$ (*).

Further, we determined the protein expression of *PARP-1* in all six iCCA cell lines. Western Blot analysis revealed a higher expression of *PARP-1* in *KRAS*-mutant iCCA cell lines CCC16, HuCCT, and RBE in comparison to *KRAS*-wildtype iCCA cell lines CCC33, WITT, and HuH28. Quantification showed a significant increase of *PARP-1* densitometry normalized to the corresponding β -actin expression (CCC33 vs. CCC16 $p = 0.0286$; WITT vs. HuCCT $p = 0.0105$; WITT vs. RBE $p = 0.0122$; HuH28 vs. HuCCT $p = 0.0162$; HuH28 vs. RBE $p = 0.0234$) (Figure 4.9 b/c). These investigations confirm the hypothesis that upregulation of *PARP-1* mRNA and protein expression is pronounced in *KRAS*-mutant iCCA *in vitro*.

4.5 PARP-1 inhibition via Olaparib treatment

Given the potential association of activating *KRAS* mutations and *PARP-1* upregulation in iCCA, we next performed selective inhibition of PARP-1 in our iCCA cell lines to further investigate the impact of *PARP-1* expression in iCCA and its role as a putative therapeutic target.

Olaparib (AZD2281/Ku-0059436) is a selective inhibitor of PARP-1 and PARP-2 [218]. Olaparib was the first PARP-1 inhibitor that received FDA- and EMA-approval as a single agent for the treatment of patients with diagnosed germline mutations in *BRCA1* or *BRCA2* genes in 2014 after one decade of research [219, 220]. Mechanistically, Olaparib traps PARP-1-DNA complexes and thereby affects the proliferation of targeted cells [188].

First, we performed dose-response analyses with Olaparib in all iCCA cell lines to determine individual IC₅₀ values. We exposed iCCA cell lines to increasing concentrations of Olaparib, incubated for 72 hours, and measured cell viability (shown as % of control) using WST-1 assay. *KRAS*-mutant iCCA cell lines CCC16, HuCCT, and RBE showed a significantly reduced viability in response to PARP-1 inhibition compared to *KRAS*-wildtype cell lines CCC33, WITT, and HuH28 (CCC33 vs. CCC16 $p = 0.0068$; WITT vs. HuCCT $p = 0.0078$; WITT vs. RBE $p = 0.0026$; HuH28 vs. HuCCT $p = 0.0725$; HuH28 vs. RBE $p = 0.0114$) (Figure 4.10).

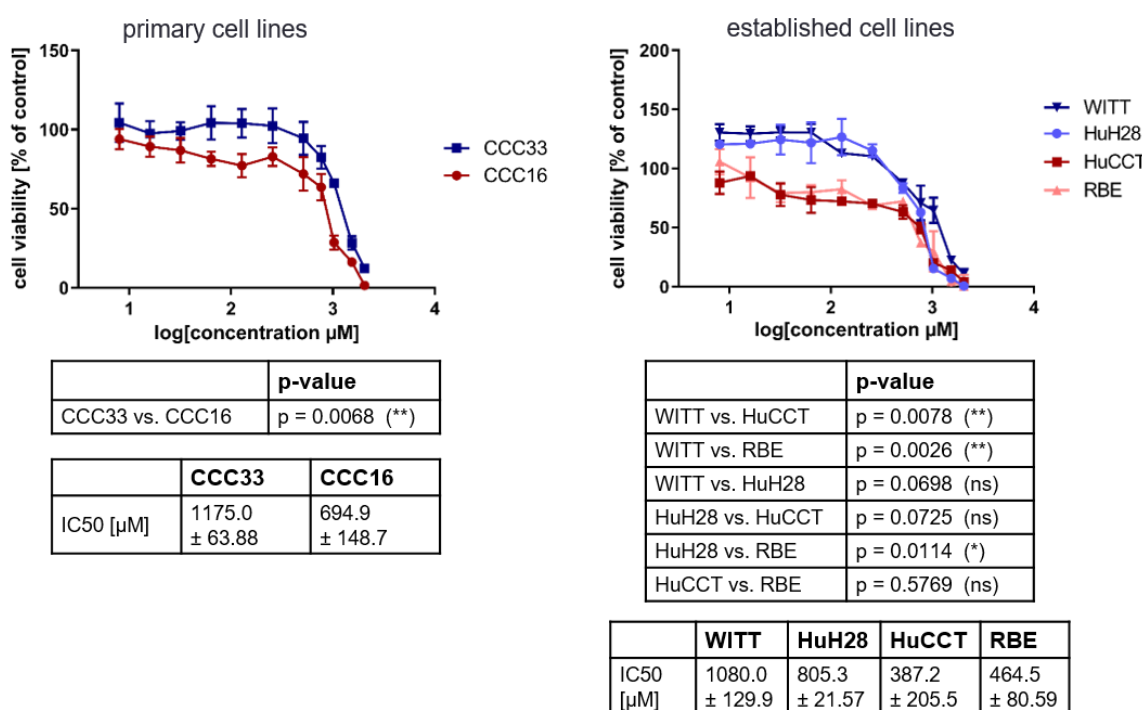


Figure 4.10: Determination of IC₅₀ values of Olaparib treatment in primary and established iCCA cell lines.

Shown are dose-response curves of *KRAS*-mutant (CCC16, HuCCT, RBE; red) and *KRAS*-wildtype iCCA cell lines (CCC33, WITT, HuH28; blue) treated with increasing concentrations of Olaparib to determine IC₅₀ value and impact on proliferation. Mean ± SD, $n=3$, $p < 0.05$ (*), $p < 0.01$ (**).

The IC₅₀ values for *KRAS*-wildtype cell lines CCC33, WITT, and HuH28 were 1175.0 μ M, 1080.0 μ M, and 805.3 μ M, whereas IC₅₀ values for *KRAS*-mutant iCCA cell lines CCC16, HuCCT, and RBE were 694.9 μ M, 387.2 μ M, and 464.5 μ M (Figure 4.10). The here determined cell line-specific IC₅₀, and subsequent IC₂₅ values were used as working concentration in the following functional experiments.

4.5.1 Transient PARP-1 inhibition by Olaparib in iCCA cell lines

Next, we aimed to investigate the impact of PARP-1 inhibition via Olaparib treatment on the proliferation and tumorigenicity by the colony and spheroid forming unit (CFU/SFU) assays. *KRAS*-wildtype and *KRAS*-mutant iCCA cell lines were treated with respective Olaparib IC₅₀ values for 72 hours and then plated in low density for the colony and spheroid formation assay. PARP-1 inhibition led to a significant decrease in the number of CFU (shown as % of control) in *KRAS*-mutant iCCA cell lines CCC16 (50.3%, $p = 0.0003$), HuCCT (51.6%, $p < 0.0001$), and RBE (49.6%, $p < 0.0001$). Similarly, *KRAS*-wildtype iCCA cell lines CCC33 (27.6%, $p = 0.0003$) and WITT (8.4%, $p = 0.0171$) showed a reduction of colony formation capacity upon PARP-1 inhibition (Figure 4.11 a). Further, all *KRAS*-mutant iCCA cell lines showed a significant reduction in spheroid forming capacity after PARP-1 inhibition (CCC16 36.6%, $p < 0.0001$; HuCCT 38.5%, $p = 0.0002$; RBE 42.1%, $p < 0.0001$). Spheroid forming capacity of *KRAS*-wildtype iCCA cell lines remained unaffected upon Olaparib treatment (Figure 4.11 b). Reduction of colony and spheroid formation capacity in *KRAS*-mutant iCCA cell lines ranged between 36.6-51.6% of control. In comparison, reduction of CFU/SFU capacity in *KRAS*-wildtype iCCA cell lines ranged between 0.0-27.6% of control.

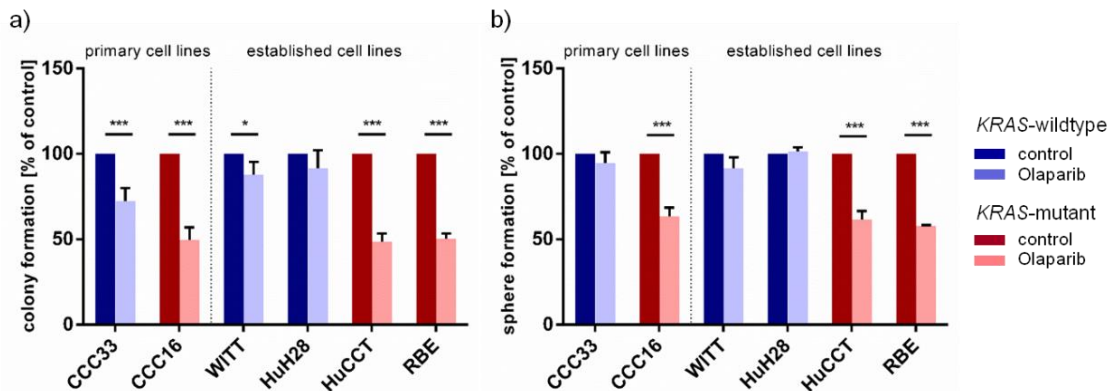


Figure 4.11: Effect of PARP-1 inhibition via Olaparib treatment on colony and sphere formation capacity.

a) Colony and b) sphere formation assay shown as % of control after Olaparib treatment in *KRAS*-mutant (CCC16, HuCCT, RBE; red) and *KRAS*-wildtype iCCA cell lines (CCC33, WITT, HuH28; blue). Mean \pm SD, $n=3$, $p < 0.05$ (*), $p < 0.001$ (***)

To investigate the effect of Olaparib in the presence of increased DNA damage, we determined cell viability after combination treatment of Olaparib and DNA-damaging agent Doxorubicin. The working concentration of Doxorubicin was established by WST assay and literature research [221, 222]. For both, Olaparib and Doxorubicin sublethal doses were employed to avoid toxic effects. *KRAS*-wildtype and *KRAS*-mutant iCCA cell lines were treated with Olaparib (IC₂₅), with Doxorubicin (60 nM), or with a combination of Olaparib and Doxorubicin for 72 hours. A single administration of Olaparib and Doxorubicin led to a

reduction in cell viability in all iCCA cell lines without noticeable differences in *KRAS*-mutant and *KRAS*-wildtype cells (Figure 4.12). Importantly, co-treatment of low levels of Olaparib and 60 nM Doxorubicin reduced cell survival in all cell lines. However, effects were more pronounced in *KRAS*-mutant iCCA cell lines and the combination treatment led to a significantly higher decrease in cell viability (shown as % of control) in *KRAS*-mutant iCCA cell lines CCC16, HuCCT, and RBE compared to *KRAS*-wildtype iCCA cell lines CCC33, WITT, and HuH28 (CCC16 vs. CCC33 $p = 0.0026$; WITT vs. HuCCT $p = 0.0373$; WITT vs. RBE $p = 0.0063$; HuH28 vs. RBE $p = 0.0413$) (Figure 4.12).

Overall, the results of our PARP-1 inhibition experiments demonstrated a higher susceptibility of *KRAS*-mutant iCCA cell lines towards Olaparib treatment and a potentially enhanced effect of the combination of PARP-inhibition and DNA damaging agents in *KRAS*-mutant iCCA *in vitro*.

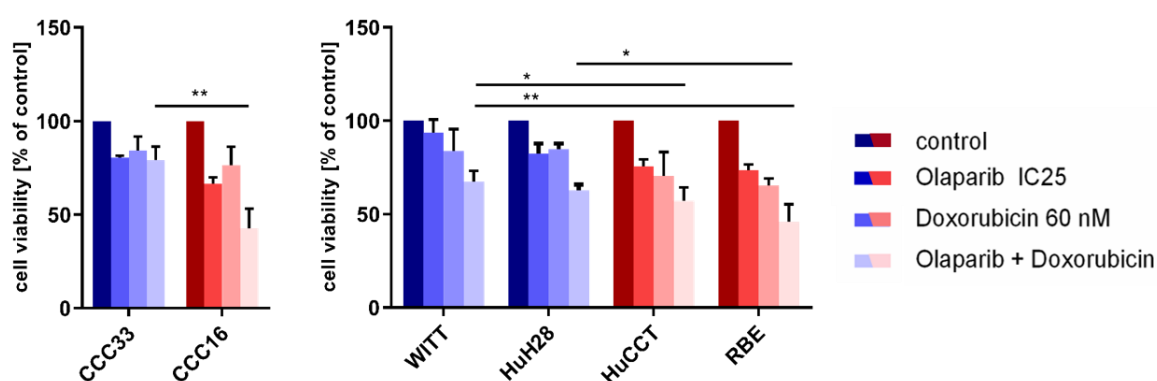


Figure 4.12: Cell viability of *KRAS*-mutant and *KRAS*-wildtype iCCA cell lines after combined treatment with Olaparib and DNA-damaging agent Doxorubicin.

Shown is cell viability as % of control in *KRAS*-mutant (CCC16, HuCCT, RBE; red) and *KRAS*-wildtype iCCA cell lines (CCC33, WITT, HuH28; blue) after treatment with Olaparib (IC25), Doxorubicin (60 nM) or co-treatment. Mean \pm SD, $n=3$, $p < 0.05$ (*), $p < 0.01$ (**).

4.6 siRNA-mediated knockdown of *PARP-1* expression in iCCA cell lines

To confirm that the observed effects are *PARP-1* specific, we next used RNA interference to selectively knock down *PARP-1* protein expression. RNA interference is an established molecular biological method for efficient and sequence-specific silencing of target genes resulting in transient posttranslational inhibition of gene expression [223].

Successful knockdown of *PARP-1* protein expression was confirmed via Western Blot (Figure 4.13 a). The protein expression was reduced by 66.6-83.8%, compared to control cells transfected with nonsense scrambled siRNA (CCC33 78.5%, $p = 0.0091$; CCC16 71.0%, $p = 0.0040$; WITT 66.6%, $p = 0.0358$; HuCCT 82.4%, $p < 0.0001$; RBE 83.8%, $p = 0.0006$) (Figure 4.13 a). This effect was independent of the *KRAS* status of the cells. Notably, the expression of *PARP-2* remained unaffected upon siRNA-mediated knockdown of *PARP-1*, confirming that no compensatory effects after short-term treatment are present (Figure 4.13 b). Due to its low proliferation rate, transfection of *KRAS*-wildtype iCCA cell line HuH28 was not successful; hence, the cell line was excluded for all subsequent analyses of siRNA-mediated knockdown.

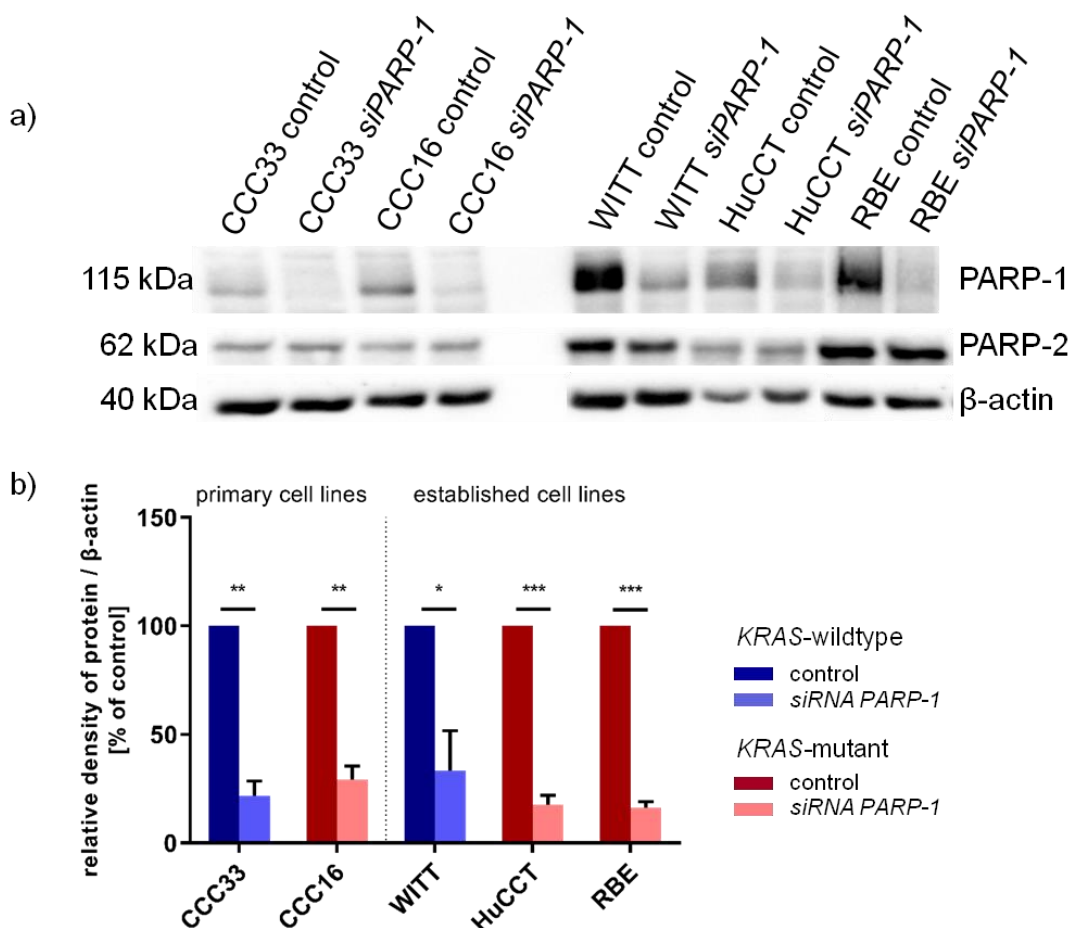


Figure 4.13: PARP-1 protein expression in primary and established iCCA cell lines after siRNA-mediated knockdown.

a) Representative Western Blot and b) densitometry analysis of siRNA-mediated knockdown of *PARP-1* protein expression in *KRAS*-mutant (CCC16, HuCCT, RBE; red) and *KRAS*-wildtype iCCA cell lines (CCC33, WITT; blue). Relative density of protein normalized to β -actin is shown. Mean \pm SD, $n=3$, $p < 0.05$ (*), $p < 0.01$ (**), $p < 0.001$ (***).

4.6.1 Functional effects of siRNA-mediated *PARP-1* knockdown in iCCA cell lines

Next, we aimed to investigate the impact of siRNA-mediated knockdown of *PARP-1* on proliferation and tumorigenicity by CFU and SFU assays (Figure 4.14). *KRAS*-wildtype and *KRAS*-mutant iCCA cell lines were transfected with siRNA against *PARP-1* and incubated for 72 hours. *PARP-1* knockdown led to a significant decrease in the number of CFU (shown as % of control) in *KRAS*-mutant iCCA cell lines CCC16 (40.5%, $p = 0.0043$), HuCCT (35.8% $p = 0.0243$), and RBE (40.4%, $p = 0.0002$) (Figure 4.14 a). Further, all *KRAS*-mutant iCCA cell lines showed a significant reduction in spheroid forming capacity after *PARP-1* knockdown via siRNA (CCC16 40.8%, $p = 0.0041$; HuCCT 41.5%, $p < 0.0001$; RBE 46.7%, $p < 0.0001$) (Figure 4.14 b). Reduction of colony and spheroid formation capacity ranged between 35.6-45.8% of control. In contrast, neither colony formation nor spheroid formation capacity of *KRAS*-wildtype iCCA cell lines was significantly affected upon *PARP-1* knockdown (reduction ranged between 0-6.9%). Taken together, these investigations confirm the preferential effect of *PARP-1* in *KRAS*-mutant iCCA cell lines.

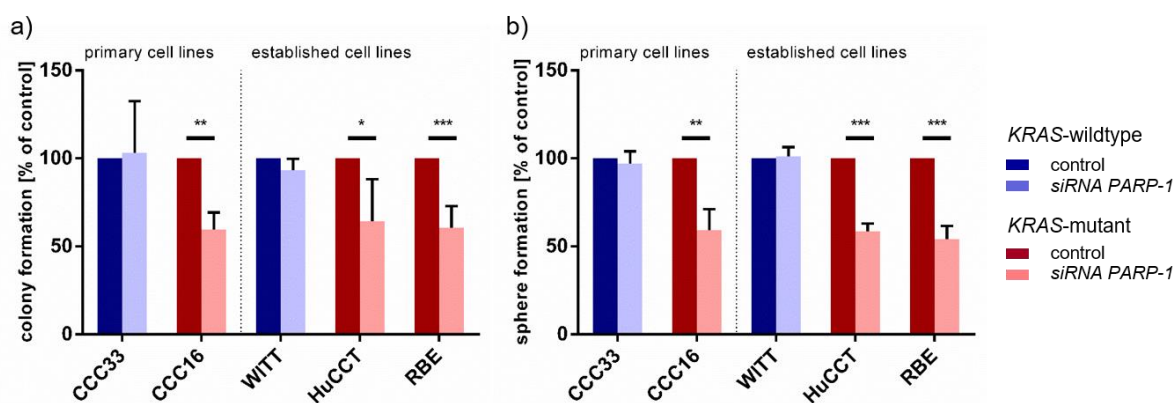


Figure 4.14: Effect of siRNA-mediated knockdown of *PARP-1* on colony and sphere formation capacity.

a) Colony and b) sphere formation assay shown as % of control after siRNA-mediated *PARP-1* knockdown in *KRAS*-mutant (CCC16, HuCCT, RBE; red) and *KRAS*-wildtype iCCA cell lines (CCC33, WITT; blue). Mean \pm SD, $n=3$, $p < 0.05$ (*), $p < 0.01$ (**), $p < 0.001$ (***).

4.7 CRISPR/Cas9-mediated *PARP-1* knockout of iCCA cell lines

PARP-1-based interventions by inhibition or siRNA-mediated knockdown suggest a selective sensitivity of *KRAS*-mutant iCCA cell lines compared to *KRAS*-wildtype iCCA cell lines. To validate these findings and to further investigate the impact of *PARP-1* on functional effects and molecular alterations in *KRAS*-mutant and *KRAS*-wildtype iCCA, we created stable *PARP-1* knockout (KO) clones using the CRISPR/Cas9 technique. The cells were transfected with a plasmid encoding for Cas9, a target-specific single guide RNA (sgRNA), and selection marker GFP (pNV-sgRNA-Cas9-2A-GFP, Applied Biological Materials Inc.). A Cas9-mediated DNA double-strand break at the target site is repaired by a error-prone process called non-homologous end joining (NHEJ). This results in frameshift insertions or deletions, which effectively silence the targeted genes. Single-cell clones were obtained based on GFP expression by fluorescence-activated cell sorting (FACS) and *PARP-1* KO was confirmed by Western Blot and Sanger sequencing (Figure 4.15 and Table 4.3).

We successfully transfected two *KRAS*-mutant iCCA cell lines (HuCCT, RBE) and two *KRAS*-wildtype iCCA cell lines (WITT, CCC33) and obtained two stable CRISPR/Cas9-mediated *PARP-1* knockout clones (referred to as *PARP-1* KO clones) for each cell line. For each iCCA cell line, a control clone transfected with scrambled sgRNA was produced following the same transfection and selection procedure as indicated above. Of note, the generation of *PARP-1* KO clones for cell lines CCC16 and HuH28 was not successful. Despite optimization of transfection conditions and selection methods, no clones with effective knockout could be obtained. Both cell lines showed low proliferation and low capacity to grow as single cells, which made transfection and subsequent selection of clones impossible.

As expected, successful *PARP-1* KO clones showed 0% protein expression (Figure 4.15). Western blot analysis of PARP-2 expression did not show a compensatory upregulation upon *PARP-1* KO. The knockout of *PARP-1* neither harmed nor changed the phenotype or morphology of the successfully transfected cells (Figure 4.16).

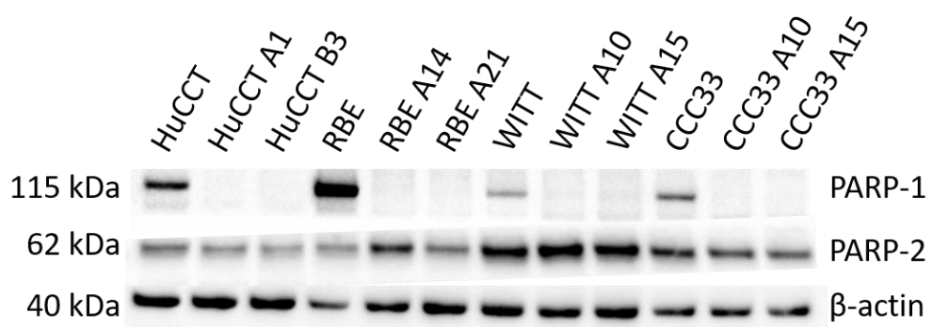


Figure 4.15: PARP-1 protein expression in primary and established iCCA cell lines after CRISPR/Cas9-mediated knockout.

Representative Western Blot of PARP-1, PARP-2, and β -actin protein levels after *PARP-1* KO in *KRAS*-mutant (HuCCT, RBE; red) and *KRAS*-wildtype iCCA cell lines (CCC33, WITT; blue).

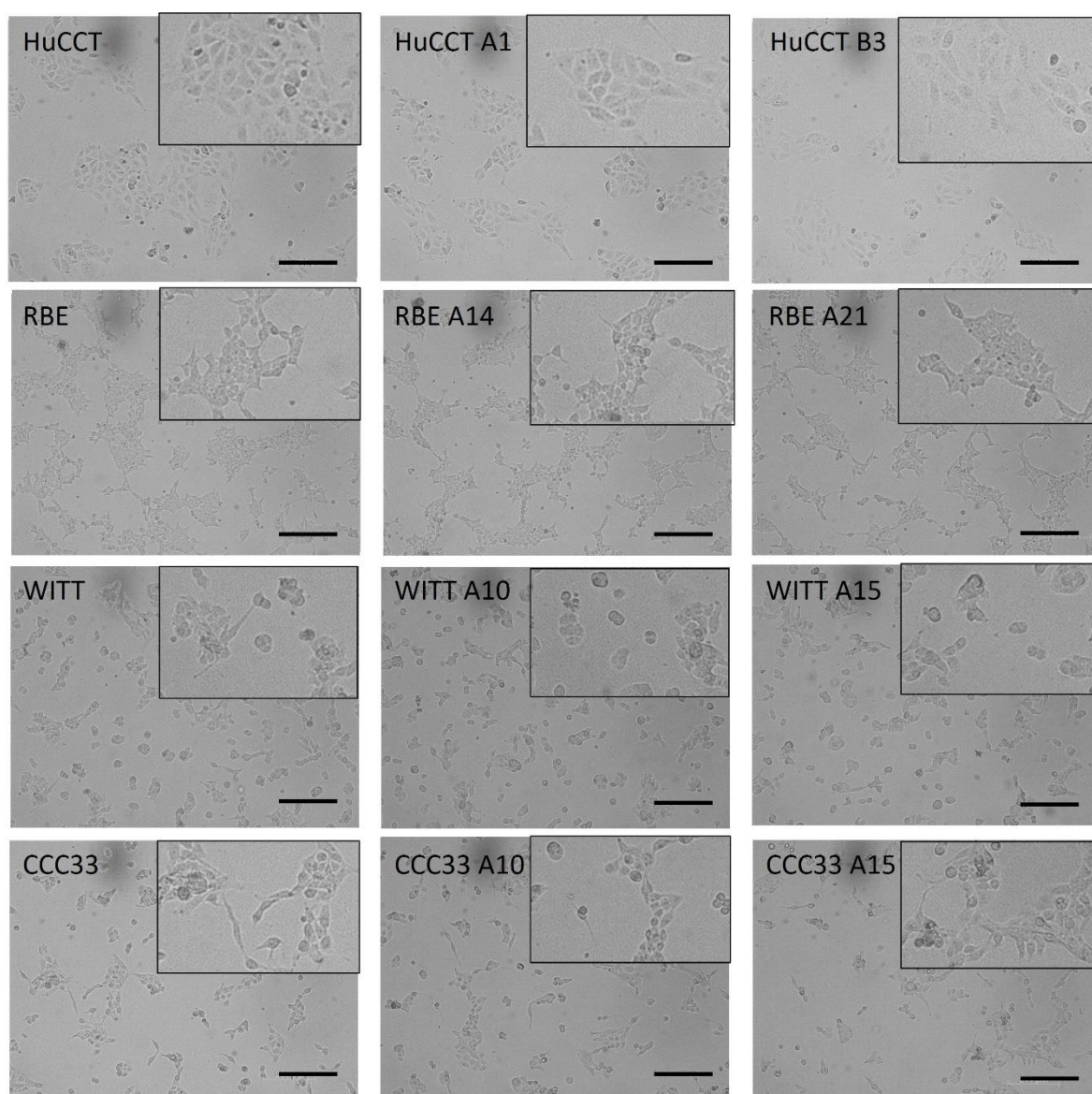


Figure 4.16: Morphology of *KRAS*-mutant and *KRAS*-wildtype iCCA cell lines and their respective *PARP-1* KO clones.

Bright-field images demonstrating morphology of *KRAS*-mutant (HuCCT, RBE) and *KRAS*-wildtype (WITT, CCC33) iCCA cell lines and their respective *PARP-1* KO clones (HuCCT A1, HuCCT B3, RBE A14, RBE A21, WITT A10, WITT A15, CCC33 A10, CCC33 A15). Scale bars indicating 200 μm . The small squared sections show 2x magnification.

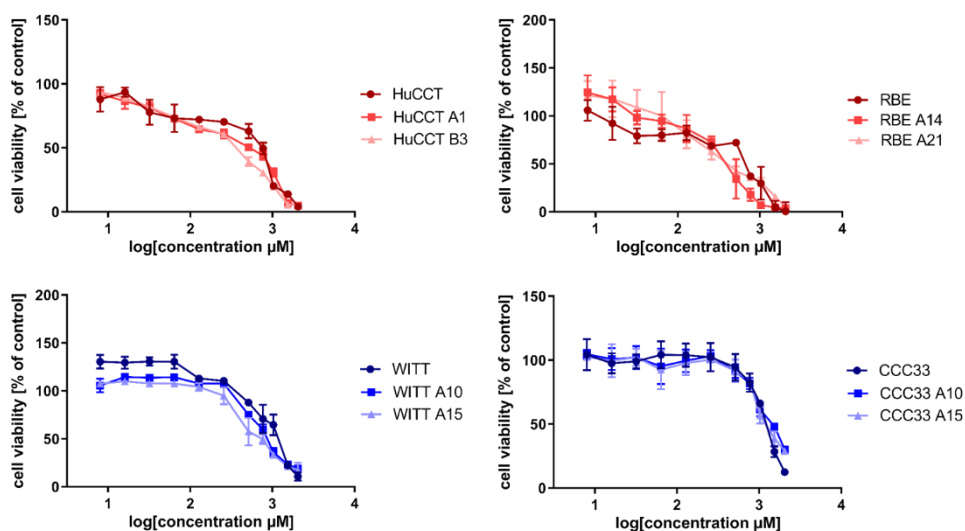
To confirm successful knockout, a 300 bp long fragment flanking the sgRNA target site in *PARP-1* exon 2 was subcloned into the expression vector pcDNA 3.1 hygro (+) and amplified in competent *E. coli* DH5 α . Isolated DNA of 5 colonies per *PARP-1* KO clone was analyzed by Sanger sequencing. Results validated successful *PARP-1* KO clones by demonstrating the exact deletions on both alleles of the selected clones (Table 4.3).

Table 4.3: Results of Sanger sequencing.

cell line	clone	sgRNA GCACCCCTGACGTTGAGGTGG	cell line	clone	sgRNA GCACCCCTGACGTTGAGGTGG
		ACTCCATCCGGCACCCCTGACGTTGAGGTGGATGGGTT			ACTCCATCCGGCACCCCTGACGTTGAGGTGGATGGGTT
HuCCT	A1	ACCCATCCACGCACCCCTA-GGTGCCGGATGGAGTGT ACCCATCCACGCACCCCTA-GGTGCCGGATGGAGTGT ACCCATCCACGCACCCCTCAGG-TGCCGGATGGAGTGT ACCCATCCACGCACCCCGCAGG--CCGGATGGAGTGT ACCCATCCACGCACCCCGCAGG--CCGGATGGAGTGT	WITT	A10	ACTCCGT-----TGAGGTGGATGGGTT ACTCCATCCGGCA-----TGAGGTGGATGGGTT ACTCCATCCGGCC--TGACGTTGAGGTGGATGGGTT ACTCCACACCCAT--TCAGCTGAGGTGGTCGGGTT ACTCCATCCGGCC--TGACGTTGAGGTGGATGGGTT
HuCCT	B3	ACCCATCC-----G-C-----T---GGATGGAGTGT ACCCATCC-----G-C-----T---GGATGGAGTGT ACCCATCCACGCACCCCTCAGG----- ACCCATCCACGCACCCCTCAGG----- ACCCATCC-----GCCGGATGGAGTGT	WITT	A15	ACTCCATCCGGCA-----GGCGTTATCCGGATGGGTT ACTCCATCCGGCA-----GACGTTGAGGTGGATGGGTT ACTCCATCCGGCA-----GACGTTGAGGTGGATGGGTT ACTCCATCCAGCA-----TGAGGGGGATGGGTT ACTCCATCCCA-----TGAGGTGGATGGGTT
RBE	A14	ACTCCATCCGGCAC--TGACGTTGAGGTGGATGGGTT ACTCCATCCGGCAC--TGACGTTGAGGTGGATGGGTT ACTCCATCCGGCAC--TGACGTTGAGGTGGATGGGTT ACTCCATCCGGCAC--TGACGTTGAGGTGGATGGGTT ACTCCATCCGGCAC--TGACGTTGAGGTGGATGGGTT	CCC33	A10	ACTCCATCCGGC--C-TGACGTTGAGGTGGATGGGTT ACTCCATCCGGC--C-TGACGTTGAGGTGGATGGGTT ACTCCATCCGGC--C-TGACGTTGAGGTGGATGGGTT ACTCCATCCGGCAC--TGACGTTGAGGTGGATGGGTT ACTCCATCCGGCAC--TGACGTTGAGGTGGATGGGTT
RBE	A21	ACTCCAT-----CCTGACGTTGAGGTGGATGGGTT ACTCCAT-----CCTGACGTTGAGGTGGATGGGTT ACTCCAT-----CCTGACGTTGAGGTGGATGGGTT ACTCCATC-----CCTGACGTTGAGGTGGATGGGTT ACTCCATC-----CCTGACGTTGAGGTGGATGGGTT	CCC33	A15	ACTCCATCCGGCAC--TGACGTTGAGGTGGATGGGTT ACTCCATCCGGCA-----ATGGGTT ACTCCATCCGGCA-----ATGGGTT ACTCCATCCGGCA-----ATGGGTT ACTCCATCCGGCA-----ATGGGTT

4.7.1 Functional analyses of CRISPR/Cas9-mediated *PARP-1* knockout in iCCA cell lines

To exclude that *PARP-2* compensates knockout of *PARP-1*, the selected *PARP-1* KO clones were treated with Olaparib. Cell viability (shown as % of control) after Olaparib treatment was slightly reduced in WITT, HuCCT, and RBE *PARP-1* KO clones in comparison to the control clones. However, IC₅₀ values of *PARP-1* KO clones showed no significant reduction in comparison to control cell lines, regardless of *KRAS* mutational status. In *KRAS*-wildtype cell line CCC33 IC₅₀ values of *PARP-1* KO clones were significantly increased (Figure 4.17).



	HuCCT	A1	B3	RBE	A14	A21	WITT	A10	A15	CCC33	A10	A15
IC ₅₀ [μM]	387.2 ± 205.5	312.0 ± 39.21	260.6 ± 8.76	464.5 ± 80.59	263.0 ± 181.3	394.2 ± 116.4	1080.0 ± 129.9	891.6 ± 67.46	735.1 ± 138.0	1175.0 ± 63.88	1410.0 ± 249.79	1295.0 ± 14.57
		p = 0.5673 (ns)	p = 0.3465 (ns)		p = 0.1534 (ns)	p = 0.4382 (ns)		p = 0.1691 (ns)	p = 0.0670 (ns)		p = 0.0024 (**)	p = 0.0284 (*)

Figure 4.17: Determination of IC₅₀ values of Olaparib treatment in *PARP-1* KO clones.

Shown are dose-response curves of *KRAS*-mutant (HuCCT, RBE; red) and *KRAS*-wildtype iCCA cell lines (WITT, CCC33; blue) and their respective *PARP-1* KO clones treated with increasing concentrations of Olaparib to determine IC₅₀ values and impact on proliferation. Mean ± SD, n=3, p < 0.05 (*), p < 0.01 (**).

Next, we aimed to investigate the impact of CRISPR/Cas9-mediated *PARP-1* KO on the proliferation and tumorigenicity by CFU and SFU assays. *PARP-1* KO led to a significant decrease in the number of CFU (shown as % of control) in all *PARP-1* KO clones, regardless of *KRAS* mutational status (CCC33 A10 $p = 0.0194$; CCC33 A15 $p = 0.0004$; WITT A10 $p = 0.0006$; WITT A15 $p = 0.0007$; HuCCT A1 $p = 0.0004$; HuCCT B3 $p < 0.0001$; RBE A14 $p < 0.0001$; RBE A21 $p < 0.0001$) (Figure 4.18 a). Similarly, all *PARP-1* KO clones showed a significant reduction in spheroid forming capacity compared to control clones (CCC33 A10 $p = 0.0035$; CCC33 A15 $p = 0.0168$; WITT A10 $p = 0.3439$; WITT A15 $p = 0.0251$; HuCCT A1 $p = 0.0244$; HuCCT B3 $p = 0.0215$; RBE A14 $p = 0.0063$; RBE A21 $p = 0.0007$) (Figure 4.18 b). Reduction of colony and spheroid formation capacity in *PARP-1* KO clones ranged between 33.4-48.5% of control. Notably, the reduction of CFU and SFU was slightly more pronounced in *KRAS*-mutant *PARP-1* KO clones, however, these differences were not significant. Overall, these results confirm the importance of functional *PARP-1* signaling for proliferation of iCCA cell lines irrespective of the *KRAS* mutation status.

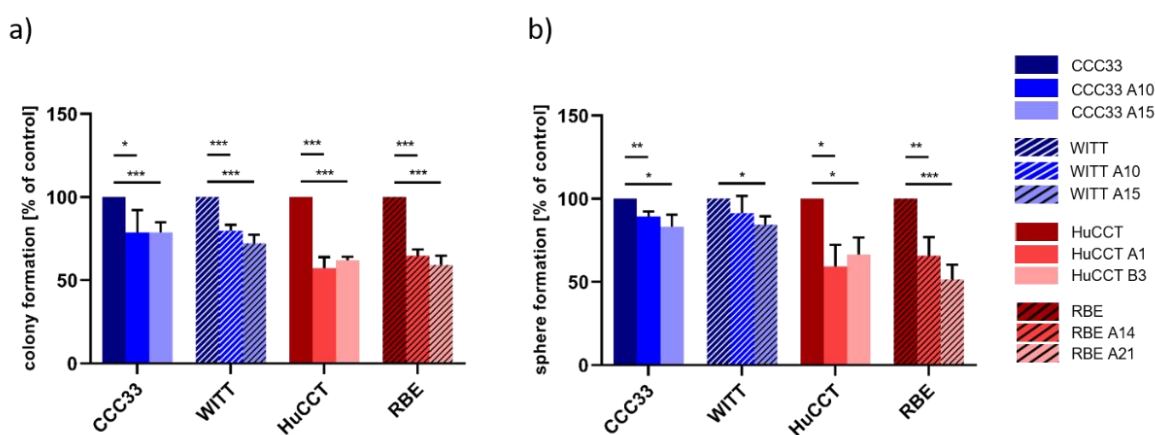


Figure 4.18: Effect of *PARP-1* KO on colony and sphere formation capacity.

a) Colony and b) sphere formation assay shown as % of control of *PARP-1* KO clones in *KRAS*-mutant (HuCCT, RBE; red) and *KRAS*-wildtype iCCA cell lines (CCC33, WITT; blue) and their respective knockout clones. Mean \pm SD, $n=3$, $p < 0.05$ (*), $p < 0.01$ (**), $p < 0.001$ (***).

To investigate the effect of *PARP-1* depletion in the presence of increased DNA damage, we determined cell viability after treatment with the DNA-damaging agent Doxorubicin. *KRAS*-wildtype and *KRAS*-mutant iCCA cell lines and their respective *PARP-1* KO clones were treated with Doxorubicin (60 nM) for 72 hours. The administration of Doxorubicin led to a reduction in cell viability in all iCCA cell lines. In *KRAS*-mutant iCCA cell line RBE both *PARP-1* KO clones and in *KRAS*-wildtype cell line CCC33 one *PARP-1* KO clone showed reduced cell viability in comparison to the control conditions (RBE A14 $p = 0.0138$; RBE A21 $p = 0.0065$; CCC33 A15 $p = 0.0376$). However, *KRAS*-mutant iCCA cell line HuCCT and *KRAS*-wildtype iCCA cell line WITT showed no differential response comparing *PARP-1* KO clones and control conditions upon Doxorubicin treatment (Figure 4.19).

Together these results indicate that *KRAS*-mutant iCCA cell lines seem to be more sensitive towards *PARP-1* depletion shown in decreased CFU and SFU forming capacity and decreased cell viability after Doxorubicin treatment. However, these effects were also visible in *KRAS*-wildtype iCCA cell lines. A permanent *PARP-1* depletion seems to be harmful to all iCCA cell lines.

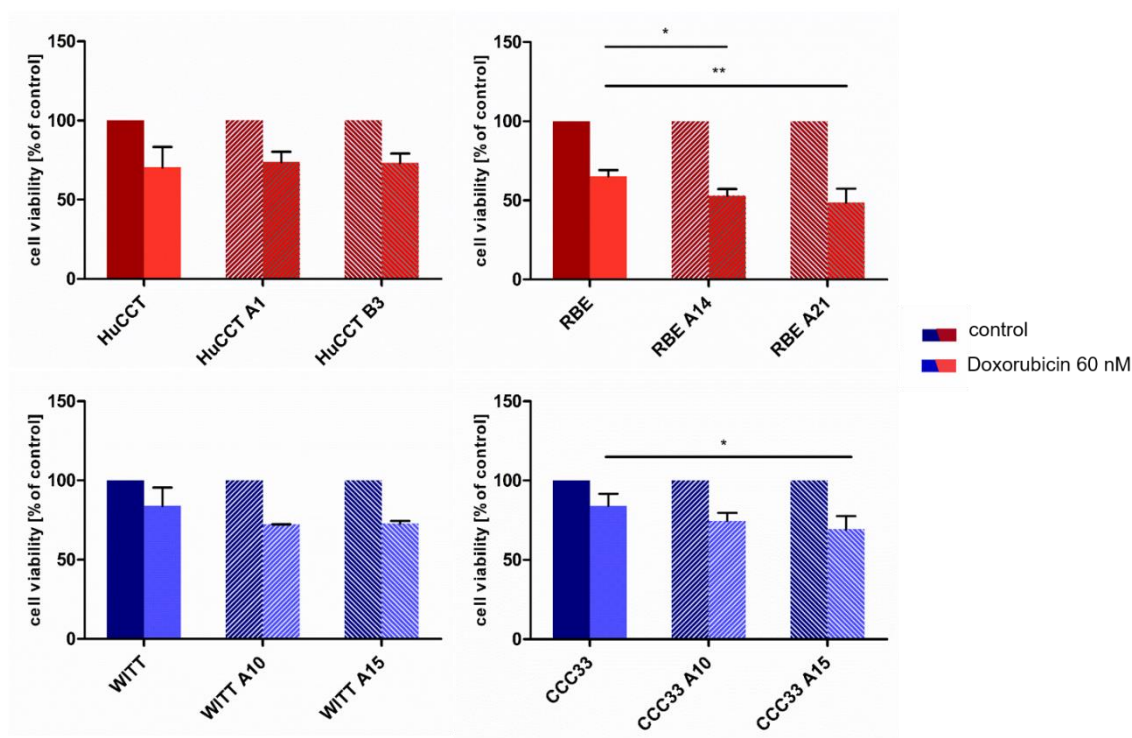


Figure 4.19: Cell viability of *PARP-1* KO clones after treatment with DNA-damaging agent Doxorubicin.

Shown is cell viability as % of control in *PARP-1* KO clones of in *KRAS*-mutant (HuCCT, RBE; red) or *KRAS*-wildtype iCCA cell lines (WITT, CCC33; blue) or and respective knockout clones after treatment Doxorubicin 60 nM. Mean \pm SD, $n=3$, $p < 0.05$ (*), $p < 0.01$ (**).

Impact of irradiation in *KRAS*-mutant and *KRAS*-wildtype iCCA cell lines upon *PARP-1* KO

Irradiation is a widely used method to induce DNA double-strand breaks besides treatment with DNA-damaging agents. Here, we investigated the impact of irradiation-induced DNA damage in *PARP-1* KO clones and measured phospho- γ H2AX foci as a marker for DNA double-strand breaks. The number of cells with more than 5 foci normalized by total cell count was determined and shown as fold change of control conditions. Irradiation led to a significantly increased number of DNA double-strand breaks in *KRAS*-mutant iCCA cell lines HuCCT and RBE only in the *PARP-1* KO clones compared to control conditions (HuCCT A1 $p = 0.0282$; HuCCT B3 $p = 0.0172$; RBE A14 $p < 0.0001$; RBE A21 $p = 0.0030$). In contrast, *KRAS*-wildtype iCCA cell lines CCC33 and WITT showed significantly increased number of DNA double-strand breaks independent of *PARP-1* KO status (WITT $p = 0.0130$; WITT A10 $p = 0.0024$; WITT A15 $p = 0.0221$; CCC33 $p = 0.0025$; CCC33 A10 $p = 0.0084$; CCC33 A15 $p = 0.0221$) (Figure 4.20). These findings indicate that *KRAS*-mutant iCCA cell lines with *PARP-1* KO show a preferential sensitivity towards irradiation, whereas *KRAS*-wildtype iCCA cell lines are affected by irradiation independently of their *PARP-1* activity.

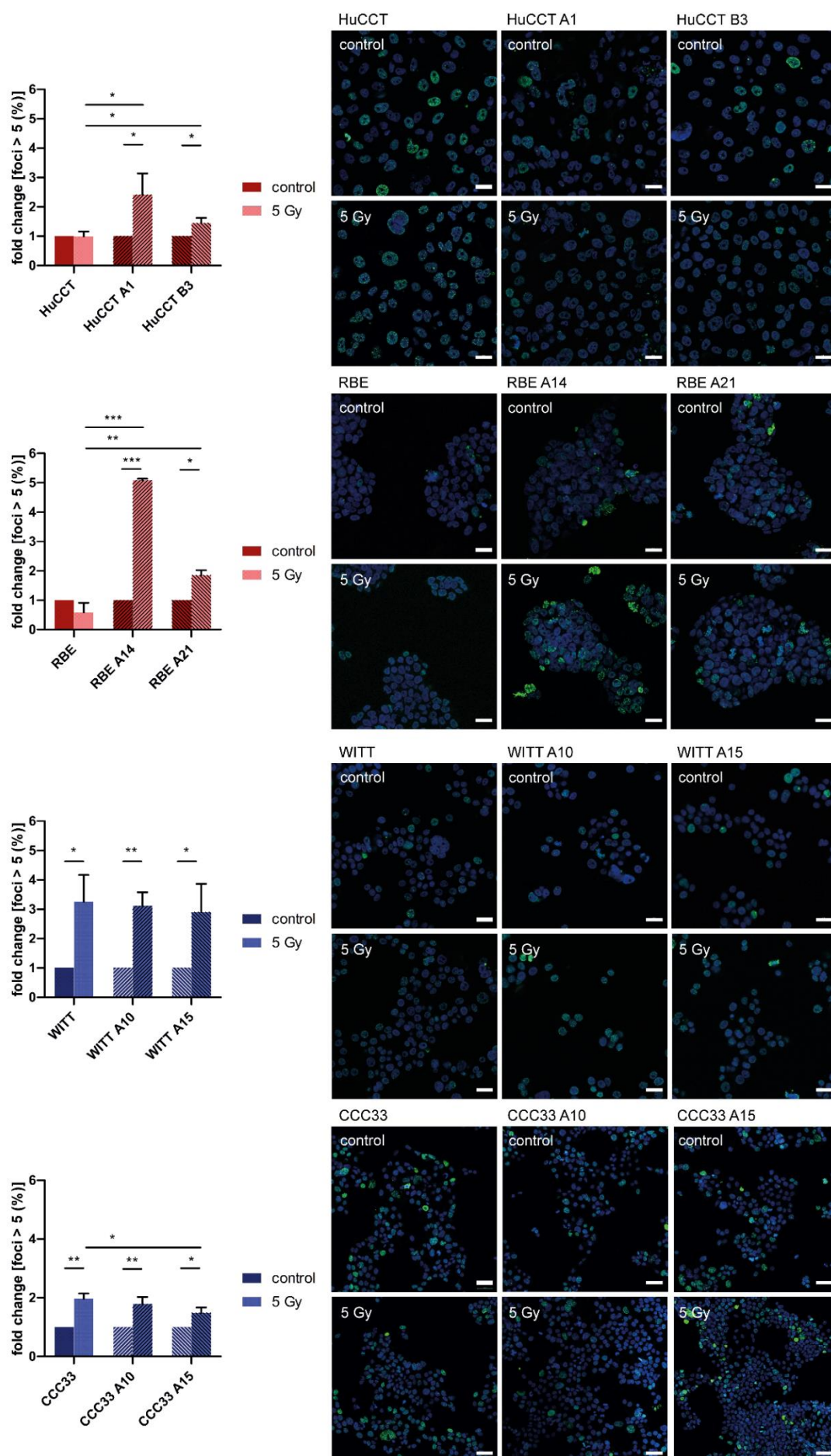


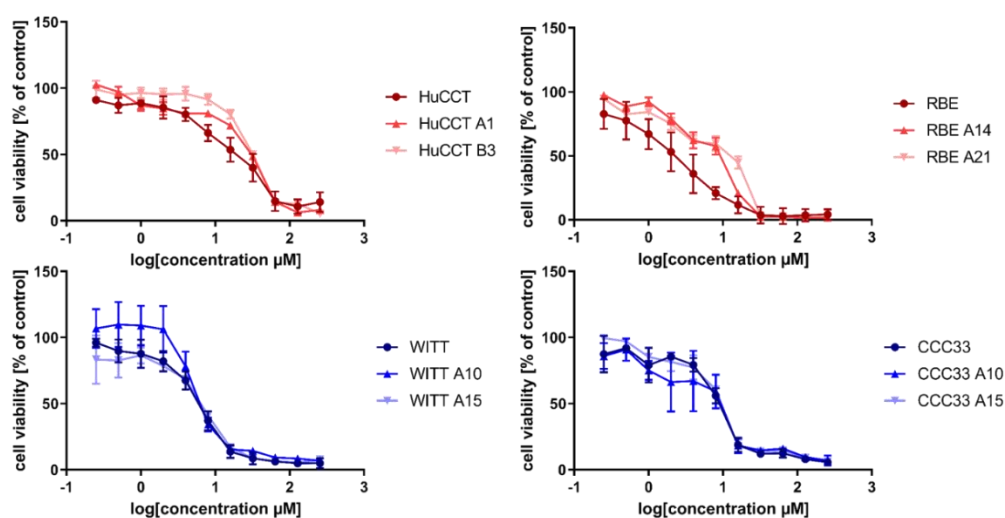
Figure 4.20: Determination of induction of DNA damage response via irradiation.

Immunofluorescence staining of p-γH2AX foci by confocal microscopy. Shown are representative images of *KRAS*-mutant (HuCCT, RBE; red) and *KRAS*-wildtype iCCA cell lines (CCC33, WITT; blue) and their respective *PARP-1* KO clones under control conditions and after irradiation with 5 Gy. Scale bars indicating 20 μm. Quantification indicating fold change of the number of cells with foci > 5 as % of total cell number. Mean ± SD, n=3, p < 0.05 (*), p < 0.01 (**).

Impact of cisplatin treatment in *KRAS*-mutant and *KRAS*-wildtype iCCA cell lines upon *PARP-1* KO

The standard of first-line chemotherapy in iCCA patients is a platinum-based therapy. Alone or in combination with gemcitabine and fluoropyrimidines, this chemotherapeutic is used for unresectable, metastasis, or recurrent cholangiocarcinoma [69]. Therefore, we aimed to determine the impact of classic chemotherapy in our CRISPR/Cas9-mediated *PARP-1* KO clones. We performed dose-response analyses of cisplatin in all iCCA cell lines and their respective *PARP-1* KO clones to determine individual IC₅₀ values and their impact on cell viability. We exposed iCCA cell lines with increasing concentrations of cisplatin, incubated for 72 hours, and measured cell viability (shown as % of control).

IC₅₀ values of *PARP-1* KO clones of *KRAS*-mutant iCCA cell lines were significantly increased indicating a higher resistance towards cisplatin treatment. Cell viability and IC₅₀ values were slightly reduced after cisplatin treatment in *PARP-1* KO clones of *KRAS*-wildtype iCCA cell lines in comparison to the scrambled control clones (Figure 4.21).



	HuCCT	A1	B3	RBE	A14	A21	WITT	A10	A15	CCC33	A10	A15
IC ₅₀ [μM]	18.96 ± 0.7805	30.11 ± 2.294	26.22 ± 0.3350	2.978 ± 1.919	8.165 ± 1.406	12.26 ± 2.597	6.436 ± 0.8431	5.726 ± 0.5141	7.231 ± 1.242	9.464 ± 0.6091	7.210 ± 1.585	5.390 ± 0.3479
		p = 0.0013 (**)	p = 0.0001 (***)		p = 0.0195 (*)	p = 0.0076 (**)		p = 0.3837 (ns)	p = 0.4504 (ns)		p = 0.0983 (ns)	p = 0.0036 (**)

Figure 4.21: Determination of IC₅₀ value of cisplatin treatment in *PARP-1* KO clones.

Shown are dose-response curves of *KRAS*-mutant (HuCCT, RBE; red) and *KRAS*-wildtype iCCA cell lines (WITT, CCC33; blue) and their respective *PARP-1* KO clones treated with increasing concentrations of cisplatin to determine IC₅₀ values and impact on proliferation. Mean ± SD, n=3, p < 0.05 (*), p < 0.01 (**), p < 0.001 (***)

Next, we investigated the impact of cisplatin-induced DNA damage in *PARP-1* KO clones and measured phospho- γ H2AX foci as a marker for DNA double-strand breaks. The number of cells with more than 5 foci normalized by total cell count was determined and shown as fold change of control conditions.

Upon cisplatin treatment, *KRAS*-mutant iCCA cell lines HuCCT and RBE showed a mild increase in DNA double-strand breaks more pronounced in *PARP-1* KO clones than under control conditions. However, this observation was not statistically significant. In contrast, cisplatin treatment led to an increase of DNA double-strand breaks in *KRAS*-wildtype iCCA cell lines CCC33 and WITT, independent of *PARP-1* knockout status. However, these findings were not uniform amongst the *PARP-1* KO clones (WITT A10 $p = 0.0459$; WITT A15 $p = 0.0008$; CCC33 A15 $p = 0.0059$) (Figure 4.22). These results indicate that *KRAS*-wildtype iCCA cell lines are affected by irradiation independently of their *PARP-1* activity.

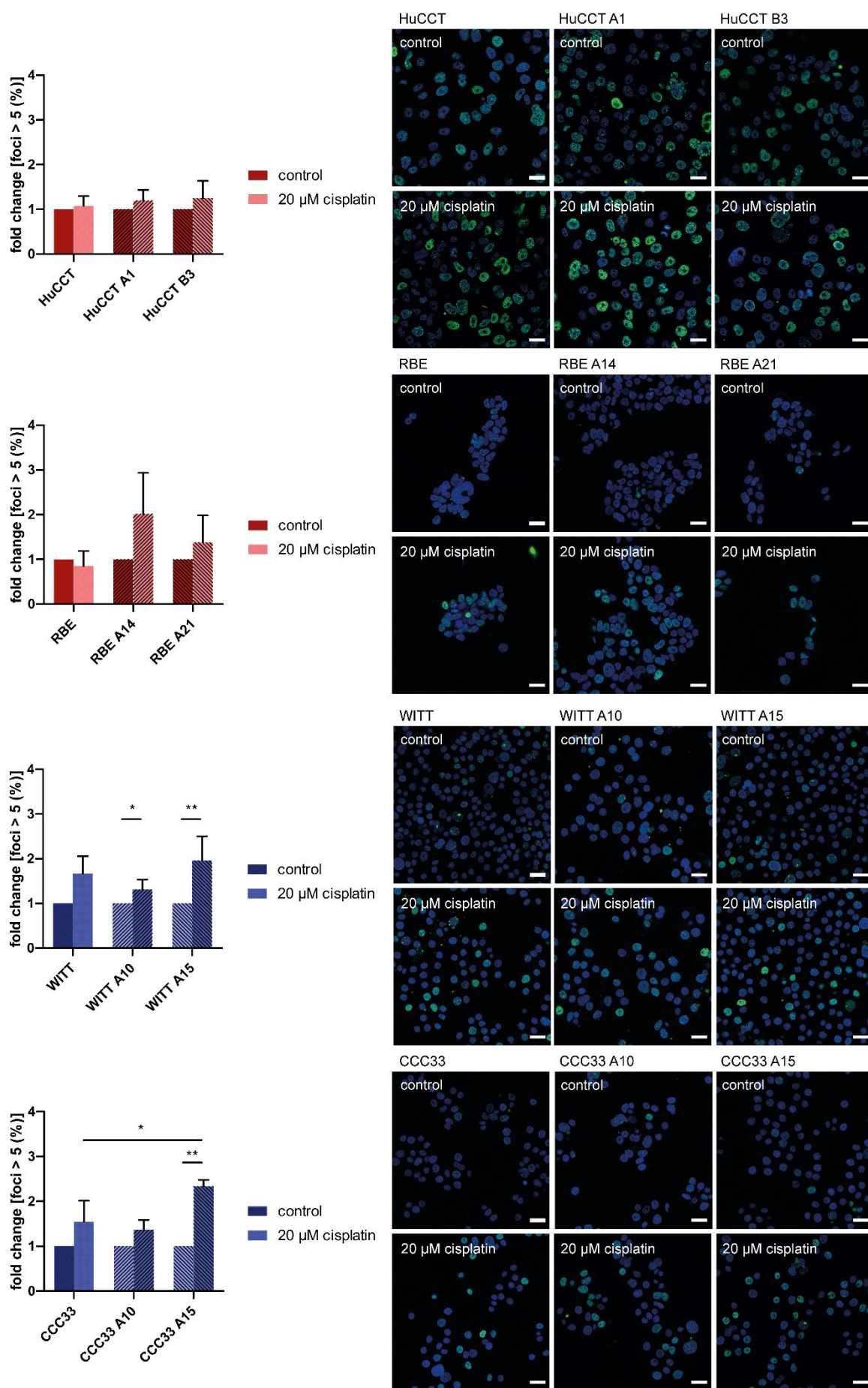


Figure 4.22: Determination of induction of DNA damage response after cisplatin treatment.

Immunofluorescence staining of p-γH2AX foci by confocal microscopy. Shown are representative images of *KRAS*-mutant (HuCCT, RBE; red) and *KRAS*-wildtype iCCA cell lines (CCC33, WITT; blue) and their respective *PARP-1* KO clones under control conditions and after cisplatin treatment (20 μM). Scale bars indicating 20 μm. Quantification indicating fold change of the number of cells with foci > 5 as % of total cell number. Mean ± SD, n=3, p < 0.05 (*), p < 0.01 (**), p < 0.001 (***)

Oxidative stress response in *KRAS*-mutant and *KRAS*-wildtype iCCA cell lines upon *PARP-1* KO

Oxidative stress is a promotor of oncogenic processes and is known to be influenced by *PARP-1* activity [149] Therefore, we investigated the level of oxidative stress in our CRISPR/Cas9-mediated *PARP-1* KO clones. The oxidative stress response was determined using an indicator for cellular reactive oxygen species (ROS) with and without induction of oxidative stress via H₂O₂ treatment. The mean fluorescence intensity of CM-H₂DCFDA was measured by spectrofluorometry. In *KRAS*-mutant iCCA cell lines HuCCT and RBE the basal ROS levels were significantly higher in the *PARP-1* KO clones when compared to their respective scrambled control clones (HuCCT A1 p = 0.0471; HuCCT B3 p = 0.0074; RBE A14 p < 0.0001; RBE A21 p = 0.0002) (Figure 4.23 a). In contrast, the basal status of ROS did not differ in *PARP-1* KO clones of *KRAS*-wildtype iCCA cell lines CCC33 and WITT (Figure 4.23 b). After treatment with H₂O₂, we observed a significant increase in DCF fluorescence intensity in *KRAS*-mutant iCCA cell lines indicating changes in redox status in *PARP-1* KO clones, when compared to their respective scrambled control clones (HuCCT A1 p = 0.0210; HuCCT B3 p = 0.0006; RBE A14 p = 0.0009; RBE A21 p = 0.0013). Further, a decrease in mean fluorescence intensity of DCF in *KRAS*-wildtype iCCA cell line WITT after H₂O₂ treatment was shown, when comparing *PARP-1* KO clones to their respective scrambled control clones (WITT A10 p = 0.0444; WITT A15 p = 0.0142). In CCC33, we could not determine changes in redox status (Figure 4.23 a/b).

In general, these findings indicate that *PARP-1* KO affects oxidative stress levels predominantly in *KRAS*-mutant iCCA cell lines under basal conditions as well as upon H₂O₂ treatment. *KRAS*-wildtype cell lines show unchanged or decreased levels of oxidative stress when comparing *PARP-1* KO clones to their scrambled controls.

Taken together the functional analyses of CRISPR/Cas9-mediated *PARP-1* KO clones showed ambiguous results, indicating that *KRAS*-mutant iCCA cell lines upon *PARP-1* KO seem to be more sensitive when challenged by increased DNA damage levels or increased oxidative stress by DNA damaging agents (Doxorubicin, cisplatin), irradiation or H₂O₂ treatment. However, permanent *PARP-1* depletion seems to be harmful also to *KRAS*-wildtype iCCA cell lines, hence the results were not as clear as upon transient siRNA-mediated *PARP-1* knockdown or PARPi. To gain more in-depth mechanistic insights, we investigated transcriptomic profiles of *PARP-1* KO clones.

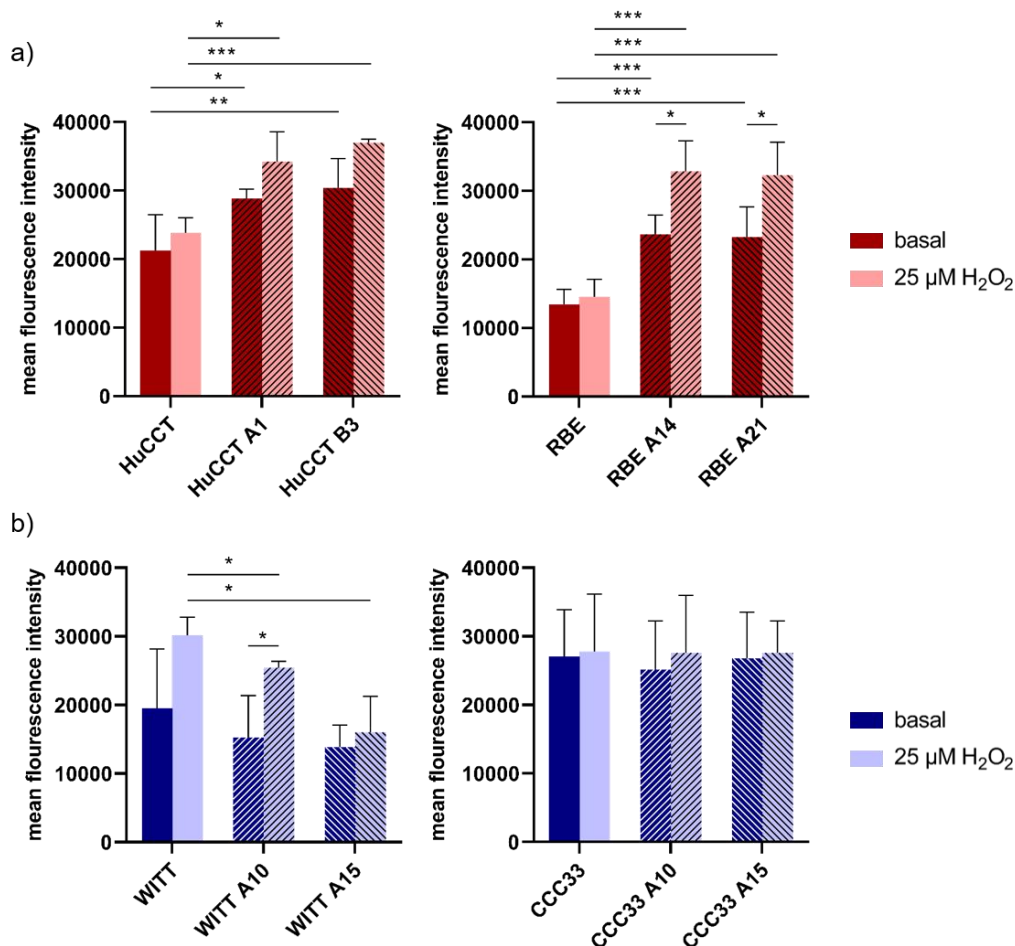


Figure 4.23: Determination of oxidative stress of *PARP-1* KO clones.

Shown are basal and H_2O_2 -induced (25 μM H_2O_2) changes in redox status using ROS-indicator CM-H₂DCF-DA in a) *KRAS*-mutant (HuCCT, RBE; red) and b) *KRAS*-wildtype iCCA cell lines (WITT, CCC33; blue) and their respective *PARP-1* KO clones. Shown is the mean fluorescence intensity. Mean \pm SD, n=3, $p < 0.05$ (*), $p < 0.01$ (**), $p < 0.001$ (***).

4.7.2 Transcriptomic profiling of CRISPR/Cas9-mediated *PARP-1* knockout

We observed functional changes between the *KRAS*-mutant and *KRAS*-wildtype iCCA cell lines upon *PARP-1*-based interventions. To further investigate molecular alterations influenced by *PARP-1* depletion, we performed RNA sequencing on *PARP-1* KO and respective control clones.

Impact of *PARP-1* KO in *KRAS*-mutant iCCA cell lines compared to scrambled control

First, we analyzed transcriptomic profiles in *KRAS*-mutant iCCA cell lines upon *PARP-1* KO compared to their scrambled control clones. By performing Wald test of log-transformed data of *PARP-1* KO in *KRAS*-mutant iCCA cell lines, we identified a total of 1171 (660 down, 511 up) differentially expressed genes ($p < 0.05$). Unsupervised hierarchical cluster analyses of the differentially expressed genes demonstrated that *PARP-1* KO clones of both *KRAS*-mutant iCCA cell lines formed a dense subcluster that separated the *PARP-1* KO clones from their respective scrambled control clones, indicating a specific gene signature upon *PARP-1* KO. Notably, the cluster of *PARP-1* KO clones shows differentially expressed genes, visible in the differential pattern on the heatmap, suggesting heterogeneity within the

group of *KRAS*-mutant iCCA cell lines. These findings were confirmed by the corresponding PCA plot (Figure 4.24).

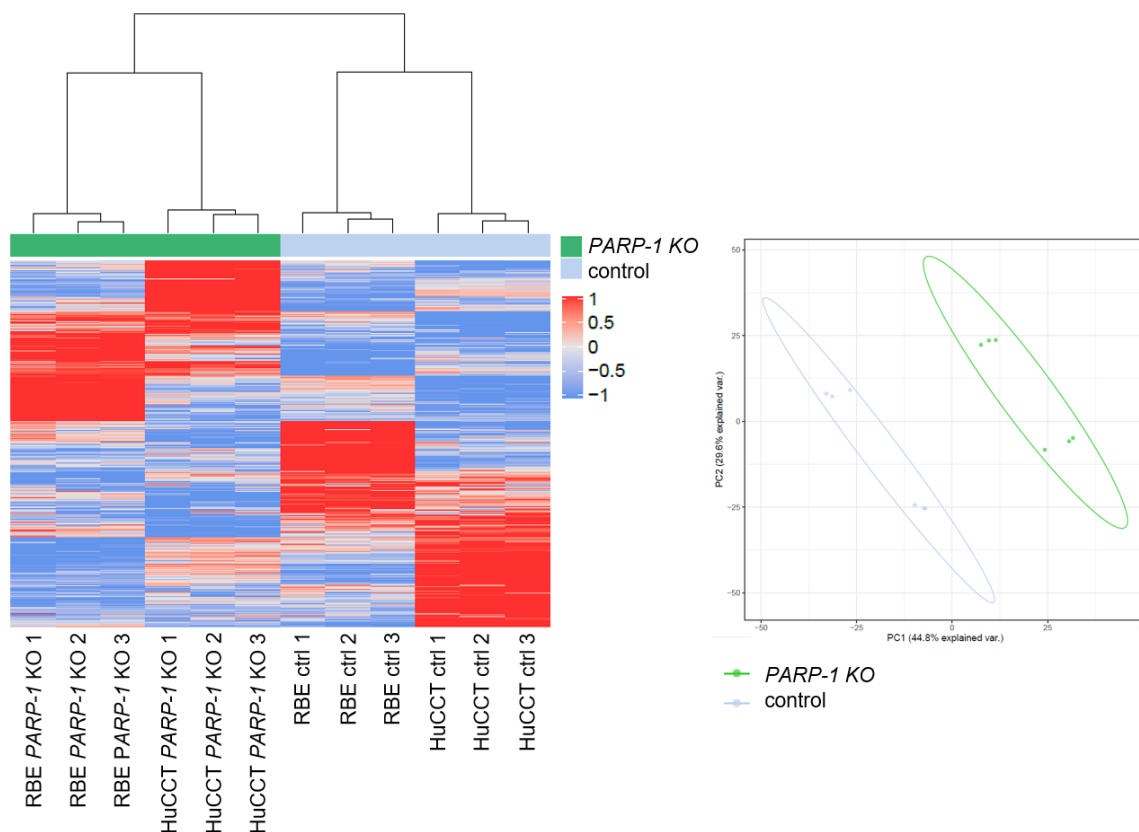


Figure 4.24: Differential gene expression in *KRAS*-mutant iCCA cell lines upon *PARP-1* KO versus control clones.

Unsupervised cluster and PCA of significant genes ($p < 0.05$) of *KRAS*-mutant iCCA cell lines (HuCCT, RBE) upon *PARP-1* KO vs. control.

Comparative pathways analyses of RNA sequencing data were performed using IPA. Here, we aimed to investigate the impact of *PARP-1* KO on cellular pathways in the *KRAS*-mutant iCCA cell lines. Hence, we uploaded datasets of significantly expressed genes in *KRAS*-mutant iCCA cell lines upon *PARP-1* KO versus control. Expression analysis was performed with a cut-off p -value < 0.05 , resulting in a total number of 1171 genes of which 511 were up- and 660 were downregulated. All pathways were selected based on significant regulation and $-\log(p\text{-value}) > 1.3$. IPA canonical pathways analysis determines the most significantly affected pathways and calculates directionality (z-score) displayed in color on pathways and networks (positive z-score = red/activated, negative z-score = blue/inhibited). Canonical pathways related to cell cycle control, like G1/S checkpoint regulation and G2/M DNA damage checkpoint regulation were found regulated with a negative z-score, indicating a dysregulation of cell cycle processes upon *PARP-1* KO (Figure 4.25 a). Further, DNA repair pathway BER and regulation of BRCA1 were affected. Oxidative stress pathways (NRF-2 mediated oxidative stress response, HIF1 α signaling) showed opposing z-scores, as well as apoptosis-related pathways (Death receptor signaling, Apoptosis signaling, Necroptosis signaling, and Myc-mediated apoptosis). These findings suggest a dysregulation of oxidative and apoptotic signaling in response to *PARP-1* KO under *KRAS*

mutation. Further, the differential regulation of several oncogenic pathways could be revealed. In *KRAS*-mutant iCCA cell lines with *PARP-1* KO a predicted inhibition of ERK/MAPK, p53, HIF1 α , and NF- κ B signaling was shown. Overall, IPA analyses confirmed that *PARP-1* KO affects cell cycle, oxidative and apoptotic signaling in *KRAS*-mutant iCCA cell lines significantly.

IPA toxicity analyses predict the association of transcriptomic data to clinical outcomes. Our analyses confirmed the regulation of oxidative stress and apoptotic features. Furthermore, signaling pathways associated with liver pathophysiology have been detected. Besides increased steatosis, and liver damage also sets of molecules known to be involved in hepatic fibrosis and cholestasis were enriched. Tumorigenesis related feature of liver proliferation was confirmed (Figure 4.25 b). Taken together these data confirm, that *PARP-1* KO enhances hepatotoxic processes in *KRAS*-mutant iCCA cell lines, which are known to promote hepatobiliary carcinogenesis.

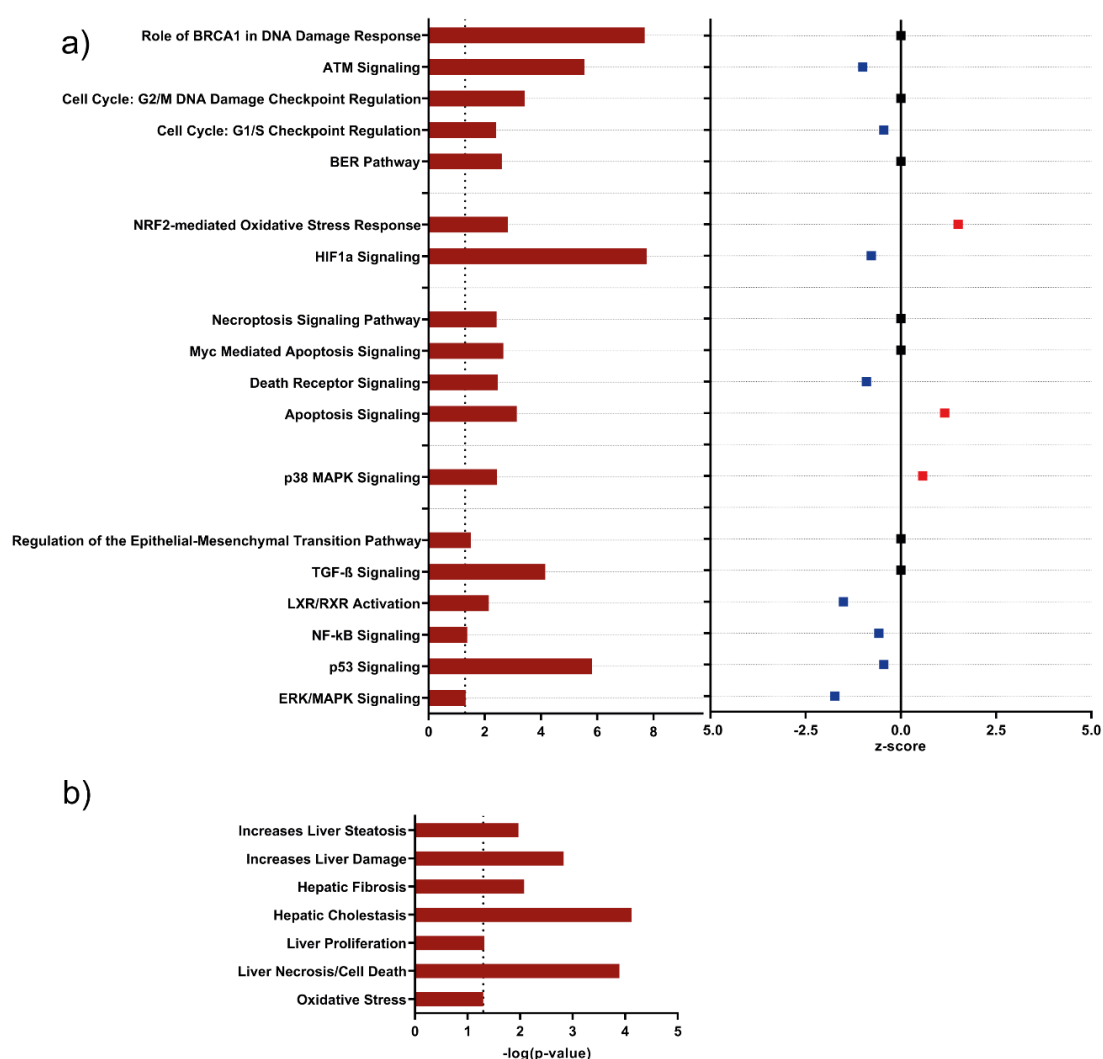
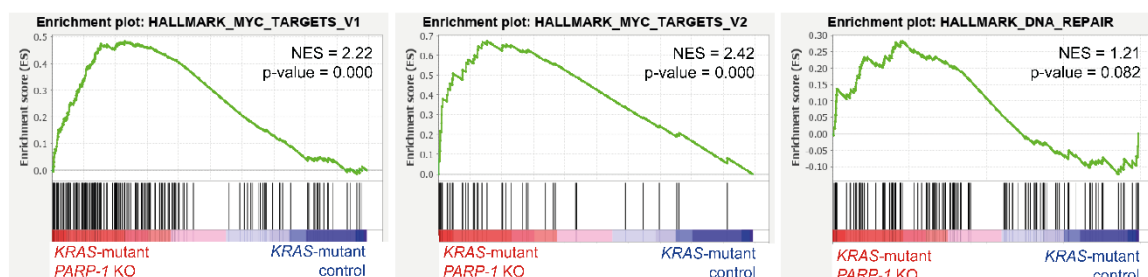


Figure 4.25: Canonical pathways and toxicity analyses of *KRAS*-mutant iCCA cell lines upon *PARP-1* KO versus control clones.

a) Canonical pathways significantly regulated in *KRAS*-mutant iCCA cell lines upon *PARP-1* KO vs. control identified by IPA. The dashed line indicates the significance threshold of $-\log(\text{p-value} > 1.3)$. Shown are z-scores of respective canonical pathways (positive z-score = red/activated, negative z-score = blue/inhibited). b) Clinical pathology endpoints and networks significantly regulated in *KRAS*-mutant iCCA cell lines upon *PARP-1* KO vs. control identified by IPA Toxicity analyses. The dashed line indicates the significance threshold of $-\log(\text{p-value} > 1.3)$.

Gene set enrichment analysis further complements the before shown IPA results (Figure 4.26). We uploaded raw count files of *KRAS*-mutant iCCA cell lines upon *PARP-1* knockout versus control clones. Only gene sets with nominal p-value < 0.05 and FDR < 0.25 were selected. Upon *PARP-1* KO *KRAS*-mutant iCCA cell lines showed enrichment in gene sets associated with myc signaling and DNA repair. In *KRAS*-mutant iCCA control clones a CCA class2 cluster, associated with poor survival was enriched. GSEA analyses confirmed enrichment in DNA repair mechanisms, such as the G2/M DNA damage checkpoint and BER. Further, apoptosis and TGF β signaling were significantly enriched. Taken together, these results indicate a dysregulation of DNA damage response mechanisms and oxidative stress response in *KRAS*-mutant iCCA cell lines upon *PARP-1* KO. In contrast, DNA damage response and apoptosis were enriched under *PARP-1* proficient conditions.

a) Gene sets enriched in *KRAS*-mutant *PARP-1* KO



b) Gene sets enriched in *KRAS*-mutant control

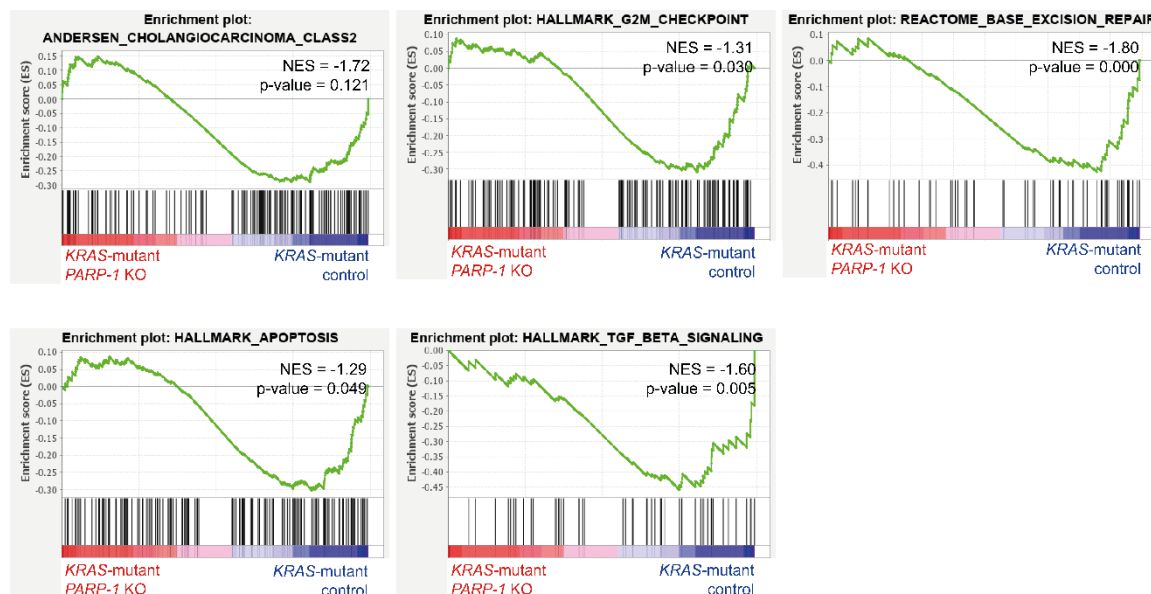


Figure 4.26: Enriched gene sets in *KRAS*-mutant iCCA cell lines upon *PARP-1* KO versus control clones.

Gene set enrichment analysis (GSEA) in *KRAS*-mutant iCCA cell lines upon a) *PARP-1* KO versus b) control clones. The selection of gene sets was based on statistical significance calculated by nominal p-value < 0.05 and FDR < 0.25. NES indicates the degree of overexpression for each group at the peak of the entire gene set.

Impact of *PARP-1* KO in *KRAS*-mutant compared to *KRAS*-wildtype iCCA cell lines

To evaluate dependency on the *KRAS* mutation status for the differences of *PARP-1* knockout, we compared *PARP-1* knockout in *KRAS*-mutant versus *KRAS*-wildtype iCCA cell lines. Comparative pathways analyses of RNA sequencing data were performed using IPA. We uploaded datasets of significantly expressed genes in *KRAS*-mutant iCCA cell lines upon *PARP-1* knockout versus *PARP-1* knockout in *KRAS*-wildtype iCCA cell lines. Expression analysis was performed with a cut-off p-value < 0.01, resulting in a total number of 5955 genes of which 3294 were up- and 2661 were downregulated. All pathways were selected by significant regulation $-\log(\text{p-value}) > 1.3$. Canonical pathways related to cell cycle control, like G1/S checkpoint regulation and G2/M DNA damage checkpoint regulation, and ATM signaling were found regulated. Further, DNA repair pathways NER and BER were regulated, while showing activation of NER and inhibition of BER. These results suggest that *PARP-1* KO in *KRAS*-mutant iCCA cell lines leads to dysregulation of cell cycle control and DNA damage response in comparison to *KRAS*-wildtype iCCA cell lines. Interestingly, DNA double-strand break repair pathways were not detected. Oxidative stress pathways (NRF-2 mediated oxidative stress response, HIF1 α signaling) showed negative z-score, as well as apoptosis-related pathways (Death receptor signaling, Apoptosis signaling, Necroptosis signaling, and Myc-mediated apoptosis), indicating that *PARP-1* KO in *KRAS*-mutant iCCA cell lines impacts oxidative and apoptotic processes. Further, the regulation of several oncogenic pathways could be revealed. In *KRAS*-mutant iCCA cell lines activation of LXR/RXR, Pi3K/AKT, HIPPO, TGF β , and NF- κ B signaling was shown upon *PARP-1* KO. Whereas inhibition of pathways of oncogenic pathways like p53, ERK/MAPK, PTEN, AMPK, and p38 signaling was revealed. Oxidative phosphorylation and immune response showed a negative z-score as well (Figure 4.27 a). IPA toxicity analyses confirmed the regulation of oxidative stress and cell death signaling. Furthermore, signaling pathways associated with liver pathophysiology have been detected. Besides increased hepatitis, steatosis, and liver damage also sets of molecules known to be involved in hepatic fibrosis and cholestasis were enriched (Figure 4.27 b).

Overall IPA analyses confirmed that pathway activation and regulation in *KRAS*-mutant iCCA cell lines upon *PARP-1* KO differed significantly from *KRAS*-wildtype iCCA cell lines. *PARP-1* KO seems to downregulate DNA damage response, besides reducing oxidative and apoptotic signaling in *KRAS*-mutant iCCA cell lines.

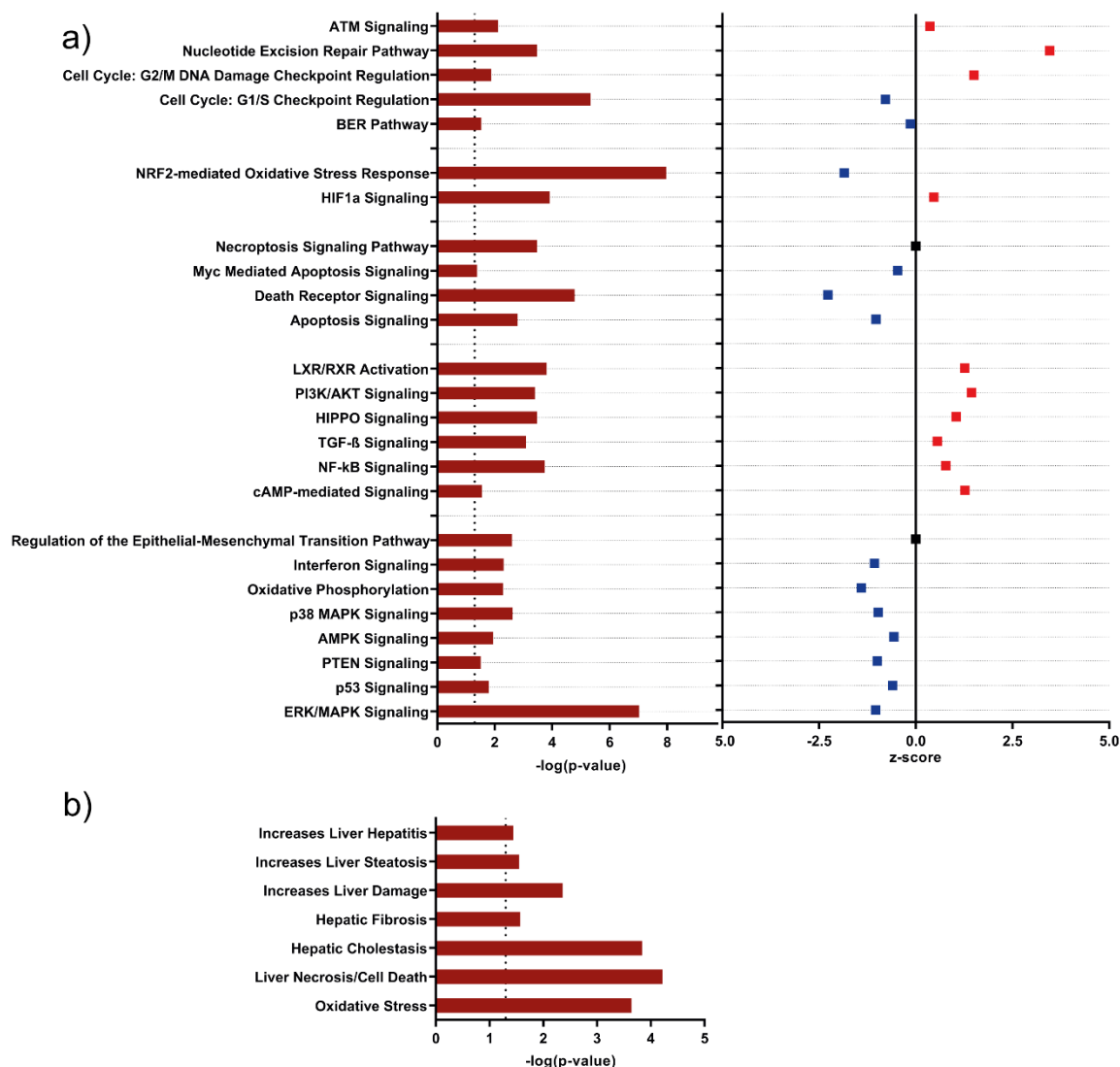


Figure 4.27: Canonical pathways and toxicity analyses of *KRAS*-mutant versus *KRAS*-wildtype iCCA cell lines upon *PARP-1* KO.

a) Canonical pathways significantly regulated in *KRAS*-mutant versus *KRAS*-wildtype iCCA cell lines upon *PARP-1* KO by IPA. The dashed line indicates the significance threshold of $-\log(p\text{-value}) > 1.3$. Shown are z-scores of respective canonical pathways (positive z-score = red/activated, negative z-score = blue/inhibited). b) Clinical pathology endpoints and networks significantly regulated in *KRAS*-mutant versus *KRAS*-wildtype iCCA cell lines upon *PARP-1* KO. The dashed line indicates the significance threshold of $-\log(p\text{-value}) > 1.3$.

Gene set enrichment analysis further confirmed and complemented the IPA results (Figure 4.28). We uploaded raw count files of *KRAS*-mutant versus *KRAS*-wildtype iCCA cell lines upon *PARP-1* knockout. Only gene sets with nominal p-value < 0.05 and FDR < 0.25 were selected. Upon *PARP-1* KO *KRAS*-mutant iCCA cell lines showed enrichment in gene sets associated with CK19 positive cholangiocarcinoma, myc signaling, and DNA single-strand break repair (NER). In *KRAS*-wildtype iCCA with *PARP-1* KO a CCA class2 cluster, associated with poor survival was enriched. Further, GSEA confirmed enrichment in DNA repair mechanisms, such as G2/M checkpoint, BER, and DNA double-strand break repair. Taken together, these results indicate that *PARP-1* KO impacts DNA damage response mechanisms more pronounced in *KRAS*-mutant iCCA cell lines in comparison to *KRAS*-wildtype iCCA cell lines.

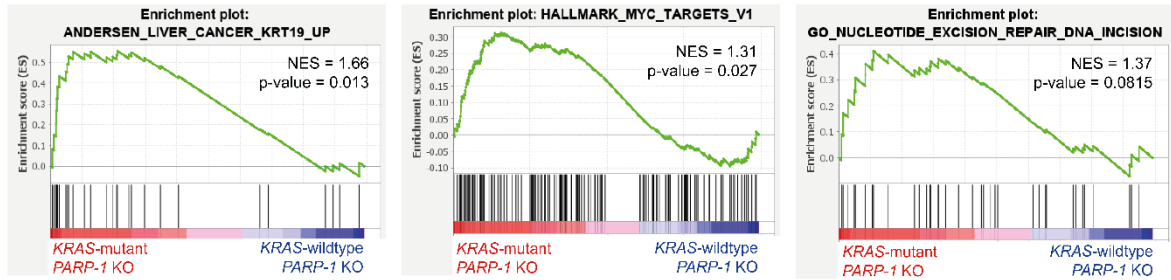
a) Gene sets enriched in *KRAS*-mutant *PARP-1* KOb) Gene sets enriched in *KRAS*-wildtype *PARP-1* KO

Figure 4.28: Enriched gene sets in *KRAS*-mutant versus *KRAS*-wildtype iCCA cell lines upon *PARP-1* KO.

Gene set enrichment analysis (GSEA) of a) *KRAS*-mutant versus b) *KRAS*-wildtype iCCA cell lines upon *PARP-1* KO. The selection of gene sets was based on statistical significance calculated by nominal p-value < 0.05 and FDR < 0.25. NES indicates the degree of overexpression for each group at the peak of the entire gene set.

IPA and GSEA analyses showed differential activation of DNA damage response pathways upon *PARP-1* KO in *KRAS*-mutant iCCA cell lines. To further dissect the activity of these DNA damage response pathways, we displayed the expression of 82 DNA damage response genes. When comparing *KRAS*-mutant iCCA *PARP-1* KO with their respective control clones only *PARP-1* expression was differentially downregulated (Figure 4.29 a). When analyzing *KRAS*-wildtype iCCA cell lines upon *PARP-1* KO upregulation of genes associated with c-NHEJ (*RAD50*, *NHEJ1*, *POLB*) and downregulation of *PARP-1* expression were found (Figure 4.29 b). When comparing the expression of *KRAS*-mutant iCCA cell lines with *KRAS*-wildtype cell lines upon *PARP-1* KO downregulation of genes associated with HR (*RAD21*, *BRCA2*, *SMC1B*) and alt-NHEJ (*NBN*, *LIG1*, *PARP-1*) was observed. Genes associated with c-NHEJ showed positive expression (*XRCC5*, *NHEJ1*) (Figure 4.29 c). These findings suggest that upon *PARP-1* KO DNA double-strand break repair mechanisms (HR and alt-NHEJ) in *KRAS*-mutant iCCA cell lines are inactive, whereas c-NHEJ seems to be unaffected.

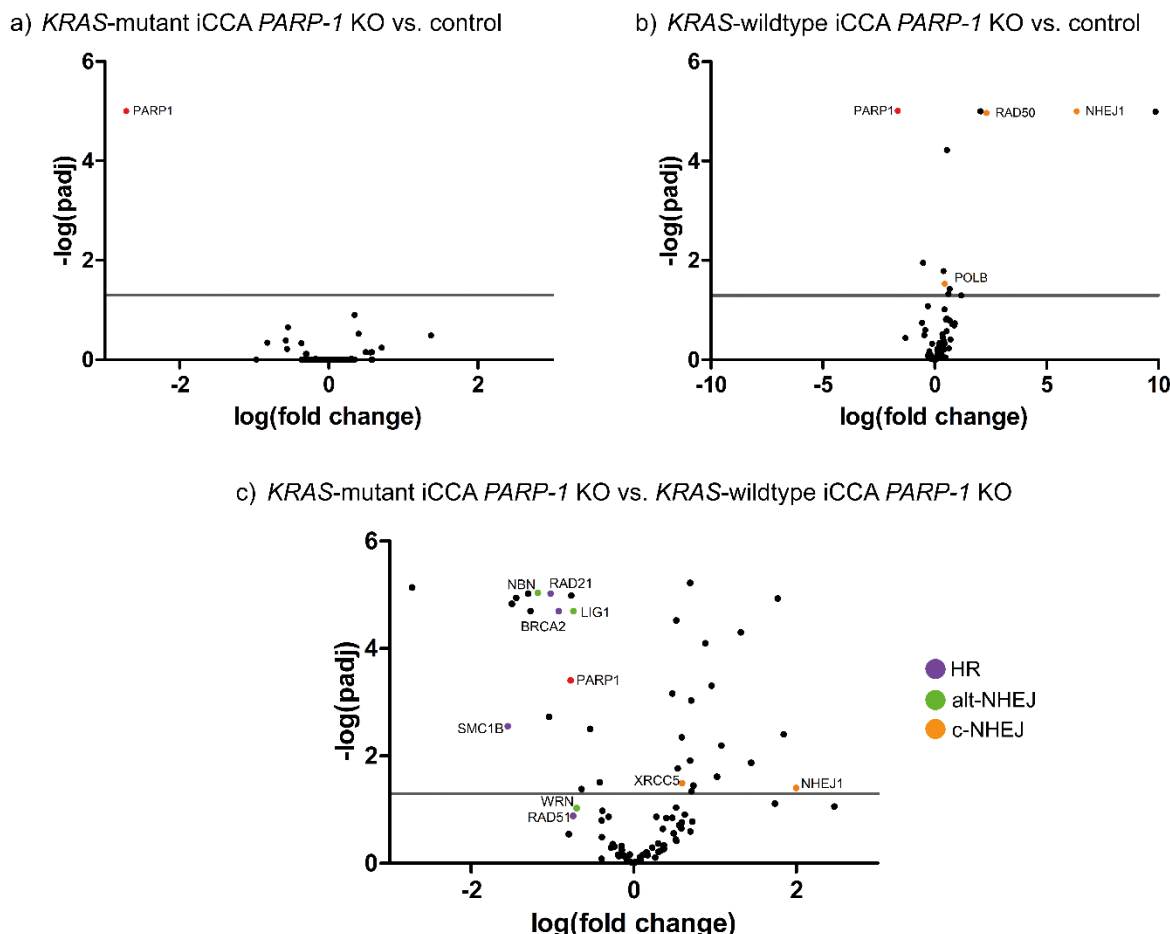


Figure 4.29: Expression of DNA damage response genes in *KRAS*-mutant and *KRAS*-wildtype iCCA cell lines.

Vulcano plots are depicted with the $\log(\text{fold change})$ of each gene and the $-\log(\text{p-adjusted})$ was calculated by performing Wald test. Selected genes associated with HR, c-NHEJ, and alt-NHEJ are colored and gene names are displayed.

Impact of *PARP-1* KO in *KRAS*-wildtype iCCA cell lines compared scrambled control

To confirm that impact of *PARP-1* KO in *KRAS*-mutant iCCA cell lines is different from *KRAS*-wildtype iCCA cell lines, we analyzed transcriptomic profiles in *KRAS*-wildtype iCCA cell lines upon *PARP-1* KO compared to scrambled control clones. By performing Wald test of log-transformed data of *PARP-1* KO in *KRAS*-wildtype iCCA cell lines, we identified a total of 3856 (1563 down-regulated, 2293 up-regulated) differentially expressed genes ($p < 0.05$). In contrast to *KRAS*-mutant iCCA cell lines, unsupervised hierarchical cluster analyses of *KRAS*-wildtype iCCA cell lines demonstrated that for each iCCA cell line WITT and CCC33 the *PARP-1* KO clones formed a cluster with their respective scrambled control clones. These findings were confirmed by the corresponding PCA plot (Figure 4.30).

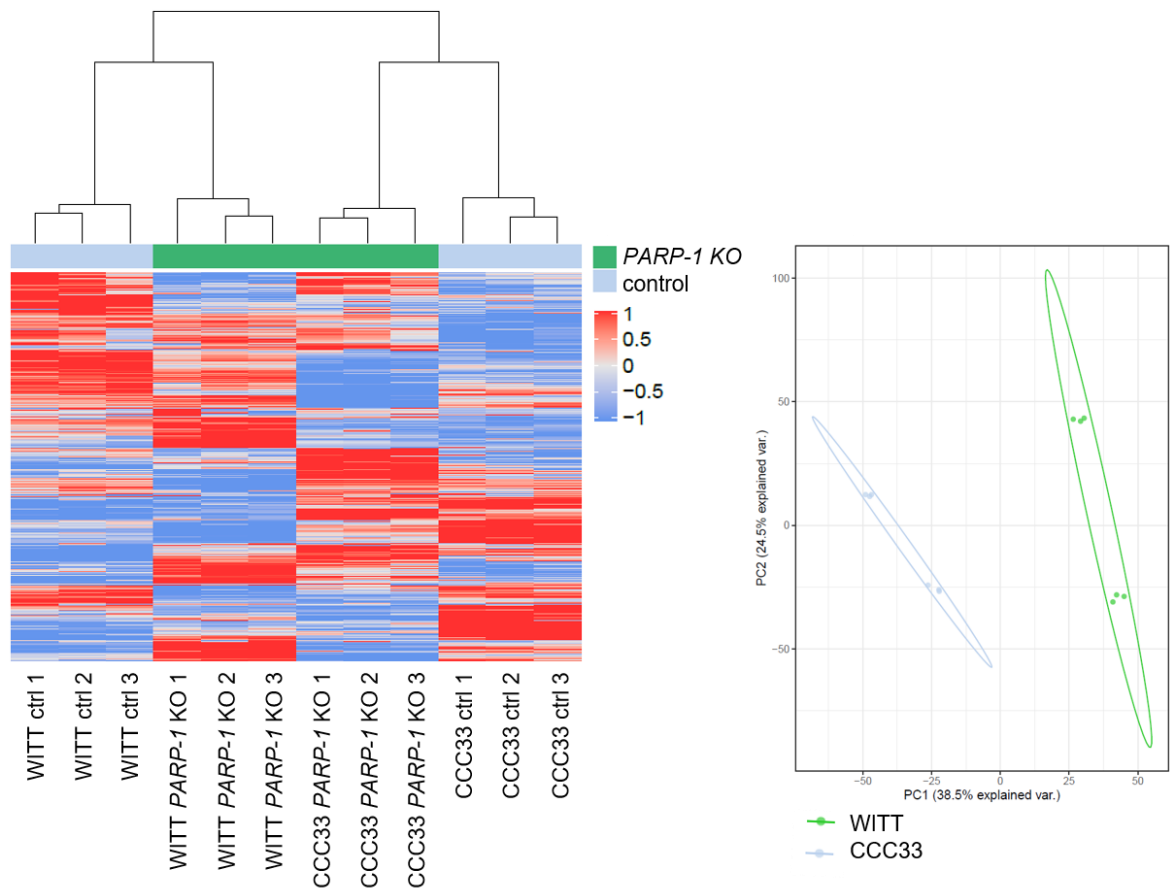


Figure 4.30: Differential gene expression genes in *KRAS*-wildtype iCCA cell lines upon *PARP-1* KO versus control clones.

Unsupervised cluster and PCA of significant genes ($p < 0.05$) of *KRAS*-wildtype iCCA cell lines (CCC33, WITT) upon *PARP-1* KO vs. control.

4.8 iCCA tumor initiation via hydrodynamic tail vein injection in *Parp-1^{+/+}* and *Parp-1^{-/-}* mice

Next, we induced sporadic tumor growth inside the livers of *Parp-1* proficient and deficient mice using hydrodynamic tail vein injection (HDTV), to investigate the influence of *Parp-1* expression during iCCA tumor initiation. The mouse strain with conditional *Parp-1* knockout used in this study was first described in 1997 [158]. The strain was kindly provided by Prof. Dr. Bernd Kaina, Institute of Toxicology, University Medical Center Mainz (Germany). The method of HDTV is based on the rapid injection of a relatively high volume of plasmid DNA solution through the tail vein resulting in a hydrodynamic pressure that enhances endothelial and parenchymal cell permeability and subsequent uptake of plasmid DNA into hepatocytes. Experimental design comprised three experimental groups: i) injection of 2000 μ g *HSB2*-plasmid (empty vector control; EV); ii) injection of 5000 μ g *Kras^{G12V}*-plasmid, 5000 μ g *shRp53*-plasmid and 2000 μ g *HSB2*-plasmid (*Kras/Tp53*); iii) injection of 2500 μ g *myrAkt*-plasmid, 2500 μ g *myc-tagged Nicd*-plasmid and 1000 μ g *HSB2*-plasmid (*Akt/Nicd*) (Figure 4.31).

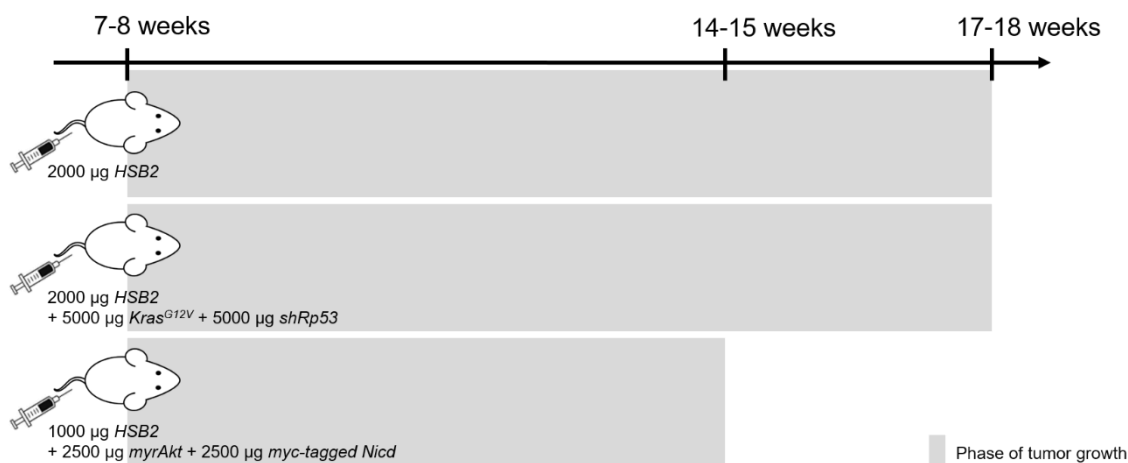


Figure 4.31: Experimental design of iCCA tumor initiation via hydrodynamic tail vein injection in *Parp-1^{+/+}* and *Parp-1^{-/-}* mice.

7-8-weeks old mice were injected with i) 2000 μ g *HSB2*-plasmid (empty vector control; EV); ii) 5000 μ g *Kras^{G12V}*-plasmid, 5000 μ g *shRp53*-plasmid and 2000 μ g *HSB2*-plasmid (*Kras/Tp53*); or iii) 2500 μ g *myrAkt*-plasmid, 2500 μ g *myc-tagged Nicd*-plasmid and 1000 μ g *HSB2*-plasmid (*Akt/Nicd*) and sacrificed at the age of 14-18 weeks.

Each plasmid combination was injected in at least 5 male mice with *Parp-1^{+/+}* and *Parp-1^{-/-}* genotype, respectively. Mice were randomly divided into groups and injected in week 7-8 after birth, depending on their body weight (20-25 g). Plasmid solution accounting for 10% of body weight was injected intravenously within 5-7 seconds. Animals were monitored weekly for signs of liver failure due to tumor growth and significant changes in body weight. Based on a predefined score sheet measuring the well-being of the experimental animals (including body weight, behavior, general appearance, mobility/activity, ascites) the mice injected with *Akt/Nicd* were sacrificed earlier than the *Kras/Tp53*-injected mice due to faster and extensive tumor growth. Livers of mice injected with EV and *Kras/Tp53* were obtained after 10 weeks. Livers of the *Akt/Nicd* experimental group were obtained after 7 weeks. Table 4.4 shows the animal IDs of the respective experimental groups and the body and liver weights on the day of sacrifice. The average body weight of the EV experimental group amounted to 32.1 g for *Parp-1^{+/+}* mice and 32.4 g for *Parp-1^{-/-}* mice. Liver weights in EV

experimental group were on average 1.46 g for *Parp-1^{+/+}* mice and 1.53 g for *Parp-1^{-/-}* mice. In mice injected with *Kras/Tp53* average body weight showed significant differences between *Parp-1^{+/+}* and *Parp-1^{-/-}* mice with 27.8 g and 29.7 g respectively ($p = 0.0234$). Further, the average liver weight significantly differed depending on the *Parp-1* genotype with 2.75 g for *Parp-1^{+/+}* and 6.10 g for *Parp-1^{-/-}* mice ($p < 0.0001$). *Akt/Nicd* experimental group showed an average body weight of 32.6 g for *Parp-1^{+/+}* mice and 30.0 g for *Parp-1^{-/-}* mice. Average liver weights amounted to 6.30 g for *Parp-1^{+/+}* and 5.18 g for *Parp-1^{-/-}* animals injected with *Akt/Nicd*.

Table 4.4: List of experimental groups.

List shows information (ID, gender, bodyweight, liver weight on the day of sacrifice) of *Parp-1^{+/+}* and *Parp-1^{-/-}* mice injected with empty vector and plasmid combinations *Kras/Tp53* and *Akt/Nicd*. *Mouse was excluded after analysis of transcriptomic data (outlier analysis).

Injection (plasmid)	genotype	ID	gender	body weight [g]	liver weight [g]
Empty vector	<i>PARP-1 +/+</i>	MAR-F947	male	32.5	1.1
		MAR-F990		32.1	1.2
		MAR-G049		32.6	1.9
		MAR-G511		31.1	1.4
		MAR-G513		32.6	1.4
	<i>PARP-1 -/-</i>	MAR-F997	male	36.3	1.6
		MAR-G003		26.9	1.3
		MAR-G048		35.3	1.8
		MAR-G060		31.3	1.7
		MAR-G507		32.3	1.3
<i>Kras/Tp53</i>	<i>PARP-1 +/+</i>	MAR-G032	male	26.5	2.7
		MAR-G149		26.0	2.4
		MAR-G419		30.1	2.6
		MAR-G457*		27.4	2.7
		MAR-G500		28.8	3.4
	<i>PARP-1 -/-</i>	MAR-G100	male	27.9	6.9
		MAR-G101		29.8	6.2
		MAR-G180		30.3	5.9
		MAR-G336		30.3	6.2
		MAR-G458		29.0	5.5
MAR-G459	30.7	5.9			
<i>Akt/Nicd</i>	<i>PARP-1 +/+</i>	MAR-F944	male	36.7	8.7
		MAR-F991		30.0	6.0
		MAR-G012		31.7	6.7
		MAR-G080		34.0	5.1
		MAR-G133		30.5	5.1
	<i>PARP-1 -/-</i>	MAR-G036	male	32.2	6.0
		MAR-G063		29.1	5.1
		MAR-G066		31.9	6.1
		MAR-G139		29.4	4.7
		MAR-G140		27.2	4.1

4.8.1 Histology and immunohistochemistry staining of HDTV-induced tumor tissue sections

To investigate morphological and histological changes in the liver tissue sections after HDTV-induced tumorigenesis, we dissected the livers of the respective animals, examined the liver morphology, and performed immunohistological staining (H&E staining). Further,

the paraffin-embedded liver tissue sections were kindly stained (Gomori's trichrome staining, and PAS reaction) by Prof. Dr. Beate Straub, Institute of Pathology, University Medical Center Mainz.

Injection of *Kras/Tp53* led to the preferential occurrence of distinct solid tumors in *Parp-1* proficient mice within 10 weeks. Histopathological staining of tumor tissue sections showed stromal, partially sarcomatoid structures with giant tumor cells. These tumor sections displayed invasive features and absence of mucin production and were classified as intrahepatic cholangiocarcinoma. In contrast, the surrounding liver tissue of *Parp-1* proficient mice represented pronounced hematogenous invasion of multiple small-cell dysplastic foci, classified as hepatocellular carcinoma. Staining for fibrotic or glycoprotein structures was negative (Figure 4.32 left, middle).

Livers resected from *Parp-1* deficient animals showed smaller nodules, distributed over all liver lobes. Histopathological staining showed multifocal diffuse hepatocarcinogenesis with pronounced hematogenous invasion. Disrupted liver parenchyma harbored multiple, partially steatotic small-cell dysplastic foci and small, trabecular, well-differentiated hepatocellular carcinoma. Staining for fibrotic or glycoprotein structures was negative (Figure 4.32 right).

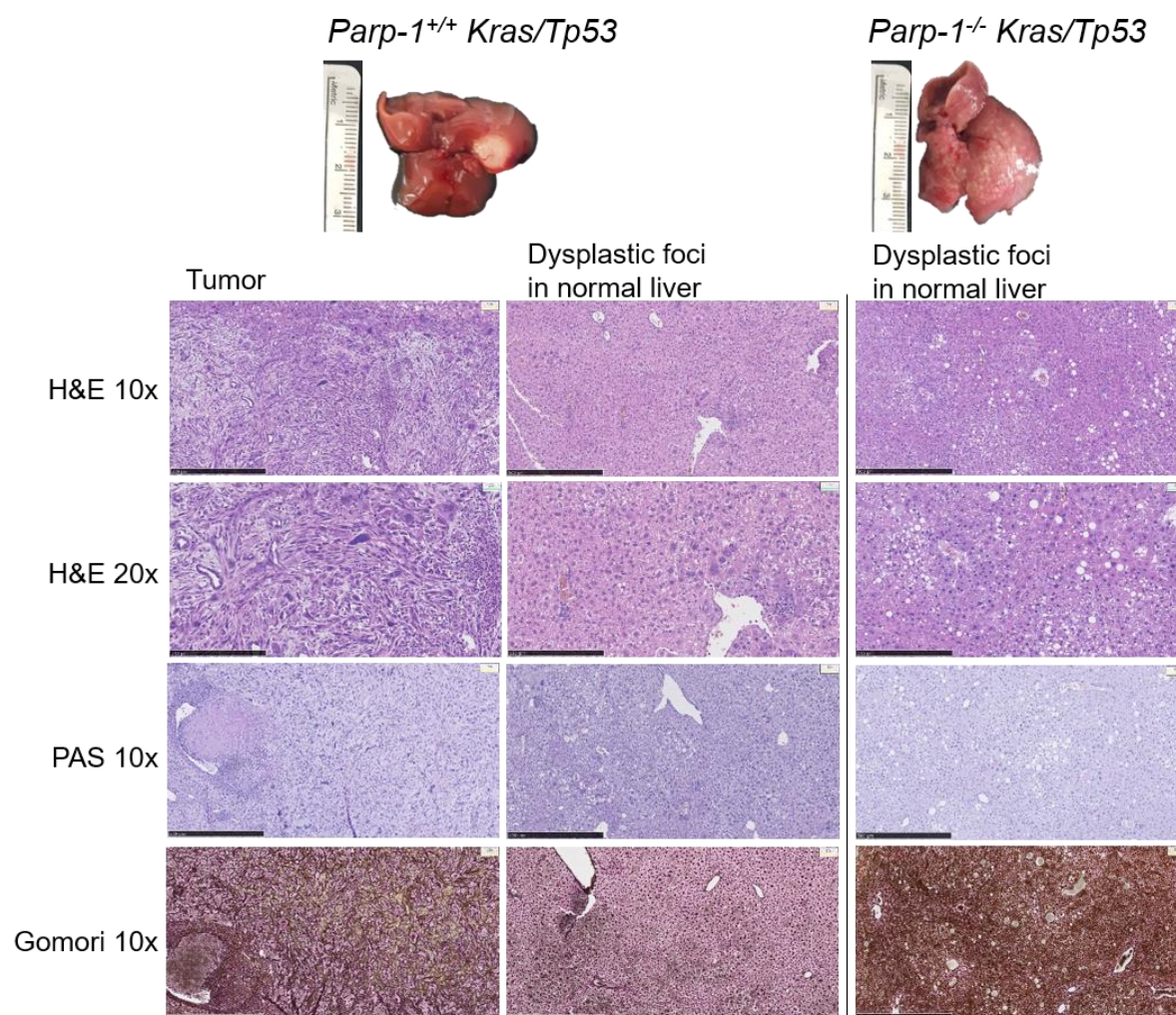


Figure 4.32: Histology of liver sections injected with *Kras/Tp53* via HDTV.

Representative images of livers with tumor induction via HDTV (*Kras/Tp53*) in *Parp-1*^{+/+} (n=5) and *Parp-1*^{-/-} mice (n=6). Shown are H&E, Gomori's trichrome staining, and PAS reaction of representative paraffin-embedded tumor sections (3.5 µm). Scale bars indicating 500 µm (10x), 250 µm (20x).

Next, we performed immunohistochemical staining of classic biliary markers (Ck19, Sox9) as well as Parp-1, Ki67, p- γ H2ax. Expression of Ck19 and Sox9 was observed in tumor sections of *Parp-1*^{+/+} mice injected with *Kras/TP53*. Dysplastic nodules in surrounding liver sections of *Parp-1*^{+/+} mice as well as of *Parp-1*^{-/-} mice were negative for Ck19 and Sox9 expression. Nuclear Parp-1 expression was detectable in all sections of *Parp-1*^{+/+} mice, whereas no Parp-1 expression was determined in *Parp-1* deficient liver sections (*Parp-1*^{+/+} tumor vs. *Parp-1*^{-/-} dysplastic foci p < 0.0001; *Parp-1*^{+/+} dysplastic foci vs. *Parp-1*^{-/-} dysplastic foci p < 0.0001). As expected, Ki67, a marker for proliferative cells, was expressed predominantly in tumor tissue of *Parp-1* proficient mice (*Parp-1*^{+/+} tumor vs. *Parp-1*^{+/+} dysplastic foci p < 0.0001; *Parp-1*^{+/+} tumor vs. *Parp-1*^{-/-} dysplastic foci p < 0.0001). Surrounding liver sections of both *Parp-1* proficient and deficient mice showed positive Ki67 staining in cells close to vessels and dysplastic areas. Further, we observed staining of p- γ H2ax, representing DNA damage sites, randomly distributed in both tumor and surrounding liver sections of *Parp-1*^{+/+} mice (*Parp-1*^{+/+} tumor vs. *Parp-1*^{-/-} dysplastic foci p < 0.0001; *Parp-1*^{+/+} dysplastic foci vs. *Parp-1*^{-/-} dysplastic foci p = 0.009). The staining of p- γ H2ax expression in liver sections of *Parp-1* deficient mice was less pronounced in comparison to *Parp-1* proficient mice (Figure 4.33 + Figure 4.34). Taken together the assessment of the *Kras/TP53*-induced tumor sections showed distinct differences in morphology and histological classification of tumors dependent on *Parp-1* genotype. *Parp-1* deficient mice developed small nodules classified as hepatocellular carcinoma with the absence of biliary markers. *Parp-1* proficient mice showed growth of intrahepatic cholangiocarcinoma and positive staining of biliary markers Ck19 and Sox9, proliferation marker Ki67, and DNA double-strand break marker p- γ H2ax.

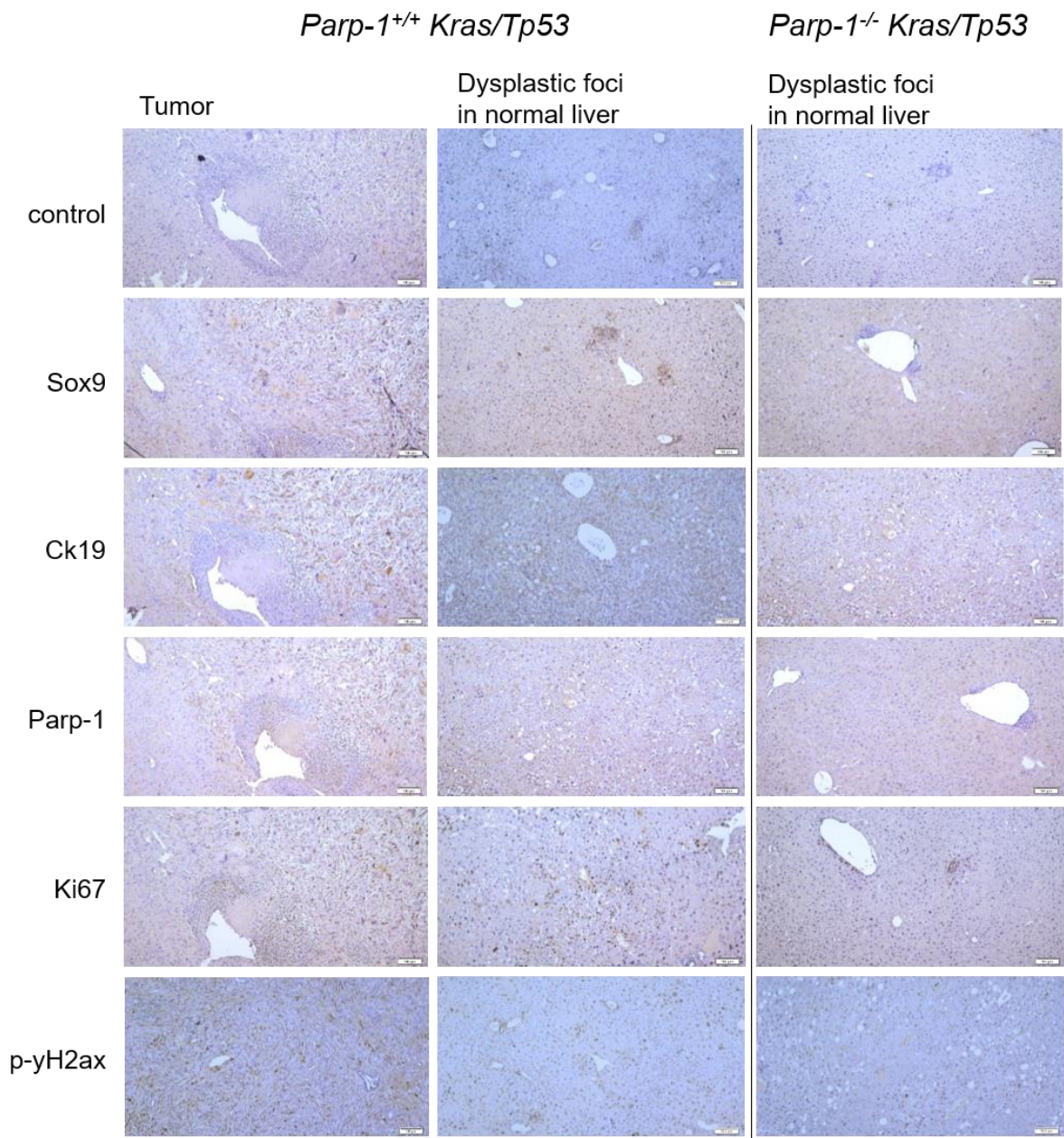


Figure 4.33: Immunohistochemistry staining of liver sections of mice injected with *Kras/Tp53* via HDTV.

Immunohistochemistry staining of selected proteins (Sox9, Ck19, Parp-1, Ki67, and p- γ H2ax). Shown are representative images of paraffin-embedded tumor sections (3.5 μ m) of tumor induction via (*Kras/Tp53*) in *Parp-1^{+/+}* (n=5) and *Parp-1^{-/-}* mice (n=6). Scale bars indicating 100 μ m (5x).

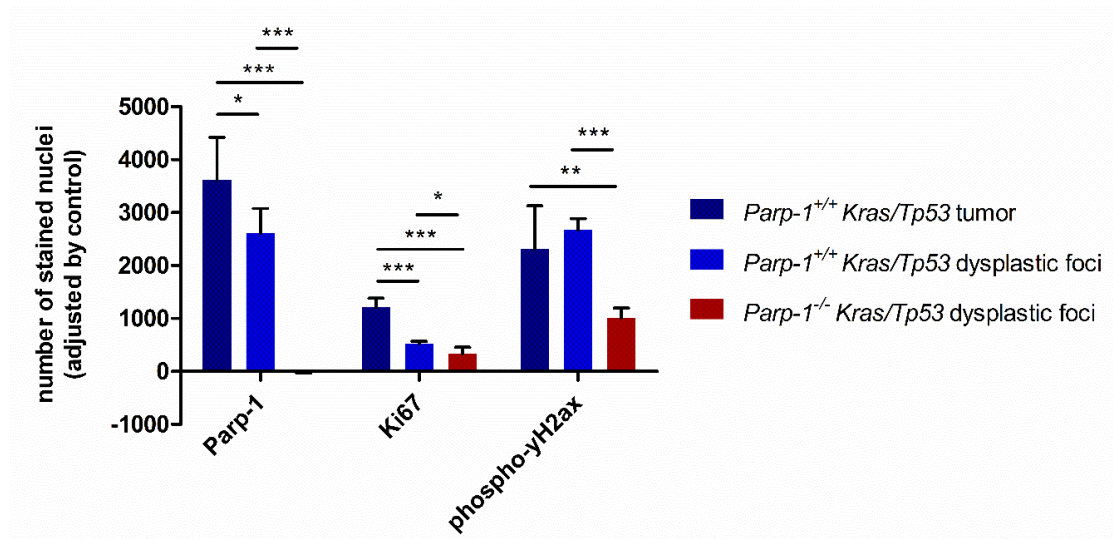


Figure 4.34: Quantification of Parp-1, Ki67 and p-yH2ax expression in liver sections after HDTV with *Kras/Tp53*.

Quantification of selected immunohistochemical markers in liver sections of mice injected with *Kras/Tp53*. The number of stained nuclei was determined by ImageJ and adjusted to control staining. Mean \pm SD, n=5, p < 0.05 (*), p < 0.01 (**), p < 0.001 (***).

Animals injected with *Akt/Nicd* developed tumors 7 weeks after HDTV with pronounced hepatomegaly and steatohepatitis visible in the images of the livers. Besides tumor nodules, liquid-filled cysts were visible. The injection of *Akt/Nicd* showed similar tumorigenic properties independent of the *Parp-1* genotype. Histopathological staining of tumor tissue sections showed multifocal small-sized tubular and acinar structures with the absence of mucin production. Staining for fibrotic or glycoprotein structures was negative. Tumors were classified as intrahepatic cholangiocarcinoma by an expert pathologist (Figure 4.35).

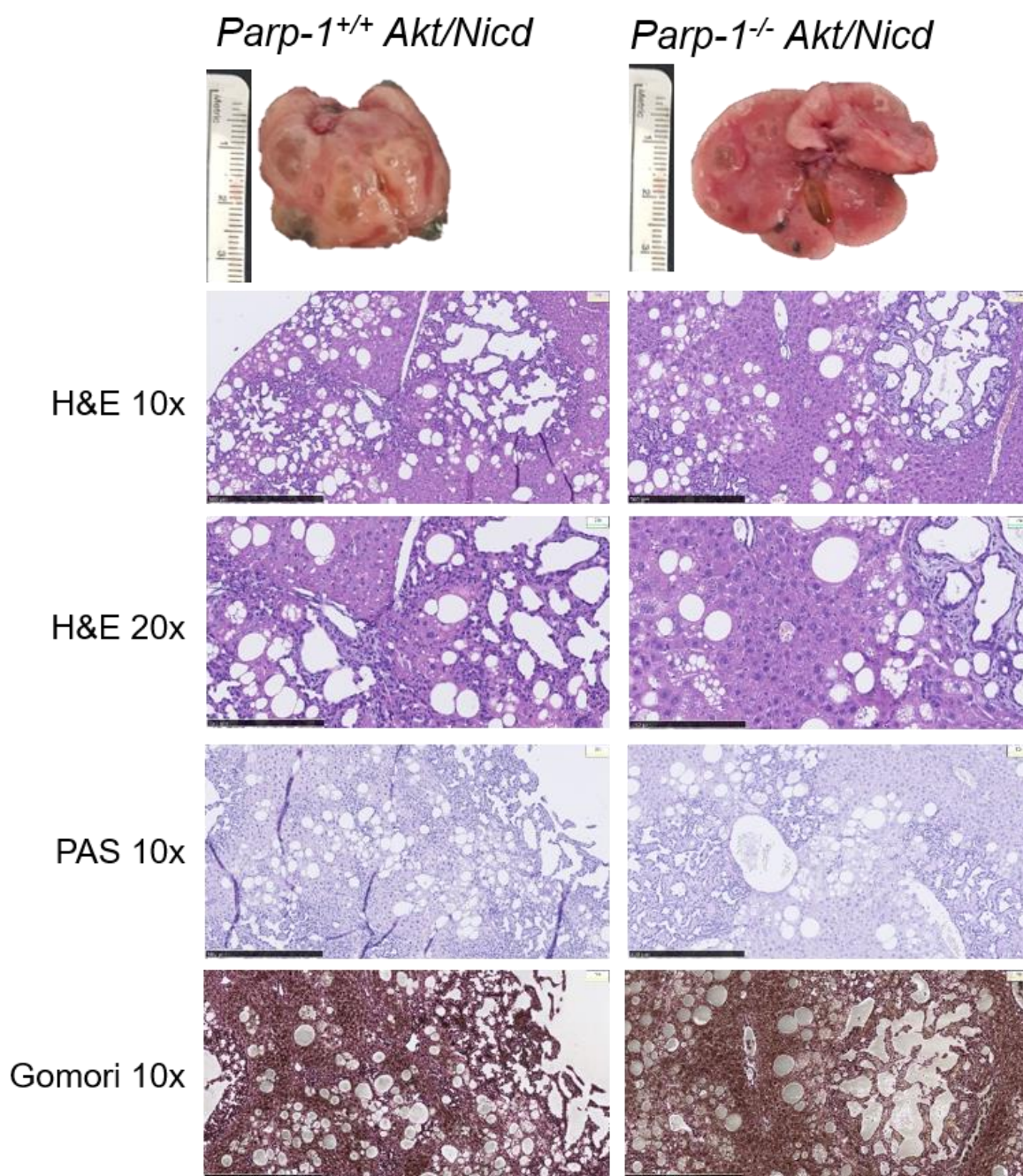


Figure 4.35: Histology of liver sections injected with *Akt/Nicd* via HDTV.

Representative images of livers with tumor induction via HDTV (*Akt/Nicd*) in *Parp-1*^{+/+} (n=6) and *Parp-1*^{-/-} mice (n=6). Shown are H&E, Gomori's trichrome staining, and PAS reaction of representative paraffin-embedded tumor sections (3.5 μ m). Scale bars indicating 500 μ m (10x), 250 μ m (20x).

In addition, we performed immunohistochemical staining of classic biliary markers (Ck19, Sox9) as well as Parp-1, Ki67, p- γ H2ax. High expression of Ck19 and Sox9 was observed in tumor sections of both *Parp-1* proficient and deficient mice injected with *Akt/Nicd*. Nuclear Parp-1 expression was detectable in sections of *Parp-1*^{+/+} mice. In *Parp-1*^{-/-} mice unspecific cytosolic staining was observed (*Parp-1*^{+/+} tumor vs. *Parp-1*^{-/-} tumor p < 0.0001). Ki67, a marker for proliferative cells, was stained predominantly in cholangiocarcinoma areas in both *Parp-1*^{+/+} and *Parp-1*^{-/-} mice. Surrounding liver sections were free of Ki67 staining. We observed weak staining of p- γ H2ax, representing DNA damage sites, in tumor sections of

Parp-1 proficient and deficient mice. For both Ki67 and p-yH2ax staining, quantification showed no differences depending on *Parp-1* genotype (Figure 4.36 + Figure 4.37). Overall and in contrast to *Kras/Tp53*-induced tumor growth, the assessment of the *Akt/Nicd*-induced tumor sections showed no differences in morphology and histological classification of tumors dependent on the *Parp-1* genotype.

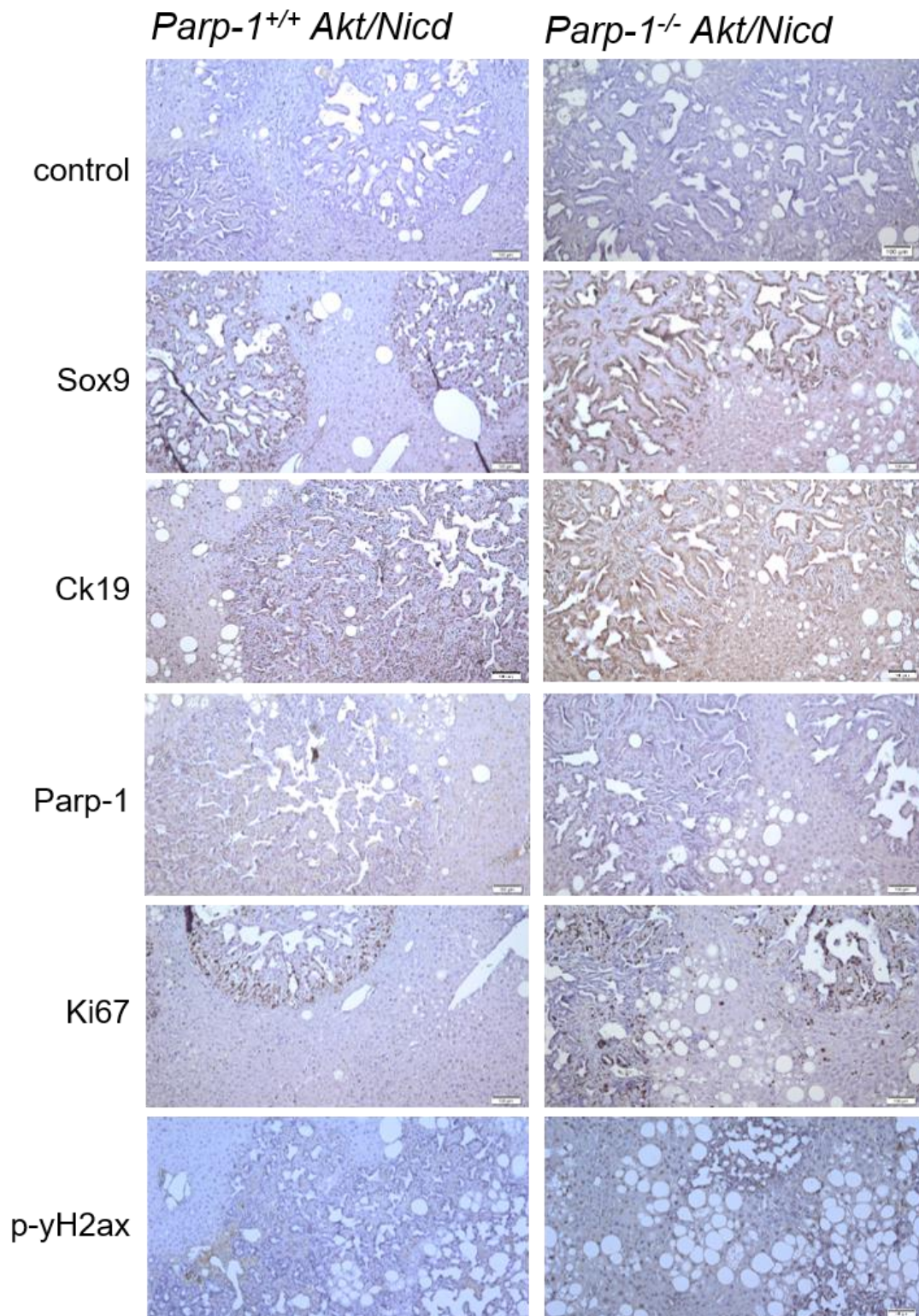


Figure 4.36: Immunohistochemistry staining of liver sections injected with *Akt/Nicd* via HDTV. Immunohistochemistry staining of selected proteins (Sox9, Ck19, Parp-1, Ki67, and p-yH2ax). Shown are representative images of paraffin-embedded tumor sections (3.5 μ m) of tumor induction via (*Akt/Nicd*) in *Parp-1*^{+/+} (n=6) and *Parp-1*^{-/-} mice (n=6). Scale bars indicating 100 μ m (5x).

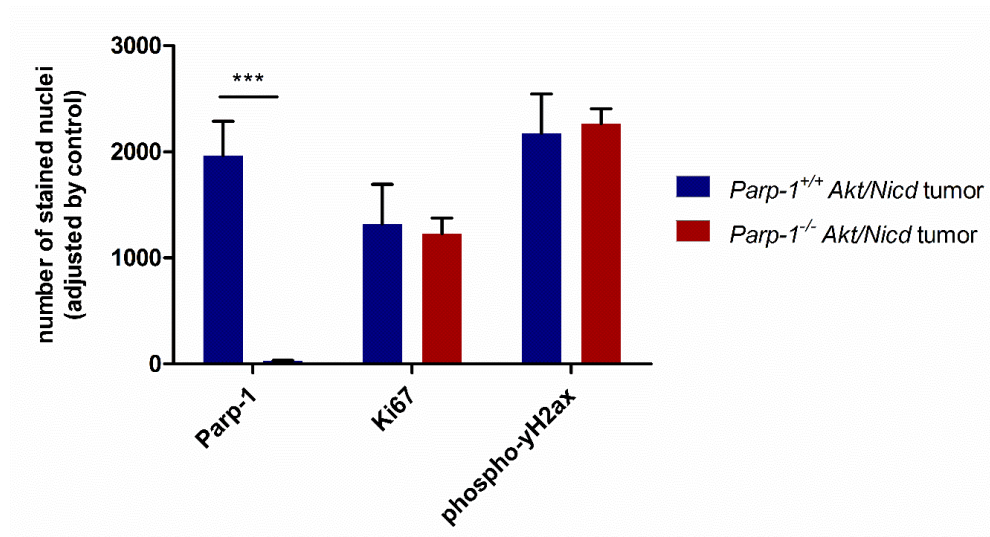


Figure 4.37: Quantification of Parp-1, Ki67 and p-yH2ax expression in liver sections after HDTV with Akt/Nicd.

Quantification of selected immunohistochemical markers in liver sections of mice injected with Akt/Nicd. The number of stained nuclei was determined by ImageJ and adjusted to control staining. Mean \pm SD, n=5, $p < 0.001$ (***)

To exclude sporadic or unspecific effects of HDTV, we assessed the liver of mice injected with empty vector control. HDTV of empty vector control in *Parp-1*^{+/+} and *Parp-1*^{-/-} mice did not result in tumor growth within 10 weeks. Morphology of liver sections showed no pathophysiological changes. Gomori's trichrome stain for reticular and collagenic fiber, as well as PAS-reaction revealing glycoprotein-containing mucin, were negative and represented physiological liver tissue morphology (Figure 4.38).

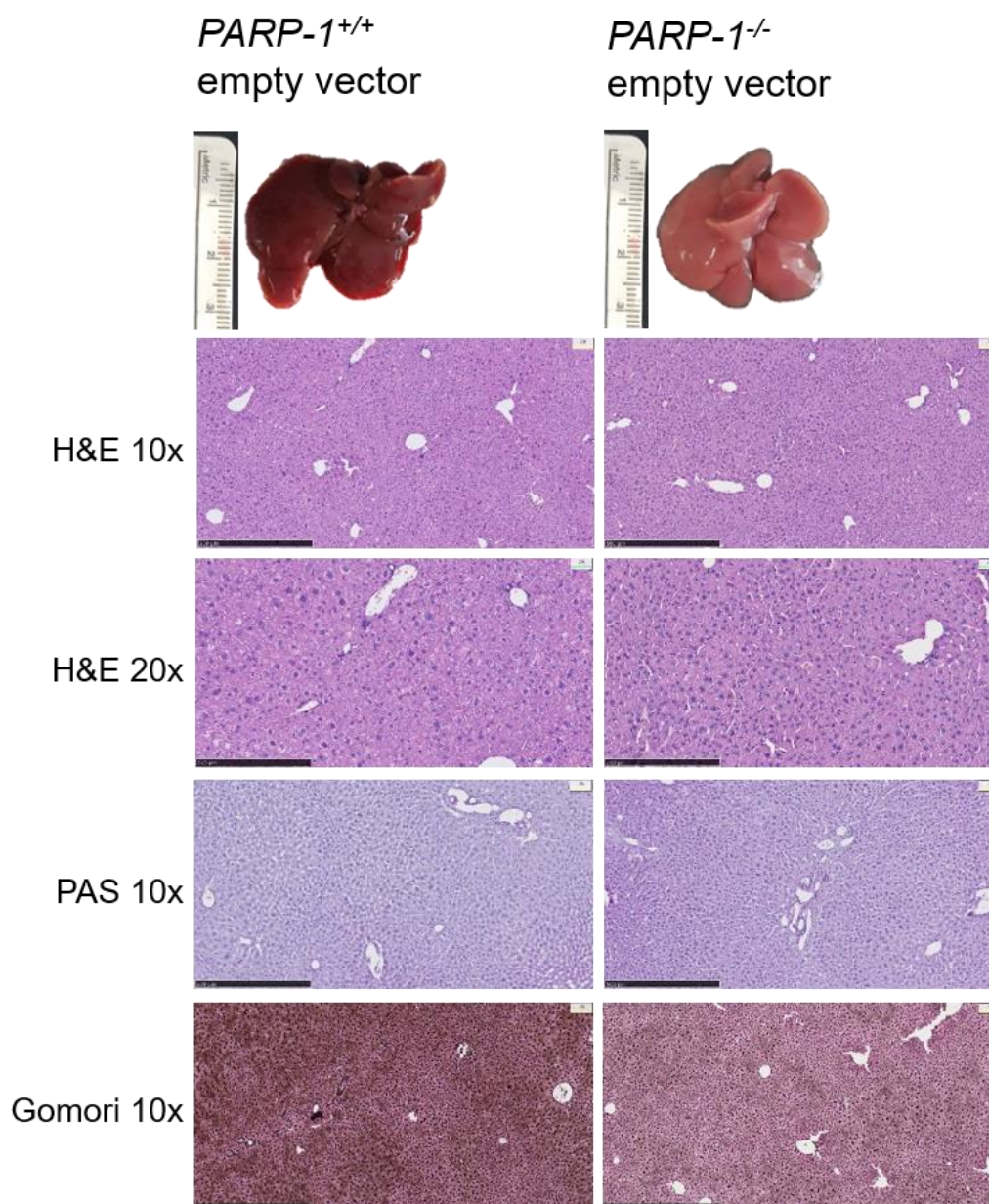


Figure 4.38: Histology of liver sections injected with empty vector via HDTV.

Representative images of livers with tumor induction via HDTV (empty vector (EV)) in *Parp-1*^{+/+} (n=6) and *Parp-1*^{-/-} mice (n=6). Shown are H&E, Gomori's trichrome staining, and PAS reaction of representative paraffin-embedded tumor sections (3.5 μ m). Scale bars indicating 500 μ m (10x), 250 μ m (20x).

4.8.2 Quantification of HDTV-induced tumor burden

To estimate tumor development and burden in the different experimental groups, we assessed the body and liver weight at the day of sacrifice. Therefore, the liver weight was related to the body weight and associated with the *Parp-1* genotype (Figure 4.39). Upon injection of *Kras/Tp53* and *Akt/Nicd* liver weight/body weight-ratio (L/B-ratio) increased significantly indicating changes in liver composition and tumor growth. Upon injection with *Kras/Tp53* we observed significant differences in L/B-ratio dependent on *Parp-1* genotype ($p < 0.0001$) (Figure 4.39). The L/B-ratio of *Parp-1*^{+/+} animals reached only 9.91%, whereas animals with *Parp-1*^{-/-} genotype showed L/B-ratio of 20.60%. This could be explained by the enlargement of the liver by multiple small nodules in *Parp-1* deficient animals. In contrast,

upon injection of *Akt/Nicd* L/B-ratio increased to 17.21% in the *Parp-1^{+/+}* experimental group and 19.25% in the *Parp-1^{-/-}* experimental group. Consistent with the phenotype, we could not observe significant differences depending on the *Parp-1* genotype in *Akt/Nicd* animals (Figure 4.39). L/B-ratio in EV experimental group showed no differences, regardless of *Parp-1* genotype. Notably, L/B-ratio was comparably low with 4.54-4.74%.

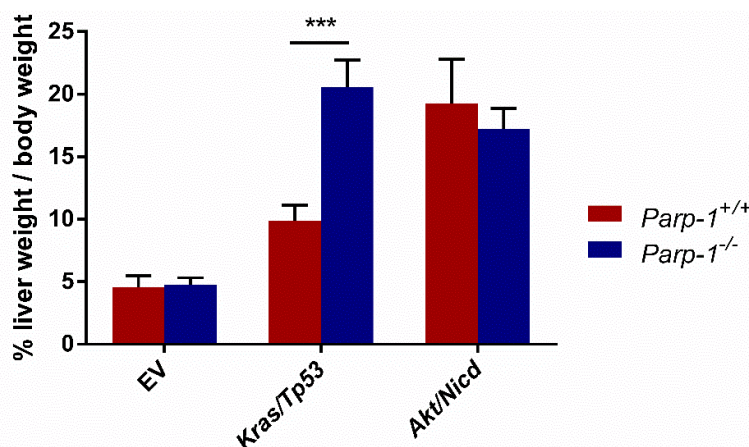


Figure 4.39: Quantification of liver weight / body weight-ratio.

Liver weight / body weight ratio (%) of *Parp-1^{+/+}* mice (blue) and *Parp-1^{-/-}* mice (red) after HDTV of empty vector (EV), *Akt/Nicd* or *Kras/Tp53* plasmid combinations with HSB2. Mean \pm SD, n=5, p < 0.05 (*), p < 0.01 (**), p < 0.001 (***)

Besides the L/B-ratio, liver morphology vastly differed between experimental groups. Quantification was performed on basis of a scoring system that distinguished three stages in dependency of the tumor evolution and progression in the model: i) no tumor; ii) nodules spread all over the liver; iii) one or several distinct solid tumors accompanied by minor visible changes in liver morphology (Figure 4.40). Comparison of the experimental groups recapitulated our findings regarding L/B-ratio. We observed pronounced differences in grading after *Kras/Tp53* injection between *Parp-1^{+/+}* and *Parp-1^{-/-}* experimental groups (p = 0.003). In contrast, injection of EV and *Akt/Nicd* showed no differences in tumor classification dependent on the *Parp-1* genotype. Overall, quantification by liver-to-body weight ratio and by scoring system confirmed the histological assessment of tumors and differences dependent on plasmid combination and *Parp-1* genotype.

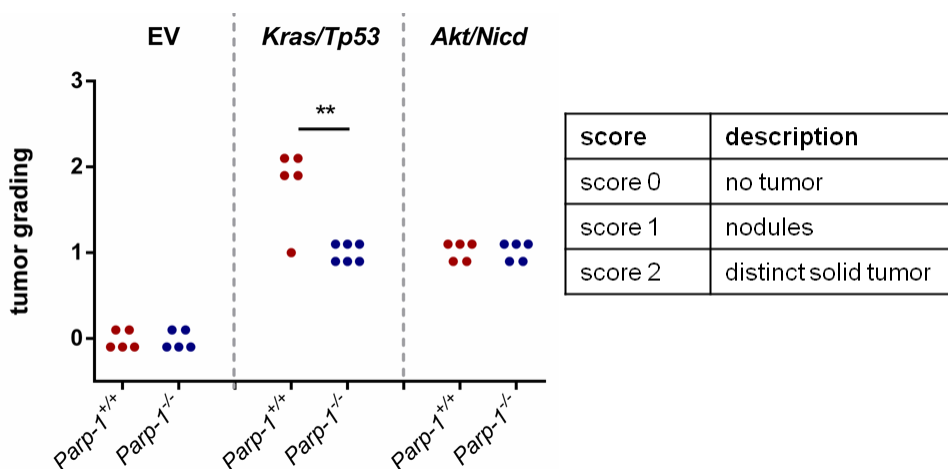


Figure 4.40: Quantification of *in vivo* tumor growth with classifications.

Shown as classifications: 0 = no tumor, 1 = nodules, 2 = distinct solid tumor. EV, *Akt/Nicd* n = 5, *Kras/Tp53* n = 5/6, p < 0.01 (**).

4.8.3 Histopathological assessment and classification of HDTV-induced tumor tissue sections

Histopathological classification of the paraffin-embedded liver tissue sections was kindly performed by Prof. Dr. Beate Straub, Institute of Pathology, University Medical Center Mainz. Examination of paraffin-embedded tumor tissue sections of *Parp-1^{+/+}* and *Parp-1^{-/-}* genotype after *Kras/Tp53* injection showed stark distinctions between the two genotypes. Four out of five *Parp-1^{+/+}* samples injected with *Kras/Tp53* were classified as intrahepatic cholangiocarcinoma with poor differentiation (G3-4). The remaining sample was classified as a mixed type iCCA-HCC tumor with poor to no differentiation (G3-4) (Table 4.5). In addition, all sections showed low-grade microvesicular steatosis (1-10%) and abolished architecture of liver parenchyma. Indications of neither inflammation nor fibrosis were observed in any section. Examination of matched surrounding liver tissue sections of *Parp-1^{+/+}* mice injected with *Kras/Tp53* showed several dysplastic nodules with pronounced hematogenous spread (V1). We observed 80-100 foci with a size of < 1 mm. All sections bore signs of low-grade microvesicular steatosis (1-10%) and abolished architecture of liver parenchyma. Neither inflammatory nor fibrotic changes were observed in any section (Table 4.6).

In striking contrast, animals with *Parp-1* deficient genotype were classified as multiple, diffuse hepatocellular carcinomas and dysplastic nodules with pronounced hematogenous invasion (20-100 foci, 1-4 mm, V1) (Table 4.5). Further, medium-grade macrovesicular steatosis (11-50%) and disrupted architecture of liver parenchyma were observed. Half of the sample showed signs of inflammation, whereas no fibrosis was observed (Table 4.6). These investigations suggest that the PARP deficiency preferentially inhibits cholangiocarcinogenesis while concomitantly permits hepatocellular cancer growth.

Importantly, the examination of paraffin-embedded liver tissue sections after *Akt/Nicd* injection confirmed the absence of any histopathological differences between mice with *Parp-1^{+/+}* and *Parp-1^{-/-}* genotype. All samples were classified as multifocal intrahepatic cholangiocarcinoma (~100 foci, 1-4 mm) with well to moderate differentiation (G1-2) (Table 4.5). Injection of *Akt/Nicd* led to severe macrovesicular steatosis (> 50%) in both mice with *Parp-1* deficient and proficient genotype accompanied by the disrupted architecture of liver parenchyma. Neither inflammation nor fibrosis was observed in any tissue section (Table 4.6). Notably, control injection with *HSB2* (EV) did not show signs of tumor growth independent of the *Parp-1* genotype. The architecture of the liver tissue remained physiological and there were no indications of steatosis, inflammation, or fibrosis (Table 4.5, Table 4.6). Overall, these investigations confirm the KRAS dependency of the model.

Table 4.5: Pathological classification of *in vivo* tumors after HDTV.

Table shows information (grading, number of foci, size, hematogenous spread) of paraffin-embedded tumor sections.

plasmid	N	genotype	tissue	classification	grading	foci	size	hematogenous spread
Empty vector (HSB2)	5	<i>PARP-1</i> +/+	normal liver	No tumor	-	-	-	-
	5	<i>PARP-1</i> -/-	normal liver	No tumor	-	-	-	-
<i>Kras/Tp53</i>	5	<i>PARP-1</i> +/+	tumor	4x iCCA, 1x iCCA-HCC	G3-4	>3	3 mm – 1 cm	-
			dysplastic foci in normal liver	5x dysplastic foci	n.A.	80-100	<1 mm	V1
	6	<i>PARP-1</i> -/-	dysplastic foci in normal liver	6x dysplastic foci, 1x HCC	n.A.	20-100	1-4 mm	V1
<i>Akt/Nicd</i>	5	<i>PARP-1</i> +/+	tumor in normal liver	Multiple iCCA	G1-2	~100	1-4 mm	-
	5	<i>PARP-1</i> -/-		Multiple iCCA	G1-2	~100	1-4 mm	-

Table 4.6: Pathological classification of *in vivo* tumors after HDTV.

Table shows information (steatosis, tissue architecture, inflammation, and fibrosis) of paraffin-embedded tumor sections.

plasmid	N	genotype	tissue	steatosis (quantity)	steatosis (quality)	architecture	inflammation	fibrosis
Empty vector (HSB2)	5	<i>PARP-1</i> +/+	normal liver	-	-	-	-	-
	5	<i>PARP-1</i> -/-	normal liver	-	-	-	-	-
<i>Kras/Tp53</i>	5	<i>PARP-1</i> +/+	tumor	1-10%	microvesicular	abolished	-	-
			dysplastic foci in normal liver	1-10%	microvesicular	abolished	-	-
	6	<i>PARP-1</i> -/-	dysplastic foci in normal liver	11-50%	macrovesicular	disrupted	3/6	-
<i>Akt/Nicd</i>	5	<i>PARP-1</i> +/+	tumor in normal liver	>50%	macrovesicular	disrupted	-	-
	5	<i>PARP-1</i> -/-		>50%	macrovesicular	disrupted	-	-

4.8.4 Transcriptomic profiling of HDTV-induced tumor samples

We observed distinct morphological and histopathological differences between the two injected plasmid combinations and dependence on the *Parp-1* genotype. To further assess these findings, we performed RNA sequencing to explore the transcriptomic profiles of HDTV-induced tumors driven by *Kras/Tp53* or *Akt/Nicd*.

First, we analyzed transcriptomic profiles of *Parp-1*^{+/+} and *Parp-1*^{-/-} mice injected with *Kras/Tp53*. By performing Wald test of log-transformed data of *Kras/Tp53*-injected *Parp-1*^{+/+} and *Parp-1*^{-/-} mice, we identified a total of 7661 differentially expressed genes (4577 downregulated, 3084 upregulated) ($p < 0.05$). Unsupervised hierarchical cluster analyses based on these differentially expressed genes demonstrated that the two experimental groups formed dense clusters according to the *Parp-1* genotype (Figure 4.41). Similar

observations were noted in the corresponding PCA plot. Notably, the distribution of *Parp-1* proficient samples on the PCA plot was more scattered than those of *Parp-1* deficient mice, which were located in close proximity (Figure 4.41).

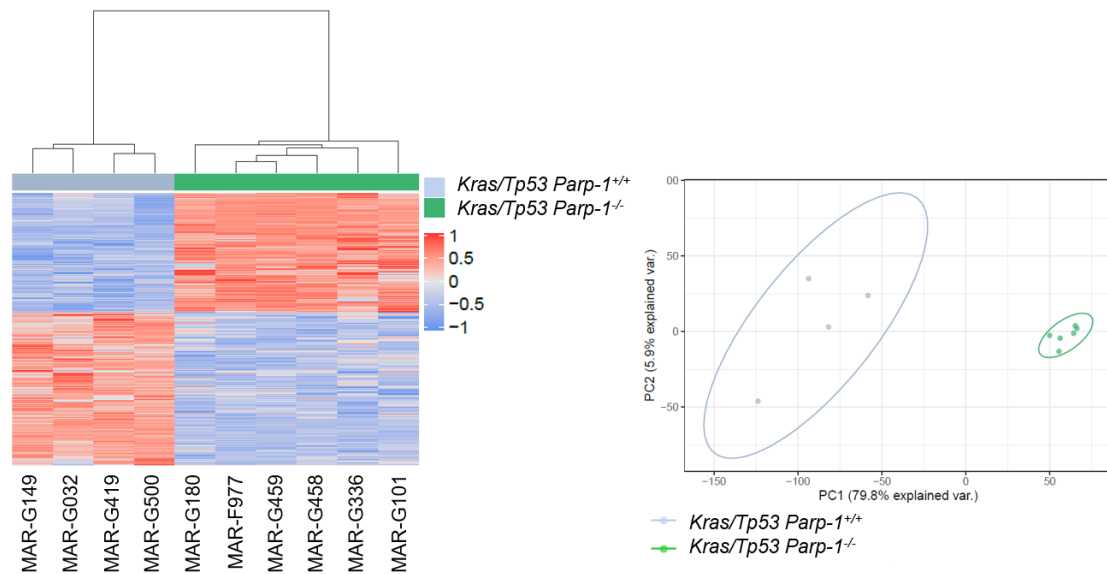


Figure 4.41: Differential expressed genes after HDTV with *Kras/Tp53* in *Parp-1*^{-/-} versus *Parp-1*^{+/+} mice.

Unsupervised cluster and PCA plot of significant genes ($p < 0.05$) after HDTV with *Kras/Tp53* in *Parp-1*^{-/-} vs. *Parp-1*^{+/+} mice.

Comparative network and pathways analyses of RNA sequencing data were then performed using IPA. We uploaded datasets of significantly expressed genes of *Parp-1* deficient versus *Parp-1* proficient mice injected with *Kras/Tp53*. Expression analysis was performed with a cut-off p -value < 0.05 , resulting in a total number of 7661 genes of which 3084 were up- and 4577 were downregulated. All pathways were selected by significant regulation $-\log(p\text{-value}) > 1.3$. IPA analyses revealed regulation of canonical pathways related to cell cycle control, like G1/S checkpoint regulation and G2/M DNA damage checkpoint regulation and ATM signaling, all with positive z-score, representing activation. Further, the DNA double-strand break repair pathway associated with BRCA1 was regulated with the prediction of inhibition. These findings suggest that DNA damage response mechanisms are dysregulated in *Kras/Tp53*-injected animals dependent on the *Parp-1* genotype. Oxidative stress pathways (NRF-2 mediated oxidative stress response, HIF1 α signaling) showed negative z-scores as well, while apoptosis-related pathways (Death receptor signaling, Apoptosis signaling, and Myc-mediated apoptosis) showed activation with a positive z-score. Further, the regulation of several key oncogenic pathways could be revealed. *Kras/Tp53* induced tumors under *Parp-1* knockout showed activation of LXR/RXR, p53, PTEN, and HIPPO signaling. Inhibition of pathways was shown in key oncogenic pathways like TGF β , NF- κ B, Notch, p38, and ERK/MAPK signaling (Figure 4.42 a). IPA toxicity analyses revealed liver-associated clinical pathology endpoints. Besides increased hepatitis, steatosis, and liver damage also sets of molecules known to be involved in hepatic fibrosis and cholestasis were enriched. Tumorigenesis-related features of liver proliferation, necrosis, and cell death as well as oxidative stress were confirmed (Figure 4.42 b). Overall, IPA analyses confirmed that pathway activation and regulation in *Kras/Tp53* induced tumors in *Parp-1*^{-/-} differed significantly in comparison to *Parp-1*^{+/+} mice.

In concordance with our *in vitro* findings, *Parp-1* deficiency led to impaired DNA damage response and dysregulation of oxidative and apoptotic processes.

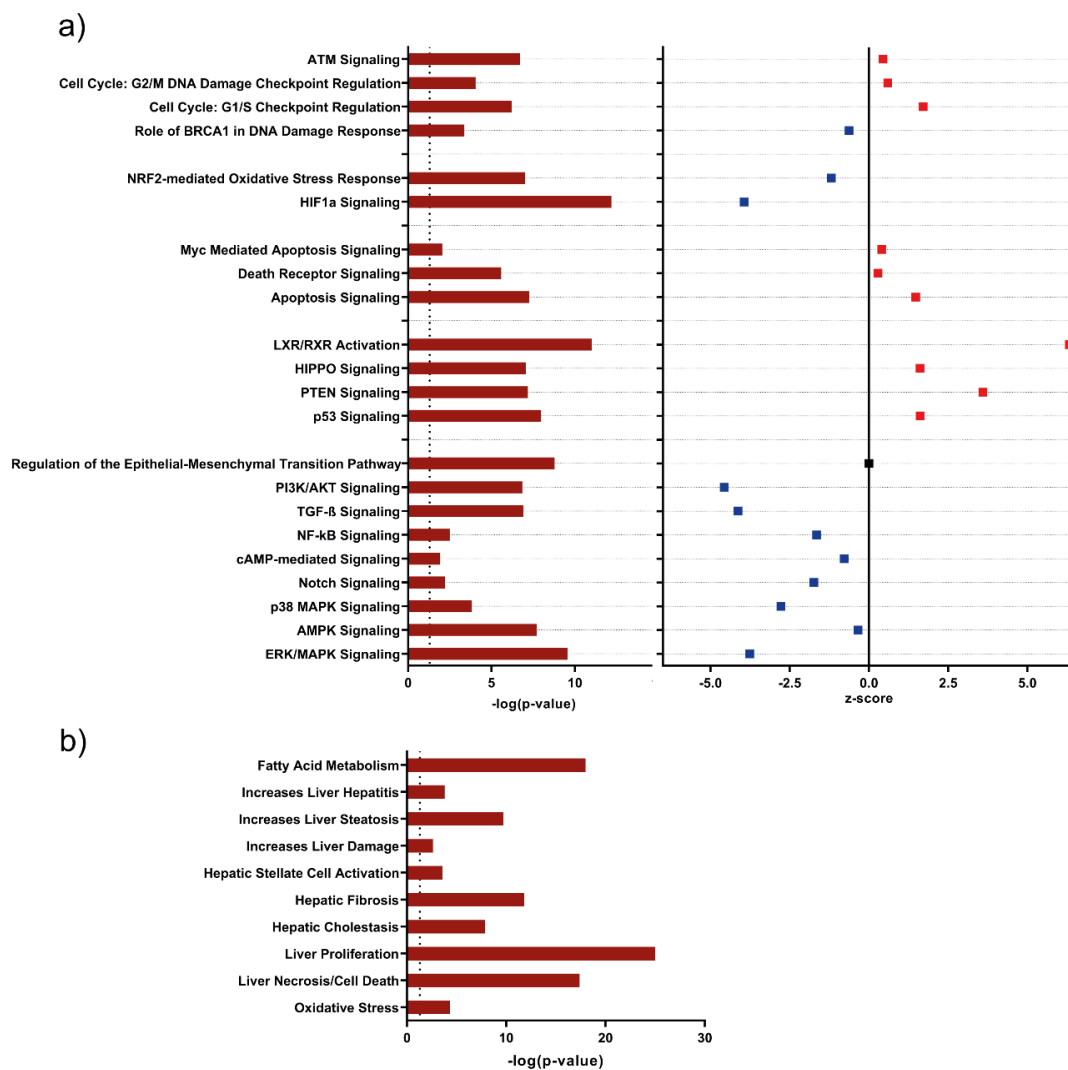


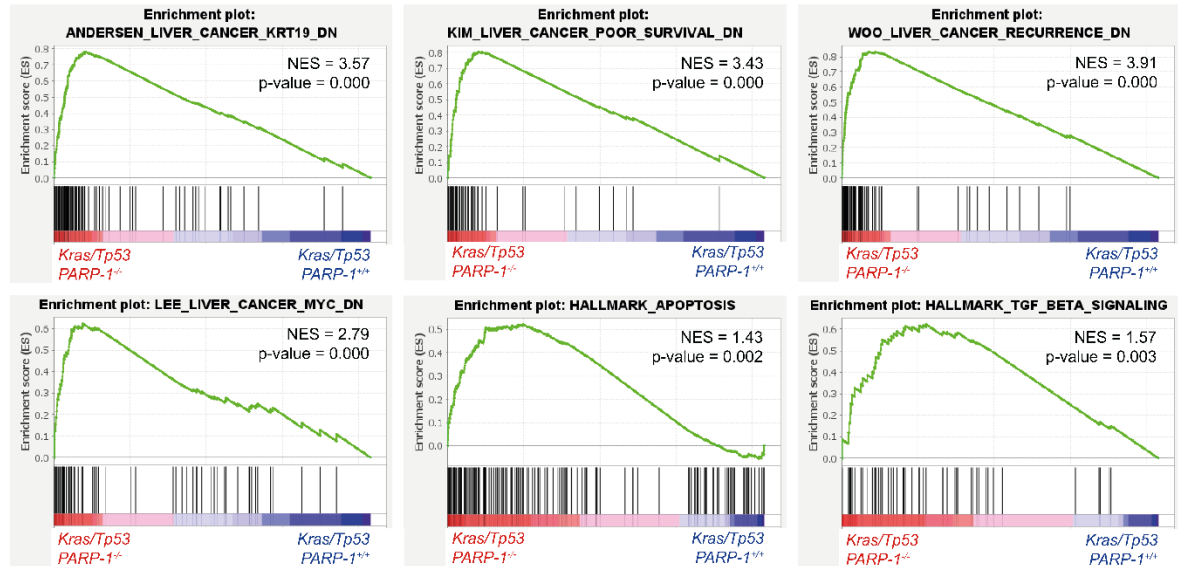
Figure 4.42: Canonical pathways and toxicity analyses upon HDTV with *Kras/Tp53* in *Parp-1*^{-/-} versus *Parp-1*^{+/+} mice.

a) Canonical pathways significantly regulated in tumors induced with *Kras/Tp53* in *Parp-1*^{-/-} vs. *Parp-1*^{+/+} mice identified by IPA. The dashed line indicates the significance threshold of $-\log(p\text{-value}) > 1.3$. Shown are z-scores of respective canonical pathways (positive z-score = red/activated, negative z-score = blue/inhibited). b) Clinical pathology endpoints and networks significantly regulated in tumors induced with *Kras/Tp53* in *Parp-1*^{-/-} vs. *Parp-1*^{+/+} mice. The dashed line indicates the significance threshold of $-\log(p\text{-value}) < 1.3$.

Gene set enrichment analysis further confirmed IPA results (Figure 4.43). We uploaded raw count files of *Parp-1* deficient versus *Parp-1* proficient mice injected with *Kras/Tp53*. Only gene sets with nominal p-value < 0.05 and FDR < 0.25 were selected. *Parp-1* deficient mice injected with *Kras/Tp53* showed enrichment in gene sets associated with the downregulation of CK19, reduced poor survival, and recurrence. Further, GSEA confirmed enrichment in apoptosis and TGFβ signaling. In addition, inactivation of MYC signaling was found. In contrast, *Parp-1* proficient mice injected with *Kras/Tp53* showed enrichment of gene sets associated with CK19 positive cholangiocarcinoma and a CCA class2 cluster, associated with poor prognosis. In addition, MYC signaling and activation of MYC targets

were found. Interestingly, several DNA repair pathways were significantly enriched in *Parp-1*^{+/-} mice injected with *Kras*/*Tp53*. Besides DNA single-strand break repair mechanisms (BER), also double-strand break repair pathways (NHEJ, HR) were enriched suggesting that *Parp-1* proficiency is important for DNA damage response and repair mechanisms in *KRAS*-driven tumorigenesis.

a) Gene sets enriched in *Kras*/*Tp53* *Parp-1*^{-/-} mice



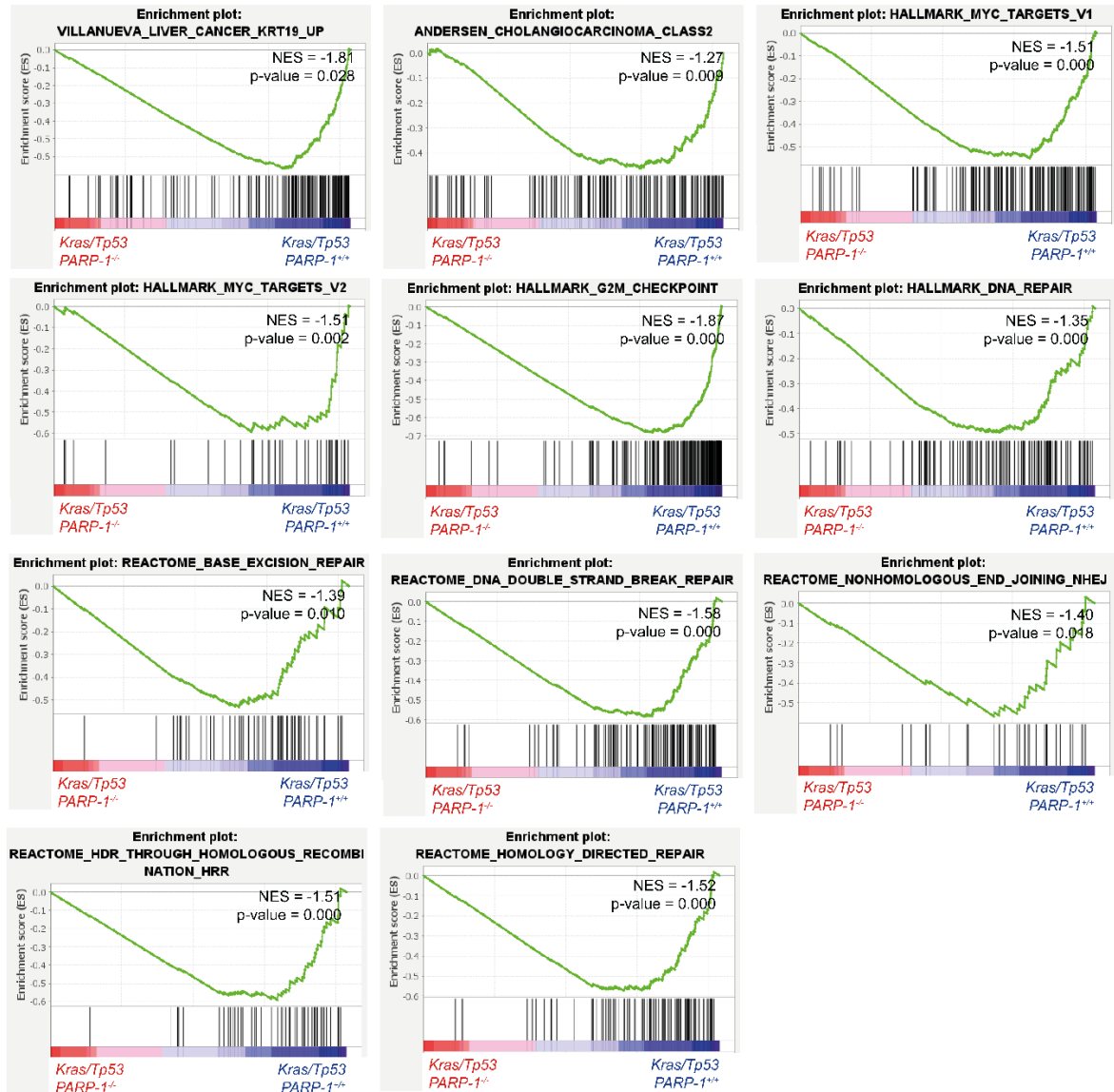
b) Gene sets enriched in *Kras/Tp53* *Parp-1*^{+/-} mice

Figure 4.43: Enriched gene sets in *Parp-1*^{-/-} mice injected with *Kras/Tp53* versus *Parp-1*^{+/+} mice.

Gene set enrichment analysis (GSEA) of a) *Parp-1*^{-/-} mice injected with *Kras/Tp53* vs. b) *Parp-1*^{+/+} mice. The selection of gene sets was based on statistical significance calculated by nominal p-value < 0.05 and FDR < 0.25. NES indicates the degree of overexpression for each group at the peak of the entire gene set.

Finally, we analyzed transcriptomic profiles of *Parp-1* deficient and proficient mice injected with *Akt/Nicd*. By performing Wald test of log-transformed data of *Akt/Nicd*-injected *Parp-1*^{+/+} and *Parp-1*^{-/-} mice, we identified a total of 158 (95 down, 63 up) differentially expressed genes ($p < 0.05$). Notably, the number of differentially expressed genes in *Kras/Tp53* injected mice (*Parp-1*^{-/-} versus *Parp-1*^{+/+}) was around 49 times higher. Unsupervised hierarchical cluster analyses based on these significantly differentially expressed genes revealed that the two experimental groups formed clusters according to their genotype. These findings were confirmed by the corresponding PCA plot (Figure 4.44). These findings are in concordance with the similar tumor growth and histopathological features of *Akt/Nicd*-induced cholangiocarcinogenesis independent of the *Parp-1* genotype.

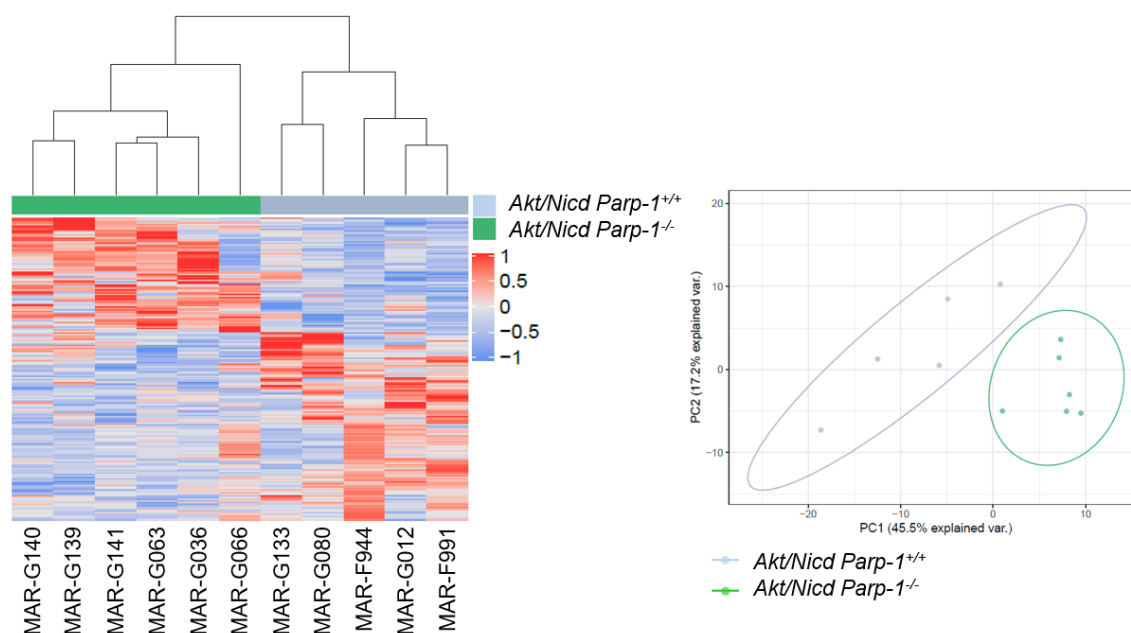


Figure 4.44: Differential expressed genes after HDTV with *Akt/Nicd* in *Parp-1^{-/-}* versus *Parp-1^{+/+}* mice.

Unsupervised cluster and PCA plot of significant genes ($p < 0.05$) after HDTV with *Akt/Nicd* in *Parp-1^{-/-}* vs. *Parp-1^{+/+}* mice.

We analyzed the network and pathway regulation of mice injected with *Akt/Nicd* (*Parp-1^{-/-}* versus *Parp-1^{+/+}*). Expression analysis was performed with a cut-off p-value < 0.05 , resulting in a total number of 158 genes of which 63 were up and 95 were downregulated. Canonical pathway analyses resulted in oxidative stress (HIF1 α signaling), Apoptosis signaling, EMT, and immune response (Interferon signaling). IPA toxicity analyses confirmed regulation of pro- and anti-apoptotic mechanisms, besides TGF β signaling (Figure 4.45). Overall IPA analyses confirmed that pathway activation and regulation in *Akt/Nicd* induced tumors in *Parp-1^{-/-}* versus *Parp-1^{+/+}* did not significantly differ.

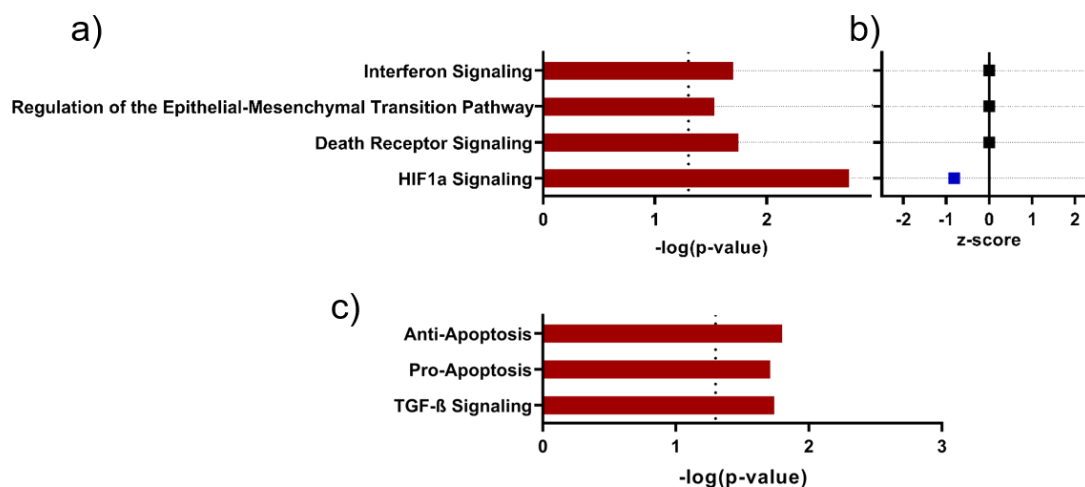


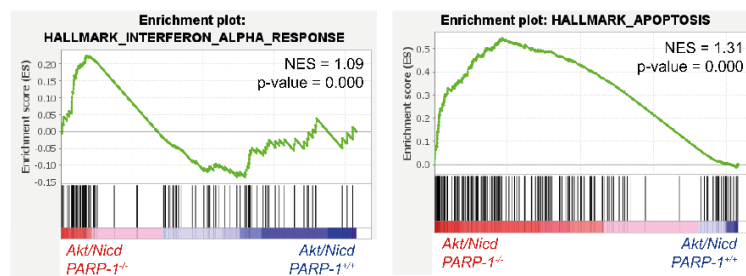
Figure 4.45: Canonical pathways and toxicity analyses upon HDTV with *Akt/Nicd* in *Parp-1^{-/-}* versus *Parp-1^{+/+}* mice.

Canonical pathways significantly regulated in tumors induced with *Akt/Nicd* in *Parp-1^{-/-}* vs. *Parp-1^{+/+}* mice identified by IPA. The dashed line indicates the significance threshold of $-\log(p\text{-value}) > 1.3$. b)

Shown are z-scores of respective canonical pathways (positive z-score = red/activated, negative z-score = blue/inhibited). c) Clinical pathology endpoints and networks significantly regulated in tumors induced with *Akt/Nicd* in *Parp-1^{-/-}* vs. *Parp-1^{+/+}* mice identified by IPA Toxicity analyses. The dashed line indicates the significance threshold of $-\log(p\text{-value} > 1.3)$.

Gene set enrichment analysis further confirmed the IPA results (Figure 4.46). We uploaded raw count files of *Parp-1^{-/-}* versus *Parp-1^{+/+}* mice injected with *Akt/Nicd*. Only gene sets with nominal p-value < 0.05 and FDR < 0.25 were selected. *Parp-1* deficient mice injected with *Akt/Nicd* showed enrichment in gene sets associated with apoptosis and immune response. In contrast, *Parp-1^{+/+}* mice injected with *Akt/Nicd* showed enrichment of gene sets associated with CK19 positive cholangiocarcinoma. In addition, activation of myc targets was found. In general, due to the limited number of differentially expressed genes, the number of enriched gene sets was limited and did not show specific associations. However, several DNA repair pathways of double-strand break repair (NHEJ, Homologous recombination) were significantly enriched in *Parp-1* proficient mice injected with *Akt/Nicd*. This indicates that *Parp-1* is essential for DNA damage control, thus this does not impact cholangiocarcinogenesis in *Akt/Nicd* experimental group, in contrast to the *Kras/Tp53* experimental group.

a) Gene sets enriched in *Akt/Nicd Parp-1^{-/-}* mice



b) Gene sets enriched in *Akt/Nicd Parp-1^{+/+}* mice

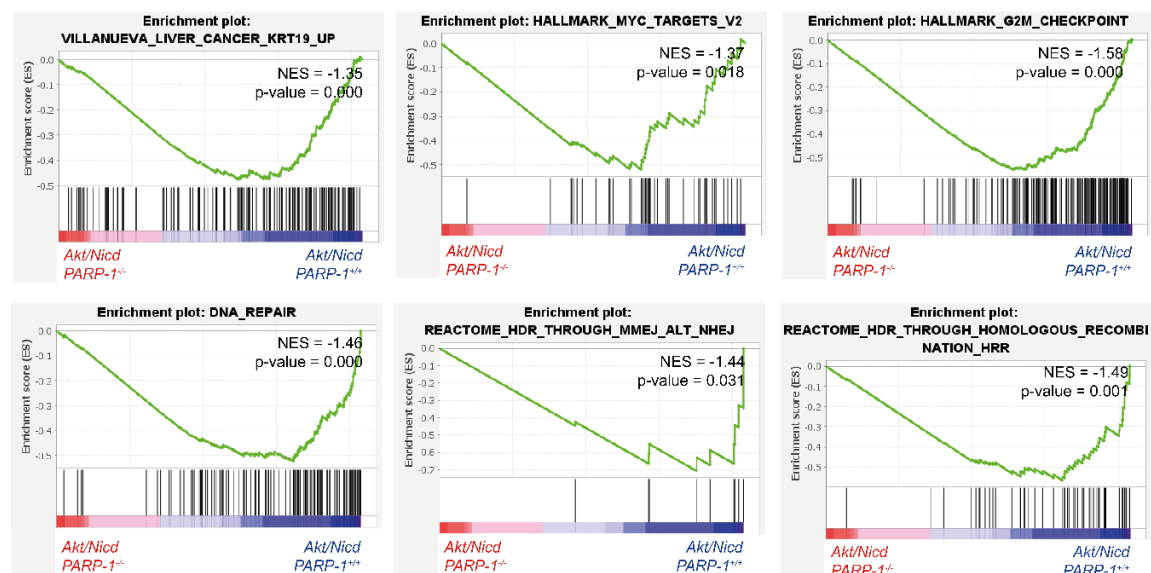


Figure 4.46: Enriched gene sets in *Parp-1^{-/-}* mice injected with *Akt/Nicd* versus *Parp-1^{+/+}* mice. Gene set enrichment analysis (GSEA) of a) *Parp-1^{-/-}* mice injected with *Akt/Nicd* vs. b) *Parp-1^{+/+}* mice. The selection of gene sets was based on statistical significance calculated by nominal p-value < 0.05 and FDR < 0.25. NES indicates the degree of overexpression for each group at the peak of the entire gene set.

IPA and GSEA analyses revealed differential activation of DNA damage response pathways in *Parp-1* proficient and deficient mice upon tumor induction with *Kras/Tp53*. To further dissect the activity of these DNA damage response pathways, we investigated the expression of 82 DNA damage response genes. When analyzing tissue of *Kras/Tp53*-induced tumors in *Parp-1* deficient mice compared to EV control, we found upregulation of genes associated with HR (*Bcr1*, *Chek1*, *Rad51*, *Rad51c*, *Rad54l*) (Figure 4.47 a). In contrast, tumor tissue of *Parp-1* proficient mice compared to EV control showed upregulation of HR associated genes (*Chek2*, *Rad51*, *Rad54l*, *Rad51b*, *Chek1*, *Exo1*, *Bard1*, *Rad21*) and expression of genes associated with alt-NHEJ (*Lig1*, *Mre11a*, *Polq*, *Rbbp8*, *Fen1*, *Parp-1*) (Figure 4.47 b). When comparing gene expression in *Parp-1* deficient mice with *Parp-1* proficient mice upon injection of *Kras/Tp53* we found downregulation of genes associated with HR (*Exo1*, *Rad21*, *Rad54l*, *Rad51*, *Chek1*, *Chek2*, *Xrcc3*, *Rad51b*, *Bard1*) and alt-NHEJ (*Rbbp8*, *Mre11a*, *Polq*, *Parp-1*) (Figure 4.47 c). These findings suggest that in *Kras/Tp53*-driven tumor tissue under *Parp-1* deficiency homologous recombination is predominantly activated, whereas alt-NHEJ is inactive.

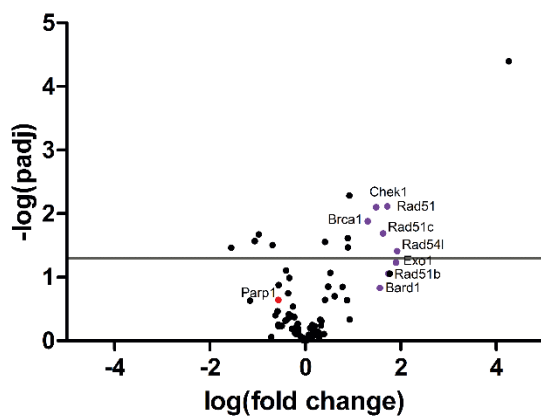
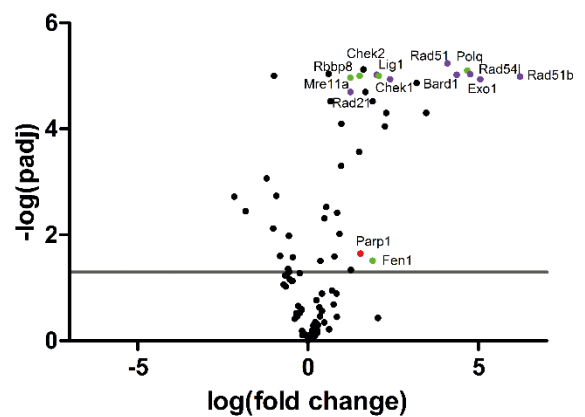
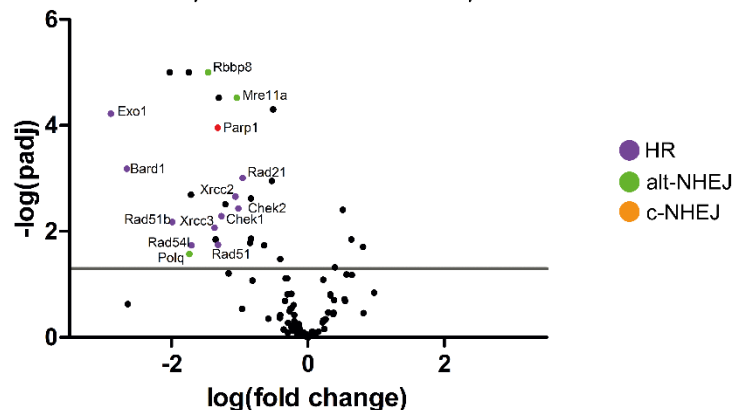
a) *PARP-1*^{-/-} *Kras/Tp53* vs. EVb) *PARP-1*^{+/+} *Kras/Tp53* vs. EVc) *PARP-1*^{-/-} *Kras/Tp53* vs. *PARP-1*^{+/+} *Kras/Tp53*

Figure 4.47: Expression of DNA damage response genes in *Parp-1*^{-/-} and *Parp-1*^{+/+} mice upon *Kras/Tp53* injection.

Vulcano plots are depicted with the $\log(\text{fold change})$ of each gene and the $-\log(\text{p-adjusted})$ was calculated by performing Wald test. Selected genes associated with HR, c-NHEJ, and alt-NHEJ are colored and gene names are displayed.

To exclude sporadic or unspecific effects of HDTV, we analyzed transcriptomic profiles of *Parp-1^{+/+}* and *Parp-1^{-/-}* mice injected with empty vector control. By performing Wald test with log-transformed data of EV-injected *Parp-1^{+/+}* and *Parp-1^{-/-}* mice, we identified a total of 161 (67 down, 94 up) differentially expressed genes ($p < 0.05$). Unsupervised hierarchical cluster analyses based on these significantly differentially expressed genes revealed that the two experimental groups form clusters according to their genotype. These findings were confirmed by the corresponding PCA plot (Figure 4.48).

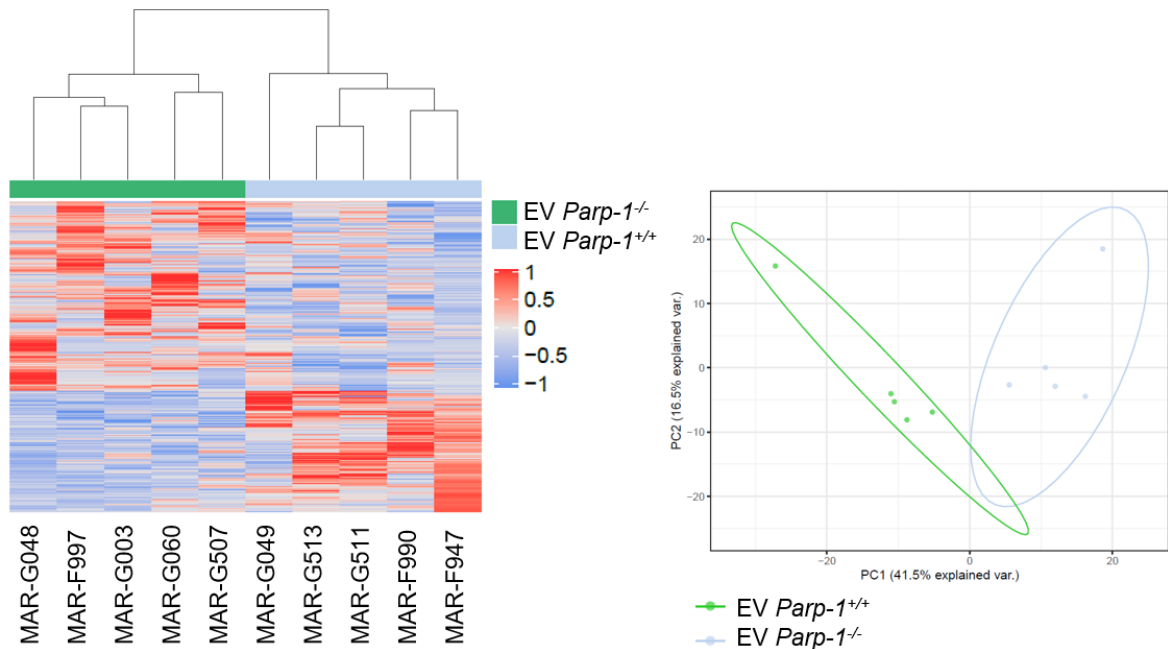


Figure 4.48: Differential expressed genes after HDTV with EV in *Parp-1^{-/-}* versus *Parp-1^{+/+}* mice. Unsupervised cluster and PCA plot of significant genes ($p < 0.05$) after HDTV with EV in *Parp-1^{-/-}* vs. *Parp-1^{+/+}* mice.

4.9 Integrative prognostic analysis of *PARP-1* depletion *in vitro* and *in vivo*

In the here presented study, we investigated the impact of *PARP-1* expression in three different models: i) in human iCCA tissue samples, ii) in iCCA cell lines, iii) in an HDTV-driven mouse model. These models were based on different underlying *KRAS* and *PARP-1* genotypes and interventions, investigating different stages in tumor development. To compare and integrate the findings of our transcriptomic analyses, we summarized the key findings from IPA and GSEA analyses, as well as expression data of DDR-associated genes. Table 4.7 compares the impact of *PARP-1* knockout or deficiency in *KRAS*-mutant iCCA tissue, iCCA cell lines, or HDTV-induced tumor tissue in comparison to control conditions (*PARP-1^{wt}* or *Parp-1^{+/+}*). In *KRAS*-mutant iCCA tissue samples we found upregulation of *PARP-1* expression (Figure 4.47) and overall activity of DDR pathways (BER, c-NHEJ, alt-NHEJ, HR). Cell cycle control checkpoints G2/M and G1/S were found inhibited. Further, activation of apoptotic, oxidative, and inflammatory processes was observed (Table 4.7). Oncogenic hallmark pathways such as ERK/MAPK, PI3K/AKT, and Notch were found upregulated. Comparison of CRISPR/Cas9-mediated KO of *PARP-1* with respective control clones revealed upregulation of single-strand break repair and active G2/M DNA damage checkpoint control in control conditions, whereas ATM signaling and DNA double-strand break repair pathways (c-NHEJ, alt-NHEJ, HR) were predicted with downregulation. Apoptosis signaling was active independent of *PARP-1* KO, whereas inhibition of oxidative and inflammatory processes was observed (Table 4.7). In the *Kras/Tp53*-induced mouse model DDR pathways, such as alt-NHEJ and HR were found upregulated in *Parp-1* proficient conditions but downregulated upon *Parp-1* deficiency. Also, cell cycle checkpoints G2/M and G1/S showed differential activity dependent on the *Parp-1* genotype. Further, we found inhibition of oxidative and inflammatory processes, besides oncogenic hallmark pathways such as ERK/MAPK, PI3K/AKT, and Notch. Interestingly, PTEN activation was predicted in *Parp-1* deficient animals (Table 4.7). Taken together, the compared *in vitro* and *in vivo* data suggest that DDR response is dysregulated upon *PARP-1* depletion in *KRAS*-mutant iCCA, accompanied by downregulation of inflammatory signaling. To elucidate the exact role of *PARP-1* in tumor initiation and progression of *KRAS*-mutant iCCA further functional investigations are needed. However, the observed sensitivity of *KRAS*-mutant iCCA cell lines and the reduced tumor burden in *Parp-1* deficient mice might indicate a synthetic vulnerability and potential therapeutic implications of PARPi in *KRAS*-mutant iCCA.

Table 4.7: Overview of transcriptomic analyses.

The table combines transcriptomic analyses from IPA, GSEA, and differentially expresses DDR-associated genes of *KRAS*-mutant human iCCA tissue, *KRAS*-mutant iCCA cell lines, and *Kras/Tp53*-induced murin tumor tissue upon *PARP-1* depletion. Significant data (p -value > 0.05) are visualized in red, blue, and grey dependent on z-score.

	<i>PARP-1^{wt} / Parp-1^{+/+}</i>			<i>PARP-1 KO / Parp-1^{-/-}</i>		
	<i>KRAS^{mut}</i>	<i>KRAS^{mut}</i>	<i>Kras/Tp53</i>	<i>KRAS^{mut}</i>	<i>Kras/Tp53</i>	
	iCCA tissue	iCCA cell lines	mice	iCCA cell lines	mice	
ATM						ns
BRCA						z-score > 0 / enrichment
G2/M						z-score < 0
G1/S						z-score = 0
BER						
NHEJ						
c-NHEJ						
alt-NHEJ						
HR						
HIF α						
Apoptosis						
TGF β						
NF- κ B						
ERK/MAPK						
PI3K/AKT						
Notch						
PTEN						

To evaluate a potential prognostic impact of our molecular profiles, we integrated our *in vitro* and *in vivo* transcriptomic data with different established prognostic subgroups of PLC (poor and good prognosis) [58]. Both dysregulated *PARP-1* expression and oncogenic *KRAS* signaling have already been associated with poor OS, early recurrence, and decreased PFS in several cancer entities including iCCA [60, 149]. Consistently, *KRAS*-mutant CRISPR/Cas9-mediated *PARP-1* knockout clones grouped with good prognosis CCA patients, whereas *KRAS*-mutant control clones recapitulated transcriptomic features of good prognosis CCA patients (Figure 4.49). Similarly, integration of *in vivo* data showed that *Parp-1* deficient mice with *Kras/Tp53* injection clustered with a good prognosis, while *Parp-1* proficient mice grouped with poor prognosis (Figure 4.50 a). Analysis of mice injected with *Akt/Nicd* revealed no distinct clustering dependent on the *Parp-1* genotype (Figure 4.50 b). Overall, these results demonstrate *PARP-1* depletion leads to a shift of iCCA samples from poor to good prognosis predominantly in presence of activating *KRAS* mutation.

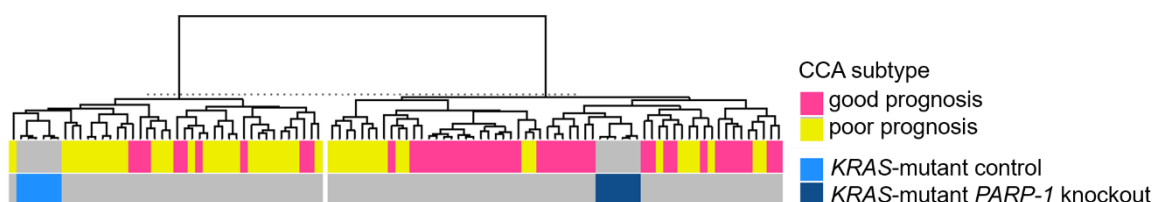


Figure 4.49: Integration of *in vitro* transcriptomic data with prognostic subgroups of CCA patients.

The graph shows the integration of *KRAS*-mutant *PARP-1* KO clones (dark blue) and respective control clones (light blue) with a previously published dataset of 45 CCA patients with good (pink) and poor (yellow) prognosis.

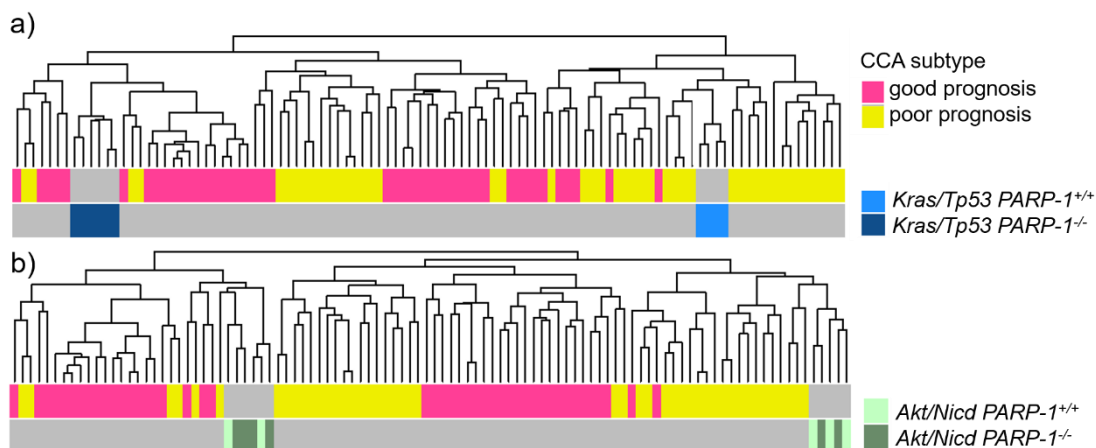


Figure 4.50: Integration of *in vivo* transcriptomic data with prognostic subgroups of CCA patients.

a) The graph shows the integration of *Parp-1*^{-/-} mice (dark blue) and *Parp-1*^{+/+} mice (light blue) with *Kras/Tp53*-induced carcinogenesis with a previously published dataset of 45 CCA patients with good (pink) and poor (yellow) prognosis. b) Graph shows integration of *Parp-1*^{-/-} mice (dark green) and *Parp-1*^{+/+} mice (light green) with *Akt/Nicd*-induced carcinogenesis with a previously published dataset of 45 CCA patients with good (pink) and poor (yellow) prognosis.

5. Discussion

The development of primary liver cancer is a multifactorial process characterized by the sequential acquisition of genetic and epigenetic alterations [14]. Despite progress in understanding the sequential evolution and targeted therapy in HCC, the underlying mechanisms and therapeutic development of iCCA are less well explored [102, 224]. However, growing evidence confirms that initiation of cholangiocarcinogenesis is a multistep process that arises on a background of chronic liver inflammation and alterations in several cellular pathways, including DNA damage response [58]. Moreover, constant remodeling of diseased liver generates a stromal and immunosuppressive environment promoting malignant transformation [217]. In iCCA, a prominent cellular pathway with somatic mutation is RAS/RAF/MAPK signaling pathway. iCCA patients that carry activating *KRAS* mutations are associated with poor OS and chemoresistance. Here, altered *KRAS* signaling enhances uncontrolled proliferation of cancer cells, reciprocal promoting DNA damage and increasing mutational burden [13, 58, 60]. Several studies in different cancer entities determined an important role of PARP-1, a protein associated with several pathways of DDR with implications in therapeutic administration. Recent findings indicate that the expression of *PARP-1* is preferentially enhanced in *KRAS*-mutant tumors [166, 201, 203]. Moreover, for both *PARP-1* and *KRAS*, genetically modified mouse models provide evidence that activation or loss-of-function have an impact on carcinogenesis [63, 64, 158, 166]. However, the exact role of *PARP-1* in *KRAS*-driven cholangiocarcinogenesis is poorly understood.

In the presented study, we aimed to investigate the abundance and association of *PARP-1* expression and *KRAS* mutation in intrahepatic cholangiocarcinoma. The potential interaction was explored using PARP-1 inhibition and depletion via Olaparib treatment, RNA interference, and CRISPR/Cas9. Further, we investigated functional alterations and examined molecular pathways impaired by PARP-1-based interventions. PARP-1 inhibition in *KRAS*-mutant tumor cells was administered to assess the impact on tumor progression *in vitro* and to investigate putative therapeutic implications. To investigate the role of PARP-1 in tumor initiation *in vivo*, we induced *KRAS*-driven tumor growth in a *Parp-1*-deficient mouse model using HDTV and characterized pathohistological alterations within the tissue samples. We also determined underlying molecular pathways using transcriptomic analyses. Finally, we aimed to translate our findings to human CCA patients in order to determine prognostic features of *PARP-1* expression in *KRAS*-mutant iCCA.

5.1 *PARP-1* expression is abundant in *KRAS*-mutant iCCA and correlates with poor prognosis

Mutational pathogenesis of cholangiocarcinoma is diverse and dependent on anatomical location as well as risk factors such as liver fluke infection or inflammatory background [11, 20]. Although more frequent in eCCA, alterations in oncogenic *KRAS* signaling are among the most abundant genetic alterations in intrahepatic cholangiocarcinoma observed in around 12-16% of the cases [14, 127]. The presence of *KRAS* alterations is associated with early recurrence, poor therapeutic response, and reduced OS [57, 225]. *KRAS* mutations, predominantly present in codon 12, have been detected early during disease progression and therefore likely to contribute to the malignant transformation of cholangiocytes [127]. The most frequent mutations *KRAS*^{G12D} and *KRAS*^{G12V} result in an amino acid substitution leading to a disturbed GTP hydrolysis and subsequently causing constitutive activation of the protein [226]. The frequency of *KRAS* mutation in the cohorts used in this study is a bit

lower than the rates previously reported (10.29%, $SD \pm 4,16$) (Table 4.2) [57-59, 225, 227]. Consistently with literature findings, *KRAS* mutations were most frequent in exon 2, codon 12 (G12D, G12C, and G12V) in our cohort [127]. Two samples revealed less common mutation in exon 3, codon 61 (Q61H) [228]. The assessment of clinicopathological data of the Mainz iCCA patient cohort revealed representative distribution of gender, a median age of 65 years at the day of surgery and mostly well to moderately differentiated tumors with an average size of 7 cm (Table 4.1) [13, 229]. The transcriptomic analyses of the iCCA cohort resected in Mainz confirmed that *KRAS*-mutant iCCA show a distinct gene expression profile in comparison to *KRAS*-wildtype iCCA and the matched normal surrounding liver tissue (Figure 4.1, Figure 4.5). Notably, *KRAS*-mutant iCCA recapitulated hallmark features of cancer and displayed activation of Notch, PI3K/AKT, ERK/MAPK signaling pathways as well as inhibition of p53 signaling (Figure 4.2 a) [168]. Inflammatory pathways such as TGF β and NF- κ B signaling as well as apoptotic processes showed activation, supported by the association to clinical endpoints linked to increased liver steatosis, fibrosis, and hepatitis (Figure 4.2 a,b) [13, 127]. Moreover, *KRAS*-mutant iCCA were enriched for gene sets centering around DNA damage response pathways (Figure 4.3). These pathways were representing both single-strand break repair (BER) and double-strand repair mechanisms (NHEJ, HR). When analysing the expression of selected DDR genes, we found activation of HR-associated and NHEJ-associated genes in both *KRAS*-mutant and -wildtype iCCA tissue samples (Figure 4.4). Expression of characteristic genes associated with both NHEJ pathways (canonical-NHEJ and alternative-NHEJ) were found enhanced. Taken together, these findings suggest activity of all DDR pathways in *KRAS*-mutant iCCA.

Alterations in *KRAS* signaling and changes in DNA damage checkpoint activation and repair mechanisms have been associated with malignant transformation in different tumor entities. Oncogenic *KRAS* leads to activation of ATR and modulation of Chk1 function, influencing genomic stability [230, 231]. A genome-wide RNAi screen revealed synthetic lethality of mutant *KRAS* and several factors of BER [232]. Hähnle *et al.* demonstrated that expression of *PARP-1* in *KRAS*-mutant AML cells was up-regulated and that inhibition of alt-NHEJ preferentially sensitized *KRAS*-mutant AML cells. Further, they found that mutant *KRAS* activates alt-NHEJ factors such as *LIG3*, *XRCC1*, and *PARP-1* [203]. In our iCCA tissue samples we found upregulation of alt-NHEJ specific factors such as *XRCC1*, *FEN1*, and *POLQ*. Additionally, specific genes associated with c-NHEJ were found upregulated such as *DCLRE1C* and *XRCC4*. However, only under *KRAS*-mutant conditions expression of *PARP-1*, an important factor for alt-NHEJ initiation was upregulated (Figure 4.4) [233]. These findings indicate that oncogenic *KRAS* contributes to the malignant transformation of the cells, by alteration of the repair mechanisms of double-strand breaks towards alt-NHEJ, which is known to be more error-prone [203]. Further, a *N*-nitroso-induced colorectal cancer (CRC) model, displaying several features of *KRAS*-mutant CRCs, revealed a significant role of *PARP-1* in tumor progression with impact on DNA damage response and inflammation [166, 234]. Together, these findings display the diverse and multifaceted cellular functions of *PARP-1*. In general, the *PARP* family gained emerging attention in the field of cancer research as several associated pathways and processes (DNA repair, genomic stability, chromatin modification, energy metabolism, apoptosis) are known to have implications in carcinogenesis [149]. Elevated *PARP-1* expression on mRNA and protein level was observed in several tumor entities, such as gastric cancer, pancreatic cancer colon carcinoma, endometrial adenocarcinoma, ovarian cancer, breast cancer, soft tissue sarcoma, and small cell lung cancer [164, 165, 235-237]. High *PARP-1* protein expression was further associated with poor prognosis, shorter OS, and proposed as a prognostic

factor for decreased PFS [238-240]. Until now, very limited information regarding PARP-1 expression in primary liver cancer, particularly for intrahepatic cholangiocarcinoma is available. Shimizu *et al.* found enhanced protein expression of PARP-1 in HCC biopsies of patients with cirrhosis and less differentiated tumors [241, 242]. In contrast, a southern Chinese population showed high *PARP-1* expression with association to higher HCC tumor stage, but no correlation to reduced OS and PFS [243]. However, survival analysis of 130 TCGA-patient data with primary liver cancer, both HCC and iCCA, demonstrated that high *PARP-1* expression is unfavorable and has prognostic impact [244].

Given the abundance of *KRAS* mutations in intrahepatic cholangiocarcinoma and the observed association with DNA pathways including PARP-1 in other cancer entities [166, 203], we investigated the expression of *PARP-1* in *KRAS*-mutant iCCA microarray data and in public available TCGA cohort using GEPIA2 [211]. Analysis of microarray data of 68 surgically resected iCCA tissue samples, including 9 samples with activating *KRAS* mutations, showed an upregulation of *PARP-1* expression in *KRAS*-mutant iCCA in comparison to normal intrahepatic bile duct tissue (Figure 4.6). Further, investigation of TCGA and GTEx cohort via GEPIA2 confirmed significantly higher expression of *KRAS* and *PARP-1* in cholangiocarcinoma (CHOL) tumor samples in comparison to normal tissue samples. Of note, analysis of TCGA cohort of hepatocellular carcinoma (LIHC) also showed higher expression of *PARP-1*, whereas *KRAS* expression was similar in tumor with normal liver tissue confirming that *KRAS* is predominantly affected during cholangiocarcinogenesis (Figure 4.7). Moreover, correlation analysis of *KRAS* and *PARP-1* expression in CHOL confirmed a positive association between the two factors with $r=0.6$. Correlation of *PARP-1* and *KRAS* expression data in LIHC was less pronounced ($r=0.35$) (Figure 4.7). These findings are in concordance with several studies characterizing *KRAS* as a driving mutation in iCCA, whereas constitutes an extremely rare mutational event in HCC [14, 245]. A recent study of Xue *et al.* analyzed genomic and transcriptomic profiles of HCC, CCA, and mixed cHCC-ICC (combined hepatocellular and intrahepatic cholangiocarcinoma), revealing *KRAS* mutations occurring more frequently in iCCA than in HCC. Based on transcriptomic profiles a cluster enriched with iCCA cases was determined. This cluster was further associated with high *KRAS* expression, high level of proliferation, frequent alterations in pathways associated with histone modification, and overall poor prognosis [246].

Next, we integrated a DNA damage response gene set with primary CCA samples and found the accurate separation of benign samples from CCA tumor samples. High number of DDR genes were found to be differentially modulated in the CCA tumor samples (Figure 4.8 a). Importantly, direct comparison of *KRAS*-mutant and *KRAS*-wildtype tissue samples revealed that among the unique genes significantly altered in *KRAS*-mutant cancer tissue was *PARP-1* activation (Figure 4.8 b). Next, we analyzed our patient-derived primary iCCA and established iCCA cell lines, including ones with and without *KRAS* mutation in codon 12 [77]. Consistently, we found an upregulation of *PARP-1* expression by qPCR and Western Blot analyses. These analyses demonstrated a higher *PARP-1* expression in the *KRAS*-mutant iCCA cell lines compared to non-mutant iCCA cancer cells (Figure 4.9).

Taken together, these results confirmed the expected mutational frequency of *KRAS* in our iCCA cohorts and showed an association between *PARP-1* upregulation in *KRAS*-mutant iCCA. Further, the findings suggest a potential functional interaction of these two pro-tumorigenic features.

5.2 *KRAS*-mutant iCCAs show preferential sensitivity towards PARP-1 inhibition *in vitro*

PARP-1 inhibitors are already being used in the clinic to treat *BRCA1/2*-mutant breast and ovarian cancer patients utilizing the PARP-1-dependency in an HR-deficient background [190]. Besides this confirmed synthetic lethality, additionally functions of PARP-1 beyond DNA repair, such as cellular differentiation, gene transcription, inflammation, cell death, and metabolism, might contribute to the antitumor properties of PARP inhibitors [167]. Since our findings pointed towards a predominant role of PARP-1 in *KRAS*-driven iCCA, we next applied Olaparib, an effective PARP-1/2 inhibitor. First, IC₅₀ values of Olaparib were determined using WST-1 assay (Figure 4.10). As expected, *KRAS*-mutant cell lines showed a higher sensitivity after Olaparib treatment, supporting the previous findings, that, indeed, survival and malignancy of iCCAs with activating *KRAS* mutations might be partly dependent on a functioning DNA damage response as well as PARP-1 activity. IC₅₀ values ranged between 387.2-694.9 μ M for *KRAS*-mutant iCCA cell lines and between 805.3-1175.0 μ M for *KRAS*-wildtype iCCA cell lines. Of note, these IC₅₀ values are considerably higher in comparison to IC₅₀ values reported in the literature (ranging 6-100 nM) [218]. These differences could be explained by cell line-specific, tumor entity-specific differences, or experimental settings. The oral prescription of Olaparib is 400 mg twice a day, resulting in a clinically relevant plasma concentration of 10 μ g/ml [23, 247]. Mao *et al.* found inhibitory concentrations of Olaparib in *KRAS*-wildtype CCA cell lines close to 10 μ M [248]. However, a comprehensive meta-analysis of Ku *et al.* confirmed a reduced proliferation upon PARP inhibition (PARPi) in *KRAS*-mutant cells compared to *KRAS*-wildtype. The researchers provide evidence that *KRAS*-mutant cells are highly dependent on DNA damage response pathways confirming a synthetic lethality in *KRAS*-mutant cancers and overall supporting our hypothesis for *KRAS*-driven iCCA [201].

Consistently, we examined whether PARPi impairs clonogenic growth by employing colony and spheroid formation assays. A significant reduction in the number of colonies and spheres was observed preferentially in *KRAS*-mutant iCCA cell lines upon PARPi (Figure 4.11). PARPi is commonly applied as maintenance therapy in ovarian, breast, prostate, and pancreas cancer. In *BRCA1/2*-mutant cancers, monotherapeutic approaches are commonly used, whereas in unselected patients combined treatment strategies are applied or under clinical investigation [249]. This treatment strategy is in line with our findings that Olaparib sensitizes *KRAS*-mutant iCCA cell lines but is not completely detrimental as monotherapy. Several lines of evidence showed that combined inhibition of PARP-1 with other DNA damaging agents, chemotherapeutics, irradiation, or inhibitors of cell cycle show synergistic effects in *KRAS*-mutant tumors of other entities. In our study, combined treatment of PARPi and DNA damaging agent Doxorubicin led to a decrease in cell viability in iCCA cell lines, with a more pronounced effect in *KRAS*-mutant iCCA cell lines (Figure 4.12). Hähnel *et al.* demonstrated that PARPi in combination with daunorubicin treatment sensitized *KRAS*-mutant AML cells to enhanced cell death [203]. In *KRAS*-mutant NSCLC cancer cells combined treatment with PARPi and cell cycle checkpoint kinase WEE1 resulted in increased cytotoxicity and enhanced radiosensitivity [250]. Data regarding PARPi in *KRAS*-mutant PLC is limited. Independent of *KRAS* mutation, few studies proposed PARPi as a promising therapeutic option in HCC. PARPi suppressed HepG2 cell growth and reduced tumor growth *in vivo*, alone or in combination with cisplatin [251-253]. Further, a recent study found decreased clonogenic survival upon PARPi in combination with irradiation in *KRAS*-wildtype iCCA cell lines, suggesting that PARPi enhanced radiosensitivity also independent of *KRAS* mutational status [248].

Since Olaparib is a PARP-1/2 inhibitor, we next specifically depleted *PARP-1* expression via siRNA-mediated knockdown. siRNA-mediated knockdown effectively decreased PARP-1 protein levels without affecting PARP-2 expression (Figure 4.13). Subsequent functional analyses of colony and sphere formation capacity recapitulated preferential sensitivity of *KRAS*-mutant iCCA cell lines after *PARP-1* depletion. Interestingly, the reduction of colony and sphere formation capacity was less pronounced than after PARPi via Olaparib (Figure 4.14). This observation might be explained by the mechanism of PARPi, which is mediated by the trapping of PARP-1-DNA-complexes and the subsequent blockage of the replication fork process and enhanced levels of DNA damage [254]. Hence, PARP-1 itself is required for PARPi-mediated toxicity [188]. Parseles and colleagues showed similar effects in *KRAS*-mutant NSCLC cells. The effect of *PARP-1* depletion on radiosensitization was decreased in comparison to PARPi [250].

To further analyze transcriptomic changes upon *PARP-1* depletion, we established stable *PARP-1* knockout clones using the CRISPR/Cas9 technique and performed RNA sequencing. Successful knockout was confirmed by western blot analysis and Sanger sequencing (Figure 4.15, Table 4.1). As described in several *Parp-1* deficient mouse models and derived cell lines, single knockout of *PARP-1* does not impair survival of transfected cell lines, displayed in unchanged phenotype and cell line-specific morphology (Figure 4.15) [158]. Comparable to siRNA-mediated knockdown, PARP-2 expression remained unaffected upon *PARP-1* knockout (Figure 4.15). To further exclude that *PARP-2* compensated *PARP-1* knockout, we treated *PARP-1* KO clones with Olaparib. *PARP-1* KO clones showed a slight decrease in cell viability in comparison to control clones (Figure 4.17). Concomitantly, the capacity of colony and sphere formation was decreased in *KRAS*-mutant *PARP-1* KO clones compared to control clones as well as to *KRAS*-wildtype *PARP-1* KO clones (Figure 4.18). However, compared to the transient siRNA-mediated *PARP-1* knockdown, under stable *PARP-1* KO conditions, even *KRAS*-wildtype cells showed a reduced rate of colony and sphere formation. These findings indicate that stable *PARP-1* absence affects all cells independently of the *KRAS* mutation status. Further, combinational treatment of *PARP-1* KO and Doxorubicin showed mildly reduced cell viability, though inconsistently amongst *KRAS*-mutant and *KRAS*-wildtype iCCA cell lines (Figure 4.19). These unexpected findings might be explained by other compensatory mechanisms overcoming *PARP-1* KO, which remain elusive. To address this discrepancy, it is essential to perform experiments with modified drug concentrations or the use of other drugs. Interestingly, Zhong *et al.* showed that combined inhibition of PARP-1 and VEGF resulted in reduced tumor growth in a xenograft model derived from *KRAS*-mutant cancer cells. However, they could not show this effect *in vitro*. They proposed hypoxic conditions in the *in vivo* tumors as a putative mechanism [255].

Overall, experiments with PARP-1 inhibition, siRNA-mediated *PARP-1* depletion, and CRISPR/Cas9-mediated *PARP-1* knockout confirmed preferential sensitivity of *KRAS*-mutant iCCA cell lines with impact on functional tumorigenic properties. These findings clearly define a new therapeutic possibility for a previously difficult-to-treat subgroup of iCCA patients. Until now, PARP-1 inhibition is clinically linked to HR-deficient tumors with *BRCA1/2* mutations [190]. However, our data indicate that the activity of PARPi could be extended to *KRAS*-mutant tumors, in particular intrahepatic cholangiocarcinoma. Although no direct interaction of *KRAS* and *PARP-1* was described yet, the here established phenotype might be explained by indirect interaction or via the multiple functions of PARP-1 beyond DNA damage repair [149, 201]. Future investigations will have to clarify whether

PARP-1 inhibition alone or in combination with DNA-damaging chemotherapy and/or irradiation is most promising in *KRAS*-mutant iCCA patients.

5.3 Ambiguous effects of CRISPR/Cas9-mediated *PARP-1* knockout clones on DNA damage and oxidative stress

Since its discovery in 1960, the different functions of PARP-1 have been extensively studied in both physiological and pathophysiological contexts. Besides influencing DNA single- and double-strand break repair, PARP-1 was associated with genomic instability, cell death signaling, cellular energy metabolism, and inflammation [167]. Several studies aimed to decipher the exact molecular mechanisms of PARP-1 in carcinogenesis and other diseases. Many direct and indirect modes of action were proposed, however, due to its multifaceted functions some mechanisms are controversial, some remain elusive and paradox [148].

Independent studies demonstrated that *Parp-1* deficient mice showed impaired and delayed DNA damage repair resulting in enhanced DNA damage levels [158, 166]. Further, enhanced radiosensitivity under *Parp-1* deficiency and upon PARPi in iCCA cell lines was earlier revealed [158, 248]. Our data also showed enhanced sensitivity in *KRAS*-mutant iCCA cell lines and functional impairment upon PARPi and depletion. Ionizing irradiation of *KRAS*-mutant *PARP-1* KO cell lines showed enhanced levels of phospho- γ H2AX foci, a marker of DNA double-strand breaks [256]. In control cells with active *PARP-1* expression, no increase in the number of p- γ H2AX foci was observed upon irradiation (Figure 4.19). In contrast, *KRAS*-wildtype iCCA cell lines displayed similar induction of DSBs independent of *PARP-1* expression (Figure 4.20). Taken together, these results suggest that *PARP-1* knockout enhances the number of DSBs in both *KRAS*-mutant and *KRAS*-wildtype iCCA cell lines. However, the unchanged rate of p- γ H2AX foci in *KRAS*-mutated cells under control conditions upon irradiation might indicate that DDR mechanisms operate differently here than under *PARP-1* KO and compared with *KRAS*-wildtype cells. This observation would confirm the hypothesis that *KRAS*-mutated tumors are more dependent on properly functioning DDR mechanisms [201]. Hähnel *et al.* showed delayed DDR kinetics in *KRAS*-mutant AML cells associated with upregulated *PARP-1* expression, indicating a shift to the more error-prone alt-NHEJ pathways. To further elucidate this hypothesis time-dependent kinetics of DSB repair via p- γ H2AX foci staining should be evaluated [201, 203].

Standard first-line therapy of patients with iCCA is platinum in combination with gemcitabine [226]. In HCC and other cancer entities, *PARP-1* depletion enhanced cytotoxic effects of cisplatin [252, 253, 257]. Unexpectedly, we observed enhanced cell viability of *KRAS*-mutant iCCA cell lines with *PARP-1* knockout upon cisplatin treatment indicated increased resistance (Figure 4.21). In addition, determination of DSB via p- γ H2AX staining did not show a clear response dependent on *KRAS* mutational status or *PARP-1* expression (Figure 4.22). Like upon irradiation, *KRAS*-mutant iCCA cell lines showed no increase in the number of p- γ H2AX foci under control conditions, whereas *PARP-1* KO clones displayed a mild, but not significant, increase in the number of foci. In *KRAS*-wildtype cell lines increase in the number of p- γ H2AX foci was independent of *PARP-1* expression. Further experiments identifying kinetics of DSB foci and different drug concentrations are needed. Huang *et al.* showed an association of PARPi with enhanced suppressive effects of cisplatin in HCC *in vitro* and *in vivo* models [252]. Also, in colorectal cancer (CRC) combined treatment of Olaparib and oxaliplatin showed impaired tumor growth and delayed disease progression in patient-derived xenografts enriched for *KRAS* mutations; however, researchers found no selective sensitivity in *KRAS*-mutant CRC [257]. These contradictory results might be explained by ineffective cisplatin concentrations, insufficient experimental

design, or cellular adaption to CRISPR/Cas9-mediated *PARP-1* KO. Of note, all described studies worked either with siRNA-mediated *PARP-1* KO or PARPi.

Generation of ROS and promotion of inflammatory routes were discovered as crucial events during *KRAS*-induced malignant transformation [258, 259]. Moreover, in later stages, oncogenic *KRAS* signaling was linked to cellular redox homeostasis by regulating ROS levels and maintaining proliferation and cell survival [260]. As *PARP-1* is crucial for cellular energy metabolism with an impact on redox status [149], the rationale for the determination of oxidative stress in *KRAS*-mutant iCCA with *PARP-1* KO was apparent. In ovarian cancer increase in oxidative stress was proposed as one aspect of the antitumor effects of *PARP-1* inhibition and depletion [261]. Our data indicate that upon *PARP-1* knockout both basal ROS levels as well as induced oxidative stress response were enhanced predominantly in *KRAS*-mutant iCCA (Figure 4.23). These results might explain the higher sensitivity of *KRAS*-mutant iCCA towards *PARP-1* depletion.

Overall, functional analyses of CRISPR/Cas9-mediated *PARP-1* knockout clones gave some indications regarding DSB repair, enhanced radiosensitivity, and oxidative stress response. *KRAS*-mutant iCCA cell lines showed higher sensitivity towards *PARP-1* KO and signs of impaired DDR and oxidative stress response. However, stable *PARP-1* KO seems to be harmful to all iCCA cell lines. Here, further investigations are needed to elucidate the exact underlying mechanisms. For *PARP-1* and *PARP-2* a shared functionality was proposed [199]; however, we could not find compensative upregulation of *PARP-2* upon *PARP-1* knockout (Figure 4.15). Thus, the results of our functional assays provide no conclusive mechanistic answer, we performed whole transcriptomic sequencing to further decipher the observed phenotype of a *PARP-1* knockout signature in *KRAS*-mutant iCCA.

5.4 Impact of *PARP-1* depletion on transcriptomic profile of *KRAS*-mutant iCCA cell lines

Over the past two decades, next-generation sequencing techniques, such as RNA sequencing, provided essential insights into the complexity and versatility of gene expression in cholangiocarcinoma [32]. Several studies have explored and described PLC-wide as well as iCCA-specific genomic, transcriptomic and epigenomic patterns. Based on this the prediction of activated or inhibited signaling pathways provided indications for prognostic or therapeutic implications [14, 15, 32].

RNA sequencing allowed us to characterize and investigate the transcriptomic changes caused by *PARP-1* KO in progressed tumor cells of *KRAS*-mutant and *KRAS*-wildtype iCCA. As expected, all iCCA cell lines showed an association with injury and inflammation of liver parenchyma, such as fibrosis, cholestasis, hepatitis, steatosis, proliferation, and necrosis (Figure 4.25 b, Figure 4.27 b). Unsupervised hierarchical cluster analyses of *KRAS*-mutant *PARP-1* KO clones revealed distinct transcriptomic profiles in comparison to control clones (Figure 4.24). In contrast, under *KRAS*-wildtype conditions, *PARP-1* KO clones formed dense clusters with their respective control clones (Figure 4.30). These differential clusters indicate that depletion of *PARP-1* affected gene expression more pronounced under *KRAS*-mutant conditions and could explain the phenotypic changes and preferential sensitivity we observed in *KRAS*-mutant iCCA cell lines upon *PARP-1*-based interventions [201]. In concordance with our functional analyses, we found enrichment and activation of both SSB and DSB pathways (BER, ATM signaling, DSB) predominantly in control conditions and *KRAS*-wildtype iCCA cell lines, indicating that DDR is impaired in *KRAS*-mutant iCCA cell lines upon *PARP-1* KO (Figure 4.24, Figure 4.25, Figure 4.26, Figure 4.27) [158, 166, 201]. To further delineate which DDR pathways and genes are

differentially affected by *PARP-1* KO, we analyzed the expression of 82 DDR-associated genes. *PARP-1* KO clones in comparison to their control conditions did not show any significantly expressed genes associated with DDR, except for decreased *PARP-1* expression (Figure 4.28 a). In *KRAS*-wildtype cell lines, *PARP-1* expression was also decreased and we observed increased expression of genes associated with c-NHEJ. Further, decreased expression of genes associated with alt-NHEJ and HR was displayed in *KRAS*-mutant iCCA *PARP-1* KO clones versus *KRAS*-wildtype *PARP-1* KO clones. Only the expression of few c-NHEJ associated genes remained unaffected upon *PARP-1* KO (Figure 4.28 b, c). This observation underlines the hypothesis that *KRAS*-mutant tumors are more dependent on functioning DDR pathways in general and show preferential impairment of *PARP-1*-associated DDR pathways alt-NHEJ [201, 203]. However, stable *PARP-1* depletion lacks the effect of *PARP-1*-DNA trapping happening during *PARP* inhibition [188], which limits therapeutic predictions in this model. Nevertheless, our data indicate dysregulation of DDR processes upon *PARP-1* depletion, which could be explained by the multiple interactions of *PARP-1* and PARylation with other DDR factors such as (e.g. Ku70, DDB2, RFC1) [262, 263]. *PARP-1* activation was associated with enhanced activation of error-prone alt-NHEJ over c-NHEJ by competing with Ku70 protein on the site of DNA damage [233, 264]. Further, auto-PARylation of *PARP-1* itself recruits DDR proteins to DNA damage sites [145]. In mammalian cells, the choice of which DDR pathway is activated is tightly regulated and dependent on the cell cycle, metabolic status, and external factors. Hence, dysregulation can lead to genomic instability and subsequent cell death [265]. Taken together, our results give first insights that *PARP-1* KO affects the activity of DDR pathways, however, to decipher the exact mechanisms, subsequent experiments with induction of specific DNA lesions and assays to determine the activity of specific DDR pathways would be beneficial. Co-knockout of specific key factors involved in the different DDR pathways could give further insights.

Besides changes in DDR pathways, comparison of *PARP-1* KO in *KRAS*-mutant clones with the respective control clones and with *KRAS*-wildtype revealed ambiguous results regarding the activation or inhibition of pathways associated with apoptotic signaling, inflammatory response, and oxidative stress (Figure 4.24, Figure 4.26). Upon *PARP-1* KO apoptosis signaling was found decreased in *KRAS*-mutant iCCA cell lines in comparison to control conditions and *KRAS*-wildtype iCCA cell lines (Figure 4.25, Figure 4.26). Moreover, inflammatory factors such as NF- κ B and TGF β were found activated upon *PARP-1* KO under *KRAS*-mutant conditions (Figure 4.26). These findings might suggest that depletion of *PARP-1* decreases apoptosis in *KRAS*-mutant iCCA cells but impairs DNA damage response and increases oxidative stress. However, the available data on *PARP-1* depletion in *KRAS*-mutant tumors are limited and our findings are contradictory to proposed pro-apoptotic and anti-inflammatory effects of *PARP-1* deficiency and *PARPi* [158, 203, 255, 266]. Hähnel *et al.* showed that *KRAS*-mutant AML cells are sensitized towards apoptosis upon *PARP-1* inhibition in combination with Daunorubicin treatment [203]. In *KRAS*-mutant CRC *PARP-1* inhibition induced cell apoptosis under hypoxic conditions [255]. Further, *PARP-1* deficiency or *PARPi* was associated with decreased gene expression of proinflammatory cytokines in previous studies [166, 253]. These studies hypothesize that *PARP-1* activity might act as a double-edged sword during carcinogenesis, affecting apoptotic and oxidative processes and proinflammatory signaling, dependent on the cellular metabolic status and state of tumorigenesis [145, 149, 166, 191, 267]. Until today a direct interaction between MAPK/ERK/Ras signaling and *PARP-1* expression has not been described. Liu *et al.* proposed an association of dysregulated ERK signaling with *PARP-1*-dependent NF- κ B activation, indicating that ERK-dependent phosphorylation enhances

PARP-1 activity and inflammatory processes [268]. In pancreatic cancer cells, a study showed that PARP-1 binds to a guanine-rich region adopting a G-quadruplex in the KRAS promoter enhancing KRAS transcription under oxidative stress conditions [269, 270]. O'Dell *et al.* showed activation of ERK/MAPK and PI3K/AKT pathways in their *Kras*^{LSL-G12D/+}/*Tp53*^{fl/fl} GEMM [59]. Conversely, our data indicated that under *PARP-1* KO ERK/MAPK is inhibited, whereas PI3K/AKT shows activation. Taken together, the stable *PARP-1* KO, established in this study, revealed ambiguous results in both functional and transcriptomic analyses, not allowing clear predictions of underlying molecular mechanisms. A putative explanation for the limited and contradictive results could be unrevealed compensatory mechanisms.

Overall, our *in vitro* results demonstrated that *KRAS*-mutant iCCA cell lines show enhanced sensitivity towards PARP-1 inhibition and *PARP-1* depletion. Subsequent analysis showed impaired proliferation and clonogenicity upon combined treatment with DNA damaging agent, leading to the suggestion that PARP-1 might be an effective new therapeutic target in *KRAS*-mutant iCCA. However, our functional and transcriptomic analyses of stable *PARP-1* knockout employing the CRISPR/Cas9 technique revealed ambiguous and controversial results, indicating that further *in vitro* and *in vivo* investigations are needed to decipher the underlying molecular mechanisms. To further determine the role of *PARP-1* in tumor initiation and development, we examined *KRAS*-driven cholangiocarcinogenesis in a *Parp-1* deficient mouse model.

5.5 Hepatobiliary carcinogenesis is altered in *Kras/Tp53*-driven tumors under *Parp-1* deficiency

Induction of hepatobiliary carcinogenesis has been the subject of several *in vivo* studies using carcinogen-based, CCA xenograft/allograft, genetic, or transduction mouse models [114, 271]. Mutations in *KRAS* and *TP53* rank amongst frequent genetic events in iCCA with prognostic implications in patients [32, 58]. Hence, several *Kras/Tp53*-driven iCCA models using different approaches (e.g., GEMM, electroporation, and liver organoids) have been established and characterized [59, 63, 64, 272]. In 2012, O'Dell *et al.* created the first combined model with *Kras* activation (*Kras*^{LSL-G12D/+}) and *Tp53*^{fl/fl} deletion in an *Alb-Cre* mouse strain. The mice developed liver tumors after 9 weeks, majorly resembling stroma-rich iCCAs (66%), while the remaining 34% developed mixed iCCA/HCC or HCC [59]. Another approach with *Kras*^{LSL-G12D/+} and *Tp53*^{fl/fl} expression under *Sox9*-driven Cre-recombinase confirmed the development of cholangiocyte- and hepatocyte-derived iCCA, indicating that *Kras/Tp53* induces iCCA with hepatocellular origin [63]. In this study, we first describe and characterize a purely HDTV-based, *Kras/Tp53*-driven iCCA mouse model under *Parp-1* proficient and deficient background (Figure 4.31, Figure 4.32).

Kras/Tp53-induced carcinogenesis showed profound differences in *Parp-1* proficient and deficient mice: *Parp-1* proficient mice showed predominant development of solid iCCA (80%) accompanied by dysplastic hepatocellular foci in surrounding liver 10 weeks after HDTV (Figure 4.32), recapitulating iCCA/HCC frequency found in the existing *in vivo* model with conditional activation of *Kras*^{LSL-G12D/+} and *Tp53*^{fl/fl} deletion [59]. Dysplastic foci were histopathologically classified to originate from hepatocellular origin and emerged into diffuse hepatocellular carcinoma with pronounced hematogenous invasion (Table 4.4, Table 4.6). Interestingly, histopathological assessment compared the appearance of the surrounding liver comparable to the liver tissue morphology of diethylnitrosamine (DEN)-treated mouse models, showing carcinogenic liver injury. Several studies investigating the mutational landscape of DEN-induced liver tumors revealed activation of RAS/RAF/MAPK signal transduction with predominant alterations in HRAS and BRAF [273, 274]. Quiles-Perez *et*

al. showed that PARPi in mice treated with DEN reduced the number of preneoplastic foci and proinflammatory signaling [253]. The solid tumors in *Parp-1* proficient mice injected with *Kras/Tp53* were classified as intrahepatic cholangiocarcinoma with poor to no differentiation, stroma-rich tissue structure, and Sox9 and Ck19 expression (Figure 4.33) [59, 63]. As expected, quantification of proliferation marker Ki67 revealed predominant expression in *Kras/Tp53* tumor tissue of *Parp-1^{+/+}* mice. p-yH2ax and Parp-1 staining showed significant upregulation in both tumor and surrounding liver tissue of *Parp-1^{+/+}* mice, indicating Parp-1 activity and a high number of DNA double-strand breaks (Figure 4.33).

In contrast, under *Parp-1* deficiency, *KRAS*-driven carcinogenesis led to multiple small nodules distributed all over the liver (Figure 4.32). Quantification of immunohistochemical staining showed reduced expression of Parp-1, Ki67, and p-yH2ax in the surrounding liver tissue with dysplastic foci of *Parp-1* deficient mice, indicating that proliferation and DDR response was lower than in tumor tissue of *Parp-1* proficient animals (Figure 4.32, Figure 4.33). Histopathological assessment classified dysplastic nodules as small HCC with pronounced hematogenous spread (Table 4.4, Table 4.6). Interestingly, iCCA development was abolished in *Parp-1^{-/-}* mice upon HDTV with *Kras/Tp53*. As HDTV only targets hepatocytes these results might lead to the suggestion, that transdifferentiation to cholangiocytes under malignant transformation and thus, development of iCCA is influenced by *Parp-1* genotype [59, 64, 123]. Quantification of HDTV-induced tumor burden via L/B-ratio and tumor grading showed significant differences between *Parp-1* proficient and deficient mice in *Kras/Tp53* experimental group (Figure 4.39, Figure 4.40). These findings are in line with previous studies, which established a link between DNA damage response and reduced carcinogenesis in *Parp-1* deficient mice [157, 158, 160, 161, 166, 275]. Further, these studies showed reduced tumor burden and reduced proinflammatory signaling in *Parp-1^{-/-}* animals in colon and liver [166, 253].

To dissect the relevance of oncogenic *Kras* in *Parp-1* deficient background, we performed the *in vivo* experiments in comparison to a non-*Kras* driven iCCA model (*Akt/Nicd*). A well-established HDTV model of *myrAkt/Nicd* showed iCCA development with ductular and cystic phenotype 4.5 weeks after injection in *FVB/N* wildtype mice [42]. In our mouse strain, HDTV-injection of *Akt/Nicd* led to iCCA development within 7 weeks independently of the *Parp-1* genotype. Morphologically livers of mice injected with *Akt/Nicd* showed multiple cysts and tumors, besides a disrupted surface and tissue structure. H&E staining showed distinct multifocal intrahepatic cholangiocarcinoma, accompanied by positive IHC staining of Sox9 and Ck19 (Figure 4.35, Figure 4.36) [42]. Quantification of the proliferation marker Ki67 and marker for DSB p-yH2ax showed no differences dependent on the *Parp-1* genotype. Only Parp-1 expression was reduced in *Parp-1* deficient mice (Figure 4.35, Figure 4.36). Histopathological assessment classified the tumors as well to moderately differentiated iCCA with steatotic and disrupted surrounding liver parenchyma (Table 4.4, Table 4.6). Changes in liver size and weight were also displayed in increased L/B-ratio in comparison to the experimental group injected with empty vector control (Figure 4.39). However, neither quantification via L/B-ratio nor tumor grading showed dependency on the *Parp-1* genotype (Figure 4.40).

Overall, in the here established HDTV-based and *KRAS*-driven *in vivo* model, we observed differences in hepatobiliary carcinogenesis dependent on the *Parp-1* genotype. To further investigate the observed differences in histopathologic classifications of *Kras/Tp53*- and *Akt/Nicd*-induced tumors dependent on the *Parp-1* genotypes, we performed next performed whole transcriptomic sequencing.

5.6 Impact of *Parp-1* deficiency on transcriptomic profile of *Kras/Tp53*-induced cholangiocarcinogenesis via HDTV

Analyses of our transcriptomic *in vivo* data resembled the *in vitro* findings and confirmed an association to injury and inflammation of liver parenchyma, such as fibrosis, cholestasis, hepatitis, steatosis, proliferation, and necrosis, consistently in all experimental groups (Figure 4.42 c, Figure 4.45 c). Unsupervised clustering of *Kras/Tp53*-induced tumors in *Parp-1* deficient mice versus *Parp-1* proficient mice showed distinct gene expression profiles (Figure 4.41, Figure 4.41). Previous studies analyzing *Parp-1* deficient mice have shown that Parp-1 has a multifaceted role in cell physiology and pathophysiology. In intact cells, Parp-1 counteracts DNA damage and DNA damage-induced apoptosis during tumor initiation, while it might promote tumor progression via induction of error-prone alt-NHEJ and proinflammatory signaling [162, 166, 199, 203]. Incoherence, our transcriptomic analyses show enrichment of DNA damage response pathways in all experimental groups of *Parp-1* proficient mice, while in *Parp-1*^{-/-} mice DDR was not enriched, but activation of apoptosis signaling. In particular, alt-NHEJ, HR, and BER were found enriched in *Parp-1* proficient mice independent of the used plasmid combination (Figure 4.43, Figure 4.46). When comparing *Parp-1*^{-/-} mice upon *Kras/Tp53* injection with animals injected with empty vector control we found differential expression of genes associated only with HR. In contrast, under *Parp-1*^{+/+} genotype also genes associated with alt-NHEJ were found expressed (Figure 4.46 a, b). Ultimately, comparing *Kras/Tp53* induced tumor and dysplastic foci dependent on *Parp-1* genotype showed downregulation of genes associated with HR and alt-NHEJ in *Parp-1* deficient animals (Figure 4.46 c). These findings are consistent with impaired DNA damage response found in our CRISPR/Cas9-mediated *PARP-1* KO clones and in *Parp-1* deficient mice reported before [157, 158]. Decreased gene expression of pro-inflammatory cytokines was already observed in *Parp-1*^{-/-} mice and upon PARPi and might explain the predicted inhibition of proinflammatory pathways (NF-κB, TGFβ) in our data (Figure 4.42) [166, 253]. O'Dell *et al.* showed activation of ERK/MAPK and PI3K/AKT pathways in their *Kras*^{LSL-G12D/+}/*Tp53*^{fl/fl} GEM model [59]. However, our data indicated that under *Parp-1* deficiency these pathways are inhibited. Moreover, our data suggest inhibition of NOTCH signaling (Figure 4.41), another established mutational driver of iCCA and predicted factor for transdifferentiation of hepatocytes towards biliary traits [42, 52]. Ilkenoue *et al.* demonstrated that activated *Kras* in combination with active *Pten* results predominantly in HCC, whereas activated *Kras* in combination with homozygous inactive *Pten* leads to iCCA development *in vivo* [44]. In line with this, *Parp-1* deficiency in our study confirms activation of *Pten*. Taken together, activation or inactivation of the above-mentioned pathways, although not being exclusively specific to cholangiocarcinogenesis, might explain the absence of iCCA and shift towards HCC development in our *Kras/Tp53*-induced tumor model under *Parp-1* deficiency.

The transcriptome analyses of *Akt/Nicd*-induced cholangiocarcinogenesis recapitulated that *Parp-1* has only minor effects in both experimental groups. Consistently, very similar transcriptomic profiles independent of the *Parp-1* genotype were retained (Figure 4.44). Accordingly, a 49-fold lower number of differentially expressed genes in comparison to *Kras/Tp53*-induced tumors was observed (158 genes *Akt/Nicd*^{-/-} vs ^{+/+} and 7761 genes *Kras/Tp53*^{-/-} vs ^{+/+}) and only a few molecular pathways and gene sets were affected (Figure 4.45, Figure 4.46).

Taken together, our *in vivo* studies underline a correlation of *Parp-1* expression and *Kras/Tp53*-driven cholangiocarcinogenesis. Reduced tumorigenesis under *Parp-1* deficiency could be explained by decreased apoptotic and inflammatory processes as well

as DNA damage response. The exact molecular mechanisms explaining the shift from iCCA to HCC development and direct interaction of Parp-1 with the above-mentioned pathways in the context of tumor initiation require further investigations.

5.7 **PARP-1 expression as prognostic factor in KRAS-mutant iCCA**

In the here presented study, we investigated the impact of *PARP-1* expression in three different models: in human iCCA tissue samples, in iCCA cell lines, and in an HDTV-driven mouse model. These models were based on different *KRAS* and *PARP-1* genotypes and interventions, investigating different stages in tumor development.

The human *KRAS*-mutant iCCA cohort served as a baseline to investigate the general features of *KRAS*-mutant iCCA in comparison to normal surrounding liver tissue and *KRAS*-wildtype tissue independent of *PARP-1* genotype. Here, we found upregulation of *PARP-1* expression and overall activity of DDR pathways (BER, c-NHEJ, alt-NHEJ, HR) accompanied with activation of apoptotic, oxidative, and inflammatory factors (Figure 4.47, Table 4.7). Enhanced *KRAS* signaling was associated with intracellular stress mechanisms such as apoptosis, accelerated proliferation, and oxidative stress response driving the malignant transformation of tumors [59, 60]. *PARP-1* KO in *KRAS*-mutant iCCA cell lines served to assess the impact on tumor progression and to investigate putative therapeutic implications. CRISPR/Cas9-mediated KO of *PARP-1* revealed downregulation of double-strand break repair pathways (c-NHEJ, alt-NHEJ, HR) and inhibition of oxidative and inflammatory processes (Table 4.7). The enhanced sensitivity of *KRAS*-mutant iCCA cell lines might result from decreased DDR response and enhanced apoptotic processes under *PARP-1* KO [203]. To investigate the role of *Parp-1* expression in tumor initiation of *Kras*-driven cholangiocarcinogenesis, we used a *Parp-1* deficient mouse model. Here, downregulation of DDR pathways and decreased activity of proinflammatory NF- κ B signaling might explain the reduced tumor burden in *Parp-1* deficient animals (Table 4.7) [166]. Further, inhibition of oncogenic hallmark pathways such as ERK/MAPK, PI3K/AKT, and Notch could explain the decreased tumorigenesis. Predominant development of HCC under *Parp-1* deficiency could be explained by *Pten* activation, which was previously described to promote hepatocarcinogenesis in combination with activated *Kras* [44].

Taken together, our compared *in vitro* and *in vivo* data suggest that DDR response is dysregulated upon *PARP-1* depletion in *KRAS*-mutant iCCA, accompanied by downregulation of inflammatory signaling. Due to the different experimental designs of *in vivo* and *in vitro* experiments the meaningful combination of these results is, however, limited. Also, in human tumorigenesis and clinical treatment, neither exclusive tumor initiation by *Kras/Tp53* nor stable *PARP-1* KO occurs. Hence, both models do not fully recapitulate tumor growth and therapeutic treatment. Further they lack the influence of an adverse tumor microenvironment present in human iCCA patients [12]. However, the observed sensitivity of *KRAS*-mutant iCCA cell lines and the reduced tumor burden in *Parp-1* deficient mice might indicate a synthetic vulnerability and potential therapeutic implications of PARPi in *KRAS*-mutant iCCA.

Due to the complexity of iCCA pathogenesis and the pronounced genetic heterogeneity, treatment options are still limited and the prognosis of iCCA patients remains dismal. Both dysregulated *PARP-1* expression and oncogenic *KRAS* signaling were associated with poor OS, early recurrence, and prognostic value for decreased PFS in several cancer entities including iCCA [149, 225]. These findings highlight the need for novel therapeutic approaches [13, 60, 149]. Despite limited options of targeting oncogenic *KRAS* directly,

targeting downstream mediators have been proven a promising therapeutic option in several cancer entities. Moreover, synergistic effects of combined MEK/ERK and PARP-1 inhibition were observed in ovarian cancer cells [276]. Our data demonstrate an enhanced sensitivity of *KRAS*-mutant iCCA upon *PARP-1* depletion and inhibition *in vitro* and decreased tumor growth in *Parp-1* deficient background *in vivo*, providing a rationale for PARP-1-based interventions in this difficult-to-treat disease [201]. Hence, translation of these experimental findings into the prognostic determination of patients is needed. Thus, we integrated our findings of *KRAS*-mutant CRISPR/Cas9-mediated *PARP-1* KO clones and our *Parp-1*-dependent mouse model with *Kras/Tp53*- and *Akt/Nicd*-induced cholangiocarcinogenesis with a previously established dataset with 45 CCA patients representing good and poor prognostic outcome [58]. The integration of our *in vitro* transcriptomic data with different established prognostic subgroups of PLC (poor and good prognosis) revealed a shift of *KRAS*-mutant iCCA cell lines from poor to good prognosis upon *PARP-1* KO (Figure 4.49). In concordance, *Parp-1* deficient samples from mice injected with *Kras/Tp53* clustered with good prognosis iCCA patient samples, whereas *Parp-1* proficient samples grouped with poor prognosis (Figure 4.50 a). Interestingly, this shift was not visible in *Akt/Nicd*-induced tumor samples. Here, *Parp-1* proficient and deficient samples clustered randomly with poor prognostic patients (Figure 4.49 b). Hence, *PARP-1* depletion leads to a shift of iCCA samples from poor to good prognosis predominantly in presence of activating *KRAS* mutation. These results underline the observed impact of *PARP-1* depletion both during tumor initiation and progression and confirm the suggested prognostic relevance of *KRAS/PARP-1*-driven synthetic vulnerability. Our results further suggest PARPi as a promising therapeutic option in our *in vitro* and *in vivo* experiments. However, additional studies deciphering the exact molecular mechanisms are needed.

6. Summary

Cholangiocarcinogenesis is a complex and multi-step process. Despite intense research to decipher the pathophysiology of intrahepatic cholangiocarcinomas in recent decades, the understanding of the underlying molecular mechanisms and impact of different risk factors is still limited. Due to the profound genetic heterogeneity and late diagnosis of iCCA, individualized risk stratification and novel therapeutic options are urgently needed. PARP-1 inhibitors are already effectively utilized in patients with *BRCA*-mutant breast or ovarian carcinoma. Over recent years, indications for the use of PARP-1 inhibitors are emerging in other tumor entities that display disruption in DNA damage repair. In addition, a potential regulatory link associates *PARP-1* and *KRAS* alterations, but its relevance for iCCA remains elusive. To address this issue, we here examined the role of *PARP-1* in a subgroup of iCCA harboring activating *KRAS* mutations.

Consistently, we identified upregulation of *PARP-1* expression predominantly in iCCA cell lines harboring *KRAS* mutations in exon 12. Results of functional analyses upon siRNA-mediated knockdown of *PARP-1* or treatment with PARP-1 inhibitor Olaparib provided evidence that *KRAS*-mutant iCCA cell lines are more sensitive towards PARP-1-based interventions. We further characterized the underlying molecular mechanisms by stable CRISPR/Cas9-mediated *PARP-1* knockout. We demonstrate differential regulation of cellular pathways involved in DNA damage response, inflammation, oxidative stress, and apoptosis.

In addition, we employed a model combining *Kras/Tp53*-induced cholangiocarcinoma by hydrodynamic tail vein injection with a *Parp-1* deficient mouse model to delineate the relevance of the *Parp-1/Kras*-interaction on tumor development *in vivo*. In striking concordance, we observed that *Kras/Tp53*-induced tumor growth in the biliary lineage was highly dependent on *Parp-1* genotype.

Integration of our *in vivo* and *in vitro* data with publically available data of CCA patient subgroups indicate a clinical relevance of a *PARP-1* gene expression signature in poor prognostic iCCA patients. Further, a shift of *KRAS*-mutant iCCA from poor to good prognosis upon *PARP-1* depletion could be demonstrated suggesting the potential of PARP-based interventions in these patients. Altogether, our *in vitro* and *in vivo* results established the principle of synthetic vulnerability based on PARP-1 inhibition in *KRAS*-driven iCCA. Further, *PARP-1* depletion showed effects on tumorigenicity of iCCA cell lines and the absence of *Parp-1 in vivo* led to decreased iCCA tumor growth. These findings suggest *PARP-1* as a promising novel therapeutic target in *KRAS*-mutant iCCA.

7. References

1. Malarkey, D.E., et al., *New insights into functional aspects of liver morphology*. *Toxicol Pathol*, 2005. **33**(1): p. 27-34.
2. Muriel, P., *Liver pathophysiology : therapies and antioxidants*. 2017.
3. Olivetti, L. and D. Volpi, *Liver, Biliary Tract, and Pancreas*, in *Atlas of Imaging Anatomy*, L. Olivetti, Editor. 2015, Springer International Publishing: Cham. p. 163-174.
4. Crawford, J.M., 1. *The Intrahepatic Biliary Tree*, in *The Liver in Biology and Disease*. 2004. p. 1-20.
5. Gilloteaux, J., *Introduction to the biliary tract, the gallbladder, and gallstones*. *Microsc Res Tech*, 1997. **38**(6): p. 547-51.
6. Keplinger, K.M. and M. Bloomston, *Anatomy and embryology of the biliary tract*. *Surg Clin North Am*, 2014. **94**(2): p. 203-17.
7. Strazzabosco, M., L. Fabris, and C. Spirli, *Pathophysiology of cholangiopathies*. *J Clin Gastroenterol*, 2005. **39**(4 Suppl 2): p. S90-S102.
8. Tariq, N.U., M.G. McNamara, and J.W. Valle, *Biliary tract cancers: current knowledge, clinical candidates and future challenges*. *Cancer Manag Res*, 2019. **11**: p. 2623-2642.
9. Charbel, H. and F.H. Al-Kawas, *Cholangiocarcinoma: epidemiology, risk factors, pathogenesis, and diagnosis*. *Curr Gastroenterol Rep*, 2011. **13**(2): p. 182-7.
10. Boyer, J.L., *Bile formation and secretion*. *Compr Physiol*, 2013. **3**(3): p. 1035-78.
11. Clements, O., et al., *Risk factors for intrahepatic and extrahepatic cholangiocarcinoma: A systematic review and meta-analysis*. *J Hepatol*, 2020. **72**(1): p. 95-103.
12. Banales, J.M., et al., *Expert consensus document: Cholangiocarcinoma: current knowledge and future perspectives consensus statement from the European Network for the Study of Cholangiocarcinoma (ENS-CCA)*. *Nat Rev Gastroenterol Hepatol*, 2016. **13**(5): p. 261-80.
13. Banales, J.M., et al., *Cholangiocarcinoma 2020: the next horizon in mechanisms and management*. *Nat Rev Gastroenterol Hepatol*, 2020. **17**(9): p. 557-588.
14. Marquardt, J.U., J.B. Andersen, and S.S. Thorgeirsson, *Functional and genetic deconstruction of the cellular origin in liver cancer*. *Nat Rev Cancer*, 2015. **15**(11): p. 653-67.
15. Nakamura, H., et al., *Genomic spectra of biliary tract cancer*. *Nat Genet*, 2015. **47**(9): p. 1003-10.
16. Arai, Y., et al., *Fibroblast growth factor receptor 2 tyrosine kinase fusions define a unique molecular subtype of cholangiocarcinoma*. *Hepatology*, 2014. **59**(4): p. 1427-34.
17. Borger, D.R., et al., *Frequent mutation of isocitrate dehydrogenase (IDH)1 and IDH2 in cholangiocarcinoma identified through broad-based tumor genotyping*. *Oncologist*, 2012. **17**(1): p. 72-9.
18. Bertuccio, P., et al., *Global trends in mortality from intrahepatic and extrahepatic cholangiocarcinoma*. *J Hepatol*, 2019. **71**(1): p. 104-114.
19. Forner, A., et al., *Clinical presentation, diagnosis and staging of cholangiocarcinoma*. *Liver Int*, 2019. **39** Suppl 1: p. 98-107.
20. Palmer, W.C. and T. Patel, *Are common factors involved in the pathogenesis of primary liver cancers? A meta-analysis of risk factors for intrahepatic cholangiocarcinoma*. *J Hepatol*, 2012. **57**(1): p. 69-76.
21. Kamsa-ard, S., et al., *Risk Factors for Cholangiocarcinoma in Thailand: A Systematic Review and Meta-Analysis*. *Asian Pac J Cancer Prev*, 2018. **19**(3): p. 605-614.
22. Cardinale, V., et al., *Intrahepatic cholangiocarcinoma: review and update*. *Hepatoma Research*, 2018. **4**(6).
23. Reddy, S.K., et al., *Prevalence of nonalcoholic steatohepatitis among patients with resectable intrahepatic cholangiocarcinoma*. *J Gastrointest Surg*, 2013. **17**(4): p. 748-55.
24. Khan, S.A., et al., *Guidelines for the diagnosis and treatment of cholangiocarcinoma: an update*. *Gut*, 2012. **61**(12): p. 1657-69.

25. Macias, R.I.R., et al., *Diagnostic and prognostic biomarkers in cholangiocarcinoma*. Liver Int, 2019. **39 Suppl 1**: p. 108-122.
26. Loosen, S.H., et al., *Elevated levels of circulating osteopontin are associated with a poor survival after resection of cholangiocarcinoma*. J Hepatol, 2017. **67**(4): p. 749-757.
27. Huang, L., et al., *Serum CYFRA 21-1 in Biliary Tract Cancers: A Reliable Biomarker for Gallbladder Carcinoma and Intrahepatic Cholangiocarcinoma*. Dig Dis Sci, 2015. **60**(5): p. 1273-83.
28. Lapitz, A., et al., *Patients with Cholangiocarcinoma Present Specific RNA Profiles in Serum and Urine Extracellular Vesicles Mirroring the Tumor Expression: Novel Liquid Biopsy Biomarkers for Disease Diagnosis*. Cells, 2020. **9**(3).
29. Andersen, R.F. and A. Jakobsen, *Screening for circulating RAS/RAF mutations by multiplex digital PCR*. Clin Chim Acta, 2016. **458**: p. 138-43.
30. Shigehara, K., et al., *Real-time PCR-based analysis of the human bile microRNAome identifies miR-9 as a potential diagnostic biomarker for biliary tract cancer*. PLoS One, 2011. **6**(8): p. e23584.
31. Voigtlander, T., et al., *MicroRNAs in Serum and Bile of Patients with Primary Sclerosing Cholangitis and/or Cholangiocarcinoma*. PLoS One, 2015. **10**(10): p. e0139305.
32. Nepal, C., et al., *Genomic perturbations reveal distinct regulatory networks in intrahepatic cholangiocarcinoma*. Hepatology, 2018. **68**(3): p. 949-963.
33. Abdel-Misih, S.R. and M. Bloomston, *Liver anatomy*. Surg Clin North Am, 2010. **90**(4): p. 643-53.
34. Strazzabosco, M. and L. Fabris, *Functional anatomy of normal bile ducts*. Anat Rec (Hoboken), 2008. **291**(6): p. 653-60.
35. Tabibian, J.H., et al., *Physiology of cholangiocytes*. Compr Physiol, 2013. **3**(1): p. 541-65.
36. Guido, M., et al., *The Anatomy and Histology of the Liver and Biliary Tract, in Pediatric Hepatology and Liver Transplantation*. 2019. p. 41-55.
37. Zatloukal, K., et al., *The keratin cytoskeleton in liver diseases*. J Pathol, 2004. **204**(4): p. 367-76.
38. Vicent, S., et al., *Experimental models to unravel the molecular pathogenesis, cell of origin and stem cell properties of cholangiocarcinoma*. Liver Int, 2019. **39 Suppl 1**: p. 79-97.
39. Roskams, T. and V. Desmet, *Embryology of extra- and intrahepatic bile ducts, the ductal plate*. Anat Rec (Hoboken), 2008. **291**(6): p. 628-35.
40. Cheung, A.C., M.J. Lorenzo Pisarello, and N.F. LaRusso, *Pathobiology of biliary epithelia*. Biochim Biophys Acta Mol Basis Dis, 2018. **1864**(4 Pt B): p. 1220-1231.
41. Sekiya, S. and A. Suzuki, *Intrahepatic cholangiocarcinoma can arise from Notch-mediated conversion of hepatocytes*. J Clin Invest, 2012. **122**(11): p. 3914-8.
42. Fan, B., et al., *Cholangiocarcinomas can originate from hepatocytes in mice*. J Clin Invest, 2012. **122**(8): p. 2911-5.
43. Holczbauer, A., et al., *Modeling pathogenesis of primary liver cancer in lineage-specific mouse cell types*. Gastroenterology, 2013. **145**(1): p. 221-231.
44. Ikenoue, T., et al., *A novel mouse model of intrahepatic cholangiocarcinoma induced by liver-specific Kras activation and Pten deletion*. Sci Rep, 2016. **6**: p. 23899.
45. Wang, H., et al., *Overexpression of SMAD7 activates the YAP/NOTCH cascade and promotes liver carcinogenesis in mice and humans*. Hepatology, 2020.
46. Guest, R.V., et al., *Cell lineage tracing reveals a biliary origin of intrahepatic cholangiocarcinoma*. Cancer Res, 2014. **74**(4): p. 1005-10.
47. Moeini, A., P.K. Haber, and D. Sia, *Cell of origin in biliary tract cancers and clinical implications*. JHEP Rep, 2021. **3**(2): p. 100226.
48. Andersen, J.B., *Molecular pathogenesis of intrahepatic cholangiocarcinoma*. J Hepatobiliary Pancreat Sci, 2015. **22**(2): p. 101-13.
49. Moeini, A., et al., *Molecular Pathogenesis and Targeted Therapies for Intrahepatic Cholangiocarcinoma*. Clin Cancer Res, 2016. **22**(2): p. 291-300.

50. Wu, W.R., et al., *Clinicopathological significance of aberrant Notch receptors in intrahepatic cholangiocarcinoma*. Int J Clin Exp Pathol, 2014. **7**(6): p. 3272-9.
51. Zhou, Q., et al., *The roles of Notch1 expression in the migration of intrahepatic cholangiocarcinoma*. BMC Cancer, 2013. **13**: p. 244.
52. Zender, S., et al., *A critical role for notch signaling in the formation of cholangiocellular carcinomas*. Cancer Cell, 2013. **23**(6): p. 784-95.
53. Kongpetch, S., et al., *Pathogenesis of cholangiocarcinoma: From genetics to signalling pathways*. Best Pract Res Clin Gastroenterol, 2015. **29**(2): p. 233-44.
54. Montal, R., et al., *Molecular classification and therapeutic targets in extrahepatic cholangiocarcinoma*. J Hepatol, 2020. **73**(2): p. 315-327.
55. Sia, D., et al., *Integrative molecular analysis of intrahepatic cholangiocarcinoma reveals 2 classes that have different outcomes*. Gastroenterology, 2013. **144**(4): p. 829-40.
56. Braconi, C., et al., *Molecular perturbations in cholangiocarcinoma: Is it time for precision medicine?* Liver Int, 2019. **39 Suppl 1**: p. 32-42.
57. Churi, C.R., et al., *Mutation profiling in cholangiocarcinoma: prognostic and therapeutic implications*. PLoS One, 2014. **9**(12): p. e115383.
58. Andersen, J.B., et al., *Genomic and genetic characterization of cholangiocarcinoma identifies therapeutic targets for tyrosine kinase inhibitors*. Gastroenterology, 2012. **142**(4): p. 1021-1031 e15.
59. O'Dell, M.R., et al., *Kras(G12D) and p53 mutation cause primary intrahepatic cholangiocarcinoma*. Cancer Res, 2012. **72**(6): p. 1557-67.
60. Grabocka, E., C. Commisso, and D. Bar-Sagi, *Molecular pathways: targeting the dependence of mutant RAS cancers on the DNA damage response*. Clin Cancer Res, 2015. **21**(6): p. 1243-7.
61. Jusakul, A., et al., *Whole-Genome and Epigenomic Landscapes of Etiologically Distinct Subtypes of Cholangiocarcinoma*. Cancer Discov, 2017. **7**(10): p. 1116-1135.
62. Ong, C.K., et al., *Exome sequencing of liver fluke-associated cholangiocarcinoma*. Nat Genet, 2012. **44**(6): p. 690-3.
63. Hill, M.A., et al., *Kras and Tp53 Mutations Cause Cholangiocyte- and Hepatocyte-Derived Cholangiocarcinoma*. Cancer Res, 2018. **78**(16): p. 4445-4451.
64. Gurlevik, E., et al., *Adjuvant gemcitabine therapy improves survival in a locally induced, R0-resectable model of metastatic intrahepatic cholangiocarcinoma*. Hepatology, 2013. **58**(3): p. 1031-41.
65. Wang, P., et al., *Mutations in isocitrate dehydrogenase 1 and 2 occur frequently in intrahepatic cholangiocarcinomas and share hypermethylation targets with glioblastomas*. Oncogene, 2013. **32**(25): p. 3091-100.
66. Sia, D., et al., *Massive parallel sequencing uncovers actionable FGFR2-PPHLN1 fusion and ARAF mutations in intrahepatic cholangiocarcinoma*. Nat Commun, 2015. **6**: p. 6087.
67. Saborowski, A., U. Lehmann, and A. Vogel, *FGFR inhibitors in cholangiocarcinoma: what's now and what's next?* Ther Adv Med Oncol, 2020. **12**: p. 1758835920953293.
68. Saborowski, A., et al., *Mouse model of intrahepatic cholangiocarcinoma validates FIG-ROS as a potent fusion oncogene and therapeutic target*. Proc Natl Acad Sci U S A, 2013. **110**(48): p. 19513-8.
69. Abou-Alfa, G.K., et al., *Ivosidenib in IDH1-mutant, chemotherapy-refractory cholangiocarcinoma (ClarIDHy): a multicentre, randomised, double-blind, placebo-controlled, phase 3 study*. Lancet Oncol, 2020. **21**(6): p. 796-807.
70. Makawita, S., et al., *Infigratinib in patients with advanced cholangiocarcinoma with FGFR2 gene fusions/translocations: the PROOF 301 trial*. Future Oncol, 2020. **16**(30): p. 2375-2384.
71. Høgdall, D., et al., *Molecular Pathogenesis and Current Therapy in Intrahepatic Cholangiocarcinoma*. Digestive Diseases, 2016. **34**(4): p. 440-451.
72. Erice, O., et al., *Molecular Mechanisms of Cholangiocarcinogenesis: New Potential Targets for Therapy*. Curr Drug Targets, 2017. **18**(8): p. 932-949.
73. Labib, P.L., G. Goodchild, and S.P. Pereira, *Molecular Pathogenesis of Cholangiocarcinoma*. BMC Cancer, 2019. **19**(1): p. 185.

74. Fava, G. and I. Lorenzini, *Molecular pathogenesis of cholangiocarcinoma*. Int J Hepatol, 2012. **2012**: p. 630543.
75. Aggarwal, B.B., *Nuclear factor-kappaB: the enemy within*. Cancer Cell, 2004. **6**(3): p. 203-8.
76. Karin, M. and F.R. Greten, *NF-kappaB: linking inflammation and immunity to cancer development and progression*. Nat Rev Immunol, 2005. **5**(10): p. 749-59.
77. Castven, D., et al., *Application of patient-derived liver cancer cells for phenotypic characterization and therapeutic target identification*. Int J Cancer, 2019. **144**(11): p. 2782-2794.
78. Liu, B., et al., *TLR2 promotes human intrahepatic cholangiocarcinoma cell migration and invasion by modulating NF-kappaB pathway-mediated inflammatory responses*. FEBS J, 2016. **283**(20): p. 3839-3850.
79. Seubwai, W., et al., *Aberrant expression of NF-kappaB in liver fluke associated cholangiocarcinoma: implications for targeted therapy*. PLoS One, 2014. **9**(8): p. e106056.
80. Sato, Y., et al., *Epithelial-mesenchymal transition induced by transforming growth factor- β 1/Snail activation aggravates invasive growth of cholangiocarcinoma*. Am J Pathol, 2010. **177**(1): p. 141-52.
81. Duangkumpha, K., et al., *BMP-7 blocks the effects of TGF-beta-induced EMT in cholangiocarcinoma*. Tumour Biol, 2014. **35**(10): p. 9667-76.
82. Fabris, L., et al., *The tumour microenvironment and immune milieu of cholangiocarcinoma*. Liver Int, 2019. **39** Suppl 1: p. 63-78.
83. Itou, R.A., et al., *Immunohistochemical characterization of cancer-associated fibroblasts at the primary sites and in the metastatic lymph nodes of human intrahepatic cholangiocarcinoma*. Hum Pathol, 2019. **83**: p. 77-89.
84. Brivio, S., et al., *Tumor reactive stroma in cholangiocarcinoma: The fuel behind cancer aggressiveness*. World J Hepatol, 2017. **9**(9): p. 455-468.
85. Jaiswal, M., et al., *Inflammatory cytokines induce DNA damage and inhibit DNA repair in cholangiocarcinoma cells by a nitric oxide-dependent mechanism*. Cancer Res, 2000. **60**(1): p. 184-90.
86. Lamarca, A., et al., *Biliary Tract Cancer: State of the Art and potential role of DNA Damage Repair*. Cancer Treat Rev, 2018. **70**: p. 168-177.
87. Carbone, M., et al., *BAP1 and cancer*. Nat Rev Cancer, 2013. **13**(3): p. 153-9.
88. Silva, V.W., et al., *Biliary carcinomas: pathology and the role of DNA mismatch repair deficiency*. Chin Clin Oncol, 2016. **5**(5): p. 62.
89. Ross, J.S., et al., *New routes to targeted therapy of intrahepatic cholangiocarcinomas revealed by next-generation sequencing*. Oncologist, 2014. **19**(3): p. 235-42.
90. Jain, A., L.N. Kwong, and M. Javle, *Genomic Profiling of Biliary Tract Cancers and Implications for Clinical Practice*. Curr Treat Options Oncol, 2016. **17**(11): p. 58.
91. Goyal, L., et al., *Mismatch repair protein loss and microsatellite instability in cholangiocarcinoma*. Journal of Clinical Oncology, 2014. **32**(3_suppl): p. 237-237.
92. Abdel-Wahab, R., et al., *Variations in DNA repair genomic alterations and tumor mutation burden in biliary tract cancer (BTC) subtypes*. Journal of Clinical Oncology, 2018. **36**(4_suppl): p. 263-263.
93. Lin, J., et al., *Alterations in DNA Damage Repair Genes in Primary Liver Cancer*. Clin Cancer Res, 2019. **25**(15): p. 4701-4711.
94. Amin, M.B., et al., *The Eighth Edition AJCC Cancer Staging Manual: Continuing to build a bridge from a population-based to a more "personalized" approach to cancer staging*. CA Cancer J Clin, 2017. **67**(2): p. 93-99.
95. Shroff, R.T., et al., *Adjuvant Therapy for Resected Biliary Tract Cancer: ASCO Clinical Practice Guideline*. J Clin Oncol, 2019. **37**(12): p. 1015-1027.
96. Mosconi, S., et al., *Cholangiocarcinoma*. Crit Rev Oncol Hematol, 2009. **69**(3): p. 259-70.
97. Primrose, J., et al., *Adjuvant capecitabine for biliary tract cancer: The BILCAP randomized study*. Journal of Clinical Oncology, 2017. **35**: p. 4006-4006.

98. Valle, J., et al., *Cisplatin plus gemcitabine versus gemcitabine for biliary tract cancer*. N Engl J Med, 2010. **362**(14): p. 1273-81.
99. de Sousa Cavalcante, L. and G. Monteiro, *Gemcitabine: metabolism and molecular mechanisms of action, sensitivity and chemoresistance in pancreatic cancer*. Eur J Pharmacol, 2014. **741**: p. 8-16.
100. Bupathi, M., D.H. Ahn, and T. Bekaii-Saab, *Therapeutic options for intrahepatic cholangiocarcinoma*. Hepatobiliary Surg Nutr, 2017. **6**(2): p. 91-100.
101. Lamarca, A., et al., *ABC-06 | A randomised phase III, multi-centre, open-label study of active symptom control (ASC) alone or ASC with oxaliplatin / 5-FU chemotherapy (ASC+mFOLFOX) for patients (pts) with locally advanced / metastatic biliary tract cancers (ABC) previously-treated with cisplatin/gemcitabine (CisGem) chemotherapy*. Journal of Clinical Oncology, 2019. **37**(15_suppl): p. 4003-4003.
102. Massironi, S., et al., *New and Emerging Systemic Therapeutic Options for Advanced Cholangiocarcinoma*. Cells, 2020. **9**(3).
103. Javle, M., et al., *Phase II Study of BGJ398 in Patients With FGFR-Altered Advanced Cholangiocarcinoma*. J Clin Oncol, 2018. **36**(3): p. 276-282.
104. Javle, M., et al., *AB051. P-19. A phase II study of infigratinib (BGJ398) in previously-treated advanced cholangiocarcinoma containing FGFR2 fusions*. Hepatobiliary Surgery and Nutrition, 2019: p. AB051.
105. Bekaii-Saab, T.S., et al., *FIGHT-302: first-line pemigatinib vs gemcitabine plus cisplatin for advanced cholangiocarcinoma with FGFR2 rearrangements*. Future Oncol, 2020. **16**(30): p. 2385-2399.
106. Borad, M.J., et al., *A phase III study of futibatinib (TAS-120) versus gemcitabine-cisplatin (gem-cis) chemotherapy as first-line (1L) treatment for patients (pts) with advanced (adv) cholangiocarcinoma (CCA) harboring fibroblast growth factor receptor 2 (FGFR2) gene rearrangements (FOENIX-CCA3)*. Journal of Clinical Oncology, 2020. **38**(4_suppl): p. TPS600-TPS600.
107. Lavingia, V. and M. Fakhri, *Impressive response to dual BRAF and MEK inhibition in patients with BRAF mutant intrahepatic cholangiocarcinoma-2 case reports and a brief review*. J Gastrointest Oncol, 2016. **7**(6): p. E98-E102.
108. Subbiah, V., et al., *Dabrafenib plus trametinib in patients with BRAF(V600E)-mutated biliary tract cancer (ROAR): a phase 2, open-label, single-arm, multicentre basket trial*. Lancet Oncol, 2020. **21**(9): p. 1234-1243.
109. Golan, T., et al., *Overall Survival and Clinical Characteristics of BRCA-Associated Cholangiocarcinoma: A Multicenter Retrospective Study*. Oncologist, 2017. **22**(7): p. 804-810.
110. Marabelle, A., et al., *Efficacy of Pembrolizumab in Patients With Noncolorectal High Microsatellite Instability/Mismatch Repair-Deficient Cancer: Results From the Phase II KEYNOTE-158 Study*. J Clin Oncol, 2020. **38**(1): p. 1-10.
111. Piha-Paul, S.A., et al., *Efficacy and safety of pembrolizumab for the treatment of advanced biliary cancer: Results from the KEYNOTE-158 and KEYNOTE-028 studies*. Int J Cancer, 2020. **147**(8): p. 2190-2198.
112. Kim, R.D., et al., *A Phase 2 Multi-institutional Study of Nivolumab for Patients With Advanced Refractory Biliary Tract Cancer*. JAMA Oncol, 2020. **6**(6): p. 888-894.
113. Oh, D.-Y., et al., *Phase II study assessing tolerability, efficacy, and biomarkers for durvalumab (D) ± tremelimumab (T) and gemcitabine/cisplatin (GemCis) in chemo-naïve advanced biliary tract cancer (aBTC)*. Journal of Clinical Oncology, 2020. **38**(15_suppl): p. 4520-4520.
114. Erice, O., et al., *Genetic Mouse Models as In Vivo Tools for Cholangiocarcinoma Research*. Cancers (Basel), 2019. **11**(12).
115. Seehawer, M., et al., *Necroptosis microenvironment directs lineage commitment in liver cancer*. Nature, 2018. **562**(7725): p. 69-75.
116. Zhang, G., V. Budker, and J.A. Wolff, *High levels of foreign gene expression in hepatocytes after tail vein injections of naked plasmid DNA*. Hum Gene Ther, 1999. **10**(10): p. 1735-7.

117. Liu, F., Y. Song, and D. Liu, *Hydrodynamics-based transfection in animals by systemic administration of plasmid DNA*. Gene Ther, 1999. **6**(7): p. 1258-66.
118. Zhang, G., et al., *Hydroporation as the mechanism of hydrodynamic delivery*. Gene Ther, 2004. **11**(8): p. 675-82.
119. Kobayashi, N., et al., *Hydrodynamics-based procedure involves transient hyperpermeability in the hepatic cellular membrane: implication of a nonspecific process in efficient intracellular gene delivery*. J Gene Med, 2004. **6**(5): p. 584-92.
120. Budker, V., et al., *Hypothesis: naked plasmid DNA is taken up by cells in vivo by a receptor-mediated process*. J Gene Med, 2000. **2**(2): p. 76-88.
121. Budker, V.G., et al., *Mechanism of plasmid delivery by hydrodynamic tail vein injection. II. Morphological studies*. J Gene Med, 2006. **8**(7): p. 874-88.
122. Suda, T. and D. Liu, *Hydrodynamic gene delivery: its principles and applications*. Mol Ther, 2007. **15**(12): p. 2063-9.
123. Chen, X. and D.F. Calvisi, *Hydrodynamic transfection for generation of novel mouse models for liver cancer research*. Am J Pathol, 2014. **184**(4): p. 912-923.
124. Yant, S.R., et al., *Somatic integration and long-term transgene expression in normal and haemophilic mice using a DNA transposon system*. Nat Genet, 2000. **25**(1): p. 35-41.
125. Plasterk, R.H., Z. Izsvak, and Z. Ivics, *Resident aliens: the Tc1/mariner superfamily of transposable elements*. Trends Genet, 1999. **15**(8): p. 326-32.
126. Ivics, Z. and Z. Izsvak, *Sleeping Beauty Transposition*. Microbiol Spectr, 2015. **3**(2): p. MDNA3-0042-2014.
127. Andersen, J.B. and S.S. Thorgeirsson, *Genetic profiling of intrahepatic cholangiocarcinoma*. Curr Opin Gastroenterol, 2012. **28**(3): p. 266-72.
128. Calvisi, D.F., et al., *Increased lipogenesis, induced by AKT-mTORC1-RPS6 signaling, promotes development of human hepatocellular carcinoma*. Gastroenterology, 2011. **140**(3): p. 1071-83.
129. Kang, T.W., et al., *Senescence surveillance of pre-malignant hepatocytes limits liver cancer development*. Nature, 2011. **479**(7374): p. 547-51.
130. Jeliaskova, P., et al., *Canonical Notch2 signaling determines biliary cell fates of embryonic hepatoblasts and adult hepatocytes independent of Hes1*. Hepatology, 2013. **57**(6): p. 2469-79.
131. Zhang, S., et al., *Hippo Cascade Controls Lineage Commitment of Liver Tumors in Mice and Humans*. Am J Pathol, 2018. **188**(4): p. 995-1006.
132. Carlson, C.M., et al., *Somatic integration of an oncogene-harboring Sleeping Beauty transposon models liver tumor development in the mouse*. Proc Natl Acad Sci U S A, 2005. **102**(47): p. 17059-64.
133. Matter, M.S., et al., *Oncogenic driver genes and the inflammatory microenvironment dictate liver tumor phenotype*. Hepatology, 2016. **63**(6): p. 1888-99.
134. Cohen, M.S. and P. Chang, *Insights into the biogenesis, function, and regulation of ADP-ribosylation*. Nat Chem Biol, 2018. **14**(3): p. 236-243.
135. Chambon, P., J.D. Weill, and P. Mandel, *Nicotinamide mononucleotide activation of new DNA-dependent polyadenylic acid synthesizing nuclear enzyme*. Biochem Biophys Res Commun, 1963. **11**: p. 39-43.
136. Nishizuka, Y., et al., *Studies on the polymer of adenosine diphosphate ribose. I. Enzymic formation from nicotinamide adenine dinucleotide in mammalian nuclei*. J Biol Chem, 1967. **242**(13): p. 3164-71.
137. Yelamos, J., et al., *PARP-1 and PARP-2: New players in tumour development*. Am J Cancer Res, 2011. **1**(3): p. 328-346.
138. Gibson, B.A. and W.L. Kraus, *New insights into the molecular and cellular functions of poly(ADP-ribose) and PARPs*. Nat Rev Mol Cell Biol, 2012. **13**(7): p. 411-24.
139. Vyas, S., et al., *A systematic analysis of the PARP protein family identifies new functions critical for cell physiology*. Nat Commun, 2013. **4**: p. 2240.
140. Han, W., X. Li, and X. Fu, *The macro domain protein family: structure, functions, and their potential therapeutic implications*. Mutat Res, 2011. **727**(3): p. 86-103.

141. Gupte, R., Z. Liu, and W.L. Kraus, *PARPs and ADP-ribosylation: recent advances linking molecular functions to biological outcomes*. *Genes Dev*, 2017. **31**(2): p. 101-126.
142. Ame, J.C., C. Spenlehauer, and G. de Murcia, *The PARP superfamily*. *Bioessays*, 2004. **26**(8): p. 882-93.
143. Alemasova, E.E. and O.I. Lavrik, *Poly(ADP-ribosylation) by PARP1: reaction mechanism and regulatory proteins*. *Nucleic Acids Res*, 2019. **47**(8): p. 3811-3827.
144. Kiehlbauch, C.C., et al., *High resolution fractionation and characterization of ADP-ribose polymers*. *Anal Biochem*, 1993. **208**(1): p. 26-34.
145. Ray Chaudhuri, A. and A. Nussenzweig, *The multifaceted roles of PARP1 in DNA repair and chromatin remodelling*. *Nat Rev Mol Cell Biol*, 2017. **18**(10): p. 610-621.
146. Pascal, J.M. and T. Ellenberger, *The rise and fall of poly(ADP-ribose): An enzymatic perspective*. *DNA Repair (Amst)*, 2015. **32**: p. 10-16.
147. Jackson, S.P. and J. Bartek, *The DNA-damage response in human biology and disease*. *Nature*, 2009. **461**(7267): p. 1071-8.
148. Burkle, A. and L. Virag, *Poly(ADP-ribose): PARadigms and PARadoxes*. *Mol Aspects Med*, 2013. **34**(6): p. 1046-65.
149. Pazzaglia, S. and C. Pioli, *Multifaceted Role of PARP-1 in DNA Repair and Inflammation: Pathological and Therapeutic Implications in Cancer and Non-Cancer Diseases*. *Cells*, 2019. **9**(1).
150. Brown, J.S., et al., *Targeting DNA Repair in Cancer: Beyond PARP Inhibitors*. *Cancer Discov*, 2017. **7**(1): p. 20-37.
151. Li, M. and X. Yu, *Function of BRCA1 in the DNA damage response is mediated by ADP-ribosylation*. *Cancer Cell*, 2013. **23**(5): p. 693-704.
152. Haince, J.F., et al., *Ataxia telangiectasia mutated (ATM) signaling network is modulated by a novel poly(ADP-ribose)-dependent pathway in the early response to DNA-damaging agents*. *J Biol Chem*, 2007. **282**(22): p. 16441-53.
153. Deriano, L. and D.B. Roth, *Modernizing the nonhomologous end-joining repertoire: alternative and classical NHEJ share the stage*. *Annu Rev Genet*, 2013. **47**: p. 433-55.
154. Ame, J.C., et al., *PARP-2, A novel mammalian DNA damage-dependent poly(ADP-ribose) polymerase*. *J Biol Chem*, 1999. **274**(25): p. 17860-8.
155. Shieh, W.M., et al., *Poly(ADP-ribose) polymerase null mouse cells synthesize ADP-ribose polymers*. *J Biol Chem*, 1998. **273**(46): p. 30069-72.
156. Riccio, A.A., G. Cingolani, and J.M. Pascal, *PARP-2 domain requirements for DNA damage-dependent activation and localization to sites of DNA damage*. *Nucleic Acids Res*, 2016. **44**(4): p. 1691-702.
157. Wang, Z.Q., et al., *Mice lacking ADPRT and poly(ADP-ribosylation) develop normally but are susceptible to skin disease*. *Genes Dev*, 1995. **9**(5): p. 509-20.
158. de Murcia, J.M., et al., *Requirement of poly(ADP-ribose) polymerase in recovery from DNA damage in mice and in cells*. *Proc Natl Acad Sci U S A*, 1997. **94**(14): p. 7303-7.
159. Masutani, M., et al., *Poly(ADP-ribose) polymerase gene disruption conferred mice resistant to streptozotocin-induced diabetes*. *Proc Natl Acad Sci U S A*, 1999. **96**(5): p. 2301-4.
160. Mangerich, A. and A. Burkle, *Pleiotropic cellular functions of PARP1 in longevity and aging: genome maintenance meets inflammation*. *Oxid Med Cell Longev*, 2012. **2012**: p. 321653.
161. Piskunova, T.S., et al., *Deficiency in Poly(ADP-ribose) Polymerase-1 (PARP-1) Accelerates Aging and Spontaneous Carcinogenesis in Mice*. *Curr Gerontol Geriatr Res*, 2008: p. 754190.
162. Shall, S. and G. de Murcia, *Poly(ADP-ribose) polymerase-1: what have we learned from the deficient mouse model? Mutat Res*, 2000. **460**(1): p. 1-15.
163. Rojo, F., et al., *Nuclear PARP-1 protein overexpression is associated with poor overall survival in early breast cancer*. *Ann Oncol*, 2012. **23**(5): p. 1156-1164.
164. Dziaman, T., et al., *PARP-1 expression is increased in colon adenoma and carcinoma and correlates with OGG1*. *PLoS One*, 2014. **9**(12): p. e115558.

165. Byers, L.A., et al., *Proteomic profiling identifies dysregulated pathways in small cell lung cancer and novel therapeutic targets including PARP1*. *Cancer Discov*, 2012. **2**(9): p. 798-811.
166. Dorsam, B., et al., *PARP-1 protects against colorectal tumor induction, but promotes inflammation-driven colorectal tumor progression*. *Proc Natl Acad Sci U S A*, 2018. **115**(17): p. E4061-E4070.
167. Weaver, A.N. and E.S. Yang, *Beyond DNA Repair: Additional Functions of PARP-1 in Cancer*. *Front Oncol*, 2013. **3**: p. 290.
168. Hanahan, D. and R.A. Weinberg, *Hallmarks of cancer: the next generation*. *Cell*, 2011. **144**(5): p. 646-74.
169. Yaku, K., et al., *NAD Metabolism in Cancer Therapeutics*. *Front Oncol*, 2018. **8**: p. 622.
170. Ha, H.C. and S.H. Snyder, *Poly(ADP-ribose) polymerase is a mediator of necrotic cell death by ATP depletion*. *Proc Natl Acad Sci U S A*, 1999. **96**(24): p. 13978-82.
171. Yu, S.W., et al., *Mediation of poly(ADP-ribose) polymerase-1-dependent cell death by apoptosis-inducing factor*. *Science*, 2002. **297**(5579): p. 259-63.
172. Wang, Y., et al., *A nuclease that mediates cell death induced by DNA damage and poly(ADP-ribose) polymerase-1*. *Science*, 2016. **354**(6308).
173. Wang, Y., et al., *Poly(ADP-ribose) (PAR) binding to apoptosis-inducing factor is critical for PAR polymerase-1-dependent cell death (parthanatos)*. *Sci Signal*, 2011. **4**(167): p. ra20.
174. Rosenthal, D.S., et al., *Detection of DNA breaks in apoptotic cells utilizing the DNA binding domain of poly(ADP-ribose) polymerase with fluorescence microscopy*. *Nucleic Acids Res*, 1997. **25**(7): p. 1437-41.
175. Rosenthal, D.S., et al., *Intact cell evidence for the early synthesis, and subsequent late apoptin-mediated suppression, of poly(ADP-ribose) during apoptosis*. *Exp Cell Res*, 1997. **232**(2): p. 313-21.
176. Molinete, M., et al., *Overproduction of the poly(ADP-ribose) polymerase DNA-binding domain blocks alkylation-induced DNA repair synthesis in mammalian cells*. *EMBO J*, 1993. **12**(5): p. 2109-17.
177. Hinz, M., et al., *A cytoplasmic ATM-TRAF6-cIAP1 module links nuclear DNA damage signaling to ubiquitin-mediated NF-kappaB activation*. *Mol Cell*, 2010. **40**(1): p. 63-74.
178. Stilmann, M., et al., *A nuclear poly(ADP-ribose)-dependent signalosome confers DNA damage-induced IkkappaB kinase activation*. *Mol Cell*, 2009. **36**(3): p. 365-78.
179. Rosado, M.M., et al., *Beyond DNA repair, the immunological role of PARP-1 and its siblings*. *Immunology*, 2013. **139**(4): p. 428-37.
180. Bai, P. and L. Virag, *Role of poly(ADP-ribose) polymerases in the regulation of inflammatory processes*. *FEBS Lett*, 2012. **586**(21): p. 3771-7.
181. Cohen-Armon, M., et al., *DNA-independent PARP-1 activation by phosphorylated ERK2 increases Elk1 activity: a link to histone acetylation*. *Mol Cell*, 2007. **25**(2): p. 297-308.
182. Rodriguez, M.I., et al., *PARP-1 regulates metastatic melanoma through modulation of vimentin-induced malignant transformation*. *PLoS Genet*, 2013. **9**(6): p. e1003531.
183. Simbulan-Rosenthal, C.M., et al., *PARP-1 binds E2F-1 independently of its DNA binding and catalytic domains, and acts as a novel coactivator of E2F-1-mediated transcription during re-entry of quiescent cells into S phase*. *Oncogene*, 2003. **22**(52): p. 8460-71.
184. Lin, Y., et al., *Identification of PARP-1 as one of the transcription factors binding to the repressor element in the promoter region of COX-2*. *Arch Biochem Biophys*, 2011. **505**(1): p. 123-9.
185. Kanai, M., et al., *Involvement of poly(ADP-Ribose) polymerase 1 and poly(ADP-Ribosyl)ation in regulation of centrosome function*. *Mol Cell Biol*, 2003. **23**(7): p. 2451-62.
186. Kim, M.Y., et al., *NAD⁺-dependent modulation of chromatin structure and transcription by nucleosome binding properties of PARP-1*. *Cell*, 2004. **119**(6): p. 803-14.
187. Reale, A., et al., *Modulation of DNMT1 activity by ADP-ribose polymers*. *Oncogene*, 2005. **24**(1): p. 13-9.

188. Murai, J., et al., *Trapping of PARP1 and PARP2 by Clinical PARP Inhibitors*. Cancer Res, 2012. **72**(21): p. 5588-99.
189. Hopkins, T.A., et al., *Mechanistic Dissection of PARP1 Trapping and the Impact on In Vivo Tolerability and Efficacy of PARP Inhibitors*. Mol Cancer Res, 2015. **13**(11): p. 1465-77.
190. Kaufman, B., et al., *Olaparib monotherapy in patients with advanced cancer and a germline BRCA1/2 mutation*. J Clin Oncol, 2015. **33**(3): p. 244-50.
191. Morales, J., et al., *Review of poly (ADP-ribose) polymerase (PARP) mechanisms of action and rationale for targeting in cancer and other diseases*. Crit Rev Eukaryot Gene Expr, 2014. **24**(1): p. 15-28.
192. Keung, M.Y.T., Y. Wu, and J.V. Vadgama, *PARP Inhibitors as a Therapeutic Agent for Homologous Recombination Deficiency in Breast Cancers*. J Clin Med, 2019. **8**(4).
193. Jain, P.G. and B.D. Patel, *Medicinal chemistry approaches of poly ADP-Ribose polymerase 1 (PARP1) inhibitors as anticancer agents - A recent update*. Eur J Med Chem, 2019. **165**: p. 198-215.
194. Ha, D.H., et al., *Antitumor effect of a WEE1 inhibitor and potentiation of olaparib sensitivity by DNA damage response modulation in triple-negative breast cancer*. Sci Rep, 2020. **10**(1): p. 9930.
195. Pillie, P.G., et al., *PARP Inhibitors: Extending Benefit Beyond BRCA-Mutant Cancers*. Clin Cancer Res, 2019. **25**(13): p. 3759-3771.
196. Yap, T.A., et al., *The DNA Damaging Revolution: PARP Inhibitors and Beyond*. Am Soc Clin Oncol Educ Book, 2019. **39**: p. 185-195.
197. Mehibel, M., et al., *Eliminating hypoxic tumor cells improves response to PARP inhibitors in homologous recombination-deficient cancer models*. J Clin Invest, 2021. **131**(11).
198. Ricks, T.K., et al., *Successes and Challenges of PARP Inhibitors in Cancer Therapy*. Front Oncol, 2015. **5**: p. 222.
199. Menissier de Murcia, J., et al., *Functional interaction between PARP-1 and PARP-2 in chromosome stability and embryonic development in mouse*. EMBO J, 2003. **22**(9): p. 2255-63.
200. Ricci, A.D., et al., *PARP Inhibitors in Biliary Tract Cancer: A New Kid on the Block?* Medicines (Basel), 2020. **7**(9).
201. Ku, A.A., et al., *Integration of multiple biological contexts reveals principles of synthetic lethality that affect reproducibility*. Nat Commun, 2020. **11**(1): p. 2375.
202. Khan, S.A., S. Tavolari, and G. Brandi, *Cholangiocarcinoma: Epidemiology and risk factors*. Liver Int, 2019. **39 Suppl 1**: p. 19-31.
203. Hähnel, P.S., et al., *Targeting components of the alternative NHEJ pathway sensitizes KRAS mutant leukemic cells to chemotherapy*. Blood, 2014. **123**(15): p. 2355-66.
204. Miyagiwa, M., et al., *A new human cholangiocellular carcinoma cell line (HuCC-T1) producing carbohydrate antigen 19/9 in serum-free medium*. In Vitro Cell Dev Biol, 1989. **25**(6): p. 503-10.
205. Enjoji, M., et al., *Sarcomatous and adenocarcinoma cell lines from the same nodule of cholangiocarcinoma*. In Vitro Cell Dev Biol Anim, 1997. **33**(9): p. 681-3.
206. Kusaka, Y., T. Tokiwa, and J. Sato, *Establishment and characterization of a cell line from a human cholangiocellular carcinoma*. Res Exp Med (Berl), 1988. **188**(5): p. 367-75.
207. Bass, D.A., et al., *Flow cytometric studies of oxidative product formation by neutrophils: a graded response to membrane stimulation*. J Immunol, 1983. **130**(4): p. 1910-7.
208. Gu, Z., R. Eils, and M. Schlesner, *Complex heatmaps reveal patterns and correlations in multidimensional genomic data*. Bioinformatics, 2016. **32**(18): p. 2847-9.
209. Subramanian, A., et al., *Gene set enrichment analysis: a knowledge-based approach for interpreting genome-wide expression profiles*. Proc Natl Acad Sci U S A, 2005. **102**(43): p. 15545-50.
210. Kramer, A., et al., *Causal analysis approaches in Ingenuity Pathway Analysis*. Bioinformatics, 2014. **30**(4): p. 523-30.

211. Tang, Z., et al., *GEPIA2: an enhanced web server for large-scale expression profiling and interactive analysis*. *Nucleic Acids Res*, 2019. **47**(W1): p. W556-W560.
212. Boehler, C., et al., *Phenotypic characterization of Parp-1 and Parp-2 deficient mice and cells*. *Methods Mol Biol*, 2011. **780**: p. 313-36.
213. Cancer Genome Atlas Research, N., et al., *The Cancer Genome Atlas Pan-Cancer analysis project*. *Nat Genet*, 2013. **45**(10): p. 1113-20.
214. Consortium, G.T., *The Genotype-Tissue Expression (GTEx) project*. *Nat Genet*, 2013. **45**(6): p. 580-5.
215. Ronen, A. and B.W. Glickman, *Human DNA repair genes*. *Environ Mol Mutagen*, 2001. **37**(3): p. 241-83.
216. Massa, A., et al., *Evolution of the Experimental Models of Cholangiocarcinoma*. *Cancers (Basel)*, 2020. **12**(8).
217. Castven, D., et al., *Adverse genomic alterations and stemness features are induced by field cancerization in the microenvironment of hepatocellular carcinomas*. *Oncotarget*, 2017. **8**(30): p. 48688-48700.
218. Menear, K.A., et al., *4-[3-(4-cyclopropanecarbonylpiperazine-1-carbonyl)-4-fluorobenzyl]-2H-phthalazin-1-one: a novel bioavailable inhibitor of poly(ADP-ribose) polymerase-1*. *J Med Chem*, 2008. **51**(20): p. 6581-91.
219. Fong, P.C., et al., *Inhibition of poly(ADP-ribose) polymerase in tumors from BRCA mutation carriers*. *N Engl J Med*, 2009. **361**(2): p. 123-34.
220. Underhill, C., M. Toulmonde, and H. Bonnefoi, *A review of PARP inhibitors: from bench to bedside*. *Ann Oncol*, 2011. **22**(2): p. 268-79.
221. Wang, D., et al., *Cytotoxic p-Terphenyls from a Marine-Derived Nocardiosis Species*. *J Nat Prod*, 2019. **82**(12): p. 3504-3508.
222. Yang, W., et al., *Genomics of Drug Sensitivity in Cancer (GDSC): a resource for therapeutic biomarker discovery in cancer cells*. *Nucleic Acids Res*, 2013. **41**(Database issue): p. D955-61.
223. Kurreck, J., *RNA interference: from basic research to therapeutic applications*. *Angew Chem Int Ed Engl*, 2009. **48**(8): p. 1378-98.
224. Craig, A.J., et al., *Tumour evolution in hepatocellular carcinoma*. *Nat Rev Gastroenterol Hepatol*, 2020. **17**(3): p. 139-152.
225. Javle, M., et al., *Biliary cancer: Utility of next-generation sequencing for clinical management*. *Cancer*, 2016. **122**(24): p. 3838-3847.
226. Hyder, O., et al., *Intra-arterial therapy for advanced intrahepatic cholangiocarcinoma: a multi-institutional analysis*. *Ann Surg Oncol*, 2013. **20**(12): p. 3779-86.
227. Sia, D., et al., *Intrahepatic cholangiocarcinoma: pathogenesis and rationale for molecular therapies*. *Oncogene*, 2013. **32**(41): p. 4861-70.
228. Stolze, B., et al., *Comparative analysis of KRAS codon 12, 13, 18, 61, and 117 mutations using human MCF10A isogenic cell lines*. *Sci Rep*, 2015. **5**: p. 8535.
229. Chung, T., et al., *Clinicopathological characteristics of intrahepatic cholangiocarcinoma according to gross morphologic type: cholangiolocellular differentiation traits and inflammation- and proliferation-phenotypes*. *HPB (Oxford)*, 2020. **22**(6): p. 864-873.
230. Gilad, O., et al., *Combining ATR suppression with oncogenic Ras synergistically increases genomic instability, causing synthetic lethality or tumorigenesis in a dosage-dependent manner*. *Cancer Res*, 2010. **70**(23): p. 9693-702.
231. Grabocka, E., et al., *Wild-type H- and N-Ras promote mutant K-Ras-driven tumorigenesis by modulating the DNA damage response*. *Cancer Cell*, 2014. **25**(2): p. 243-56.
232. Luo, J., et al., *A genome-wide RNAi screen identifies multiple synthetic lethal interactions with the Ras oncogene*. *Cell*, 2009. **137**(5): p. 835-48.
233. Wang, M., et al., *PARP-1 and Ku compete for repair of DNA double strand breaks by distinct NHEJ pathways*. *Nucleic Acids Res*, 2006. **34**(21): p. 6170-82.
234. Fahrner, J. and B. Kaina, *O6-methylguanine-DNA methyltransferase in the defense against N-nitroso compounds and colorectal cancer*. *Carcinogenesis*, 2013. **34**(11): p. 2435-42.

235. Liu, Y., et al., *High PARP-1 expression is associated with tumor invasion and poor prognosis in gastric cancer*. *Oncol Lett*, 2016. **12**(5): p. 3825-3835.
236. Bi, F.F., D. Li, and Q. Yang, *Hypomethylation of ETS transcription factor binding sites and upregulation of PARP1 expression in endometrial cancer*. *Biomed Res Int*, 2013. **2013**: p. 946268.
237. Xu, F., et al., *Cytoplasmic PARP-1 promotes pancreatic cancer tumorigenesis and resistance*. *Int J Cancer*, 2019. **145**(2): p. 474-483.
238. Kim, K.M., et al., *Individual and Combined Expression of DNA Damage Response Molecules PARP1, gammaH2AX, BRCA1, and BRCA2 Predict Shorter Survival of Soft Tissue Sarcoma Patients*. *PLoS One*, 2016. **11**(9): p. e0163193.
239. Gan, A., et al., *Poly(adenosine diphosphate-ribose) polymerase expression in BRCA-proficient ovarian high-grade serous carcinoma; association with patient survival*. *Hum Pathol*, 2013. **44**(8): p. 1638-47.
240. Zhai, L., et al., *Polymorphisms in poly (ADP-ribose) polymerase-1 (PARP1) promoter and 3' untranslated region and their association with PARP1 expression in breast cancer patients*. *Int J Clin Exp Pathol*, 2015. **8**(6): p. 7059-71.
241. Shimizu, S., et al., *Expression of poly(ADP-ribose) polymerase in human hepatocellular carcinoma and analysis of biopsy specimens obtained under sonographic guidance*. *Oncol Rep*, 2004. **12**(4): p. 821-5.
242. Nomura, F., et al., *Enhancement of poly-adenosine diphosphate-ribosylation in human hepatocellular carcinoma*. *J Gastroenterol Hepatol*, 2000. **15**(5): p. 529-35.
243. Li, J., et al., *PARP-1 serves as a novel molecular marker for hepatocellular carcinoma in a Southern Chinese Zhuang population*. *Tumour Biol*, 2017. **39**(7): p. 1010428317706914.
244. Uhlen, M., et al., *A human protein atlas for normal and cancer tissues based on antibody proteomics*. *Mol Cell Proteomics*, 2005. **4**(12): p. 1920-32.
245. Taketomi, A., et al., *A rare point mutation in the Ras oncogene in hepatocellular carcinoma*. *Surg Today*, 2013. **43**(3): p. 289-92.
246. Xue, R., et al., *Genomic and Transcriptomic Profiling of Combined Hepatocellular and Intrahepatic Cholangiocarcinoma Reveals Distinct Molecular Subtypes*. *Cancer Cell*, 2019. **35**(6): p. 932-947 e8.
247. Dean, E., et al., *Phase I study to assess the safety and tolerability of olaparib in combination with bevacizumab in patients with advanced solid tumours*. *Br J Cancer*, 2012. **106**(3): p. 468-74.
248. Mao, Y., et al., *PARP inhibitor olaparib sensitizes cholangiocarcinoma cells to radiation*. *Cancer Med*, 2018. **7**(4): p. 1285-1296.
249. Sachdev, E., et al., *PARP Inhibition in Cancer: An Update on Clinical Development*. *Target Oncol*, 2019. **14**(6): p. 657-679.
250. Parsels, L.A., et al., *PARP1 Trapping and DNA Replication Stress Enhance Radiosensitization with Combined WEE1 and PARP Inhibitors*. *Mol Cancer Res*, 2018. **16**(2): p. 222-232.
251. Wang, C., et al., *Rational combination therapy for hepatocellular carcinoma with PARP1 and DNA-PK inhibitors*. *Proc Natl Acad Sci U S A*, 2020. **117**(42): p. 26356-26365.
252. Huang, S.H., et al., *PJ34, an inhibitor of PARP-1, suppresses cell growth and enhances the suppressive effects of cisplatin in liver cancer cells*. *Oncol Rep*, 2008. **20**(3): p. 567-72.
253. Quiles-Perez, R., et al., *Inhibition of poly adenosine diphosphate-ribose polymerase decreases hepatocellular carcinoma growth by modulation of tumor-related gene expression*. *Hepatology*, 2010. **51**(1): p. 255-66.
254. Lord, C.J. and A. Ashworth, *PARP inhibitors: Synthetic lethality in the clinic*. *Science*, 2017. **355**(6330): p. 1152-1158.
255. Zhong, L., et al., *Dual inhibition of VEGF and PARP suppresses KRAS-mutant colorectal cancer*. *Neoplasia*, 2020. **22**(9): p. 365-375.
256. Rogakou, E.P., et al., *Megabase chromatin domains involved in DNA double-strand breaks in vivo*. *J Cell Biol*, 1999. **146**(5): p. 905-16.

257. Arena, S., et al., *A Subset of Colorectal Cancers with Cross-Sensitivity to Olaparib and Oxaliplatin*. Clin Cancer Res, 2020. **26**(6): p. 1372-1384.
258. Jinesh, G.G., et al., *Molecular genetics and cellular events of K-Ras-driven tumorigenesis*. Oncogene, 2018. **37**(7): p. 839-846.
259. Park, M.T., et al., *Novel signaling axis for ROS generation during K-Ras-induced cellular transformation*. Cell Death Differ, 2014. **21**(8): p. 1185-97.
260. Ferino, A., V. Rapozzi, and L.E. Xodo, *The ROS-KRAS-Nrf2 axis in the control of the redox homeostasis and the intersection with survival-apoptosis pathways: Implications for photodynamic therapy*. J Photochem Photobiol B, 2020. **202**: p. 111672.
261. Hou, D., et al., *Increased oxidative stress mediates the antitumor effect of PARP inhibition in ovarian cancer*. Redox Biol, 2018. **17**: p. 99-111.
262. Isabelle, M., et al., *Investigation of PARP-1, PARP-2, and PARG interactomes by affinity-purification mass spectrometry*. Proteome Sci, 2010. **8**: p. 22.
263. Pines, A., et al., *PARP1 promotes nucleotide excision repair through DDB2 stabilization and recruitment of ALC1*. J Cell Biol, 2012. **199**(2): p. 235-49.
264. Paddock, M.N., et al., *Competition between PARP-1 and Ku70 control the decision between high-fidelity and mutagenic DNA repair*. DNA Repair (Amst), 2011. **10**(3): p. 338-43.
265. Scully, R., et al., *DNA double-strand break repair-pathway choice in somatic mammalian cells*. Nat Rev Mol Cell Biol, 2019. **20**(11): p. 698-714.
266. Schreiber, V., et al., *A dominant-negative mutant of human poly(ADP-ribose) polymerase affects cell recovery, apoptosis, and sister chromatid exchange following DNA damage*. Proc Natl Acad Sci U S A, 1995. **92**(11): p. 4753-7.
267. Swindall, A.F., J.A. Stanley, and E.S. Yang, *PARP-1: Friend or Foe of DNA Damage and Repair in Tumorigenesis?* Cancers (Basel), 2013. **5**(3): p. 943-58.
268. Liu, L., et al., *Lipopolysaccharide activates ERK-PARP-1-RelA pathway and promotes nuclear factor-kappaB transcription in murine macrophages*. Hum Immunol, 2012. **73**(5): p. 439-47.
269. Cinque, G., et al., *Role of Poly [ADP-ribose] Polymerase 1 in Activating the Kirsten ras (KRAS) Gene in Response to Oxidative Stress*. Int J Mol Sci, 2020. **21**(17).
270. Cogoi, S., et al., *The KRAS promoter responds to Myc-associated zinc finger and poly(ADP-ribose) polymerase 1 proteins, which recognize a critical quadruplex-forming GA-element*. J Biol Chem, 2010. **285**(29): p. 22003-16.
271. Loeuillard, E., et al., *Animal models of cholangiocarcinoma*. Biochim Biophys Acta Mol Basis Dis, 2019. **1865**(5): p. 982-992.
272. Saborowski, A., et al., *Murine Liver Organoids as a Genetically Flexible System to Study Liver Cancer In Vivo and In Vitro*. Hepatol Commun, 2019. **3**(3): p. 423-436.
273. Connor, F., et al., *Mutational landscape of a chemically-induced mouse model of liver cancer*. J Hepatol, 2018. **69**(4): p. 840-850.
274. Jaworski, M., et al., *B-raf and Ha-ras mutations in chemically induced mouse liver tumors*. Oncogene, 2005. **24**(7): p. 1290-5.
275. Tong, W.M., et al., *Null mutation of DNA strand break-binding molecule poly(ADP-ribose) polymerase causes medulloblastomas in p53(-/-) mice*. Am J Pathol, 2003. **162**(1): p. 343-52.
276. Sun, C., et al., *Rational combination therapy with PARP and MEK inhibitors capitalizes on therapeutic liabilities in RAS mutant cancers*. Sci Transl Med, 2017. **9**(392).

8. Appendix

Supplementary Table 1: List of genes used for analysis of transcriptomic data of human iCCA samples, *in vitro*, *in vivo* data, and CCA tissue microarray.

APEX1	APEX2	ATM	ATR	ATXN3	BARD1	BRCA1	BRCA2
CCNH	CCNO	CHEK1	CHEK2	CDK7	DCLRE1C	DDB1	DDB2
DMC1	ERCC1	ERCC2	ERCC3	ERCC4	ERCC5	ERCC6	ERCC8
EXO1	FEN1	LIG1	LIG3	LIG4	MGMT	MMS19	MRE11A
MPG	MUTYH	NBN	NEIL1	NEIL2	NEIL3	NHEJ1	NTHL1
OGG1	PARP1	PARP2	PARP3	PNKP	POLB	POLL	POLQ
PRKDC	RBBP8	RAD18	RAD21	RAD23A	RAD50	RAD51	RAD51C
RAD51B	RAD51D	RAD52	RAD54L	RFC1	RPA1	RPA2	SMC1
SLK	SMUG1	TDG	TOP3A	TOP3B	UIMC1	UNG	WRN
XAB2	XPA	XPC	XRCC1	XRCC2	XRCC3	XRCC4	XRCC5
XRCC6	XRCC6BP1						

Friederike Luise Keggenhoff (née Mahn)

Address:

████████████████████

████████████████████

Phone:

████████████████████

E-mail:

████████████████████

Date of Birth:

27.08.1990

Nationality:

German



Education

- 10.2016 - **Doctoral Researcher**
08.2021
University Medical Center of the Johannes Gutenberg University, Mainz, Germany
Research Group for Molecular Hepatocarcinogenesis
Head: Prof. Dr. Jens Marquardt
Doctoral Thesis: Impact of Poly(ADP-ribose) polymerase 1 on phenotypic and molecular features in KRAS-driven intrahepatic cholangiocarcinoma
- 10.2013 - **Master of Science in Nutritional Sciences**
02.2016
Justus Liebig University of Gießen, Germany
Focus: Molecular Biology, Toxicology, Food Law
Grade: 1.0 (scale 1 of 6, 1 is highest)
Master Thesis: VAPA and VAPB as positive modulators of autophagy
- 10.2010 - **Bachelor of Sciences in Nutritional Sciences**
09.2013
Justus Liebig University of Gießen, Germany
Grade: 1.4 (scale 1 of 6, 1 is highest)
Bachelor Thesis: The influence of Resveratrol on the proteostasis in an Alzheimer's disease model of *Caenorhabditis elegans*

Professional Experience

- 03.2021 - **Scientific Management - Assistant Coordinator**
present
Institute of Molecular Biology gGmbH, Mainz, Germany
- Management of International PhD Programme (IPP) and SFB 1361
 - Planned and managed scientific seminars, workshops, and events
 - Monitored and controlled third party funding
 - Established and maintained research collaborations
 - Wrote project proposals and reports
- 10.2016 - **Doctoral Researcher / Research Associate**
08.2021
University Medical Center Mainz, JGU, Mainz, Germany
- Deputy project manager of the genetic engineering facility and animal testing project

- Planned and managed scientific projects, experimental setup organization, data collection and analysis of results
- Established and maintained research collaborations
- Organized and moderated seminars, supervised undergraduate students
- Presented and published scientific data on national and international conferences

03.2016 - Intern Global Regulatory Affairs

08.2016

Merck Consumer Healthcare, Darmstadt, Germany

- Assessed regulatory data for new product developments
- Assisted with notifications/renewals of products in contact with national authorities
- Set up of overviews and presentations to summarize regulatory information and assessments

Qualifications

Laboratory skills

- Molecular biology (DNA/RNA isolation, molecular cloning, gel electrophoresis, transformation, RNA Sequencing)
- Proteinbiochemistry (protein isolation, SDS-page, Western Blotting)
- Eukaryotic cell culture handling (primary cell culture (2D, organoid) functional assays, transfection (siRNA, CRIPSR/Cas))
- Immunohistochemistry, Immunofluorescence, Flow cytometry
- Spectrophotometry/fluorimetry
- Animal handling (mouse, HDTV), preparation of animal research proposals

Selected courses

03.2020 IPMA Project Management - Basic certificate
 11.2019 Safety in genetic engineering
 02.2019 Writing for the public / Scientific writing
 09.2018 CRISPR Genome editing workshop and symposium
 04.2018 Bioinformatics: Introduction to R
 03.2018 Ingenuity Pathway Analysis (IPA) Workshop
 03.2018 Introduction to Biostatistics
 02.2017 FELASA B certificate

Conferences attended

01.2021 GASL Annual Meeting 2020, digital, Germany (oral presentation)
 02.2020 EASL Liver Cancer Summit, 2020 Prague, Czech Republic (poster)
 02.2020 GASL Annual Meeting 2020, Mainz, Germany (poster)
 11.2019 GARPS Annual Meeting 2019, Bad Kreuznach, Germany (poster)
 11.2019 The Liver Meeting, AASLD, Boston MA, USA (poster)
 09.2019 2nd UCT Science Day 2019, Mainz, Germany (oral presentation)
 02.2019 20th AEK conference 2019, Heidelberg, Germany (poster)
 11.2018 GARPS Annual Meeting 2018, Bad Kreuznach, Germany (poster)
 09.2018 UCT Science Day 2018, Mainz, Germany (poster)

Language skills

German (native)
 English (advanced)

IT-skills

Microsoft Office, IPA, GSEA
 Graphpad Prism, Adobe Illustrator, Image J, Image Lab, ZEN

Awards and Scholarship

02.2020	Young Investigator Registration Bursary, EASL Liver Cancer Summit
11.2019	Poster Prize „Basic Science“, GARPS Annual Meeting 2019
09.2019	Best Talk Award, 2 nd UCT Science Day
2016 – 2021	Fellowship, International PhD Program (IPP), Institute of Molecular Biology gGmbH (IMB)
2012 – 2016	Undergraduate Scholarship, German Academic Scholarship Foundation (Studienstiftung des Deutschen Volkes)

[REDACTED]

[REDACTED]

[REDACTED] [REDACTED]
[REDACTED] [REDACTED]
[REDACTED] [REDACTED]

[REDACTED] [REDACTED]
[REDACTED] [REDACTED]
[REDACTED] [REDACTED]
[REDACTED] [REDACTED]
[REDACTED] [REDACTED]

[REDACTED] [REDACTED]
[REDACTED] [REDACTED]

List of Publications

- Keggenhoff, F.L.**, Castven, D., Becker, D., Hajduk, J., Czauderna, C., Straub, B., Fahrner, J., Andersen, J.B., Matter, M.S., Sina, C., Derer, S., Roessler, S., Kaina, B., Galle, P.R., Marquardt, J.U.
"Poly(ADP-ribose) polymerase 1 selectively impairs phenotypic and molecular features of KRAS-driven intrahepatic cholangiocarcinoma." (*manuscript in preparation*)
Castven, D., Czauderna, C., Becker, D., Pereira, S., Schmitt, J., Weinmann, A., Shah, V., Hajduk, J., **Keggenhoff, F.**, et al. (2021).
"Acquired Resistance to Antiangiogenic Therapies in Hepatocellular Carcinoma Is Mediated by Yes-Associated Protein 1 Activation and Transient Expansion of Stem-Like Cancer Cells." *Hepatology* 71(4):1869-1880. doi:10.1002/hep4.1869.
- Mahn, F.L.**, Franck, S., Czauderna, C., Marquardt, J.U. (2019).
"Nutrition, (Cancer-)Stem Cells and Cancer Prevention." Chapter in *Nutrition and Cancer Prevention: From Molecular Mechanisms to Dietary Recommendations*. The Royal Society of Chemistry 2020.
Czauderna, C., Castven, D., **Mahn, F.L.**, Marquardt, J.U. (2019).
"Context-Dependent Role of NF-kappaB Signaling in Primary Liver Cancer-from Tumor Development to Therapeutic Implications." *Cancers (Basel)* 11(8).
Castven, D., Becker, D., Czauderna, C., Wilhelm, D., Andersen, J. B., Strand, S., Hartmann, M., Heilmann-Heimbach, S., Roth, W., Hartmann, N., Straub, B. K., **Mahn, F. L.**, Franck, S. et al. (2019).
"Application of patient-derived liver cancer cells for phenotypic characterization and therapeutic target identification." *Int J Cancer* 144(11): 2782-2794.
Czauderna, C., Palestino-Dominguez, M., Castven, D., Becker, D., Zanon-Rodriguez, L., Hajduk, J., **Mahn, F.L.**, Herr, M., Strand, D., Strand, S., Heilmann-Heimbach, S., Gomez-Quiroz, L.E., et al. (2018).
"Ginkgo biloba induces different gene expression signatures and oncogenic pathways in malignant and non-malignant cells of the liver." *PLoS One* 13(12): e0209067.
Regitz, C., Fitzenberger, E., **Mahn, F.L.**, Dußling, L.M., Wenzel, U (2016).
"Resveratrol reduces amyloid-beta (Aβ₁₋₄₂)-induced paralysis through targeting proteostasis in an Alzheimer model of *Caenorhabditis elegans*." *Eur J Nutr* 55(2): 741-747.

Acknowledgements

[REDACTED]

[REDACTED]

[REDACTED]

[REDACTED]

[REDACTED]

[REDACTED]

[REDACTED]

[REDACTED]

[REDACTED]

[REDACTED]

